Technische Universität München
TUM School of Natural Sciences

Real Space Approach to Electronic and Optical Excitations in Organic and Inorganic Semiconductors

Konrad Merkel

Vollständiger Abdruck der von der TUM School of Natural Sciences der Technischen Universität München zur Erlangung eines

Doktors der Naturwissenschaften (Dr. rer. nat.)

genehmigten Dissertation.

Vorsitz:
Prof. Dr. Jürgen Hauer

Prüfende der Dissertation:
1. Prof. Dr. Frank Ortmann
2. Prof. Dr. Christopher Stein
3. Prof. Dr. Wolf-Gero Schmidt

Die Dissertation wurde am 28.02.2024 bei der Technischen Universität München eingereicht und durch die TUM School of Natural Sciences am 03.04.2024 angenommen.

To Matthäa and my parents.

Abstract

Electronic and optical excitations in solid-state materials determine the properties of a material. A precise understanding is therefore essential for developing novel applications and improving the performance of many (opto-)electronic devices. In this dissertation, we mainly focus on three aspects that are relevant for applied and fundamental research. The first aspect is the effect of electron-phonon coupling on charge transport, which is illustrated using the example of organic molecular crystals, where the effect is particularly strong. The second aspect concerns the structure-property relationship of the electronic structure, which is important for material selection. It is particularly crucial for covalent organic frameworks, which is a class of organic materials where different molecular building blocks are combined into a single crystal structure. They show a remarkably high flexibility in combining various different chemical structures, which increases the need for precise understanding and predictions. The third aspect addresses the efficient calculation of optical properties. Such properties are computationally expensive, as they require a quantum many-body description that cannot be simplified by an effective single-particle approach. In all these cases, we show that a localized real-space basis, which can consist of either (symmetrized) molecular orbitals or, equivalently, maximally localized Wannier functions, enables calculations with superior performance while being chemically intuitive. With this real-space approach it is possible to implement the coupling to low-frequency phonon modes as vibrational disorder and to analyze the electronic properties of the π-system and aromaticity in detail. Furthermore, we show that the exciton Hamiltonian becomes very sparse within a basis of maximally localized Wannier functions, which allows a very efficient calculation of optical properties. We demonstrate that this approach scales linearly with system size, which is a remarkable improvement over other established approaches. With this newly developed method we therefore envision optical calculations even for large system which have been too costly before.

Zusammenfassung

Elektronische und optische Anregungen in Festkörpermaterialien bestimmen deren Eigenschaften. Ein genaues Verständnis ist daher für die Entwicklung neuer Anwendungen und Leistungsverbesserungen zahlreicher (opto-)elektronischer Bauelemente unerlässlich. In dieser Dissertation konzentrieren wir uns auf drei Aspekte, die sowohl für angewandte als auch Grundlagenforschung relevant sind. Der erste Aspekt ist die Auswirkung der Elektron-Phonon-Kopplung auf den Ladungstransport, die am Beispiel von organischen Molekülkristallen veranschaulicht wird, wo der Effekt besonders stark ist. Der zweite Aspekt betrifft die Struktur-Eigenschafts-Beziehung der elektronischen Struktur, die für die Materialauswahl entscheidend ist. Dies ist besonders wichtig für kovalent-organische Gerüststrukturen, eine Klasse von organischen Materialien, bei denen verschiedene molekulare Bausteine in einer gemeinsamen Kristallstruktur kombiniert werden. Sie weisen eine bemerkenswert hohe Flexibilität bei der Kombination verschiedener chemischer Strukturen auf, was ein präzises Verständnis und Vorhersagen erforderlich macht. Der dritte Aspekt ist die effiziente Berechnung von optischen Eigenschaften. Solche Eigenschaften sind sehr rechenintensiv, da sie eine Quanten-Mehrteilchen-Beschreibung erfordern, die nicht durch einen effektiven Ein-Teilchen-Ansatz vereinfacht werden kann. In all diesen Fällen zeigen wir, dass eine Basis aus lokalisierten Funktionen, die entweder aus (symmetrisierten) Molekülorbitalen oder, äquivalent dazu, aus maximal lokalisierten Wannier-Funktionen bestehen kann, Berechnungen mit überragender Performance ermöglicht und gleichzeitig chemisch intuitiv ist. Mit diesem Realraum-Ansatz ist es möglich, die Kopplung an niederfrequente Phononmoden als Unordnung zu implementieren und die elektronischen Eigenschaften des π-Systems und die Aromatizität im Detail zu analysieren. Darüber hinaus zeigen wir, dass der Exciton-Hamiltonian in der Basis von maximal lokalisierten Wannier-Funktionen sehr dünn besetzt ist, was eine sehr effiziente Berechnung optischer Eigenschaften ermöglicht. Wir zeigen, dass dieser Ansatz linear mit der Systemgröße skaliert, was eine bemerkenswerte Verbesserung gegenüber anderen etablierten Ansätzen darstellt. Mit dieser neu entwickelten Methode sind optische Berechnungen auch für große Systeme denkbar, die bisher zu rechenaufwändig waren.

Publication list

Relevant for this dissertation:

1. Merkel, K., Panhans, M., Hutsch, S., & Ortmann, F. Interplay of band occupation, localization, and polaron renormalization for electron transport in molecular crystals: Naphthalene as a case study. Physical Review B, 105(16), 165136 (2022).
   https://doi.org/10.1103/PhysRevB.105.165136

2. Merkel, K., Greiner, J., & Ortmann, F. Understanding the electronic pi-system of 2D covalent organic frameworks with Wannier functions. Scientific Reports, 13(1), 1685 (2023).
   https://doi.org/10.1038/s41598-023-28285-w

3. Merkel, K. & Ortmann, F. Linear scaling approach for optical excitations using maximally localized Wannier functions. Journal of Physics: Materials 7, 015001 (2023).
   https://dx.doi.org/10.1088/2515-7639/ad06cd

Additional publications:

4. Merkel, K., Link, V., Luoma, K., & Strunz, W. T. Phase space theory for open quantum systems with local and collective dissipative processes. Journal of Physics A: Mathematical and Theoretical, 54(3), 035303 (2020).
   https://dx.doi.org/10.1088/1751-8121/abd155

Acknowledgment / Danksagung

Ich möchte an dieser Stelle den Menschen danken, die es mir ermöglicht haben diese Arbeit zu schreiben und mich auf dem Weg dahin unterstützt haben. Dies ist vor allem mein Doktorvater Prof. Frank Ortmann, der mich über die Jahre betreut hat und mir ein sehr guter Mentor war. Ich schätze es sehr, dass er sich immer ausreichend Zeit für offene Fragen und Probleme genommen hat und mich damit tatkräftig unterstützt hat. Dies ist keineswegs selbstverständlich und zeichnet in meinen Augen unsere Forschungsgruppe aus. Innerhalb unserer Gruppe gilt ein besonderer Dank Max Dorfner mit dem ich über die Jahre sehr viele anregende Gespräche hatte und der diese Dissertation mit viel Sorgfalt gegen-gelesen hat. Insbesondere schätze ich unseren freundschaftlichen Diskurs, der uns gegenseitig oft ein Stück weiter gebracht hat und zu einem wesentlich tieferen Verständnis beigetragen hat. Obwohl unsere Forschungsgebiete sich nicht direkt überlappen, konnten wir uns oft gegenseitig weiterhelfen und einander neue Perspektiven aufzeigen. Weiterhin möchte ich den Mitautoren meiner Publikationen Michel Panhans, Sebastian Hutsch, Johannes Grainer und Frank Ortmann für ihre Beiträge und zahlreiche Diskussionen danken. Durch ihre Arbeit war es möglich die entstandenen Publikationen reichhaltiger und attraktiver zu machen. Weiterhin möchte ich auch Moritz Richter für sprachliche Korrekturen an dieser Dissertation danken.

Auch aus meinem privaten Umfeld möchte ich zahlreichen Menschen für ihre Unterstützung danken. Allen voran möchte ich meiner Freundin Matthäa Ebersbach danken, die extra wegen meiner Promotion mit mir nach München gezogen ist und mich stets in schönen und schwierigen Momenten unterstützt hat. Durch sie ist mein Leben um viele Aspekte schöner und reicher geworden, worüber ich sehr froh bin. Zu guter Letzt möchte ich noch meinen Eltern danken, die über mein gesamtes Leben hinweg für mich immer eine große Stütze und ein Anker waren. Ohne ihre vielseitige Unterstützung wäre ich heute nicht derjenige der ich bin und wäre sicherlich auch nicht so weit gekommen.

Contents

1 Introduction

The properties of a material often result from microscopic interactions and quantum behavior of electrons and nuclei. For example, optical properties of a material, such as its ability to absorb or reflect light, are closely related to the behavior of bound electron-hole pairs, called excitons, which must be described quantum mechanically. [1, 2, 3] Also other properties, such as electrical conductivity, depend strongly on the delocalization and energies of charge carriers and their interaction with lattice vibrations. It is quite remarkable that such microscopic processes, which typically take place at length scales of around 10^{-10} meter and time scales of 10^{-15} seconds, lead to macroscopic properties that can be experienced in every day life. To understand material properties it is therefore important to understand the occurring processes on a quantum scale. Such an understanding of material properties is extremely beneficial. One example where this becomes obvious is the field of organic electronics [4, 5] and optoelectronic devices, like field-effect transistors [6, 7], organic light-emitting diodes [8], organic solar cells [9, 10] or organic sensors [11]. For all these devices the performance depends to a large extent on the chosen materials. The search for suitable high-performance materials is therefore of central importance and has been, and continues to be, a major challenge. As a result, advances in material selection and purification techniques have led to vast improvements in device performance and commercial products are now available.

It is reasonable to believe that this trend will continue in the future, since the number of materials that are available is huge and the number of materials that could be synthesized is even larger. In addition, developments in synthesis have also led to new material classes like covalent organic frameworks. [12, 13, 14] These are crystalline 2D and 3D polymers which consist of organic molecular building blocks that can be tailored as desired. [15, 16, 17] They are considered to have a huge potential for applications because they have an ordered long-range structure [18] and at the same time are light and flexible like thin films of organic molecules. It is believed that those materials can achieve improved performance for many applications, if the corresponding building units are chosen appropriately. In addition, combinations of materials, e.g., in blends, interfaces, or by doping, allow for further device variations. This creates enormous potential for improvement and innovation, but also requires a detailed theoretical understanding of the underlying quantum processes. Theoretical approaches can help in rationalizing trends, explaining results and thus supplementing experimental efforts by providing additional insights that cannot be obtained otherwise. Furthermore, it is possible to guide material selection by predicting material properties even for materials that have not been synthesized yet. This requires a sufficient theoretical model and efficient numerical approaches that allow accurate computation of large systems with hundreds or thousands of atoms.

The goal of this work is to develop new approaches to model and evaluate organic and inorganic semiconductors and therefore push the boundaries towards better descriptions and larger system sizes. For this, we focus on three aspects that are relevant for modern applications. The first one is the coupling of electronic and vibrational degrees of freedom, known as electron-phonon coupling, and its impact on the electrical conductivity of materials. It has a particularly strong effect between organic molecules that are bound with weak van-der-Waals interaction, such as organic molecular crystals. This makes these materials ideal test systems. The second aspect is the π-conjugation and electronic coupling of different molecular building blocks within a covalent organic framework. This is particularly important for choosing optimal building blocks and tailoring the electronic structure towards specific needs. The third aspect are optical excitations and bounded electron-hole pairs that are important for calculating optical absorption and reflection spectra. Here, a new method is developed that is able to calculate optical properties very efficiently. It scales linearly with the system size and is therefore able to evaluate very large systems that are not accessible with other techniques.

For all our investigations we use localized real space orbitals as basis functions. These are either molecular orbitals in the case of organic molecular crystals or maximally localized Wannier functions in

the case of covalently bonded crystals. The description obtained in this way is particularly well suited, since breaking of translational symmetry, e.g., when considering disorder or electron-phonon coupling, can easily be included. Moreover, we show that the resulting Hamiltonians become very sparse, which can be exploited to achieve excellent performance, e.g., compared to a common used plane-wave descriptions.

This thesis is structured as follows. First, we will introduce linear response theory, which forms the basis for evaluating the electrical conductivity and linear optical properties which we are interested in. This also provides the connection to classical physics and experiment, which might be helpful for understanding. In chapter 3, we will give an overview of the common methods to calculate the electronic structure, such as density functional theory, the Green's functions approach, and sketch the derivation of the exciton Hamiltonian, which is the starting point for our optical calculations. Finally, chapters 4, 5 and 6 are dedicated to the results which are provided in the form of peer-reviewed publications.

2 Response to electromagnetic fields and link to experiment

We want to start by describing the response of a quantum system to external fields and establish the connection to experiments from the very beginning. We are specifically interested in charge transport and optical excitations of semiconductors, which both result as a response to an electric field. From a theoretical point of view, those quantities can be calculated using the framework of linear response theory [19, 20, 21, 22, 23], which allows to handle such properties quantum mechanically. The interaction with external fields can be treated quite generally, which is why we do not need to make any assumptions about the material or modeling of the electronic structure. This will be presented later in Chapter 3 using various established methods. In the following we provide a brief summary of linear response theory. For further details we recommend Ref. [21] and Ref. [23].

2.1 Linear response theory

Starting with the mathematical description, we assume an undisturbed quantum system which is described by the Hamiltonian $\hat{H}_0$ and a time-dependent classical external field $V_{\text{ext}}(t)$ which is coupled to the system through an operator $\hat{A}$. The resulting Hamiltonian for the perturbed system is then described by the Hamiltonian

$$\hat{H} = \hat{H}_0 - \hat{A}V_{\text{ext}}(t). \tag{2.1}$$

We furthermore assume that the field is not present at times $t \to -\infty$ and is switched on adiabatically. For the general formalism it is not important to specify $\hat{H}_0$, $\hat{A}$ or the field explicitly. They will be chosen based on the physical setting, which is provided in later sections.

The expectation value of an observable $\hat{B}$ can be obtained from the density operator $\hat{\rho}$ of the system by $\langle \hat{B} \rangle = \text{tr}\left\{\hat{\rho}\hat{B}\right\}$. Without any external field ($t \to -\infty$), the system is in equilibrium and the density operator is given by the (grand) canonical ensemble. To obtain the density operator for the perturbed system it is useful to change to the interaction (Dirac) picture of quantum mechanics, which is more convenient when considering perturbations. Within the interaction picture the equation of motion for the density operator is then obtained as a von Neumann equation,

$$\frac{d}{dt}\hat{\rho}(t) = \frac{i}{\hbar}[\hat{A}V_{\text{ext}}(t), \hat{\rho}(t)], \tag{2.2}$$

where only the coupling term from Eq. (2.1) appears in the commutator on the right-hand side. Please note, that the overall sign is positive because the coupling term is negative. We can formally integrate and iterate the expression and obtain

$$\begin{aligned}\hat{\rho}(t) &= \hat{\rho}_0 + \frac{i}{\hbar}\int_{-\infty}^{t} dt' \, [\hat{A}(t'), \hat{\rho}_0]V_{\text{ext}}(t') + \left(\frac{i}{\hbar}\right)^2 \int_{-\infty}^{t} dt' \int_{-\infty}^{t'} dt'' \, [\hat{A}(t'), [\hat{A}(t''), \hat{\rho}_0]]V_{\text{ext}}(t')V_{\text{ext}}(t'') + ... \\ &\approx \hat{\rho}_0 + \frac{i}{\hbar}\int_{-\infty}^{t} dt' \, [\hat{A}(t'), \hat{\rho}_0]V_{\text{ext}}(t').\end{aligned} \tag{2.3}$$

The iterated expression in the first line represents a power series with respect to V_{ext}, which is an exact expression. However, it is generally too complicated to solve. If we assume that the external perturbation is sufficiently small compared to the unperturbed system, we can truncate the power series and approximate

it to linear order, which is shown in the second line. Experience shows that this is often the dominant contribution and is already sufficient to describe many physical phenomena. However, higher orders can be added systematically if necessary and could lead, e.g., to non-linear optical phenomena such as second harmonics generation. [24]

Using $\hat{\rho}(t)$ and the cyclic property of the trace, we can calculate the expectation values of any observable,

$$\langle \hat{B}(t) \rangle = \mathrm{tr}\left\{ \hat{\rho}(t)\hat{B}(t) \right\} = \langle \hat{B} \rangle_0 + \int_{-\infty}^{+\infty} dt' \, \chi_{B,A}(t,t') V_{\mathrm{ext}}(t'), \tag{2.4}$$

where $\langle \hat{B} \rangle_0 = \mathrm{tr}\left\{ \hat{\rho}_0 \hat{B} \right\}$ is the expectation value of the unperturbed system and we have introduced the retarded correlation function $\chi_{B,A}(t,t')$ as

$$\chi_{B,A}(t,t') = \frac{i}{\hbar} \Theta(t-t') \langle [\hat{B}(t), \hat{A}(t')] \rangle_0. \tag{2.5}$$

The linear response of a system can therefore be expressed as a correlation between two operators with respect to the unperturbed system. The Heaviside function $\Theta(t-t')$ guarantees the causality, i.e., the response of the system can only happen after the field is applied. It is easy to show that the correlation function only depends on the time difference $\chi_{B,A}(t,t') = \chi_{B,A}(t-t')$, which follows directly from the cyclic property of the trace. This suggests a Fourier transform of the expression and we obtain $\chi_{B,A}$ in the spectral representation [21, 25],

$$\begin{aligned} \chi_{B,A}(\omega + i\eta) &= \int_{-\infty}^{\infty} d(t-t') \, \chi_{B,A}(t-t') e^{i(\omega+i\eta)t} \\ &= -\frac{1}{Z_0} \sum_{mn} \frac{\langle n|\hat{B}|m\rangle \langle m|\hat{A}|n\rangle}{\hbar\omega + i\hbar\eta + E_n - E_m} \left(e^{-\beta E_n} - e^{-\beta E_m} \right). \end{aligned} \tag{2.6}$$

In this formula, $|n\rangle$ and $|m\rangle$ are eigenstates of the unperturbed system, and Z_0 its partition function. E_m and E_n are the corresponding energies and $\beta = 1/k_{\mathrm{B}}T$ is the inverse temperature. η is a positive infinitesimal that ensures convergence of the integral and the boundary condition for $t \to -\infty$. The resulting correlation function $\chi_{B,A}$ is analytical in the complex upper half plane. [3] From Eq. (2.6) we can see that it has poles at the excitation energies of the undisturbed system.

Having established the general linear response theory, we now turn to specific cases that are relevant for this work.

2.2 Electrical conductivity

A very important application of linear response theory is the calculation of charge carrier transport and electrical conductivity, which is also used later in chapter 4 for calculating charge transport in organic molecular crystals. The electrical conductivity σ is defined by Ohm's law as the proportionality factor between electrical field $\boldsymbol{F}$ and current density $\boldsymbol{j}$,

$$\boldsymbol{j}(\omega) = \sigma(\omega) \boldsymbol{F}(\omega). \tag{2.7}$$

For the calculation of the conductivity we start by coupling the electric field to the Hamiltonian. In accordance with experiment, we assume an alternating electric field that is switched on adiabatically and is constant in space $\boldsymbol{F}(t) = \boldsymbol{F}_0 e^{-i(\omega+i\eta)t}$. From this approach, we can also obtain the DC-conductivity by taking the limit $\omega \to 0$, which we will use at the end. The coupling to the Hamiltonian is performed by minimal coupling of the momentum operator and vector potential, i.e., by substituting $\hat{\boldsymbol{p}} \to \hat{\boldsymbol{p}} - \frac{e}{c}\boldsymbol{A}(\hat{\boldsymbol{x}}, t)$, where the vector potential $\boldsymbol{A}$ and scalar potential Φ corresponding to the electrical field can be chosen as

$$\boldsymbol{A}(t) = -i\frac{c}{\omega + i\eta} \boldsymbol{F}_0 e^{-i(\omega+i\eta)t}, \qquad \Phi = 0. \tag{2.8}$$

We ignore the spin of the particles as they are irrelevant for longitudinal transport and express everything in terms of the current density operator $\hat{\boldsymbol{j}}$ and number density operator $\hat{n}$. The resulting Hamiltonian is then obtained as [21]

$$\hat{H} = \hat{H}_0 + \int d^3x' \left[-\frac{1}{c}\hat{\boldsymbol{j}}(\boldsymbol{x}')\boldsymbol{A}(\boldsymbol{x}',t) - \frac{e^2}{2mc^2}\hat{n}(\boldsymbol{x}')\boldsymbol{A}^2(\boldsymbol{x}',t) \right]. \tag{2.9}$$

The first term of the coupling is similar to the general case Eq. (2.1). In this case we have the current operator $\hat{\boldsymbol{j}}$ which describes a linear coupling to the external field, given by the vector potential $\boldsymbol{A}$. The second term is already proportional to $\boldsymbol{A}^2$ and therefore beyond linear response.

The current density operator $\hat{\boldsymbol{j}}$ is usually split into two parts $\hat{\boldsymbol{j}} = \hat{\boldsymbol{j}}^{(\mathrm{P})} + \hat{\boldsymbol{j}}^{(\mathrm{D})}$, a paramagnetic contribution $\hat{\boldsymbol{j}}^{(\mathrm{P})}$ and a diamagnetic contribution $\hat{\boldsymbol{j}}^{(\mathrm{D})}$. They can be obtained from the continuity equation for a system with N electrons (or holes) and are given by [21]

$$\hat{\boldsymbol{j}}^{(\mathrm{P})}(\boldsymbol{x}) = \frac{e}{2m}\sum_{i=1}^{N}\left[\hat{\boldsymbol{p}}_i\delta(\boldsymbol{x}-\hat{\boldsymbol{x}}_i) + \delta(\boldsymbol{x}-\hat{\boldsymbol{x}}_i)\hat{\boldsymbol{p}}_i\right], \qquad \hat{\boldsymbol{j}}^{(\mathrm{D})}(\boldsymbol{x}) = \frac{e^2}{mc}\hat{n}(\boldsymbol{x})\boldsymbol{A}(\boldsymbol{x},t), \tag{2.10}$$

where $\hat{\boldsymbol{p}}_i$ and $\hat{\boldsymbol{x}}_i$ denote the momentum and position operators for every particle i respectively and the number density operator $\hat{n}$ is given by $\hat{n}(\boldsymbol{x}) = \sum_{i=1}^{N}\delta(\boldsymbol{x}-\hat{\boldsymbol{x}}_i)$. Without external field the current operator would just consists of the paramagnetic contribution. The diamagnetic part emerges from the minimal coupling procedure of the momentum operators.

Having established the coupling of our system to the external electric field we can now use the results from the previous section to calculate the linear response of the current operator. Utilizing Eq. (2.4), we obtain for the expectation value

$$\langle\hat{j}_\alpha(\boldsymbol{x},t)\rangle = \langle\hat{j}_\alpha^{(\mathrm{D})}(\boldsymbol{x},t)\rangle + \langle\hat{j}_\alpha^{(\mathrm{P})}(\boldsymbol{x},t)\rangle \tag{2.11}$$

$$= -\frac{e^2}{mc}\langle\hat{n}(\boldsymbol{x})\rangle_0 A_\alpha(\boldsymbol{x},t) + \int d^3x' \int dt' \left[-\frac{1}{c}\sum_{\gamma=1}^{3}\chi_{j_\alpha^{(\mathrm{P})}(\boldsymbol{x})j_\gamma^{(\mathrm{P})}(\boldsymbol{x}')}(t-t')A_\gamma(\boldsymbol{x}',t') \right], \tag{2.12}$$

where the retarded current-current correlation function is obtained from Eq. (2.5),

$$\chi_{j_\alpha^{(\mathrm{P})}j_\gamma^{(\mathrm{P})}}(t-t') = \frac{i}{\hbar}\Theta(t-t')\langle[\hat{j}_\alpha^{(\mathrm{P})}(t),\hat{j}_\gamma^{(\mathrm{P})}(t')]\rangle_0. \tag{2.13}$$

Finally, to obtain Ohm's law Eq. (2.7), we average the current density over a volume V and obtain the measured quantity $\langle\boldsymbol{j}\rangle = \frac{1}{V}\int d^3x\,\langle\boldsymbol{j}(\boldsymbol{x})\rangle$. Similarly, the average particle density is obtained as $n = \frac{1}{V}\int d^3x\,\langle n(\boldsymbol{x})\rangle$. Together with Eq. (2.8) we can rewrite everything in terms of Ohm's law and identify the conductivity tensor as

$$\sigma_{\alpha\gamma}(\omega+i\eta) = i\frac{ne^2}{m(\omega+i\eta)}\delta_{\alpha\gamma} - \frac{i}{V(\omega+i\eta)}\chi_{j_\alpha^{(\mathrm{P})}j_\gamma^{(\mathrm{P})}}(\omega+i\eta), \tag{2.14}$$

which is also known as the Kubo formula. [20, 21, 22] The first term describes the diamagnetic contribution which only contributes to the diagonal of the conductivity tensor. The second term contains all paramagnetic contributions, which is determined by the current-current correlation function in equilibrium Eq. (2.13).

We are usually interested in the real part of the conductivity for the case where the field and current density have the same direction, i.e., the diagonal elements of the tensor. In the case of an effective single-particle Hamiltonian, we can use Eq. (2.6) and after a few manipulations we obtain [21]

$$\mathrm{Re}\,\sigma_{\alpha\alpha}(\omega) = \frac{\pi\hbar}{V}\int dE\,\frac{f(E)-f(E+\hbar\omega)}{\hbar\omega}\mathrm{tr}\left\{\delta(E-\hat{H}_0)\hat{j}_\alpha^{(\mathrm{P})}\delta(E+\hbar\omega-\hat{H}_0)\hat{j}_\alpha^{(\mathrm{P})}\right\}, \tag{2.15}$$

where $f(E)$ is the Fermi-Dirac distribution. By taking the static limit we finally obtain the DC-conductivity,

$$\mathrm{Re}\,\sigma_{\alpha\alpha}(\omega\to 0) = \frac{\pi\hbar}{V}\int dE\,\left(-\frac{df(E)}{dE}\right)\mathrm{tr}\left\{\delta(E-\hat{H}_0)\hat{j}_\alpha^{(\mathrm{P})}\delta(E-\hat{H}_0)\hat{j}_\alpha^{(\mathrm{P})}\right\}. \tag{2.16}$$

This equation is called Kubo-Greenwood equation and will be used in section 4 together with an adequate model for electron-phonon coupling.

2.3 Optical absorption and reflection

Another important application of linear response theory is the calculation of optical properties of a material, which is also used in chapter 6. For this we need to calculate the *macroscopic* dielectric function ϵ^{M}, which contains information about the absorption and reflection spectrum and is directly related to the refractive index $n(\omega)$ and extinction coefficient $\kappa(\omega)$ by

$$\sqrt{\epsilon^{\mathsf{M}}(\omega)} = n(\omega) + i\kappa(\omega). \tag{2.17}$$

It is therefore accessible in experiments. Before calculating ϵ^{M} we first need to introduce the *microscopic* dielectric function ϵ, which describes the microscopic polarization and screening within a material and can be obtained from linear response theory but is not directly accessible in experiments. From this we can derive the *macroscopic* dielectric function in the second part of this section.

As before we start our derivation by coupling the Hamiltonian to an electromagnetic field. We follow the standard approach as presented, e.g., in Ref. [3, 22, 23] and couple the system to an external potential $V_{\text{ext}}(\boldsymbol{x}, t)$ that is oscillating in time and space and is coupled via the density operator $\hat{n}$,

$$\hat{H} = \hat{H}_0 + \int d^3x' \, V_{\text{ext}}(\boldsymbol{x}', t)\hat{n}(\boldsymbol{x}'). \tag{2.18}$$

Alternatively, one could also use a coupling through a vector potential $\boldsymbol{A}$ as in the previous section, which would yield the same result albeit being more complicated in the derivation. [26]

The oscillating external field then causes fluctuations of the charge density inside the materials which are also oscillating in time and space. These fluctuations lead to an induced charge density δn that can be evaluated in linear response (c.f. Eq. (2.4)) as

$$\delta n(\boldsymbol{x}, t) = \int d^3x' \int dt' \, \chi_{nn}(\boldsymbol{x}\boldsymbol{x}', t - t')V_{\text{ext}}(\boldsymbol{x}', t'), \tag{2.19}$$

using the density-density correlation function $\chi_{nn}(\boldsymbol{x}\boldsymbol{x}', t - t') = \frac{-i}{\hbar}\Theta(t - t')\langle[\hat{n}(\boldsymbol{x}, t), \hat{n}(\boldsymbol{x}', t')]\rangle_0$.

According to classical electrodynamics, the induced charge density δn in turn creates an electric potential that counteracts the external field and (partially) screens it,

$$V_{\text{ind}}(\boldsymbol{x}, t) = \int d^3x' \, V(\boldsymbol{x} - \boldsymbol{x}')\delta n(\boldsymbol{x}', t), \tag{2.20}$$

where $V(\boldsymbol{x})$ is the Coulomb potential. The change of the total potential $\delta V_{\text{tot}}(\boldsymbol{x}, t)$ is then obtained as the sum of external and induced potentials. Additionally, we can also relate the total and external potentials via the inverse *microscopic* dielectric function ϵ^{-1} that describes the screening within the material. Together with Eq. (2.19) and Eq. (2.20) we obtain

$$\delta V_{\text{tot}}(\boldsymbol{x}, t) = V_{\text{ext}}(\boldsymbol{x}, t) + V_{\text{ind}}(\boldsymbol{x}, t) = \int d^3x' \int dt' \, \epsilon^{-1}(\boldsymbol{x}, t, \boldsymbol{x}', t')V_{\text{ext}}(\boldsymbol{x}', t') \tag{2.21}$$

$$\Rightarrow \epsilon^{-1}(\boldsymbol{x}, t, \boldsymbol{x}', t') = \delta(\boldsymbol{x} - \boldsymbol{x}')\delta(t - t') + \int d^3x'' \int dt'' \, V(|\boldsymbol{x}' - \boldsymbol{x}''|)\chi_{nn}(\boldsymbol{x}''\boldsymbol{x}', t'' - t'). \tag{2.22}$$

The microscopic screening is therefore obtained by the density-density correlation function of the system. ϵ^{-1} not only describes the screening but also contains optical properties that we want to calculate. In the case of a periodic crystal we can take a Fourier transform with respect to time and space and obtain

$$\epsilon^{-1}_{\boldsymbol{G}\boldsymbol{G}'}(\boldsymbol{q}, \omega) = \delta_{\boldsymbol{G}\boldsymbol{G}'} + V(|\boldsymbol{q} + \boldsymbol{G}|)\chi_{\boldsymbol{G}\boldsymbol{G}'}(\boldsymbol{q}, \omega), \tag{2.23}$$

where $\boldsymbol{G}$ and $\boldsymbol{G}'$ are reciprocal lattice vectors. Eq. (2.23) points out that $\epsilon^{-1}_{\boldsymbol{G}\boldsymbol{G}'}$ has the form of a second rank tensor rather than a scalar function. This must be taken into account when calculating the inversion.

Before we establish the connection to the *macroscopic* dielectric function we want to introduce the polarization function, which is particularly helpful for practical calculations since it can often be obtained

easier than the density-density correlation function. So far δn was obtained by the response to an external field (c.f. Eq. (2.19)). Analogously, we can also calculate the response to the *total* field. For this we apply the same linear response formulation as before and introduce the retarded polarization function P. Together with Eq. (2.21) we obtain

$$\delta n(\boldsymbol{x}, t) = \int d^3x' \int dt'\, P(\boldsymbol{x}, t, \boldsymbol{x}', t') V_{\text{tot}}(\boldsymbol{x}', t') \tag{2.24}$$

$$= \int d^3x' \int dt' \int d^3x'' \int dt''\, P(\boldsymbol{x}, t, \boldsymbol{x}', t') \epsilon^{-1}(\boldsymbol{x}', t', \boldsymbol{x}'', t'') V_{\text{ext}}(\boldsymbol{x}'', t''), \tag{2.25}$$

where we can identify the relationship between polarization function and density-density correlation function,

$$\chi_{nn}(\boldsymbol{x}, t, \boldsymbol{x}', t') = \int d^3x'' \int dt''\, P(\boldsymbol{x}, t, \boldsymbol{x}'', t'') \epsilon^{-1}(\boldsymbol{x}'', t'', \boldsymbol{x}', t'). \tag{2.26}$$

By taking the Fourier transform and inserting this in Eq. (2.23) we obtain a Dyson equation, which can formally be solved by a matrix inversion. The solution then yields the microscopic dielectric function $\epsilon_{\boldsymbol{G}\boldsymbol{G}'}$,

$$\epsilon^{-1}_{\boldsymbol{G}\boldsymbol{G}'}(\boldsymbol{q}, \omega) = \delta_{\boldsymbol{G}\boldsymbol{G}'} + \sum_{\boldsymbol{G}''} V(|\boldsymbol{q} + \boldsymbol{G}|) P_{\boldsymbol{G}\boldsymbol{G}''} \epsilon^{-1}_{\boldsymbol{G}''\boldsymbol{G}'} \tag{2.27}$$

$$\Rightarrow \epsilon_{\boldsymbol{G}\boldsymbol{G}'} = \delta_{\boldsymbol{G}\boldsymbol{G}'} - V(|\boldsymbol{q} + \boldsymbol{G}|) P_{\boldsymbol{G}\boldsymbol{G}'}. \tag{2.28}$$

With Eqs. (2.23) and (2.28) we have obtained two ways to calculate the (inverse) *microscopic* dielectric function from either χ_{nn} or P. In particular, the polarization function is of interest since it can be obtained from a Bethe-Salpeter equation, which will be introduced in section 3.3.1.

2.3.1 Microscopic and macroscopic dielectric function

We now calculate the *macroscopic* dielectric function, which is measured in experiments, from the *microscopic* dielectric function obtained in the previous section by linear response.

In an experiment the light source is usually far away from the sample, so the external perturbation includes only the far field and is therefore macroscopic, i.e., $V_{\text{ext}}(\boldsymbol{q} + \boldsymbol{G}', \omega) \to \langle V_{\text{ext}}(\boldsymbol{q}, \omega) \rangle \delta_{\boldsymbol{G}',0}$. The macroscopic perturbation still results in a total field that has microscopic and macroscopic components. Since the detector is also far away from the sample and a measurement process averages over a small area in space, an experimental setup measures only the macroscopic total field $\langle V_{\text{tot}}(\boldsymbol{q}, \omega) \rangle$. Taking these averages in Eq. (2.21), we obtain

$$\langle \delta V_{\text{tot}}(\boldsymbol{q}, \omega) \rangle = \epsilon^{-1}_{\boldsymbol{G}\boldsymbol{G}'}(\boldsymbol{q}, \omega) \Big|_{\boldsymbol{G}=\boldsymbol{G}'=0} \langle V_{\text{ext}}(\boldsymbol{q}, \omega) \rangle. \tag{2.29}$$

This leads to the definition of the *macroscopic* dielectric function ϵ^{M}, which is directly related to the optical reflection and absorption spectra,

$$\epsilon^{\text{M}}(\boldsymbol{q}, \omega) := \frac{1}{\epsilon^{-1}_{00}(\boldsymbol{q}, \omega)} \neq \epsilon_{00}(\boldsymbol{q}, \omega). \tag{2.30}$$

It is important to consider the tensor character of the dielectric function $\epsilon_{\boldsymbol{G}\boldsymbol{G}'}(\boldsymbol{q}, \omega) = \left(\left[\epsilon^{-1}(\boldsymbol{q}, \omega) \right]^{-1} \right)_{\boldsymbol{G}\boldsymbol{G}'}$, which makes clear that $\epsilon^{\text{M}}(\boldsymbol{q}, \omega) \neq \epsilon_{00}(\boldsymbol{q}, \omega)$. The difference to the head ($\boldsymbol{G} = \boldsymbol{G}' = 0$) of the *microscopic* dielectric function $\epsilon_{00}(\boldsymbol{q}, \omega)$ are called local field effects and are important for a correct evaluation of optical properties. Physically they originate from microscopic fluctuations of the charge density that are smaller than a unit cell.

The difference between ϵ^{M} and ϵ has some important computational consequences, depending on whether one uses the density-density correlation function in Eq. (2.23) or the polarization function in Eq. (2.28). In the first case, we can put the obtained *inverse* dielectric function directly into Eq. (2.30)

without further complications. However, the second case requires more care since the obtained microscopic dielectric function in Eq. (2.28) cannot be used directly, i.e., one has to perform a matrix inversion to obtain $\epsilon^{-1}_{\boldsymbol{G}\boldsymbol{G}'}$ and then setting $\boldsymbol{G} = \boldsymbol{G}' = 0$ afterwards. It is therefore necessary to compute all components of $\epsilon_{\boldsymbol{G}\boldsymbol{G}'}$ before taking the inverse. This, together with the matrix inversion, is computationally expensive and should be avoided. A better way would be to compute ϵ^{M} directly. This can be done by introducing a *macroscopic* polarization function which will be discussed in section 3.3.2. Since the macroscopic polarization function can also be obtained from a Bethe-Salpeter equation (similar to P), it is more convenient to use this approach instead of calculating the density-density correlation function.

Finally, we can perform the optical limit for the macroscopic dielectric function. For UV-VIS spectra the photon momentum is orders of magnitude smaller than the electron momentum. Therefore, it is sufficient to take the limit $\boldsymbol{q} \to 0$. The macroscopic dielectric function then only depends on the direction of the photon momentum $\boldsymbol{e}_q = \boldsymbol{q}/|\boldsymbol{q}|$ and the frequency ω, [3, 23]

$$\epsilon^{\mathsf{M}}(\boldsymbol{e}_q, \omega) = \lim_{\boldsymbol{q}\to 0} \epsilon^{\mathsf{M}}(\boldsymbol{q}, \omega). \tag{2.31}$$

3 Microscopic description of materials

To gain a comprehensive understanding of material properties, it is important to have an adequate quantum description from first principles, i.e., based exclusively on fundamental physical laws. To obtain such a description is an elaborate task, as a typical macroscopic sample consists of about 10^{23} particles and the corresponding Hilbert space grows exponentially. In such an extremely high-dimensional vector space, it is not even possible to store a many-particle wave function or even to solve the many-body Schrödinger equation directly. Furthermore, the problem is complicated by the long-range mutual electron-electron interactions, which are extremely difficult to solve in a many-particle description, forcing the use of more advanced methods.

A very efficient approach in this regard is density functional theory [27, 28], which can be used to calculate ground state properties. It is extremely popular and often a precursor step for more costly methods. It is also relevant for this work and will be revised briefly in the beginning of this chapter. Another approach that is relevant for this work is the field-theoretic description in terms of Green's functions, which circumvents the use of many-body wave functions and can also provide access to excitations beyond the ground state. From the Green's function formalism and Hedin's set of equations we will then derive the exciton Hamiltonian, which is the basis for our calculations of optical properties.

3.1 Density functional theory (DFT)

In DFT [27, 28], the electron density is the central object that has been shown to be sufficient to describe the ground state properties of the system. This reduces the computational complexity of the problem significantly since the density only depends on a single position, while the many-body wave function scales exponentially with system size. The theoretical justification is provided by the Hohenberg-Kohn theorems that we introduce in the following. For more details about the methods and their implementation we refer to Ref. [3] and Ref. [23].

We start by considering N electrons within a material and assume that the positions of the nuclei are fixed. The electrons are then described by a Hamiltonian $\hat{H}_0$ which contains the kinetic energy $\hat{T}$, electron-electron interaction $\hat{U}$ and an external potential V_{ext} that couples through the density operator $\hat{n}$,

$$\hat{H}_0 = \hat{T} + \hat{U} + \int d^3x \, V_{\text{ext}}(\boldsymbol{x})\hat{n}(\boldsymbol{x}). \tag{3.1}$$

The external potential originates from the nuclei and possible external fields and therefore depends on the concrete system, while $\hat{T}$ and $\hat{U}$ are universal for any electron gas.

The ground state of the system $|\Psi_0\rangle$ obeys the many-body Schrödinger equation,

$$\hat{H}_0|\Psi_0\rangle = E_0|\Psi_0\rangle, \tag{3.2}$$

where E_0 is the ground state energy. Since the Hamiltonian only depends on $V_{\text{ext}}(\boldsymbol{x})$ it becomes clear that the ground state also depends on the external potential $|\Psi_0\rangle = |\Psi_0[V_{\text{ext}}]\rangle$. Having the ground state we can easily calculate the ground state density,

$$n_{\text{g}}(\boldsymbol{x}) = \langle\Psi_0|\hat{n}(\boldsymbol{x})|\Psi_0\rangle, \tag{3.3}$$

which is uniquely defined by $|\Psi_0\rangle$. We can therefore map V_{ext} exactly to one ground state density $n_{\text{g}}(\boldsymbol{x})$. The Hohenberg-Kohn theorem I then states that also the inverse map exists and is unique up to a constant.

Hohenberg-Kohn theorem I:

> *"For a system of interacting electrons in an external potential $V_{ext}(\boldsymbol{x})$, the potential itself is uniquely determined, except for a constant, by the ground-state density $n_g(\boldsymbol{x})$."* [3]

From the Hohenberg-Kohn theorem I it follows directly that we can express the ground state energy and any other observable as a functional of $n_{\mathsf{g}}(\boldsymbol{x})$,

$$E_0 = \langle \Psi_0[n_{\mathsf{g}}] | \hat{H}_0 | \Psi_0[n_{\mathsf{g}}] \rangle = E_{V_{\mathsf{ext}}}[n_{\mathsf{g}}]. \tag{3.4}$$

This makes $n_{\mathsf{g}}(\boldsymbol{x})$ the central quantity of interest and circumvents the problems of dealing with a high-dimensional many-body wave function. The Hohenberg-Kohn theorem II then provides a possibility to obtain the ground state density by showing the variational character of the energy functional.

Hohenberg-Kohn theorem II:

> *"For a non-degenerate ground state $|\Psi_0\rangle$ and a given external potential $V_{ext}(\boldsymbol{x})$ the energy functional $E_{V_{ext}}[n]$ assumes its global minimum value E_0 varying the density $n(\boldsymbol{x})$ toward the true ground-state density $n_g(\boldsymbol{x})$."* [3]

This is a manifestation of the Rayleigh-Ritz principle. In order to get physically meaningful results we need to constrain the variation of the density such that $n(\boldsymbol{x})$ is positive $n(\boldsymbol{x}) \geq 0$, continuous and conserves the number of particles $N = \int d^3x\, n(\boldsymbol{x})$.

As for the Hamiltonian Eq. (3.1), the energy functional Eq. (3.4) can be further split into a universal Hohenberg-Kohn functional $F_{\mathsf{HK}}[n]$, which holds for any electron gas, and a contribution of $V_{\mathsf{ext}}(\boldsymbol{x})$, which depends on the specific system,

$$E_{V_{\mathsf{ext}}}[n] = F_{\mathsf{HK}}[n] + \int d^3x\, V_{\mathsf{ext}}(\boldsymbol{x}) n(\boldsymbol{x}), \tag{3.5}$$

$$\text{with } F_{\mathsf{HK}}[n] = \langle \Psi_0[n] | \left(\hat{T} + \hat{U} \right) | \Psi_0[n] \rangle. \tag{3.6}$$

Up to this point, the theory is exact in the sense that we have not made any approximation. However, the Hohenberg-Kohn theorems only prove the existence of the energy functional and establish the density as the central object. The universal functional $F_{\mathsf{HK}}[n]$ remains unknown in general, and the theorems do not provide a sufficient computational scheme that can be used for practical calculations.

To overcome this problem Kohn and Sham have presented an approach which makes practical calculations feasible. [29] The basic idea is to map the complicated interacting system to a fictitious system of N non-interacting particles $|\phi_i^{\mathsf{KS}}\rangle$, so called Kohn-Sham-particles, for which the Schrödinger equation can be solved much easier. The non-interacting system is constructed such that it has the same number of electrons and the same ground state density,

$$n_{\mathsf{g}}(\boldsymbol{x}) = n(\boldsymbol{x}) = \sum_{i=1}^{N} |\phi_i^{\mathsf{KS}}(\boldsymbol{x})|^2. \tag{3.7}$$

For convenience, we only consider a closed shell system, where an equal amount of electrons with spin up and spin down exists. The ground state of the system is according to the Pauli principle filled with two electrons per orbital.

The Kohn-Sham particles are placed in an effective potential $V_{\mathsf{eff}}(\boldsymbol{x})$ and obey the Schrödinger equation,

$$\left(-\frac{\hbar^2}{2m} \Delta + V_{\mathsf{eff}}(\boldsymbol{x}) \right) |\phi_i^{\mathsf{KS}}\rangle = \epsilon_i^{\mathsf{KS}} |\phi_i^{\mathsf{KS}}\rangle. \tag{3.8}$$

The remaining challenge is to obtain $V_{\text{eff}}(\boldsymbol{x})$. For this we can use the Hohenberg-Kohn theorems, that are also valid for the non-interacting system. The energy functional is then found as

$$E_{\text{s}}[n] = T_{\text{s}}[n] + \int d^3x\, V_{\text{eff}}(\boldsymbol{x}) n(\boldsymbol{x}) \tag{3.9}$$

and can be easily calculated in contrast to the interacting system. We can use the variational character of the energy functional and apply the Hohenberg-Kohn theorem II,

$$\begin{aligned} 0 &= \frac{\delta}{\delta n(\boldsymbol{x})} \left[T_{\text{s}}[n] + \int d^3x'\, V_{\text{eff}}(\boldsymbol{x}') n(\boldsymbol{x}') - \mu_{\text{s}} \left(\int d^3x'\, n(\boldsymbol{x}') - N \right) \right] \\ &= \frac{\delta}{\delta n(\boldsymbol{x})} T_{\text{s}}[n] + V_{\text{eff}}(\boldsymbol{x}) - \mu_{\text{s}}, \end{aligned} \tag{3.10}$$

where μ_{s} is a Lagrange multiplier, which ensures that the number of particles is conserved.

An equivalent expression can also be obtained for the interacting system. For this we introduce the Hartree energy $E_{\text{H}}[n]$, which is the electrostatic interaction of a charge density with itself,

$$E_{\text{H}}[n] = \frac{1}{2} \int d^3x \int d^3x' \frac{n(\boldsymbol{x}') n(\boldsymbol{x})}{|\boldsymbol{x} - \boldsymbol{x}'|}, \tag{3.11}$$

and the exchange correlation energy $E_{\text{XC}}[n]$, which contains all complicated many-body effects and contributions of the electron-electron interaction that go beyond the classical Hartree interaction,

$$E_{\text{XC}}[n] = \langle \Psi_0[n] | (\hat{T} + \hat{U}) | \Psi_0[n] \rangle - T_{\text{s}}[n] - E_{\text{H}}[n]. \tag{3.12}$$

The exchange correlation also contains the difference between the kinetic energy of the interacting system and non-interacting system $T[n] - T_{\text{s}}[n]$. Using these definitions allows us to rewrite the universal Hohenberg-Kohn functional as

$$F_{\text{HK}}[n] = E_{\text{XC}}[n] + T_{\text{s}}[n] + E_{\text{H}}[n], \tag{3.13}$$

and applying the Hohenberg-Kohn theorem II together with the constraint of particle number conservation yields

$$\begin{aligned} 0 &= \frac{\delta}{\delta n(\boldsymbol{x})} \left[T_{\text{s}}[n] + \int d^3x'\, V_{\text{H}}(\boldsymbol{x}') n(\boldsymbol{x}') + \int d^3x'\, V_{\text{ext}}(\boldsymbol{x}') n(\boldsymbol{x}') + E_{\text{XC}}[n] - \mu \left(\int d^3x'\, n(\boldsymbol{x}') - N \right) \right] \\ &= \frac{\delta}{\delta n(\boldsymbol{x})} T_{\text{s}}[n] + V_{\text{H}}(\boldsymbol{x}) + V_{\text{ext}}(\boldsymbol{x}) + V_{\text{XC}}(\boldsymbol{x}) - \mu, \end{aligned} \tag{3.14}$$

where the exchange correlation and Hartree potential are defined as

$$V_{\text{XC}}(\boldsymbol{x}) = \frac{\delta E_{\text{XC}}[n]}{\delta n(\boldsymbol{x})}, \qquad V_{\text{H}}(\boldsymbol{x}) = \int d^3x' \frac{n(\boldsymbol{x}')}{|\boldsymbol{x} - \boldsymbol{x}'|}. \tag{3.15}$$

We can compare Eq. (3.10) and Eq. (3.14) and find the effective potential by exploiting that both systems have the same ground state density,

$$V_{\text{eff}}(\boldsymbol{x}) = V_{\text{ext}}(\boldsymbol{x}) + V_{\text{H}}(\boldsymbol{x}) + V_{\text{XC}}(\boldsymbol{x}) + \mu_{\text{s}} - \mu. \tag{3.16}$$

Inserting $V_{\text{eff}}(\boldsymbol{x})$ into Eq. (3.8) and shifting the energies by the constant term $\mu_{\text{s}} - \mu$ yields the Kohn-Sham equation,

$$\left(-\frac{\hbar^2}{2m} \Delta + V_{\text{ext}}(\boldsymbol{x}) + V_{\text{H}}(\boldsymbol{x}) + V_{\text{XC}}(\boldsymbol{x}) \right) |\phi_i^{\text{KS}}\rangle = \epsilon_i^{\text{KS}} |\phi_i^{\text{KS}}\rangle. \tag{3.17}$$

In this equation, the Hartree and exchange correlation potentials depend on the electron density. Therefore, the solution must be self-consistent. The usual procedure is to start with an initial estimate of the

density, e.g., by using typical atomic orbitals, and to calculate the potentials. From this, one can solve Eq. (3.17) and obtain new Kohn-Sham orbitals. These can be used to update the electron density and repeat the process until convergence. Although the exchange correlation potential is in general unknown, it can be approximated. There are different approximation schemes one can use. [30, 31, 32] One popular choice are functionals of the GGA family (generalized gradient approximation), where the functional is approximated locally by the value and gradient of the ground state density. [33, 34]

With the Kohn-Sham scheme it is possible to perform calculations for materials with hundreds or thousands of atoms per unit cell, where a direct evaluation of the many-body problem is clearly illusive. Furthermore, it can be applied to a wide range of materials and is now one of the standard approaches in theoretical material science. This is because DFT provides a good balance between computational cost and accuracy. It has been shown to align well with experiments in many cases, e.g., bond lengths can be predicted with very high accuracy [28, 35, 36]. Nevertheless, there are also drawbacks of the DFT method. For example, the Kohn-Sham energies ϵ_i^{KS} have little physical meaning themselves, since they are not associated with any observable. A direct evaluation of ionization energies or electron affinities therefore requires more care. Especially because the available functionals lead to an underestimation of the band gap in insulators. [37, 38, 3] Moreover, DFT is, by construction, only able to calculate ground state properties. The method is therefore not suitable to evaluate optical properties since they depend on excited states. Those cases must be investigated with other approaches that we introduce next.

3.2 Green's function approach and Hedin's set of equations

The Green's function approach offers an alternative way to compute properties of quantum many-body systems that does not require complicated many-body wave functions, which are difficult to obtain. Instead, it focuses on the propagation of individual (quasi-)particles and their mutual interactions. Unlike DFT, the Green's function approach is not limited to ground state properties, but can also be used to calculate certain properties of exited states, which will be important for the evaluation of optical properties. For example, it is possible to calculate ionization energies, electron affinities and the resulting fundamental band gaps consistent with experiment. [37, 39, 40, 41, 42, 43, 3] Moreover, it is possible to include finite temperatures without conceptual difficulties. There are even extensions for non-equilibrium problems, which, however, are beyond the scope of this work.

As before, we intend to provide a comprehensive summary of the method. For a further and more detailed review, we recommend Refs. [38, 3, 23, 44].

3.2.1 Field operators and Green's functions

The basic idea is that we do not need to calculate the many-body wave functions explicitly if it is possible to calculate measurable quantities directly. These could be ground state properties like, e.g., the ground state energy, expectation values of observables, but also properties of excited states like ionization energies and electron affinities.

We start by introducing quantum field operators $\hat{\psi}^\dagger(\boldsymbol{x})$ and $\hat{\psi}(\boldsymbol{x})$ that create and annihilate a particle at position $\boldsymbol{x}$, respectively. Here we define $\boldsymbol{x} = (\boldsymbol{r}, s)$ as the position vector $\boldsymbol{r}$ together with the spin s in order to obtain concise expressions. For an explicit treatment of the spin and more details about spin-polarized system we refer to Ref. [3]. For fermions the field operators obey the anti-commutation relations $[\hat{\psi}(\boldsymbol{x}), \hat{\psi}^\dagger(\boldsymbol{x}')]_+ = \delta(\boldsymbol{x} - \boldsymbol{x}') = \delta(\boldsymbol{r} - \boldsymbol{r}')\delta_{ss'}$ and $[\hat{\psi}^\dagger(\boldsymbol{x}), \hat{\psi}^\dagger(\boldsymbol{x}')]_+ = [\hat{\psi}(\boldsymbol{x}), \hat{\psi}(\boldsymbol{x}')]_+ = 0$. From the field operators we can define the causal Green's function which is the central object of this approach. Physically it describes the propagation of a particle between $(\boldsymbol{x}_1, t_1)$ and $(\boldsymbol{x}_2, t_2)$,

$$G(\boldsymbol{x}_1 t_1, \boldsymbol{x}_2 t_2) = \frac{1}{i\hbar}\langle\Psi_0|\mathcal{T}\left[\hat{\psi}(\boldsymbol{x}_1, t_1)\hat{\psi}^\dagger(\boldsymbol{x}_2, t_2)\right]|\Psi_0\rangle, \tag{3.18}$$

where $|\Psi_0\rangle$ is the many-body ground state of the system, $\mathcal{T}$ is the Wick time ordering operator that orders the field operators such that time is increasing from right to left and the field operators are in the Heisenberg picture. Depending on the time ordering we either describe the propagation of an electron or hole.

This definition might seem rather abstract at first glance. However, the benefit of the Green's function becomes clear when we consider a single-particle observable $\hat{O}$ in second quantization, which can be expressed as

$$\hat{O} = \int d^3x \int d^3x' \, \hat{\psi}^\dagger(\boldsymbol{x}') O(\boldsymbol{x}, \boldsymbol{x}') \hat{\psi}(\boldsymbol{x}). \tag{3.19}$$

If we now calculate the expectation value for this operator we can easily express it in terms of a Green's function,

$$\begin{aligned} \langle O \rangle = \langle \Psi_0 | O | \Psi_0 \rangle &= \int d^3x \int d^3x' \, \langle \Psi_0 | \hat{\psi}^\dagger(\boldsymbol{x}') O(\boldsymbol{x}, \boldsymbol{x}') \hat{\psi}(\boldsymbol{x}) | \Psi_0 \rangle \\ &= \int d^3x \int d^3x' \, O(\boldsymbol{x}, \boldsymbol{x}') \lim_{t \to t'^+} G(\boldsymbol{x}t, \boldsymbol{x}'t'). \end{aligned} \tag{3.20}$$

An explicit knowledge of the ground state $|\Psi_0\rangle$ is therefore not necessary. Rather, it is sufficient to obtain the Green's function. Using the Green's function we can also calculate other properties of our system, e.g., the ground state energy can be directly obtained from the Galitskii-Migdal formula [45]. Furthermore, we can obtain the density of states, magnetization, or current densities directly from the Green's function.

Finally, the Green's function also provides access to various excited states properties since it has poles at the excitation energies of the system. To see this we use that $G(\boldsymbol{x}_1 t_1, \boldsymbol{x}_2 t_2)$ only depends on the time difference $G(\boldsymbol{x}_1 \boldsymbol{x}_2, t_1 - t_2)$ and perform a Fourier transformation with respect to time, [3]

$$G(\boldsymbol{x}\boldsymbol{x}', \omega) = \lim_{\eta \to +0} \frac{1}{2\pi} \int_{-\infty}^{\infty} d\omega' \frac{A(\boldsymbol{x}\boldsymbol{x}', \omega')}{\omega - \omega' + i\eta \, \mathrm{sgn}(\hbar\omega' - \mu)}, \tag{3.21}$$

where $A(\boldsymbol{x}\boldsymbol{x}', \omega')$ is the spectral function and μ the chemical potential. From the analysis of the poles we can then obtain ionization energies and electron affinities [38, 44], which are measured by photoemission spectroscopy experiments.

However, we have to emphasize that the single-particle Green's function $G(\boldsymbol{x}_1 t_1, \boldsymbol{x}_2 t_2)$ or $G(\boldsymbol{x}\boldsymbol{x}', \omega)$ only contains information about single-particle observables. For this reason we cannot use it directly to obtain optical absorption spectra, which are intrinsic two-particle properties. For this we would need to consider a two-particle propagation, which will be discussed in terms of the polarization function in section 3.3.

All these examples show that a detailed knowledge of the many-body wave function is not necessary to obtain predictions for an experiment. The knowledge of the Green's function is therefore enough to obtain any single-particle property we would like to calculate. The remaining challenge is to obtain G without an explicit calculation of $|\Psi_0\rangle$. For this, we derive the equation of motion for the Green's function.

3.2.2 Equation of motion

For concise expressions we introduce a short hand notation $1 = (\boldsymbol{x}_1, t_1) = (\boldsymbol{r}_1, s_1, t_1)$, where the Green's function becomes $G(\boldsymbol{x}_1 t_1, \boldsymbol{x}_2 t_2) = G(12)$. The equation of motion for a Green's function can be obtained from the Heisenberg equation of motion for the field operators,

$$i\hbar \frac{\partial}{\partial t} \hat{\psi}(\boldsymbol{x}, t) = \left[\hat{\psi}(\boldsymbol{x}, t), \hat{H} \right]. \tag{3.22}$$

We use the identity $\partial_t \Theta(t) = \delta(t)$ and obtain the equation of motion of the Green's function, [3]

$$\underbrace{\left\{ i\hbar \frac{\partial}{\partial t_1} - h^0(\boldsymbol{x}_1) \right\} G(11') = \delta(1 - 1')}_{\text{= math. def. of a Green's function}} \underbrace{- i\hbar \int d2 V(1-2) G_2(12, 1'2^+)}_{\text{= el-el interaction}}. \tag{3.23}$$

In this expression $h^0(\boldsymbol{x}) = -\frac{\hbar^2}{2m} \nabla_{\boldsymbol{x}}^2 + V_{\text{ext}}(\boldsymbol{x})$ contains all single-particle contributions of the Hamiltonian, i.e., kinetic energy, crystal potential and possible external fields. Two-particle contributions from the electron-electron interaction are contained in the second term on the right-hand side, where $V(1-2) =$

$V(\boldsymbol{x}_1 - \boldsymbol{x}_2)\delta(t_1 - t_2)$ is the Coulomb potential and $G_2(12, 1'2^+) = \frac{1}{(i\hbar)^2}\langle \mathcal{T}\psi(1)\psi(2)\psi^\dagger(2^+)\psi^\dagger(1')\rangle$ is the time-ordered two-particle Green's function, where 2^+ indicates an infinitesimal shift to obtain the correct time order.

In the case of independent particles, i.e., without electron-electron interaction, we can see that $G(11')$ aligns with the definition of a mathematical Green's function for the Schrödinger differential operator. This is the reason for the name Green's function, although in the general case G and G_2 are not Green's functions in the mathematical sense, and should rather be understood as propagators or correlation functions.

Similar as for G we can derive the equation of motion for the two-particle Green's function G_2, which would contain a three-particle Green's function. The three-particle Green's function is then determined by a four-particle Green's function and so on. Following this idea we could obtain a hierarchy of equations with ever increasing orders of Green's functions. [25] Therefore, one strategy could be to approximate the higher order Green's function to obtain a closed set of equations that can then be solved. Although this strategy has some advantages, it is usually not numerically tractable and will therefore not be considered further.

Alternatively, we can relate the problem to an effective single-particle problem. To do this, we consider the propagation of a particle together with the collective excitations of the environment. For example, instead of a single electron, we consider the electron together with the polarized environment as a screened charge cloud that moves together with the electron and can form a so-called quasiparticle. Formally, this is achieved by introducing the self-energy operator $\Sigma(12)$ of a quasiparticle, which is implicitly defined by a modification of the equation of motion, [3]

$$\left\{i\hbar\frac{\partial}{\partial t_1} - h^0(\boldsymbol{x}_1)\right\} G(11') - \int d2\, \Sigma(12)G(21') = \delta(1 - 1'), \tag{3.24}$$

or equivalently after taking a Fourier transform with respect to time,

$$\left\{\hbar\omega - h^0(\boldsymbol{x}_1)\right\} G(\boldsymbol{x}_1, \boldsymbol{x}_1', \omega) - \int dx_2\, \Sigma(\boldsymbol{x}_1, \boldsymbol{x}_2, \omega)G(\boldsymbol{x}_2, \boldsymbol{x}_1', \omega) = \delta(\boldsymbol{x}_1 - \boldsymbol{x}_1'). \tag{3.25}$$

The self-energy Σ contains collective excitations due to electron-electron interaction and is therefore in general non-local in space, time and spin. Moreover, it is not Hermitian, which leads to complex eigenvalues whose imaginary part results in a finite lifetime.

In Eq. (3.24) Σ contains the entire electron-electron interaction. For practical calculations it is often useful to shift some parts of the interaction into h^0. One prominent choice would be to split the interaction into Hartree and exchange-correlation interaction, like it was done previously in section 3.1 (c.f. Eq. (3.15)) and shift the Hartree contribution into the single-particle Hamiltonian $\tilde{h}^0(\boldsymbol{x}_1) = h^0(\boldsymbol{x}_1) + V_{\mathsf{H}}(\boldsymbol{x}_1)$. The self-energy would then only contain the exchange and correlation interactions, which we denote as $\tilde{\Sigma}$. This has not only advantages for the calculation of the self-energy, but can also be used for an effective computational scheme. For this we introduce the Hartree Green's function $G^{\mathsf{H}}(11')$ that obeys the equation of motion,

$$\left\{i\hbar\frac{\partial}{\partial t_1} - \tilde{h}^0(\boldsymbol{x}_1)\right\} G^{\mathsf{H}}(11') = \delta(1 - 1'). \tag{3.26}$$

A comparison with Eq. (3.24) then yields the Dyson equation for the full Green's function,

$$G(11') = G^{\mathsf{H}}(11') + \int d2 \int d3\, G^{\mathsf{H}}(12)\tilde{\Sigma}(23)G(31'). \tag{3.27}$$

This equation can in principle be solved iteratively. [3]

Another approach to solve Eq. (3.24) can be obtained by expanding $G(11')$ in a basis of single-particle wave functions $\phi_i(\boldsymbol{x})$, which are often assumed to be Kohn-Sham wave functions in practical calculations. The Green's function is then obtained as [46, 23]

$$G(\boldsymbol{x}, \boldsymbol{x}', \omega) = \sum_i \frac{\phi_i(\boldsymbol{x})\phi_i^*(\boldsymbol{x}')}{\hbar\omega - \epsilon_i^{\mathsf{QP}}}, \tag{3.28}$$

where ϵ_i^{QP} denotes the quasiparticle energies. By inserting this in Eq. (3.25) we obtain the quasiparticle equation,

$$\tilde{h}^0(\boldsymbol{x})\phi_i(\boldsymbol{x}) + \int dx' \tilde{\Sigma}(\boldsymbol{x}, \boldsymbol{x}', \epsilon_i^{\mathsf{QP}}/\hbar)\phi_i(\boldsymbol{x}') = \epsilon_i^{\mathsf{QP}}\phi_i(\boldsymbol{x}), \tag{3.29}$$

which is a generalization of the single-particle Schrödinger equation with a non-local, energy dependent potential. By choosing specific $\tilde{\Sigma}$ we can obtain typical approximations, e.g., the Kohn-Sham equation with $\tilde{\Sigma}^{\mathsf{DFT}}(12) = V_{\mathsf{xc}}(1)\delta(12)$, the Hartree-Fock equation with $\tilde{\Sigma}^{\mathsf{HF}}(12) = i\hbar G(12)V(1^+2)$, or the Hartree theory by setting $\tilde{\Sigma} = 0$. The formulation in terms of Dyson equation Eq. (3.27) or quasiparticle equation Eq. (3.29) are equivalent and one might chose the most appealing description for a given problem. The remaining task is to obtain a general expression for $\tilde{\Sigma}$, which can be obtained from the Hedin's set of equations.

3.2.3 Hedin's set of equations

A systematic way to obtain the self-energy and therefore the Green's function is given by the Hedin's set of equations, which represents the quantum-many-body problem exactly without any approximation and can be derived from first principles, [47]

$$G(11') = G^{\mathsf{H}}(11') + \int d2 \int d3\, G^{\mathsf{H}}(12)\tilde{\Sigma}(23)G(31') \tag{3.30}$$

$$\tilde{\Sigma}(12) = -i\hbar \int d4 \int d5\, G(14)\Gamma(42,5)W(1^+5) \tag{3.31}$$

$$W(11') = V(1-1') + \int d3 \int d4\, V(1-3)P(34)W(41') \tag{3.32}$$

$$P(12) = i\hbar \int d3 \int d4\, G(13)\Gamma(34,2)G(41^+) \tag{3.33}$$

$$\Gamma(12,3) = -\delta(1-2)\delta(1-3) + \frac{1}{i\hbar}\int d4 \int d5\, \frac{\delta\tilde{\Sigma}(12)}{\delta G(45)}P(45,33^+). \tag{3.34}$$

The first equation was already obtained before by introducing the self-energy $\tilde{\Sigma}$. The self-energy itself can be obtained from the dynamically screened Coulomb potential W and the vertex function Γ, which describes the interaction between electrons and holes in the system. The dynamically screened Coulomb potential can furthermore be obtained from the polarization function P and $V(1-2)$ is the bare Coulomb potential as before.

From this system of equations we can in principle obtain the Green's function of a system and therefore have access to spectroscopic quantities and other single-particle observables. Furthermore, we can obtain the polarization function from which we can obtain two-particle properties like the dielectric function Eq. (2.28) which includes optical properties. Although this system of equations can in principle be solved iteratively, this is generally not feasible. It is therefore necessary to find suitable approximations. One of the most important is the GW approximation, which we present next.

3.2.4 GW approximation

One typical approximation of the Hedin's set of equations is the GW approximation. It simplifies the numerical treatment tremendously while, at the same time, showing very good agreement with experiment. For this we neglect vertex corrections by setting $\Gamma(12,3) = -\delta(1-2)\delta(1-3)$. Eq. (3.31) then becomes

$$\tilde{\Sigma}^{\mathsf{GW}}(12) = i\hbar G(12)W(1^+2), \tag{3.35}$$

which is the reason for the name GW. It is a conserving approximation, i.e., energy and particle number are conserved. [48, 49] A comparison with the self-energy of the Hartree-Fock approximation $\tilde{\Sigma}^{\mathsf{HF}}(12) =$

$i\hbar G(12)V(1^+2)$ shows that GW can be seen as an extension, where the bare Coulomb potential is replaced by the dynamically screened potential W. It can therefore be seen as an improvement on the Hartree-Fock method, where many-body correlation effects are included. In addition, unlike the pure Coulomb potential, the screened Coulomb potential is not divergent, which makes it possible to obtain physically meaningful results, especially for metals where a pure Hartree-Fock approach is often not reliable. [50]

Today, the GW approximation has become the state-of-the-art method for calculating ionization energies, electron affinities and electronic (fundamental) band gaps with high precision. It has been shown to give results that are close to experimental measurements [37, 39, 40, 41, 42, 43, 3]. However, performing numerical GW calculations is still computationally very expensive compared to DFT and therefore only possible for relatively small systems. Furthermore, the complete omission of vertex corrections limits GW to the level of individual quasiparticles. Two-particle states such as bound electron-hole pairs (excitons) are not included. This can be seen from the polarization function Eq. (3.33) that simplifies to the polarization function for independent (quasi-)particles, which we want to denote as L^0,

$$P^{\text{GW}} = -i\hbar G(12')G(21') =: L^0(11', 22'). \tag{3.36}$$

This makes the GW approximation incapable of obtaining correct optical spectra. [3] For the evaluation of optical properties we have to go one step further and derive the Bethe-Salpeter equation, which is subject of the next section.

3.3 Excitons

The GW approximation is sufficient to calculate single-particle excitation energies like electron affinities or ionization energies. However, it is not sufficient to calculate charge neutral excitation such as optical excitations. In those cases an excited electron interacts with a hole via Coulomb interaction. This often leads to bound electron hole pairs that are called excitons. These states are crucial for optical properties and it is thus very important to have an adequate description of them. Excitations are inherently two-particle states and generally cannot be simplified to a single quasiparticle level. However, we can use Hedin's set of equations and derive an equation of motion for the two-particle polarization function, which is the Bethe-Salpeter equation. Form this, we can finally derive the exciton Hamiltonian, which will be the basis for the evaluation of optical properties later on.

3.3.1 Two-particle propagation and Bethe-Salpeter equation

First we generalize the polarization function $P(12)$ to a two-particle polarization function $P(11', 22')$, which are connected by $P(12) = P(11, 22)$. To obtain the equation of motion for the two-particle polarization function we combine Eq. (3.33) and Eq. (3.34) and using the definition Eq. (3.36), which yields

$$P(11', 22') = L^0(11', 22') + \int d3 \int d4 \int d5 \int d6\, L^0(11', 34)\Xi(34, 56)P(56, 22'), \tag{3.37}$$

with the integration kernel $\Xi(34, 56) = -\frac{1}{i\hbar}\frac{\delta\tilde{\Sigma}(43)}{\delta G(56)}$. This equation is called Bethe-Salpeter equation (BSE) [51, 52, 53, 54, 46, 38, 3, 55]. It describes the simultaneous propagation of two particles and is very similar to a Dyson equation Eq. (3.27) in the single quasiparticle case.

The variational derivative in the integration kernel $\Xi(34, 56)$ is unsuitable for a direct numerical evaluation. However, we can approximate the kernel by using the GW approximation for the self-energy Eq. (3.35) as before. This allows us to calculate the derivative and we obtain

$$\begin{aligned}\Xi(1'1, 22') &= -\delta(1-2)\delta(1'-2')W(1^+1') - G(11')\frac{\delta W(1^+1')}{\delta G(22')} \\ &\approx -\delta(1-2)\delta(1'-2')W(1^+1').\end{aligned} \tag{3.38}$$

It can be shown that the second term (variational derivative of W) is of the order $\propto W^2$. Thus we can neglect this term and obtain the linearized BSE [3],

$$P(11', 22') = L^0(11', 22') - \int d3 \int d4\, L^0(11', 4^+3) W(34) P(34^+, 22'). \tag{3.39}$$

This equation now contains the interaction of electrons and holes via the screened Coulomb interaction. With this description, it is possible to calculate charge neutral excitations and bound exciton states. Moreover, the polarization function is directly related to the microscopic dielectric function by Eq. (2.28), which allows us to calculate optical properties from first principles.

3.3.2 Bethe-Salpeter equation for the macroscopic polarization and local field effects

The polarization function that is obtained from the Bethe-Salpeter equation Eq. (3.39) is directly related to the microscopic dielectric function $\epsilon_{\boldsymbol{G}\boldsymbol{G}'}$ by virtue of Eq. (2.28). As explained in section 2.3.1, an experiment is only able to measure the *macroscopic* dielectric function ϵ^{M}, which means that we have to calculate ϵ^{M} rather than $\epsilon_{\boldsymbol{G}\boldsymbol{G}'}$. Both functions are related to each other by Eq. (2.30). A straightforward solution could be to compute all components of $\epsilon_{\boldsymbol{G}\boldsymbol{G}'}$ and perform a complete matrix inversion to yield $\epsilon^{-1}_{\boldsymbol{G}\boldsymbol{G}'}$ from which we can obtain the ϵ^{M} by Eq. (2.30). However, it turns out that this approach is computationally extremely demanding and usually not feasible. [3]

A better approach is to compute ϵ^{M} directly. For this, we introduce the macroscopic (spin-summed) polarization function P^{M} in analogy to Eq. (2.28),

$$\epsilon^{\mathsf{M}}(\boldsymbol{e}_q, z) = \lim_{\boldsymbol{q}\to 0} \epsilon^{\mathsf{M}}(\boldsymbol{q}, z) = 1 - \lim_{\boldsymbol{q}\to 0} 2\tilde{V}(|\boldsymbol{q}|) P^{\mathsf{M}}(\boldsymbol{q}, \boldsymbol{q}, z), \tag{3.40}$$

where $\boldsymbol{e}_q = \boldsymbol{q}/|\boldsymbol{q}|$ is the direction of the photon momentum, $\tilde{V}(|\boldsymbol{q}|)$ is the Fourier transformed Coulomb potential and the factor 2 is due to the spin summation. Pick, Cohen and Martin [56] have outlined an approach to find the BSE for P^{M}, which we present shortly. We start by splitting the tensor $\epsilon_{\boldsymbol{G}\boldsymbol{G}'}$ into head, wings and body,

$$\epsilon = \left(\begin{array}{c|ccc} \epsilon_{00} & \dots & \epsilon_{0\boldsymbol{G}'} & \dots \\ \hline \vdots & & & \\ \epsilon_{\boldsymbol{G}0} & & S & \\ \vdots & & & \end{array}\right) = \left(\begin{array}{c|ccc} \text{head} & \dots & \text{wing} & \dots \\ \hline \vdots & & & \\ \text{wing} & & \text{body} & \\ \vdots & & & \end{array}\right), \tag{3.41}$$

and perform a formal matrix inversion, similar to a blockwise numerical inversion [57]. Taking the 00-element ($\boldsymbol{G} = \boldsymbol{G}' = 0$) and inverting it again we obtain ϵ^{M},

$$\epsilon^{\mathsf{M}}(\boldsymbol{e}_q, z) = \lim_{\boldsymbol{q}\to 0} \left[\epsilon(\boldsymbol{q}, \boldsymbol{q}, z) - \sum_{\boldsymbol{G},\boldsymbol{G}'\neq 0} \epsilon(\boldsymbol{q}, \boldsymbol{q}+\boldsymbol{G}, z) S^{-1}(\boldsymbol{q}+\boldsymbol{G}, \boldsymbol{q}+\boldsymbol{G}', z) \epsilon(\boldsymbol{q}+\boldsymbol{G}', \boldsymbol{q}, z) \right]. \tag{3.42}$$

The difference between the macroscopic and the microscopic dielectric function $\epsilon^{\mathsf{M}}(\boldsymbol{q}, \boldsymbol{q}, z) - \epsilon(\boldsymbol{q}, \boldsymbol{q}, z)$, usually called local field effects, is now clearly visible. It is caused by the wing and body elements on the right-hand side. We can now insert Eq. (2.28) into Eq. (3.42) and compare it with Eq. (3.40) to obtain an expression for the macroscopic polarization function,

$$P^{\mathsf{M}}(\boldsymbol{q}, \boldsymbol{q}, z) = P(\boldsymbol{q}, \boldsymbol{q}, z) + 2 \sum_{\boldsymbol{G},\boldsymbol{G}'\neq 0} P(\boldsymbol{q}, \boldsymbol{q}+\boldsymbol{G}, z) S^{-1}(\boldsymbol{q}+\boldsymbol{G}, \boldsymbol{q}+\boldsymbol{G}', z) \tilde{V}(|\boldsymbol{q}+\boldsymbol{G}'|) P(\boldsymbol{q}+\boldsymbol{G}', \boldsymbol{q}, z). \tag{3.43}$$

For a compact notation we introduce the truncated, short range Coulomb potential as

$$\tilde{\tilde{V}}(|\boldsymbol{q}+\boldsymbol{G}|) = \begin{cases} 0 & \text{for } \boldsymbol{G} = 0, \\ \tilde{V}(|\boldsymbol{q}+\boldsymbol{G}|) & \text{for } \boldsymbol{G} \neq 0 \end{cases}. \tag{3.44}$$

Using this and after some reformulations, we can obtain the relation between P and P^{M} in terms of the BSE for the macroscopic polarization function $P^{\mathsf{M}} = P + P2\bar{\bar{V}}P^{\mathsf{M}}$. In the final step we use Eq. (3.39) for the polarization function P and perform an inverse Fourier transform to obtain the BSE for the *macroscopic* polarization function in real space,

$$P^{\mathsf{M}}(11', 22') = L^0(11', 22') + \int d3 \int d4 \int d5 \int d6 L^0(11', 43)\Xi^{\mathsf{M}}(34, 56)P^{\mathsf{M}}(56, 22'), \tag{3.45}$$

with the kernel

$$\Xi^{\mathsf{M}}(34, 56) = -\delta(4-5)\delta(3-6)W(4^+, 3) + \delta(3-4)\delta(5^+-6)\bar{V}(3-5). \tag{3.46}$$

Here $\bar{V}(1-2)$ is the inverse Fourier transform of the truncated, short range Coulomb potential Eq. (3.44). A comparison with Eq. (3.39) shows that the local field effects can be expressed in terms of an additional short range interaction $\bar{V}(1-2)$. With the BSE (3.45), we now have direct excess to optical properties and avoid costly calculations of the microscopic dielectric function and explicit matrix inversions. With Eq. (3.45) and Eq. (3.40) we therefore have all necessary ingredients to calculate linear optical properties. The next step is to use this formulation to perform practical numerical calculations.

Before we proceed with the numerical evaluation, we want to introduce the static screening approximation, which we will use in the following. This assumes that the screening is instantaneous and the Coulomb interaction becomes

$$W(34) \approx W(\boldsymbol{x}_3, \boldsymbol{x}_4)\delta(t_3 - t_4). \tag{3.47}$$

This approximation is justified for semiconductors because the screening is usually very fast. For a homogeneous electron gas the timescale is in the order of $2\pi/\omega_p$, where ω_p is the plasma frequency. [3] As a result of this approximation, the macroscopic polarization function depends only on a single time difference and thus only on one frequency, which leads to enormous simplifications in numerical calculations. In this regard $P^{\mathsf{M}}(11', 22')$ can be simplified to $P^{\mathsf{M}}(\boldsymbol{x}_1\boldsymbol{x}_1', \boldsymbol{x}_2\boldsymbol{x}_2'; z)$, where z is a complex frequency.

3.3.3 Basis of quasiparticle wave functions and generalized eigenvalue problem

A direct evaluation of Eq. (3.45) is usually not suitable and would be inefficient. However, we can express the polarization function in terms of single-particle wave functions $\phi_\rho(\boldsymbol{x})$ similar to what we did for the Green's function in Eq. (3.28), to obtain the quasiparticle Eq. (3.29). We choose the basis functions $\phi_\rho(\boldsymbol{x})$ such that they satisfy the quasiparticle equation. With this we can express the macroscopic polarization function as

$$P^{\mathsf{M}}(\boldsymbol{x}_1\boldsymbol{x}_1', \boldsymbol{x}_2\boldsymbol{x}_2'; z) = \sum_{\rho_1, \rho_1', \rho_2, \rho_2'} P^{\mathsf{M}}(\rho_1\rho_1', \rho_2\rho_2'; z)\phi_{\rho_1}(\boldsymbol{x}_1)\phi^*_{\rho_1'}(\boldsymbol{x}_1')\phi_{\rho_2}(\boldsymbol{x}_2)\phi^*_{\rho_2'}(\boldsymbol{x}_2'), \tag{3.48}$$

where $P^{\mathsf{M}}(\rho_1\rho_1', \rho_2\rho_2'; z)$ are the coefficients within this basis. In the same manner we can express L^0 and Ξ^{M} in the same basis. The corresponding coefficients then satisfy the algebraic equation

$$P^{\mathsf{M}}(\rho_1\rho_1', \rho_2\rho_2'; z) = \frac{f(\epsilon_{\rho_1}) - f(\epsilon_{\rho_1'})}{\epsilon_{\rho_1} - \epsilon_{\rho_1'} - \hbar z}\left(\delta_{\rho_1\rho_2'}\delta_{\rho_2\rho_1'} + \sum_{\rho_3, \rho_4} \Xi^{\mathsf{M}}(\rho_1'\rho_1, \rho_3\rho_4)P^{\mathsf{M}}(\rho_3\rho_4, \rho_2\rho_2'; z)\right), \tag{3.49}$$

where $f(\epsilon_{\rho_1})$ is the occupation number of a state $|\rho_1\rangle$ according to the Fermi-Dirac distribution. In addition, the problem can be further simplified by noting that the solution can be traced back to the solution of the generalized eigenvalue problem [52],

$$\mathcal{F}\mathcal{H}|\Phi_\Lambda\rangle = \mathcal{E}_\Lambda|\Phi_\Lambda\rangle. \tag{3.50}$$

Matrices $\mathcal{F}$ and $\mathcal{H}$ are given by

$$\mathcal{F}(\rho_1\rho_2,\rho_3\rho_4) = -\frac{f(\epsilon_{\rho_1}) - f(\epsilon_{\rho_2})}{|f(\epsilon_{\rho_1}) - f(\epsilon_{\rho_2})|}\delta_{\rho_1\rho_3}\delta_{\rho_2\rho_4}, \tag{3.51}$$

$$\mathcal{H}(\rho_1\rho_2,\rho_3\rho_4) = |\epsilon_{\rho_1} - \epsilon_{\rho_2}|\delta_{\rho_1\rho_3}\delta_{\rho_2\rho_4} - |f(\epsilon_{\rho_1}) - f(\epsilon_{\rho_2})|^{\frac{1}{2}}\Xi^{\mathsf{M}}(\rho_2\rho_1,\rho_3\rho_4)|f(\epsilon_{\rho_3}) - f(\epsilon_{\rho_4})|^{\frac{1}{2}}. \tag{3.52}$$

From the solution of the eigenvalue problem Eq. (3.50) we can finally obtain the macroscopic polarization function as

$$P^{\mathsf{M}}(\rho_1\rho_1',\rho_2\rho_2';z) = -\left[|f(\epsilon_{\rho_1}) - f(\epsilon_{\rho_1'})| \cdot |f(\epsilon_{\rho_2'}) - f(\epsilon_{\rho_2})|\right]^{\frac{1}{2}} \sum_{\Lambda} \mathrm{sgn}(\mathcal{E}_\Lambda) \frac{\Phi_\Lambda(\rho_1\rho_1')\Phi_\Lambda^*(\rho_2'\rho_2)}{\mathcal{E}_\Lambda - \hbar z}. \tag{3.53}$$

$\mathcal{F}$ and $\mathcal{H}$ are both Hermitian, but the product $\mathcal{F}\mathcal{H}$ is not. However, it can be shown that the product has real eigenvalues [58]. Because of the definition of $\mathcal{F}$ the entire matrix $\mathcal{F}\mathcal{H}$ is antisymmetric and for every eigenvalue $\mathcal{E}_\Lambda$ there exists a Λ' with $\mathcal{E}_\Lambda = -\mathcal{E}_{\Lambda'}$ and the corresponding eigenvectors obey the relation $\Phi_{\Lambda'}(\rho_1,\rho_1') = \Phi_\Lambda^*(\rho_1',\rho_1)$.

Finally, we obtain the macroscopic dielectric function from Eq. (3.40) and the eigenvectors $|\Phi_\Lambda\rangle$ after a Fourier transform, [3]

$$\epsilon^{\mathsf{M}}(\boldsymbol{e}_q,z) = 1 + \lim_{\boldsymbol{q}\to 0}\tilde{V}(|\boldsymbol{q}|)\frac{1}{\Omega}\sum_{\Lambda}\frac{\mathrm{sgn}(\mathcal{E}_\Lambda)}{\mathcal{E}_\Lambda - \hbar z}\left|\sum_{\rho_1\rho_1'}\left[B_{\rho_1\rho_1'}(\boldsymbol{q})\right]^*\Phi_\Lambda(\rho_1,\rho_1')\sqrt{\left|f(\epsilon_{\rho_1}) - f(\epsilon_{\rho_1'})\right|}\right|^2, \tag{3.54}$$

with the Bloch integrals that come from the Fourier transformation,

$$B_{\rho_1\rho_1'}(\boldsymbol{q}+\boldsymbol{G}) = \int d^3x\, \phi_{\rho_1}^*(\boldsymbol{x})e^{i(\boldsymbol{q}+\boldsymbol{G})\boldsymbol{x}}\phi_{\rho_1'}(\boldsymbol{x}). \tag{3.55}$$

The problem of solving the BSE is therefore reduced to solving the generalized eigenvalue problem Eq. (3.50). The eigenfunctions $|\Phi_\Lambda\rangle$ describe two-particle states of electrons and holes that interact with each other and the description is therefore similar to a stationary Schrödinger equation. However, caution is required since the product $\mathcal{F}\mathcal{H}$ is not Hermitian. In the next step we simplify the eigenvalue equation further by applying the Tamm-Dancoff approximation, from which we obtain a Hermitian exciton Hamiltonian.

3.3.4 Exciton Hamiltonian in Tamm-Dancoff approximation

We want to take a closer look at the eigenvalue Eq. (3.50) which needs to be solved in order to obtain the macroscopic dielectric function. As a simplification we consider a periodic crystal with completely occupied valence bands and completely unoccupied conduction bands. Thus, the occupation function $f(\epsilon_{\rho_1})$ becomes zero or one and $|\rho_1\rangle$ is a state in the valence $|v\boldsymbol{k}\rangle$ or conduction $|c\boldsymbol{k}\rangle$ band. Furthermore, we only consider transitions with vanishing wave vector $\boldsymbol{q} \to 0$, which is reasonable because in UV-VIS spectra the photon momentum is negligibly small compared to electron and hole momentum. We therefore only have vertical transitions $|v\boldsymbol{k}m_v\rangle \to |c\boldsymbol{k}m_c\rangle$. With this assumptions, the exciton Hamiltonian $\mathcal{F}\mathcal{H}$ consists of pair excitations of all possible combinations of v, v', c and c' with the same number of particles,

$$(\mathcal{F}\mathcal{H})_{\rho_1\rho_2,\rho_3\rho_4} = \begin{pmatrix}(\mathcal{F}\mathcal{H})_{cv,c'v'} & (\mathcal{F}\mathcal{H})_{vc,c'v'}\\ (\mathcal{F}\mathcal{H})_{cv,v'c'} & (\mathcal{F}\mathcal{H})_{vc,v'c'}\end{pmatrix} = \begin{pmatrix}H & \Xi^{\mathsf{M}}\\ -\Xi^{\mathsf{M}^+} & -H^+\end{pmatrix}. \tag{3.56}$$

The entire matrix $\mathcal{F}\mathcal{H}$ can be split into four blocks that are described by the matrices H and Ξ^{M}. Along the diagonal we find resonant pair-excitation (H) and anti-resonant excitations ($-H^+$), with positive and negative excitation energies respectively. These diagonal parts contain all single-particle contributions,

i.e., the quasiparticle band structure, together with the two-particle contributions from (screened) Coulomb interaction and local field effects,

$$H(c\boldsymbol{k}\, v\boldsymbol{k}, c'\boldsymbol{k}'\, v'\boldsymbol{k}') = [\epsilon_c(\boldsymbol{k}) - \epsilon_v(\boldsymbol{k})]\, \delta_{cc'}\delta_{vv'}\delta_{\boldsymbol{k}\boldsymbol{k}'} - W_{cc',vv'}(\boldsymbol{k}-\boldsymbol{k}') + \bar{V}_{cv,v'c'}(\boldsymbol{k}-\boldsymbol{k}'). \tag{3.57}$$

The off-diagonal parts describe the coupling between pairs of positive and negative excitation energies described by Ξ^{M}. In many cases the off-diagonal parts are small. Neglecting these parts is called *Tamm-Dancoff approximation* (TDA) [59, 60, 3]. In this approximation we only need to solve the eigenvalue equation for H,

$$\sum_{v'c'\boldsymbol{k}'} H(c\boldsymbol{k}\, v\boldsymbol{k}, c'\boldsymbol{k}'\, v'\boldsymbol{k}') A_\Lambda(c'\boldsymbol{k}'\, v'\boldsymbol{k}') = E_\Lambda A_\Lambda(c'\boldsymbol{k}'\, v'\boldsymbol{k}'). \tag{3.58}$$

Since H is Hermitian, this equation is of the form of a Schrödinger equation and we call H the exciton Hamiltonian. As before the dielectric function follows from Eq. (3.54) together with the eigenvectors A_Λ and excitation energies E_Λ. Performing the TDA is a huge simplification. However, it should be pointed out that there are also systems where this approximation fails. [61, 62]

So far, we have not explicitly considered the spin of electrons and holes. In non-spin-polarized systems, the BSE splits into a singlet and a triplet part, which can be solved independently. The screened Coulomb interaction contributes to both singlet and triplet, whereas local field effects are only present in the singlet case. Optical excitations can only excite the singlet states and cannot cause a spin flip, which can also be seen in Eq. (3.55). It is thus sufficient to consider the singlet case only. [3]

Finally, we can write down the single parts of the Hamiltonian Eq. (3.57) in the basis of single-particle wave functions $|\phi\rangle$. The screened Coulomb interaction is given in reciprocal space,

$$\begin{aligned} W_{cc',vv'}(\boldsymbol{k},\boldsymbol{k}') &= \int dx \int dx'\, \phi^*_{c\boldsymbol{k}}(\boldsymbol{x})\phi^*_{v'\boldsymbol{k}'}(\boldsymbol{x}')V_{\mathsf{sc}}(\boldsymbol{x},\boldsymbol{x}')\phi_{v\boldsymbol{k}}(\boldsymbol{x}')\phi_{c'\boldsymbol{k}'}(\boldsymbol{x}) \\ \text{with } V_{\mathsf{sc}}(\boldsymbol{x},\boldsymbol{x}') &= \frac{1}{\Omega}\sum_{\boldsymbol{q}}\sum_{\boldsymbol{G}\boldsymbol{G}'} \epsilon^{-1}(\boldsymbol{q}+\boldsymbol{G},\boldsymbol{q}+\boldsymbol{G}')\tilde{V}(|\boldsymbol{q}+\boldsymbol{G}'|)e^{i\boldsymbol{q}(\boldsymbol{x}-\boldsymbol{x}')}e^{i\boldsymbol{G}\boldsymbol{x}}e^{-i\boldsymbol{G}'\boldsymbol{x}'}, \end{aligned} \tag{3.59}$$

and local field effects are given by

$$\bar{V}_{cv,v'c'}(\boldsymbol{k},\boldsymbol{k}') = \int dx \int dx'\, \phi^*_{c\boldsymbol{k}}(\boldsymbol{x})\phi^*_{v'\boldsymbol{k}'}(\boldsymbol{x}') \left[\frac{1}{\Omega}\sum_{\boldsymbol{G}\neq 0}\tilde{V}(|\boldsymbol{G}|)e^{i\boldsymbol{G}(\boldsymbol{x}-\boldsymbol{x}')}\right]\phi_{v\boldsymbol{k}}(\boldsymbol{x})\phi_{c'\boldsymbol{k}'}(\boldsymbol{x}'). \tag{3.60}$$

With this we have obtained a complete description and tractable computational scheme for the calculation of linear optical properties. The exciton Hamiltonian is implemented in many established codes [63, 64, 65] and represents today's state-of-the-art approach. Although we have simplified the two-particle problem tremendously, it still is a computational very demanding task. This is because converged calculations usually require a lot of $\boldsymbol{k}$-points, which makes the exciton Hamiltonian a high-rank matrix that is in general not sparse. In chapter 6 we will derive a further refinement of this method which solves this issue and enables high-performance calculations for large systems. This is achieved by using maximally localized Wannier function, which we introduce in the next section.

3.4 Periodic systems and maximally localized Wannier functions (MLWF)

Many solid-state materials have a periodic crystal structure in which a unit cell with one or more atoms repeats itself periodically in different directions. This translational symmetry simplifies the theoretical description of the material enormously and also has important physical consequences. For example, single-particle excitation energies depend on the (crystal) momentum $\boldsymbol{k}$ and form a continuous band structure $E_{n\boldsymbol{k}}$. The associated (quasi-)particle wave functions $|\phi_{n\boldsymbol{k}}\rangle$, which satisfy Eq. (3.17) or Eq. (3.29) are then in the form of Bloch waves,

$$\langle\, \boldsymbol{x} \,|\, \phi_{n\boldsymbol{k}} \,\rangle = \phi_{n\boldsymbol{k}}(\boldsymbol{x}) = u_{n\boldsymbol{k}}(\boldsymbol{x})e^{i\boldsymbol{k}\boldsymbol{x}}, \tag{3.61}$$

where $u_{n\boldsymbol{k}}(\boldsymbol{x})$ is a periodic function with respect to a unit cell vector $\boldsymbol{R}$, i.e., $u_{n\boldsymbol{k}}(\boldsymbol{x}) = u_{n\boldsymbol{k}}(\boldsymbol{x}+\boldsymbol{R})$. The periodicity of the crystal and wave functions suggest an evaluation in Fourier space (reciprocal space), where $\boldsymbol{k}$ is already a good quantum number. For numerical calculations it is therefore convenient to express $|\phi_{n\boldsymbol{k}}\rangle$ in terms of plane waves. Such a procedure has proven to be very efficient and is usually implemented in common ab-initio simulation codes that use periodic boundary conditions. [66, 67, 68, 69]

The obtained Bloch waves are by construction delocalized over the entire crystal, which can be disadvantageous in some situations. For example the analysis of chemical bonds or comparisons with molecular systems is not straightforward. Also perturbations that break the translational symmetry of the crystal, e.g., when considering disorder or doping, are difficult to describe in such a basis. In such situations it is beneficial to transform into a localized basis of atomic or molecular orbitals.

One systematic approach to obtain a localized basis in real space is to transform the Bloch waves using a Fourier transformation. The obtained wave functions are then called Wannier functions $w_{n\boldsymbol{R}}(\boldsymbol{x})$ [70],

$$|w_{n\boldsymbol{R}}\rangle = \frac{1}{\sqrt{N_\Omega}} \sum_{\boldsymbol{k}} e^{-i\boldsymbol{k}\boldsymbol{R}} |\phi_{n\boldsymbol{k}}\rangle, \tag{3.62}$$

where N_Ω is the volume of the Brillouin zone and $\boldsymbol{R}$ is a unit cell vector.

Eq. (3.62) has already been used for qualitative considerations in the 1930s. [70] However, performing this transformation in numerical calculations causes two severe problems. First, band crossings and degeneracies are not taken into account, which means that Eq. (3.62) is only valid for single bands that are isolated in the entire Brillouin zone. Second, the underlying Bloch functions are obtained only up to a $\boldsymbol{k}$-dependent gauge phase. Choosing a different gauge $|\tilde{\phi}_{n\boldsymbol{k}}\rangle = e^{i\theta_n(\boldsymbol{k})}|\phi_{n\boldsymbol{k}}\rangle$ would be perfectly legitimate for Bloch functions, but would have a huge impact on shape and spread of the obtained Wannier functions. The gauge freedom of the Bloch functions therefore leads to a strong non-uniqueness of the Wannier functions. If one chooses the gauge phase such that the Bloch functions are smooth with respect to $\boldsymbol{k}$, i.e. $\nabla_{\boldsymbol{k}}|\tilde{\phi}_{n\boldsymbol{k}}\rangle$ is regular, one obtains very localized Wannier functions, which originates from general properties of a Fourier transform. Therefore, it is possible to define maximally localized Wannier functions (MLWF) by generalizing Eq. (3.62) to [71, 72]

$$|w_{m\boldsymbol{R}}\rangle = \frac{1}{\sqrt{N_\Omega}} \sum_{n\boldsymbol{k}} e^{-i\boldsymbol{k}\boldsymbol{R}} U_{mn}(\boldsymbol{k}) |\phi_{n\boldsymbol{k}}\rangle, \tag{3.63}$$

where the sum over n is usually restricted to certain groups of bands, e.g., all valence bands or the lowest conduction bands, and $U_{mn}(\boldsymbol{k})$ is a unitary matrix that takes care of band mixing and gauge phases. It is obtained by applying an optimization procedure in which the spread functional,

$$\Omega = \sum_m \left[\langle w_{m0}|r^2|w_{m0}\rangle - \langle w_{m0}|\boldsymbol{r}|w_{m0}\rangle^2 \right], \tag{3.64}$$

is minimized [71, 72, 73] and the obtained Wannier functions are thus maximally localized. This criterion is equivalent to the localization criterion of Foster and Boys [74, 75, 76, 73] used in quantum chemistry. The obtained MLWF are also similar to molecular or atomic orbitals, e.g., s and p_z orbitals in hydrocarbons or combinations of sp^3 hybrid orbitals for the valence electrons of silicon if all valence bands are contained in the transformation. At larger distances they show an exponential decay [77].

Moreover, Wannier functions with the same index m but different unit cell indexes $\boldsymbol{R}$ are related to each other by $w_{n\boldsymbol{R}}(\boldsymbol{x}) = w_{n0}(\boldsymbol{x}-\boldsymbol{R})$. That means they are transferable building blocks with the same shape. In that sense they are a generalization of molecular orbitals in a periodic crystal. For single molecules they are indeed similar to molecular orbitals if all valence states are included in the Wannier transformation.

From Eq. (3.63) it becomes clear that MLWF are directly related to the Boch functions of the system by a unitary transformation. They can be obtained at different levels of theory, e.g., from DFT wave functions

or at GW level [78]. Starting with a quasiparticle description, e.g., by using the Kohn-Sham approach, we can express the Hamiltonian in terms of Wannier functions,

$$\begin{aligned} H &= \sum_{n\boldsymbol{k}} |\phi_{n\boldsymbol{k}}\rangle \epsilon_{n\boldsymbol{k}} \langle \phi_{n\boldsymbol{k}}| = \sum_{mm'} \sum_{\boldsymbol{R}\boldsymbol{R}'} H_{mm'}(\boldsymbol{R}' - \boldsymbol{R}) |w_{m\boldsymbol{R}}\rangle \langle w_{m'\boldsymbol{R}'}| \\ &= \sum_{mm'} \sum_{\boldsymbol{R}\boldsymbol{R}'} H_{mm'}(\boldsymbol{R}' - \boldsymbol{R}) |w_{m\boldsymbol{0}}\rangle \langle w_{m',\boldsymbol{R}'-\boldsymbol{R}}|, \end{aligned} \tag{3.65}$$

where matrix elements of the Hamiltonian in Wannier representation are obtained from the band energies $\epsilon_{n\boldsymbol{k}}$,

$$H_{mm'}(\boldsymbol{R}) = \frac{1}{N_\Omega} \sum_{n\boldsymbol{k}} e^{-i\boldsymbol{k}\boldsymbol{R}} U_{m'n}(\boldsymbol{k}) \epsilon_{n\boldsymbol{k}} U^*_{nm}(\boldsymbol{k}). \tag{3.66}$$

$H_{mm'}(\boldsymbol{R})$ represents a tight-binding model, where matrix elements with $m = m'$ represent the onsite-energies of every Wannier orbital $|w_{m\boldsymbol{R}}\rangle$ and $H_{mm'}(\boldsymbol{R} - \boldsymbol{R}')$ the transfer integral between sites $|w_{m\boldsymbol{R}}\rangle$ and $|w_{m'\boldsymbol{R}'}\rangle$. The transfer integrals contain the probability of a particle to go from one site to another, together with the corresponding phase shift. Since the Wannier functions are strongly localized, the transfer integrals decrease exponentially with distance between Wannier functions. Using the real space tight-binding model one can perform an interpolation of the band structure by doing the reverse transformation for arbitrary $\boldsymbol{k}$-points. [73] Furthermore, the real-space tight-binding description is particularly useful for the investigation of disorder, doping and electron-phonon coupling, which we will exploit in the following chapters.

3.5 Including vibrational degrees of freedom: the Holstein-Peierls model

So far, we have assumed a rigid atomic lattice inside the material and focused on the electronic structure. Now, we want to remove this assumption and include lattice vibrations using the Holstein-Peierls model [79, 25]. We begin by expressing the quasiparticle Hamiltonian in a localized, orthonormal basis. This can be, for example, a basis of MLWF, Gaussian functions or orthogonalized atomic or molecular orbitals. The electronic structure is then obtained as a tight-binding model in second quantization,

$$\hat{H}_{\text{el}} = \sum_{ij} \epsilon_{ij} \hat{a}^\dagger_i \hat{a}_j, \tag{3.67}$$

where $\hat{a}^{(\dagger)}_i$ annihilates (creates) a fermion at orbital i. If we chose a basis of MLWF we obtain Eq. (3.65) with $i \equiv (m, \boldsymbol{R})$ and $j \equiv (m', \boldsymbol{R}')$.

The motion of the nucleus around its equilibrium positions leads to harmonic oscillations that also contribute to the Hamiltonian and can be expressed using bosonic annihilation (creation) operators $\hat{b}^{(\dagger)}_{\boldsymbol{Q}}$ of a specific phonon mode $\boldsymbol{Q}$ with frequency $\omega_{\boldsymbol{Q}}$,

$$\hat{H}_{\text{ph}} = \sum_{\boldsymbol{Q}} \hbar\omega_{\boldsymbol{Q}} \left(\hat{b}^\dagger_{\boldsymbol{Q}} \hat{b}_{\boldsymbol{Q}} + \frac{1}{2} \right). \tag{3.68}$$

Moreover, lattice vibrations change the distance between atoms and thus electronic onsite energies and transfer integrals. They are therefore functions of the nuclear positions $\boldsymbol{R}_{n\mu}$, which we denote as $\epsilon_{ij}(\{\boldsymbol{R}_{n\mu}\})$, where n denotes the unit cell and μ labels the atom in a unit cell. We can perform a Taylor expansion of $\epsilon_{ij}(\{\boldsymbol{R}_{n\mu}\})$ around the equilibrium lattice positions $\boldsymbol{R}^0_{n\mu}$ up to linear order,

$$\epsilon_{ij}(\{\boldsymbol{R}_{n\mu}\}) = \epsilon_{ij}(\{\boldsymbol{R}^0_{n\mu}\}) + \sum_{n\mu} (\boldsymbol{R}_{n\mu} - \boldsymbol{R}^0_{n\mu}) \frac{\partial \epsilon_{ij}}{\partial \boldsymbol{R}_{n\mu}}\bigg|_{\boldsymbol{R}_{n\mu} = \boldsymbol{R}^0_{n\mu}} + \dots . \tag{3.69}$$

Here, localization in real space causes only displacements $\boldsymbol{R}_{n\mu}$ near the orbitals $|i\rangle$ and $|j\rangle$ to contribute. We can express the replacement $(\boldsymbol{R}_{n\mu} - \boldsymbol{R}^0_{n\mu})$ in terms of phonon creation and annihilation operators and obtain the electron-phonon-coupling part of the Hamiltonian as

$$\hat{H}_{\text{el-ph}} = \sum_{ij} \sum_{\boldsymbol{Q}} \hbar\omega_{\boldsymbol{Q}} g^{\boldsymbol{Q}}_{ij} \left(\hat{b}^\dagger_{\boldsymbol{Q}} + \hat{b}_{-\boldsymbol{Q}} \right) \hat{a}^\dagger_i \hat{a}_j, \tag{3.70}$$

where the coupling constants are obtained as $g^{\boldsymbol{Q}}_{ij} = (2\hbar\omega^3_{\boldsymbol{Q}} N_\Omega)^{-\frac{1}{2}} \frac{\partial \epsilon_{ij}}{\partial X_{\boldsymbol{Q}}}$ and $X_{\boldsymbol{Q}}$ is the normal vector of a phonon mode. Putting everything together, we obtain the Holstein-Peierls model Hamiltonian [79, 25], which is the starting point for our transport calculations,

$$\hat{H} = \hat{H}_{\text{el}} + \hat{H}_{\text{ph}} + \hat{H}_{\text{el-ph}}. \tag{3.71}$$

The Holstein-Peierls Hamiltonian is particularly well suited to model organic molecular crystals. Those materials show significant electron-phonon coupling across multiple energy scales, i.e., simultaneously coupling to very low and high energy vibrations. [80] As a result the corresponding model hosts a variety of different phenomena. For example, the coupling to high-frequency modes leads to the emergence of polarons. [81, 25, 82, 83] This is a quasiparticle that consists of an electron (or hole) together with high-frequency lattice vibrations that form a polarization cloud. On the other hand, the coupling to low-frequency modes leads to scattering of charge carriers and can better be described by hopping models or disordered lattices. [84, 85] The coexistence of both regimes poses a significant theoretical challenge and it is difficult to find effective and tractable descriptions. [85, 86] In the next chapter, we will present an approach to overcome such problems and show that the combination of low- and high-frequency modes gives rise to new physical effects that are not present in either regimes.

4 Publication: Interplay of band occupation, localization, and polaron renormalization for electron transport in molecular crystals: Naphthalene as a case study

Summary:

Organic molecular crystals are a class of organic materials, in which single molecules are arranged in a crystal structure with long range order. Such crystals hold together by weak van-der-Waals interaction, which makes them particularly susceptible for electron-phonon coupling.

In this publication [87] we investigate the charge transport in the presence of electron-phonon coupling to high- and low-frequency modes exemplarily for a naphthalene crystal. For this a real-space formalism based on molecular orbitals is used in which low-frequency modes are described as vibrational disorder and high-frequency modes contribute through polaron renormalization. The approach explicitly considers the symmetry of electron-phonon coupling and allows to capture the dispersion relation of the coupling, which is a great improvement to previous approaches. The so obtained vibrational disorder is correlated between adjacent molecules. Taking the electronic structure into consideration, we were able to show that a symmetric coupling has a strong effect on states near the band edge, i.e., near the Fermi level, whereas anti-symmetric coupling has a strong impact for states in the middle of the band. Depending on the temperature, different states within the band contribute to transport. As a result, at low temperatures the symmetric coupling dominates whereas anti-symmetric coupling has only a small effect. This changes for larger temperatures when more states towards the middle of the band contribute to transport. This leads to typical features in the temperature dependence of the charge carrier mobility which agree with experimental observations. Furthermore, the simultaneous coupling of high and low frequency modes is investigated which leads to the surprising and counter-intuitive effect that the coupling to high-frequency modes can improve the mobility of charge carriers. The reason is found in the occupation of the band, which changes upon polaron renormalization.

For the numerical calculations we have used a real space description in terms of molecular orbitals. In such a formulation it is easy to implement disorder, which would not be straightforward in a $\boldsymbol{k}$-space description since the translational symmetry is broken. Furthermore, the Hamiltonian becomes very sparse which allows to calculate large supercells of the crystal very efficiently.

Individual contribution:

The first author (K.M.) derived and implemented the electron-phonon coupling according to the described method using a real-space tight-binding description. This contains the symmetric and anti-symmetric coupling to low-frequency modes which leads to correlated vibrational disorder and the integration of existing polaron models for high-frequency modes within the same model. For numerical calculation K.M. implemented the method in a pre-existing transport code and performed extensive tests to ensure correct results. The resulting model and implementation is the main aspect of the publication.

To illustrate the performance of the model, we have used the example of naphthalene. For this all numerical transport calculations, subsequent evaluation and post-processing of the data were performed by K.M.. This also includes the detailed evaluation of the energy dependence of symmetric and anti-symmetric coupling and the resulting consequences for low and high-temperature regimes and creation of all figures.

Structure relaxation, mode analysis and the calculation of necessary material parameters for the tight-binding system and electron-phonon couplings were calculated by other authors of the paper. F.O. supervised the project. All authors contributed to the writing of the manuscript.

Interplay of band occupation, localization, and polaron renormalization for electron transport in molecular crystals: Naphthalene as a case study

Konrad Merkel, Michel Panhans, Sebastian Hutsch, and Frank Ortmann
Department of Chemistry, Technische Universität München, 85748 Garching b. München, Germany

(Received 15 February 2022; revised 29 March 2022; accepted 29 March 2022; published 19 April 2022)

Understanding electronic properties and charge transport in organic semiconductors is important for improving organic electronic materials and devices. Here we investigate the impact of electronic band occupation, charge-carrier concentration, and symmetry of phonon modes on the electron mobility in naphthalene crystals for various temperatures. Our theoretical approach is based on the description of the electron-phonon coupling (EPC), where the coupling to low-frequency modes is treated by an effective vibrational disorder potential with local and nonlocal contributions and the coupling to high-frequency modes is included by a polaron treatment. Surprisingly, the coupling to high-frequency modes leads to an increase in the mobility in presence of the low-frequency modes, which is explained by localization and band occupation effects that further depend on the carrier density. A symmetry analysis sheds additional light on the energy dependence of the EPC, which is important to describe transport properties as a function of charge density and temperature. We also find that coupling to low-frequency phonons together with band occupation effects can lead to a vanishing slope of the mobility versus temperature that is known from experiments.

DOI: 10.1103/PhysRevB.105.165136

I. INTRODUCTION

Over the last decades, organic semiconductors have received increasing attention in fundamental and applied research. The progress in material synthesis, purification techniques and electronic optimization strategies led to a constant improvement of electronic device performance, which makes organic semiconductors very promising candidates for low-cost and easy-to-process electronic and optoelectronic applications [1,2]. This development has resulted in applications such as organic light-emitting diodes [3], organic field-effect transistors [4,5], organic solar cells [6,7], and organic sensors [8], which are now becoming commercially available. Despite the number of applications, there are still great challenges in describing the microscopic charge transport in those materials. Even in the same material such as naphthalene, electrons and holes can behave very differently [9–12] and elude a satisfactory description. While at room temperature the electron mobility along a certain direction is almost temperature-independent, the hole mobility shows a steep power-law behavior [13,14]. A deep understanding of a number of microscopic aspects is essential but has not been achieved yet.

In general, the properties of organic semiconductors depend very sensitively on intra- and intermolecular vibrations. For instance, to understand charge transport it is essential to find a suitable description of the electron-phonon coupling (EPC) that is intrinsic to all organic materials. Within the broad class of organic semiconductors, organic molecular crystals have long-range order, which reduces the complexity as compared to blends or polymers and makes them ideal model systems to study. One important milestone was the development of polaron theories [15–21] that describe the impact of EPC through the formation of a polaron, a charge carrier coherently dressed by dynamic molecular vibrations. This dressing causes a reduction of the electronic bandwidth, also known as band narrowing. This polaronic description is suitable for high-frequency vibrations but questionable for slow (low-frequency) modes [22,23], for which a quasistatic treatment generating electronic disorder was suggested to be more appropriate [22,24]. This disorder and the dynamic change of the same (also referred to as dynamic disorder) is the basis for a description of the transient localization scenario [25–27] at ultrashort time scales. Time-scale analysis become more important in recent research since the molecular vibration spectra are broad and cover two orders of magnitude in energy [28]. A single analytical limit to describe all molecular vibrations, i.e., either dynamic polaron dressing or quasistatic disorder, appears inappropriate and recent models perform a separation into multiple frequency regimes [28–30]. Additionally, numerical methods treating the full dynamics of the molecular vibrations are emerging [31,32].

In this work, we use linear response theory and a dedicated treatment of EPC for low- and high-frequency phonons that combines a vibrational-disorder approach with a polaron approach to calculate electron mobilities in naphthalene crystals. We concentrate on the coupling to only low-frequency phonon modes first and later extend our considerations to all phonon modes. We show that the simultaneous coupling to low- and high-frequency vibrations leads to an unexpected increase of mobility, which is explained in detail. We shed light on temperature dependences of the electron mobility, the role of the charge-carrier density and band-occupation effects, as well as the impact of correlated vibrational disorder across the conduction band.

II. THEORY AND METHODS

A. Holstein-Peierls Hamiltonian

The arrangement of organic molecules in a periodic crystal structure leads to an overlap of molecular orbitals, which enable charge carriers to spread across the crystal. Inter- and particularly intramolecular vibrations in the crystal change the overlap of orbitals and thus directly affect the electronic properties and charge transport, which is called EPC. We model these properties of organic crystals by utilizing the Holstein-Peierls Hamiltonian [17,19],

$$H = H_{\mathrm{el}} + H_{\mathrm{ph}} + H_{\mathrm{el-ph}}. \tag{1}$$

The electronic Hamiltonian is given by an *effective tight-binding* model, where every molecule represents a single site

$$H_{\mathrm{el}} = \sum_{ij} \epsilon_{ij}\, a_i^\dagger a_j, \tag{2}$$

$a_i^{(\dagger)}$ annihilates (creates) an electron at the lowest unoccupied molecular orbital (LUMO) of the ith molecule. Inter- and intramolecular vibrations (phonons) are described by harmonic oscillators

$$H_{\mathrm{ph}} = \sum_{\boldsymbol{Q}} \hbar\omega_{\boldsymbol{Q}} \left(b_{\boldsymbol{Q}}^\dagger b_{\boldsymbol{Q}} + \frac{1}{2} \right), \tag{3}$$

where the index $\boldsymbol{Q} \equiv (\lambda,\ \boldsymbol{q})$ is composed of λ the mode index and $\boldsymbol{q}$ the phonon momentum. The EPC Hamiltonian is given by

$$H_{\mathrm{el-ph}} = \sum_{ij} \sum_{\boldsymbol{Q}} \hbar\omega_{\boldsymbol{Q}} g_{ij}^{\boldsymbol{Q}} (b_{\boldsymbol{Q}}^\dagger + b_{-\boldsymbol{Q}}) a_i^\dagger a_j, \tag{4}$$

where the coupling constant $g_{ij}^{\boldsymbol{Q}}$ can be written as

$$g_{ij}^{\boldsymbol{Q}} = \frac{1}{\sqrt{2N_\Omega \hbar\omega_{\boldsymbol{Q}}^3}} \sum_{n\mu} \boldsymbol{e}_{n\mu}^\lambda(\boldsymbol{q}) \boldsymbol{C}_{ij}^{n\mu}, \tag{5}$$

with polarization vectors

$$\boldsymbol{e}_{n\mu}^\lambda(\boldsymbol{q}) = \boldsymbol{e}_\mu^\lambda(\boldsymbol{q}) e^{i\boldsymbol{q}\boldsymbol{R}_n^0}, \tag{6}$$

and the gradients of the transfer integrals with respect to atomic displacements

$$\boldsymbol{C}_{ij}^{n\mu} = \frac{1}{\sqrt{M_\mu}} \frac{\partial \epsilon_{ij}}{\partial \boldsymbol{R}_{n\mu}} \bigg|_{\boldsymbol{R}_{n\mu} = \boldsymbol{R}_{n\mu}^0}. \tag{7}$$

Here, the index n runs over all unit cells and μ over all atoms inside the unit cell. $\boldsymbol{R}_{n\mu}$ is the position of an atom, $\boldsymbol{R}_{n\mu}^0$ the associated equilibrium position, and M_μ its mass. The vectors $\boldsymbol{C}_{ij}^{n\mu}$ account for changes in the electronic structure due to displacements of atoms and have the full crystal symmetry. Information about phonon mode patterns are contained in the polarization vectors, which are composed of the mode patterns $\boldsymbol{e}_\mu^\lambda(\boldsymbol{q})$, which are the eigenvectors of the dynamical matrix [33], and a phase factor $e^{i\boldsymbol{q}\boldsymbol{R}_n^0}$ due to a finite wave vector $\boldsymbol{q}$.

Unfortunately, the Holstein-Peierls Hamiltonian cannot be solved analytically for large crystals with many phonon modes. Typical problems are the phonon dispersion and the large number of modes, which lead to an exponentially increasing Hilbert space with increasing system size. In the following, we discuss an analytic approach how such obstacles can be approached.

B. Phonon symmetry and phonon dispersion relation

The challenge of describing the $\boldsymbol{q}$ dependence of the EPC is often circumvented by assuming dispersionless optical phonons [34–37,12,18]. However, such a description could leave out essential physics as has been demonstrated for one-dimensional (1D) models of organic molecular crystals [38,39]. Notwithstanding, in 3D bulk crystals the influence of phonons with a nontrivial $\boldsymbol{q}$ dispersion relation is rarely explored but we believe that this would contribute to a better description of charge transport in crystalline organic semiconductors [40].

To interpolate $g_{ij}^{\boldsymbol{Q}}$ throughout the Brillouin zone (BZ), we start with Eq. (5) and restrict the sum over all unit cells n to the unit cells of the involved transfer integral, i.e., the unit cell which contains the sites $\boldsymbol{R}_i$ or $\boldsymbol{R}_j$. For organic molecular crystals, this is a good approximation because of the rapidly decaying orbital overlap, which also entails rapidly decaying couplings with orbital distance. As a result, changes in the geometry outside the involved unit cells do not affect the transfer integral. Performing this approximation allows us to continue analytically and yields

$$g_{ij}^{\boldsymbol{Q}} \approx \frac{1}{\sqrt{2N_\Omega \hbar\omega_\lambda^3}} \sum_\mu \left(\boldsymbol{e}_{n(i)\mu}^\lambda(\boldsymbol{q}) \boldsymbol{C}_{ij}^{n(i)\,\mu} + \boldsymbol{e}_{n(j)\mu}^\lambda(\boldsymbol{q}) \boldsymbol{C}_{ij}^{n(j)\,\mu} \right). \tag{8}$$

The indexes i and j run over all molecules in the crystal and can also be described by their corresponding unit cell index $n(i)$ or $n(j)$ and molecule indexes μ within their unit cell. The vectors $\boldsymbol{e}_{n(i)\mu}^\lambda$ denote the corresponding mode patterns according to unit cell $n(i)$, which is related to the mode pattern in unit cell $n(j)$ by,

$$\boldsymbol{e}_{n(j)\mu}^\lambda = \boldsymbol{e}_{n(i)\mu}^\lambda e^{i\boldsymbol{q}\left(\boldsymbol{R}_{n(j)}^0 - \boldsymbol{R}_{n(i)}^0\right)}, \tag{9}$$

where $\boldsymbol{R}_{n(i)}^0$ is the *position of the unit cell*, in which site i is located. It is not to be confused with the *position of the ith molecule* $\boldsymbol{R}_i$. As a result, the EPC constants are solely determined by the mode patterns inside the unit cell and neighboring unit cells in the crystal lattice, which corresponds to an interpolation of the $\boldsymbol{q}$ dispersion of $g_{ij}^{\boldsymbol{Q}}$ on the basis of two wave functions. A systematic improvement with more terms is straightforward but not in the scope of the present work.

We next define the symmetric (s) and antisymmetric (a) EPC parameters as

$$g_{ij}^{\mathrm{s}\,\lambda}(\boldsymbol{q}) := \frac{1}{\sqrt{2\hbar\omega_\lambda^3(\boldsymbol{q})}} \sum_\mu \boldsymbol{e}_\mu^\lambda(\boldsymbol{q}) \boldsymbol{C}_{ij}^{n_{\mathrm{s}}(i)\,\mu},$$

$$g_{ij}^{\mathrm{a}\,\lambda}(\boldsymbol{q}) := \frac{1}{\sqrt{2\hbar\omega_\lambda^3(\boldsymbol{q})}} \sum_\mu \boldsymbol{e}_\mu^\lambda(\boldsymbol{q}) \boldsymbol{C}_{ij}^{n_{\mathrm{a}}(i)\,\mu}, \tag{10}$$

with the symmetrized and antisymmetrized gradients of the transfer integrals,

$$\begin{aligned} \boldsymbol{C}_{ij}^{n_\mathrm{s}(i)\,\mu} &= \boldsymbol{C}_{ij}^{n(i)\,\mu} + \boldsymbol{C}_{ij}^{n(j)\,\mu}, \\ \boldsymbol{C}_{ij}^{n_\mathrm{a}(i)\,\mu} &= \boldsymbol{C}_{ij}^{n(i)\,\mu} - \boldsymbol{C}_{ij}^{n(j)\,\mu}, \end{aligned} \tag{11}$$

respectively, and obtain

$$\begin{aligned} g_{ij}^{\boldsymbol{Q}} = &\frac{g_{ij}^{\mathrm{s}\,\lambda}(\boldsymbol{q})}{2\sqrt{N_\Omega}}\left(e^{i\boldsymbol{q}\boldsymbol{R}_{n(i)}^0} + e^{i\boldsymbol{q}\boldsymbol{R}_{n(j)}^0}\right) \\ &+ \frac{g_{ij}^{\mathrm{a}\,\lambda}(\boldsymbol{q})}{2\sqrt{N_\Omega}}\left(e^{i\boldsymbol{q}\boldsymbol{R}_{n(i)}^0} - e^{i\boldsymbol{q}\boldsymbol{R}_{n(j)}^0}\right). \end{aligned} \tag{12}$$

The EPC is hereby (without further approximations) expressed in terms of symmetric and antisymmetric coupling constants and therefore the $\boldsymbol{q}$ dependence of the EPC constant can be split into symmetric and antisymmetric contributions, which turns out to be very useful for later analysis. The EPC constants $g_{ij}^{\mathrm{s(a)}\,\lambda}(\boldsymbol{q})$ themselves are still a function of phonon momentum. From Eq. (12), we see that the symmetric coupling has the strongest impact for $\boldsymbol{q} = 0$ and the weakest for $\boldsymbol{q}$ being at the edge of the BZ. For antisymmetric coupling the behavior is opposite [39]. The symmetric coupling constant $g_{ij}^{\mathrm{s}\,\lambda}(\boldsymbol{q})$ can be evaluated at the BZ center (Γ point) and the antisymmetric coupling constant $g_{ij}^{\mathrm{a}\,\lambda}(\boldsymbol{q})$ at the edge of the BZ. From Eqs. (10) to (12), we can immediately see that the antisymmetric coupling vanishes for $n(i) = n(j)$, i.e., when both molecular sites i and j are located in the same unit cell. That is, inside a unit cell $[n(i) = n(j)]$ the EPC constant has only symmetric contributions.

The symmetrization of the EPC is illustrated schematically in Fig. 1 for the example of two sites i and j. In this figure, the atom index μ is neglected for simplicity in the mode patterns $\boldsymbol{e}_{n(i)}^{\lambda}$ and in the gradients of the transfer integrals $\boldsymbol{C}_{ij}^{n(i)}$ and the projection $\boldsymbol{e}_{n(i)}^{\lambda}\boldsymbol{C}_{ij}^{n(i)} + \boldsymbol{e}_{n(j)}^{\lambda}\boldsymbol{C}_{ij}^{n(j)}$ is proportional to the EPC coupling constant [cf. Eq. (8)]. Figure 1(a) illustrates that the gradients (orange arrows) are in general different, i.e., $\boldsymbol{C}_{ij}^{n(i)} \neq \boldsymbol{C}_{ij}^{n(j)}$. Symmetrization leads to the symmetrized gradients $\boldsymbol{C}_{ij}^{n_\mathrm{s}(i)}$ in Fig. 1(b) and the antisymmetric gradients $\boldsymbol{C}_{ij}^{n_\mathrm{a}(i)}$ in Fig. 1(c). The sum of $\boldsymbol{C}_{ij}^{n_\mathrm{a}(i)}$ and $\boldsymbol{C}_{ij}^{n_\mathrm{s}(i)}$ gives the original gradient $\boldsymbol{C}_{ij}^{n(i)}$. Please note that the mode pattern is not symmetrized. The $\boldsymbol{q}$ dependence of the EPC constant can then be expressed in terms of the (anti)symmetric $\boldsymbol{C}_{ij}^{n_{\mathrm{s(a)}}(i)}$ gradients projected onto the mode patterns in the unit cells $n(i)$ and $n(j)$ yielding the $\boldsymbol{q}$ dispersion given in Eqs. (10) and (12).

Further extending Eqs. (8) and (12) to more neighboring unit cells is possible and would lead to additional symmetry flavors besides (anti-)symmetric EPC. However, such an systematic extension is computationally demanding [40], because it involves simulating large supercells to obtain the material parameters. It is not in the scope of the present work and we focus on symmetric and antisymmetric coupling, which is an improvement over previous publications that are exclusively based on Γ-point phonon modes.

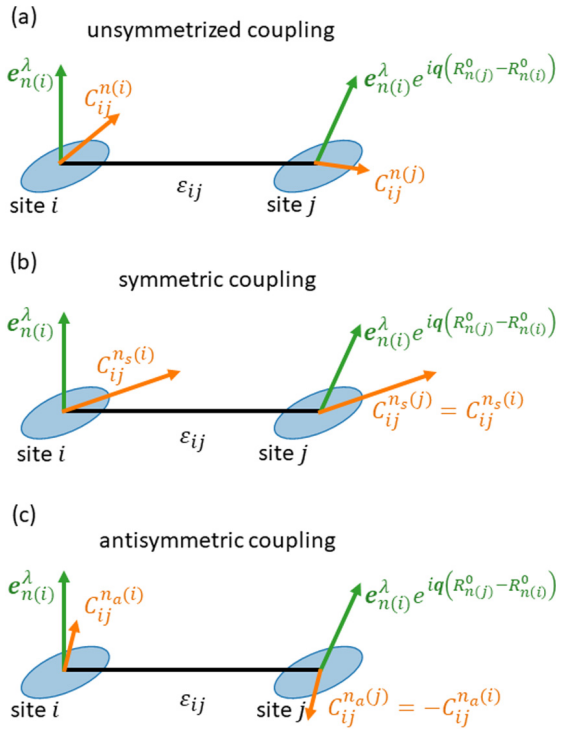

FIG. 1. Schematic view on the relevant contributions to the $\boldsymbol{q}$ dependence of the EPC constants for neighboring molecular sites i and j with transfer integral ε_{ij}. For simplicity, we have dropped the atomic index μ in the mode patterns $\boldsymbol{e}_{n(i)}^{\lambda}$ and $\boldsymbol{e}_{n(j)}^{\lambda}$ and in the gradients $\boldsymbol{C}_{ij}^{n(i)}$ and $\boldsymbol{C}_{ij}^{n(j)}$(see Eq. (7) for their definition). (a) Unsymmetrized gradients used in Eq. (8). (b) Symmetrized gradients $\boldsymbol{C}_{ij}^{n_\mathrm{s}(i)}$ as introduced in Eq. (10) to define the $\boldsymbol{q}$ dependence of the symmetric part of the EPC constant $g_{ij}^{\mathrm{s}\,\lambda}(\boldsymbol{q})$. (c) Antisymmetrized gradients $\boldsymbol{C}_{ij}^{n_a(i)}$ as introduced in Eq. (10) to define the $\boldsymbol{q}$ dependence of the antisymmetric part of the EPC constant $g_{ij}^{a\,\lambda}(\boldsymbol{q})$.

C. Effective description of electron-phonon coupling

1. EPC to low-energy phonon modes

In our study, we combine the two different theoretical concepts of (adiabatic) quasistatic disorder and polaron narrowing to cover the effect of EPC of different modes with improved accuracy. The first treats the phonon modes within the adiabatic limit of EPC, in which the vibrational mode energies are small compared to the electronic transfer integrals. This leads to an effective description of EPC in terms of dynamic or vibrational disorder for EPC to low-frequency modes. The effectiveness of vibrational disorder treatments has been shown for model systems by previous studies [38,39,41]. They show that not only the high-frequency modes but also the coupling to quasistatic modes are essential to understand the dynamics of charge carriers.

Here, we introduce a real-space formulation of the nonlocal, temperature-dependent vibrational disorder operator $V(T)$ that generalizes local vibrational disorder used previously [42,28]. More details on the derivation of vibrational disorder can be found in the Supplemental Material [43]. We account for the symmetry of the EPC in terms of symmetric and antisymmetric vibrational disorder and

obtain

$$V(T) = V^{\mathrm{s}}(T) + V^{\mathrm{a}}(T), \quad \text{with}$$
$$V^{\mathrm{s(a)}}(T) = \sum_{\lambda ij} \sigma_{ij}^{\mathrm{s(a)}\,\lambda}(T) \frac{\left(\phi_i^\lambda + (-)\phi_j^\lambda\right)}{2} a_i^\dagger a_j, \qquad (13)$$

where ϕ_i^λ are independent, normal-distributed random numbers with zero mean and variance of one. Note that this is a nonlocal disorder potential, which results from the nonlocal EPC. The disorder strengths $\sigma_{ij}^{\mathrm{s(a)}\,\lambda}(T)$ for each mode with its symmetric and antisymmetric coupling parameters are given by

$$\sigma_{ij}^{\mathrm{s(a)}\,\lambda}(T) = g_{ij}^{\mathrm{s(a)}\,\lambda} \hbar\omega_\lambda \sqrt{(1 + 2\langle n_\lambda \rangle_T)}. \qquad (14)$$

Here, $\langle n_\lambda \rangle_T$ denotes the occupation according to the Bose-Einstein distribution function for phonon mode λ at the absolute temperature T. The absolute values of $\sigma_{ij}^{\mathrm{s(a)}\,\lambda}$ denote the standard deviation of the random disorder. According to Eq. (14), $\sigma_{ij}^{\mathrm{s(a)}}$ consists of a temperature-independent and a temperature-dependent contribution. The temperature-independent part originates from quantum mechanical zero-point vibrations of the phonon modes and is the main difference to a classical description [37]. Please note that the random numbers ϕ_i^λ in Eq. (13) only depend on the site index i and mode λ. Consequently, two transfer integrals t_{ij} and t_{ik}, which share the same site, share the same ϕ_i^λ but may differ in the second random number ϕ_j^λ and ϕ_k^λ if $j \neq k$. The partly randomized transfer integrals are therefore not independent but correlated with an autocorrelation A, whereas on-site energies are not correlated. This corresponds to the physical picture, where, e.g., a molecular vibration would lead to a decrease in distance to a neighboring site and therefore increase the distance to another neighbor in opposite direction. The transfer integrals at one site would increase due to a stronger overlap of molecular orbitals and decrease by the same amount in opposite direction. Thus, the vibrational disorder is correlated.

The sign of $\sigma_{ij}^{\mathrm{s(a)}\,\lambda}$ is related to the autocorrelation between neighboring sites. From the hermiticity of the Hamiltonian, it follows directly that $\sigma_{ij}^{\mathrm{s}} = \sigma_{ji}^{\mathrm{s}}$ and $\sigma_{ij}^{\mathrm{a}} = -\sigma_{ji}^{\mathrm{a}}$. The symmetry of a phonon mode manifests with different correlations of neighboring transfer integrals. Total (anti)symmetric modes generate an autocorrelation of $A = +(-)0.5$ for adjacent transfer integrals along a certain crystal-direction. The mixture of symmetric and antisymmetric modes in a real system would lead to smaller values, i.e., between -0.5 and $+0.5$.

2. EPC to high-frequency phonon modes

The appropriate concept to treat phonon modes which vibrate significantly faster than a typical charge-transfer time can be described suitably by using polaron theories [17–21,5]. It is assumed that the polaron is instantaneously formed after the excess electron (or hole) has been created. In other words, the time scales entail a relaxation of the geometry upon charging that is faster than the charge transfer. The polaron description here is based on the Lang-Firsov (LF) transformation [44], which is a unitary transformation of both electron and phonon operators given by the operator

$$S = \sum_{i\boldsymbol{Q}} g_{ii}^{\boldsymbol{Q}} (b_{\boldsymbol{Q}}^\dagger - b_{-\boldsymbol{Q}}) a_i^\dagger a_i. \qquad (15)$$

This transformation is performed for vibration modes with intramolecular EPC only, whereas the modes with finite intermolecular EPC are effectively described using the vibrational disorder potential. This assumption is always justified when the EPC to typical high-energy phonon modes is dominated by the intramolecular coupling constants $g_{ii}^{\boldsymbol{Q}}$. If we use the proposed model for the $\boldsymbol{Q}$ dependence of the EPC constants we find the real-space representation of the operator S,

$$S = \sum_{i\lambda} g_{ii}^{\mathrm{s}\,\lambda} (b_{i,\lambda}^\dagger - b_{i,\lambda}) a_i^\dagger a_i, \qquad (16)$$

which indicates that only the intramolecular couplings at the Γ point contribute. This is reasonable since prototypical high-energy phonon modes only possess an intramolecular EPC constant. The transformed Hamiltonian is then treated by a mean-field approach that substitutes the transformed electronic part by the phonon average [45,20],

$$\tilde{H}_{\mathrm{el}} \to \langle \tilde{H}_{\mathrm{el}} \rangle_{\mathrm{ph}} = \sum_{ij} (\delta_{ij}(\epsilon_{ii} + V_{ii}(T) - \Delta) + (1 - \delta_{ij})\tilde{P}(\epsilon_{ij} + V_{ij}(T))) \, a_i^\dagger a_j, \qquad (17)$$

where Δ is the polaron shift $\Delta = \sum_\lambda \hbar\omega_\lambda (g_{ii}^{\mathrm{s}\,\lambda})^2$ and $\tilde{P}$ is the polaron renormalization factor

$$\tilde{P} = \exp\left(- \sum_\lambda \left(g_{ii}^{\mathrm{s}\,\lambda}\right)^2 (1 + 2\langle n_\lambda \rangle_T) \right). \qquad (18)$$

Equation (17) therefore considers both the EPC to the low-energy modes by using the vibrational disorder potential $V(T)$ and the EPC to high-energy modes yielding the polaron renormalization factor $\tilde{P}$ for the electronic transfer integrals as well as the polaron shift Δ of the on-site energies. Details on the chosen mode energy which separates the modes according to the two treatments of the EPC are discussed below.

At this point, we note that, for consistency, the LF transformation also transforms the intermolecular part of the EPC and leads to a renormalization of the vibrational disorder that is caused by intermolecular EPC in the same way as for the electronic transfer integrals [cf. second term on the rhs of Eq. (17)]. This is because only electronic operators in the intermolecular EPC are affected by the LF transformation since phonon operators of different vibrational modes commute with each other.

The effective mean-field Hamiltonian in Eq. (17) is used below to evaluate the current-current correlation function for the coherent contributions to charge transport (cf. [45]) with an *ab initio* description of the Hamiltonian parameters. We note that the high-frequency modes do not lead to incoherent transport contributions because they are not thermally activated.

D. Charge transport simulations

We use the framework of linear-response theory by applying the Kubo formula [46–48] for the longitudinal electrical

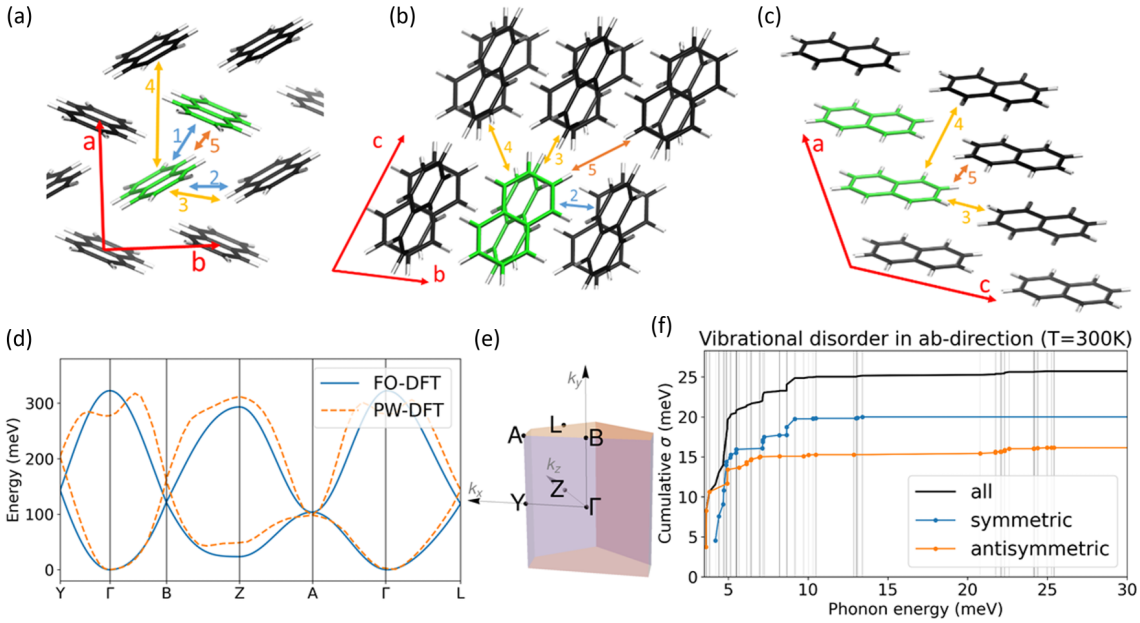

FIG. 2. (a)–(c) Naphthalene crystal and definition of transfer integrals with their ordering number (see Table I). Molecules of a single, primitive unit cell are shown in green. (d) Band structure from fragment-orbital (FO) and plane-wave (PW) DFT simulations. The energy zero is set to the valence band minimum. (e) Half of the Brillouin zone and definition of k points. The used k points in the plot include: Y = (0.5, 0.0, 0.0), Γ = (0.0, 0.0, 0.0), B = (0.0, 0.5, 0.0), Z = (0.0, 0.0, 0.5), A = (0.5, 0.5, 0.0), L = (0.0, 0.5, 0.5). (f) Cumulative variance of the vibrational disorder in the *ab* direction for symmetric (blue) and antisymmetric (orange) EPCs as well as combined σ (black line) plotted against the energy cutoff for quasistatic phonons. Vertical gray lines indicate phonon modes. Every phonon mode is either symmetric or antisymmetric. To show if a phonon mode couples (anti-)symmetrically small blue (orange) dots are used.

conductivity $\sigma_{\alpha\alpha}$ in the form

$$\sigma^{\mathrm{dc}}_{\alpha\alpha} = \frac{1}{\Omega}\int_0^\beta d\lambda \int_0^\infty dt \mathrm{Tr}[\rho\ j_\alpha(t + i\hbar\lambda)\ j_\alpha(0)], \qquad (19)$$

where $\rho = e^{-\beta(H-\zeta N)}/Z_{\mathrm{gc}}$ denotes the grand-canonical density operator of the unperturbed system with Hamiltonian H, chemical potential ζ, partition function Z_{gc}, and inverse temperature $\beta = 1/k_B T$. Ω denotes the volume of the crystal and $j_\alpha(t) = e_0 v_\alpha(t)$ is the current operator for the charge carriers, where α is the cartesian component and e_0 the elementary charge.

We evaluate Eq. (19) based on an *ab initio* description of the electronic structure using density-functional theory (DFT) whose details are given further below. Through this connection to DFT, one can treat electron-electron interaction in mean field and continue with effectively noninteracting Kohn-Sham particles for the calculation of the density of states $D(E) = \frac{1}{\Omega}\mathrm{Tr}\{\delta(E-H)\}$ and the energy-resolved mean square displacement

$$\Delta X^2(E,t) = \langle (x(0) - x(t))^2 \rangle_E, \qquad (20)$$

with effective single-quasiparticle wave packets [49]. The notation $\langle O\rangle_E := \frac{\mathrm{Tr}\{\delta(E-H)\ O\}}{\mathrm{Tr}\{\delta(E-H)\}}$ for an operator O denotes the corresponding energy-projected averages.

We employ the efficient Lanczos recursion and continued fraction methods [49–51] to tridiagonalize the Hamiltonian. The time evolution of the system is performed by a Chebyshev polynomial expansion of the time evaluation operator [52]. Furthermore, we apply periodic boundary conditions. The initial state is a random phase state, which allows us to calculate traces as expectation values over the random phase state if the sample is large enough [53]. For our study on naphthalene, we find that a supercell consisting of 325 × 416 × 180 primitive unit cells is sufficiently large to calculate numerically converged results.

Finally, the longitudinal mobility is obtained as [49]

$$\mu_{\alpha\alpha}(t) = \frac{\beta e_0}{2n}\frac{d}{dt}\int_{-\infty}^{\infty} dE\ f(E)[1-f(E)]D(E)\Delta X^2(E,t), \qquad (21)$$

where n denotes the charge-carrier density and we have used $\frac{\partial f(E)}{\partial E} = -\beta\ f(E)[1-f(E)]$ with the Fermi function $f(E) = 1/(e^{\beta(E-\zeta)}+1)$. Equation (21) is used to calculate the time-dependent mobility for a single wave packet propagating coherently in time and space. In a measurement setup, such wave packets could in principle decohere, which we do not model explicitly. The influence of such stochastic decoherence can be captured by introducing an empirical coherence time τ_c, which leads to an exponential decay over time [54],

$$\mu^{\mathrm{dc}}_\alpha = \frac{1}{N}\int_0^{t_{\max}} dt\ e^{-\frac{t}{\tau_c}}\ \mu_\alpha(t), \qquad (22)$$

where $N = \int_0^{t_{\max}} dt\ e^{-\frac{t}{\tau_c}}$ is needed for normalization and $t_{\max}$ is the maximum time of our simulation. The coherence time is usually unknown for real systems. However, it needs to be chosen consistently with the energy cutoff for quasistatic modes. A meaningful choice would be $\tau_c = \frac{\hbar}{E_{\mathrm{cut}}}$, where E_{cut} is the energy cutoff for quasistatic phonons.

TABLE I. Transfer integrals for electrons in a naphthalene crystal.

Number	Direction	Symbol	Value [meV]
1	$\pm(\boldsymbol{a}/2 \pm \boldsymbol{b}/2)$	ϵ_{ab}	−37.0
2	$\pm\boldsymbol{b}$	ϵ_{b}	9.9
3	$\pm\boldsymbol{c}$	ϵ_{c}	−3.8
4	$\pm(\boldsymbol{a}+\boldsymbol{c})$	ϵ_{ac}	4.5
5	$\pm(\boldsymbol{a}/2 \pm \boldsymbol{b}/2+\boldsymbol{c})$	ϵ_{abc}	−3.3

III. RESULTS

A. Material parameters for naphthalene

We apply the above theoretical framework to naphthalene as a concrete example. Naphthalene is an organic molecular crystal with two molecules per unit cell arranged in a herringbone-stacking fashion [Figs. 2(a)–2(c)]. We determine all Hamiltonian parameters based on the experimental crystal structure [55,56].

1. Electronic structure

We perform the DFT parametrization of the Hamiltonian for the two lowest conduction bands that are derived from the molecular LUMO states of naphthalene and map them, by representing every LUMO in the crystal by a single site, on an effective tight-binding model, Eq. (2). The transfer integrals between the sites are calculated with the fragment-orbital approach [57–59] using DFT (FO-DFT) and the Gaussian16 code [60] with the basis set 6–311G** [61] and the exchange-correlation-functional B3LYP [62,63]. The obtained transfer integrals are shown in Figs. 2(a)–2(c) with their ordering number used here. The values for all finite transfer integrals are listed in Table I. Only a small number of neighbors have a significant contribution and long-range transfer integrals are exponentially suppressed. The on-site energies ϵ_{ii} can be set to zero.

A straightforward calculation of the band structure from the electronic Hamiltonian Eq. (2) and the transfer integrals in Table I leads to the band energies

$$\begin{aligned}\epsilon(\mathbf{k}) = \epsilon_0 + \sum_{i\in\{b,c\}} 2\epsilon_i \cos\mathbf{k}\mathbf{R}_i + 2\epsilon_{ac}\cos\mathbf{k}(\mathbf{a}+\mathbf{c}) \\ \pm 2\epsilon_{ab}\left(\cos\mathbf{k}\frac{\mathbf{a}+\mathbf{b}}{2} + \cos\mathbf{k}\frac{\mathbf{a}-\mathbf{b}}{2}\right) \pm 2\epsilon_{abc} \\ \times\left(\cos\mathbf{k}\frac{\mathbf{a}+\mathbf{b}+2\mathbf{c}}{2} + \cos\mathbf{k}\frac{\mathbf{a}-\mathbf{b}+2\mathbf{c}}{2}\right). \quad (23)\end{aligned}$$

Figure 2(d) shows the resulting FO-DFT band structure in blue. As a reference, we have also calculated the band structure with plane-wave DFT (PW-DFT) and B3LYP hybrid functional using the projector augmented-wave method [64,65] of the VASP program package [66,67]. The reference PW-DFT band structure is shown as dashed orange line in Fig. 2(d). The PW-DFT and FO-DFT model agree very well at the bottom of the conduction band, where electron transport takes place. However, differences emerge at higher energies and in the $\boldsymbol{c}$ direction, where distances between molecules are largest. The model is in agreement with previous calculations [68] and for transport properties up to room temperature, such differences should be negligible.

2. Phononic properties and EPC

In the present approach we distinguish between local EPC to the onsite energies of a molecule and the nonlocal EPC to the transfer integrals between two different molecules. In the case of naphthalene, the former predominantly contribute to the polaron renormalization, while local and nonlocal contributions together generate the disorder potential. The local EPC is calculated for an isolated gas-phase molecule using a frozen phonon approach [69] with vibrational patterns and mode frequencies obtained with DFT using Gaussian 16 [60], the basis set 6–311G** [61], and the exchange-correlation-functional B3LYP [62,63].

The nonlocal EPC is calculated with phonon mode patterns and vibration frequencies obtained with the density functional based tight-binding method (DFTB) [70,71]. It has been shown that DFTB yields appropriate estimations of vibrational properties in a computationally efficient way although being less accurate than DFT [72]. We used the DFTB+ program [73] with the 3ob-3-1 parameter set [74,75] for third-order density functional tight binding [76] and included Grimme's dispersion correction [77]. We apply a frozen phonon approach [69], where the atoms in a supercell are displaced according to the phonon mode patterns and changes in ϵ_{ij} (calculated with DFT as explained above) are tracked to obtain $g_{ij}^{\boldsymbol{Q}}$. To sample both the Γ point and BZ edge of the crystal vibrations we have used a supercell with $2\times2\times1$ primitive unit cells (8 molecules).

Antisymmetric modes are located at the BZ edge of the *primitive* unit cell (see the Methods section) and are folded into the BZ center of the *supercell*. Because of the chosen size of the supercell only symmetric and antisymmetric $g_{ij}^{n_{\mathrm{s(a)}}\,\lambda}$ are located at the Γ point of the *supercell's* BZ. The distinction between symmetric and antisymmetric modes can be achieved afterwards by checking if $g_{ij}^{\lambda\,\boldsymbol{q}=0}$ is periodic with respect to the *primitive* unit cell (symmetric) or only with respect to the *supercell* (antisymmetric). Finally, we calculate the (anti)symmetric coupling constants $g_{ij}^{\mathrm{s(a)}\,\lambda}$ according to Eq. (10) for every phonon mode and the overall vibrational disorder strength $\sigma_{ij}^{\mathrm{s(a)}}(T)$ using Eq. (14).

The method of vibrational disorder is strictly valid only if the phonons are static with respect to the electrons dynamics. Therefore only the lowest-energy modes can be treated quasistatically and we need to find a cutoff energy to separate high- and low-frequency modes. Figure 2(f) shows the cumulative vibrational disorder $\sigma_{ij}^{\mathrm{s(a)}}(T)$ over different cutoff energies along the largest transfer integral ϵ_{ab} at $T = 300$ K. Vertical lines represent phonon energies. The overall vibrational disorder changes very much for small energy cutoffs and barely changes for higher energies, where more phonon modes are involved.

We performed test simulations for several cutoff energies and compared the electrons dynamics in terms of displacement and localization with the oscillation period of the highest frequency phonon that is treated quasistatically. We found that treating the eight lowest-frequency nonlocal phonon modes with a maximum energy of 4.9 meV as

quasistatic modes yields consistent results, i.e., where the phonon oscillations are quasistatic compared to the electrons dynamics. Similar cutoff energies of 5 meV have been chosen previously for similar organic molecular crystals [41]. In our case the standard deviation $|\sigma_{ij}^{s(a)}|$ of nonlocal vibrational disorder at 300 K is highly anisotropic and reaches from 1.7 meV (38% of ϵ_{ac}) in the ac direction to 23.9 meV (241% of ϵ_b) in the b direction. The vibrational disorder from local modes is an order of magnitude smaller with a maximum standard deviation of only 0.45 meV.

B. Phonon-mode symmetries and correlation of transfer integrals for quasistatic modes

An important precursor for transport properties is the density of states (DOS). We therefore investigate the influence of the quasistatic phonons and their associated vibrational disorder on the states in the conduction band. Figure 3(a) shows a broadening of the DOS with increasing temperature (increasing vibrational disorder). Higher temperatures lead to an activation of more phonon modes and hence a stronger vibrational disorder. Consequently, the DOS broadens with increasing temperature. Despite the temperature dependence, our data shows that the part of the vibrational disorder [cf. Eq. (14)], which originates from quantum mechanical zero-point vibrations, is significant at all considered temperatures including room temperature. We note that a classical description of EPC, e.g., in the form of a molecular dynamics simulation, would therefore not be able to capture such contributions.

EPC does not homogeneously broaden the DOS but can have a different impact at different energies within the band. To analyze the energy-dependent influence of the EPC on the DOS, we now introduce the energy-resolved absolute coupling constant $G_\lambda^{s(a)}(E)$ of (anti)symmetric modes to establish a measure of the EPC strength projected onto the crystal band energy [38,39] based on the band structure $\epsilon(\boldsymbol{q})$ [cf. Eq. (23)],

$$G_\lambda^{s(a)}(E) = \frac{1}{N_\Omega} \int_{BZ} d^3\boldsymbol{q}\, G_\lambda^{s(a)}(\boldsymbol{q}) \delta(E - \varepsilon(\boldsymbol{q})), \tag{24}$$

with

$$G_\lambda^{s(a)}(\boldsymbol{q}) = \sum_{\langle i,j \rangle} \left| g_{ij}^{s(a)}\, \boldsymbol{Q} \right|^2. \tag{25}$$

The sum includes couplings over all the nearest neighbors that are also connected via a transfer integral.

Figures 3(b) and 3(c) show the impact of the EPC for symmetric and antisymmetric contributions across the band for three different crystal directions (three transfer integrals). In these figures, $G_\lambda^{s(a)}(E)$ is divided by the DOS for better comparison of the couplings. The purely electronic DOS without EPC (gray lines) indicates the energetic position of the electronic band. It is clearly visible that the symmetric coupling is strongest at the band edges, whereas the antisymmetric coupling is dominant in the middle of the band. From Eq. (12) it gets clear that modes with $\boldsymbol{q} = 0$ only couple symmetrically, whereas for $\boldsymbol{q}$ at the edge of the BZ, the antisymmetric coupling is stronger. From the band structure [see Fig. 2(d)] it can be seen that points near the Γ point are related to energies at the band edge and points near the BZ edges are related to energies at the band center. Thus, the symmetry of the coupling (and therefore the autocorrelation of disorder) has a very distinct impact on different energy regions in the band. We note that similar effects were observed in theoretical studies of nonlocal, (anti)symmetric EPC in 1D pentacene chains [39].

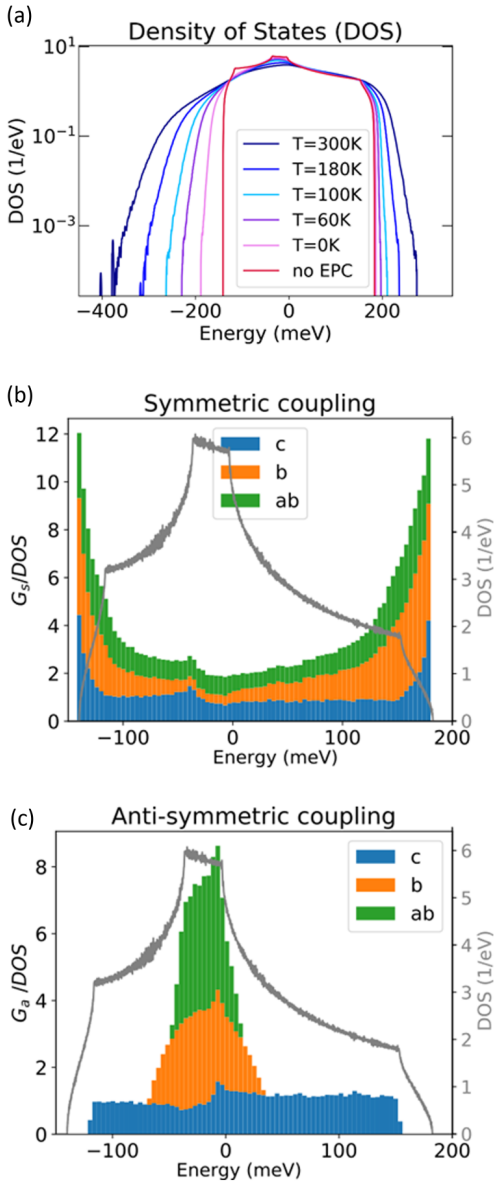

FIG. 3. (a) Temperature dependence of the DOS. Vibrational disorder broadens the DOS even at zero temperatures due to temperature-independent zero-point fluctuations in Eq. (14). For comparison the DOS without any vibrational disorder is shown in red (no EPC). (b), (c) Energy-resolved coupling strength (see Eq. (24) for definition) of purely symmetric EPC (b) and purely antisymmetric EPC (c) for three different directions. DOS without EPC is indicated in gray for clarity.

This observation can be further related to the influence of the couplings at different temperatures and carrier densities. For small temperatures and small charge densities, electrons only populate states near the band edge and therefore symmetric modes dominate EPC. On the other hand, antisymmetric

coupling is more important at higher temperatures and larger charge-carrier densities, because states in the middle of the band become occupied. A detailed analysis of the band occupation is given in the next section.

We next analyze the autocorrelation of the vibrational disorder. The combined vibrational disorder from all phonon modes is correlated with an autocorrelation between the neighboring transfer integrals along a given direction that ranges from $A = 0.1$ (b direction) up to $A = 0.3$ (abc direction). This indicates that both symmetric and antisymmetric modes contribute substantially but symmetric modes are more dominant for every transfer integral. Previous studies of pentacene crystals also have shown a dominance of symmetric coupling with an autocorrelation of 0.25 [22], which agrees with our results on naphthalene.

C. Influence of quasistatic phonon modes on 3D electronic transport in naphthalene crystals

Before we address the influence of EPC on charge transport in all its complexity, we want to investigate the influence of band occupation on transport first. We focus on the case of quasistatic modes only and generalize our findings later systematically to the whole phonon spectrum. We start with the observation that in our model we identify two underlying temperature dependences. One is related to the ensemble of phonons and affects vibrational disorder (see previous section) while the other is bound to the ensemble of electrons, which determines the band occupation and transport energies.

1. Transport level and band occupation

According to the Kubo-Formula in Eq. (21), the mobility depends on the density of transport states defined by $f(E)[1-f(E)]D(E)$, which is to be distinguished from the occupied density of states $f(E)D(E)$. Figure 4 shows the energetic distribution of transport states (colored bold lines) for two temperatures and different charge-carrier densities. Colored areas show the occupation of the band, which differs from the distribution of transport states especially at the band edge. The distribution gets very narrow for low temperatures [Fig. 4(a)] as its full-width-at-half-maximum is proportional to $4k_BT$. For high temperatures [Fig. 4(b)] the distribution gets broader and energy regions close to the band center contribute more to the overall mobility. In general, those states in the middle of the band are more delocalized and a broader distribution would therefore increase the overall mobility if the DOS would remain unchanged.

It becomes clear that the underlying temperature dependences for phonons and electrons have opposite effects on the charge transport. How these temperature dependences influence the mobility will be the subject of discussions in the next sections. We start with the time-dependent mobility of a single electronic wave packet, which than leads to the dc mobility $\mu_\alpha^{\mathrm{dc}}(T)$ in Sec. III C 3.

2. Time-dependent mobility

To calculate transport properties, we use the approach described above (Sec. II D), the calculated DOS, and $\Delta X^2(E,t)$ according to Eq. (20).

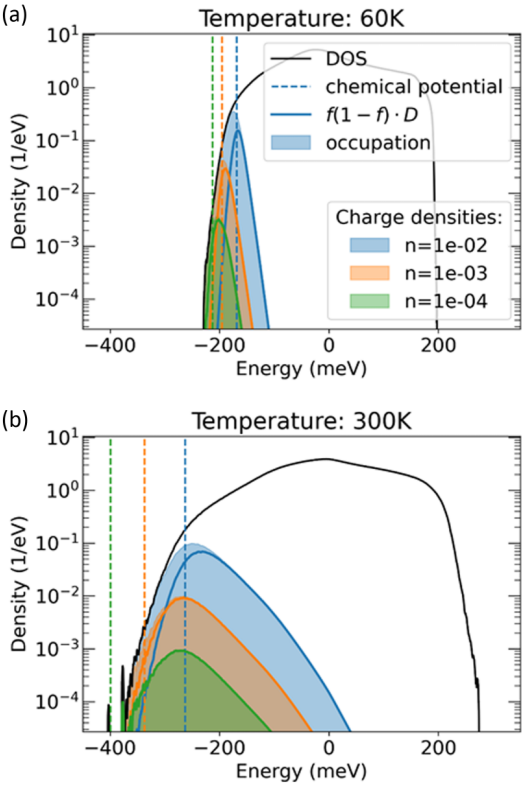

FIG. 4. Occupied density of states (colored areas) and associated density of transport states $\propto f(E)[1-f(E)]D(E)$ (solid lines) for three different charge densities at 60 K (a) and 300 K (b). (a) and (b) use the same legend.

Figure 5 shows the mobility over time in the b direction for three different charge-carrier densities. The vibrational disorder and therefore DOS and $\Delta X^2(E,t)$ are independent of the density. All figures show a typical time dependence. At the shortest times, electrons start spreading across the crystal ballistically (linear increase of mobility up to ∼10 fs, see insets) and eventually get scattered by local and nonlocal vibrational disorder, which leads to destructive interference. Consequently, the mobility decreases and transport becomes diffusive. We find that for a 3D naphthalene crystal vibrational disorder does not lead to a complete localization of electrons.

In Fig. 5(a) we observe that small charge-carrier densities show a sharper and more pronounced initial mobility peak compared to larger densities [cf. Fig. 5(c)]. Small carrier densities lead to transport levels near the band edge. With increasing carrier densities, we observe in Fig. 4 that the density of transport states does not increase as strongly as the density n itself that appears in the $1/n$ prefactor. This leads to a reduced mobility-peak height for larger density, i.e., a lower mobility at short times. For longer times, localization effects set in and lead to a mobility decay. The stronger these effects the sharper is the mobility peak. Consequently, the mobility has a more pronounced peak for small charge densities. A small temperature amplifies this effect, because a smaller energy range is thermally active and higher energy states do not contribute.

At the initial peak, $\mu(t)$ is larger for small temperatures than for larger temperatures. However, for longer times the

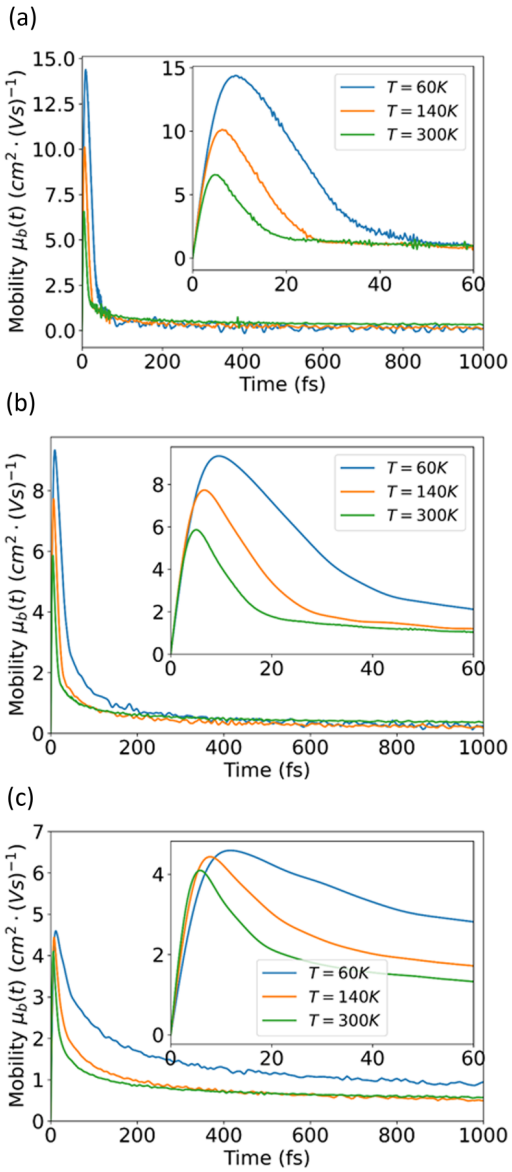

FIG. 5. Time dependent mobility in b-direction for three different charge-carrier densities and temperatures. Charge-carrier density is set to (a) 10^{-4}, (b) 10^{-3} and (c) 10^{-2}. Insets show behaviors at ultrashort times.

order is reversed and the mobility at 300 K becomes larger than in the case of 60 or 140 K. This is related to the stronger delocalization of states in the middle of the band, which eventually dominate over the more localized states at the band edge. As discussed in Sec. III B, symmetric coupling has the strongest impact at the band edge while antisymmetric coupling dominates the band center. From this we can conclude that symmetric modes influence the ballistic regime and the initial mobility peak stronger than antisymmetric modes do.

It becomes clear that at different times different energy regions in the conduction band dominate transport. Therefore it depends on the coherence time τ_c how much weight the initial mobility peak gets and how strong the influence of the long-time behavior is. The energy regions of transport are thus influenced by τ_c.

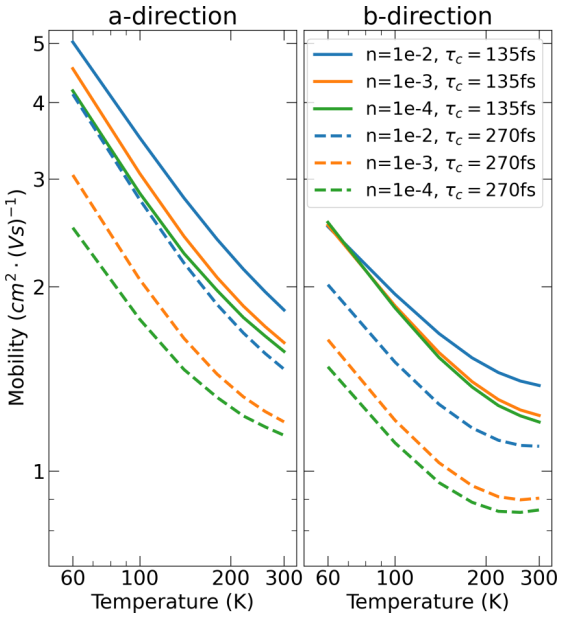

FIG. 6. Temperature-dependent dc mobility for two directions in the herringbone plane. Vibrational disorder stems from the eight lowest quasistatic phonon modes (see main text). Solid lines show the dc mobility for a coherence time of 135 fs, which is consistent with the phonon cutoff energy. Dashed lines indicate a higher coherence time of 270 fs. Colors indicate different charge-carrier densities. The legend applies to both panels.

3. Coherence time and dc mobility

Figure 6 shows the dc mobility $\mu_\alpha^{\mathrm{dc}}(T)$ in the herringbone plane according to Eq. (22) for $\tau_c = 135$ fs that is chosen in consistency with the energy cutoff for vibrational disorder and for $\tau_c = 270$ fs which, for comparison, allows for a possibly larger coherence time. Regardless of this choice, the mobility decreases with temperature and shows power law behavior below 150 K. We further analyze the phononic and electronic contributions to the temperature dependency, which affect the mobility additional to the $\beta \propto \frac{1}{T}$ prefactor in Eq. (21). At low T the broadening of the DOS due to EPC and the broader density of transport states are significant and therefore phononic and electronic temperature dependences both codetermine the slope of the power law in Fig. 6. We find that the peak of $\mu_\alpha(t)$ (see Fig. 5) dominates the dc mobility. Therefore the stronger initial mobility peak at lower T leads also to higher mobilities at low T in Fig. 6 and the mobility decreases with increasing temperatures up to 150 K.

At high temperatures, the behavior of μ_α^{dc} in Fig. 6 changes and the slope of the mobility flattens and even suggests the emergence of a high-temperature plateau in the b direction above 200 K. The phonon-induced changes in the DOS are much less pronounced at higher temperatures for the relevant energies around the chemical potential. This is in contrast to low temperatures where the shape of the DOS changes significantly, especially near the chemical potential. However, the broadening of the density of transport states still increases significantly leading to an increased contribution of delocalized states. Thus, the main temperature dependence originates from the thermal occupation of electronic states and not from the temperature-dependent broadening due to vibrational dis-

order. The high-temperature change in the mobility slope (i.e., $\frac{d\mu_\alpha^{\mathrm{dc}}(T)}{dT}$) in Fig. 6 is therefore identified as an effect of band occupation (at constant carrier density).

Figure 6 additionally shows μ_α^{dc} for a larger coherence time. Larger coherence times represent a case in which a charge carrier has more time to localize (see Fig. 5) and the differences between localized and delocalized states appear more strongly. The localization leads to a lower overall mobility and the relevance of the small amount of delocalized states for the mobility increases slightly. Figure 6 shows an emphasized high-T plateau behavior for larger coherence time ($\tau_c = 270$ fs). This indicates that the high-T plateau is mainly driven by the influence of delocalized states in the diffusive transport regime, which, in the middle of the conduction band, are increasingly accessible upon thermal occupation. Additionally, the high-T plateau is more pronounced at higher charge densities. Both observations support the reasoning that the high-temperature plateau is an effect of band occupation.

We want to note that decoherence is a complex phenomenon, where all kinds of external and internal processes, which are not part of the model, can contribute. Any assumed value for the coherence time can therefore only be understood as a simplification, where the whole complexity is reduced to a single parameter. For this reason, we have considered a possible variation of such a number. In general, the coherence time could also be temperature-dependent and would probably decrease with temperature. However, such models are beyond the scope of the present work.

Experimental data on naphthalene electron transport [14,78] show also a power-law behavior for small temperatures and high-temperature plateaus in the b and c directions. In the herringbone-plane (a and b direction) our results coincide qualitatively. However, the simulations cannot describe the out-of-plane direction c. One reason might be that the c direction shows the smallest transfer integrals and therefore possibly has the largest numerical error. More likely, however, we believe the reason lies in the fact that our approach does not contain any inelastic phonon creation or annihilation processes, which might be necessary and have been conjectured in literature [20].

D. Simultaneous modeling of EPC to high-frequency and quasistatic phonon modes

So far, we have discussed EPC due to low-frequency phonon modes only. Now, we want to include the high-frequency modes in a combined model. Below, we discuss the phonon mode spectrum and the associated polaron renormalization, which is used in Sec. III D 2 to calculate the mobility in the presence of low- and high-frequency phonons.

1. Polaron-renormalization and coupling to high-frequency phonon modes

From the EPC parameters $g_{ij}^{\mathrm{s(a)}\,\lambda}$, we obtain the polaron renormalization for high-frequency local phonon modes by applying Eq. (18). We consider all phonons as high-frequency modes whose phonon energy is above a certain threshold. Figure 7 shows the cumulative polaron renormalization of the transfer integrals for different threshold energies over the whole spectrum and for two temperatures. High threshold energies mean only a few modes are considered, whereas low thresholds correspond to situations, where almost all phonons are treated as high-frequency modes. Figure 7 shows that for threshold energies above 70 meV no significant temperature dependence exists, because those modes are not thermally active for either temperatures and only contribute via their quantum mechanical zero-point fluctuations. For threshold energies below 70 meV the occupation of phonon modes (thermal activation) becomes significant and a difference between high and low temperatures is clearly visible.

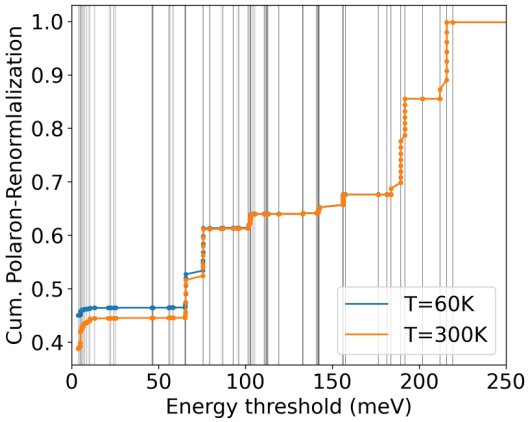

FIG. 7. Polaron renormalization of transfer integrals due to local phonon modes that are above an energy cutoff (abscissa). The cumulated plot indicates no renormalization on the right and increasingly stronger renormalization from right to left due to an increased number of involved modes. Vertical gray lines indicate phonon energies.

In the subsequent transport calculation we treat all quasistatic modes below 4.9 meV with the method of vibrational disorder as before. Higher-frequency modes are treated by polaron renormalization. For this cutoff energy, the polaron renormalization becomes temperature dependent. The corresponding renormalization factor varies from $P = 0.453$ at 60 K to $P = 0.399$ at 300 K.

2. Transport properties

Figure 8 shows the temperature-dependent mobility in the herringbone plane for coupling to high- and low-frequency modes (solid lines), which are compared to simulations with only low-frequency modes from above (dashed lines). We can see that the coupling to high-frequency modes counteracts the formation of the high-temperature plateau at elevated temperatures, but does not add new characteristic features. Surprisingly, polaron renormalization causes an increase of the mobility for all temperatures. Usually, one would expect the opposite since polaron renormalization reduces the transfer integrals, which is expected to impede transport.

A detailed analysis of the DOS in the presence of phononic renormalization shows a narrowing of the band according to Eq. (18) in Fig. 9. The narrowing of the band counteracts the band broadening from vibrational disorder. We can see that the energy rescales but the Fermi-Dirac distribution, which determines the band occupation and density of transport states, remains broad. Only the chemical potential changes to ensure the same charge-carrier density for every simulation. This

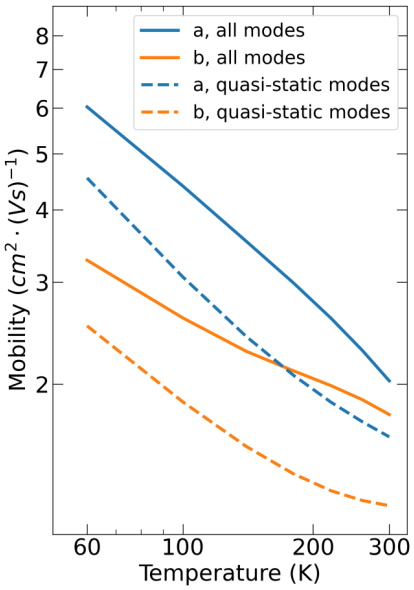

FIG. 8. Combined effects of vibrational disorder and polaron renormalization on electron mobility (solid lines) compared to the case of absence of renormalization (dashed lines). Phonon modes with energies below $E_{\text{cut}} = 4.9$ meV are treated as vibrational disorder. Coherence time is consistent with energy cutoff for quasistatic modes at 135 fs. Charge density is constant at 10^{-3}.

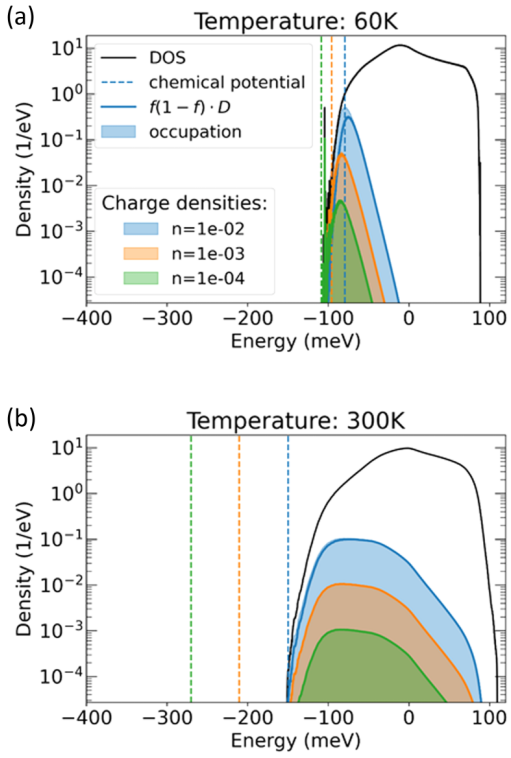

FIG. 9. Occupation of density of states (colored areas) and associated density of transport states $\propto f(E)[1-f(E)]D(E)$ (solid lines) for three different charge densities at 60 K (a) and 300 K (b). (a) and (b) use the same legend. Polaron renormalization leads to band narrowing, which enables the occupation of delocalized states in the middle of the band.

leads to an occupation of states in the middle of the band, which did not contribute before. States in the middle of the band are more delocalized and by occupying those states the effect of the renormalization of the transfer integrals can be overcompensated, which leads to higher mobilities. We want to emphasize that this is a feature of the band structure of naphthalene. Whether polaron renormalization has generally a positive or negative impact on the overall mobility depends on the relative increase of delocalization towards the middle of the band. Microscopic investigations by Vukmirović *et al.* [23] suggest that polaron-renormalization has only a small influence on transport, while we find a factor below two for the present case that is not negligible.

Finally we note that the high-temperature plateau seen in the experiment and our simulations, cannot be associated to polaron renormalization because we observe a stronger decrease of mobility at high temperatures, which counteracts the plateau formation. In any event, our results stress again the importance of EPC to low-frequency modes and the role of band occupation.

IV. CONCLUSIONS

In this paper, we have presented an efficient way to calculate transport properties of a 3D organic molecular crystal in the presence of EPC based on a tight-binding-like representation of the DFT electronic structure and a thoughtful evaluation of the Kubo formula for the electrical conductivity. By splitting the phonon spectrum into quasistatic and dynamical modes, we were able to find effective descriptions in terms of vibrational disorder for low-frequency modes and polaron-renormalization for high-frequency modes. We have shown that not only the variance of vibrational disorder is important, but also the symmetries of the phonon modes. Depending on the symmetry, different regions of the conduction band are affected by EPC to low-frequency phonons, which contribute to charge transport depending on the band occupation.

An in-depth analysis of electron transport in naphthalene has shown the importance of band occupation effects and the role of charge-carrier density. The overall temperature dependency of transport properties originates from the thermal occupation of electronic states, the temperature-dependent broadening of the DOS (due to vibrational disorder), and polaron renormalization when EPC to high-frequency phonons is considered. We found that the experimentally observed high-temperature flattening in the *b* direction can be caused by band occupation and the coupling to low-frequency phonons even when inelastic phonon creation and annihilation processes are not included.

Finally, we investigated the combined effects of EPC to high- and low-frequency modes simultaneously and found the interesting result that the mobility increases by including the interaction to high-frequency modes, i.e., formation of polarons. This counterintuitive finding could be explained as the combined effect of band narrowing and vibrational disorder, which leads to an occupation of delocalized states in the middle of the band that would not contribute otherwise. The occupation effect overcompensates the decrease of transfer integrals between molecular sites due to polaron renormalization.

ACKNOWLEDGMENTS

We thank the Deutsche Forschungsgemeinschaft for financial support [CRC 1415 and projects No. OR 349/1 and No. OR 349/3 and the Cluster of Excellence e-conversion (Grant No. EXC2089)]. Grants for computer time from the Zentrum für Informationsdienste und Hochleistungsrechnen of TU Dresden and the Leibniz Supercomputing Centre in Garching are gratefully acknowledged.

[1] M. E. Gershenson, V. Podzorov, and A. F. Morpurgo, Rev. Mod. Phys. **78**, 973 (2006).

[2] O. Ostroverkhova, Chem. Rev. **116**, 13279 (2016).

[3] S. Reineke, M. Thomschke, B. Lüssem, and K. Leo, Rev. Mod. Phys. **85**, 1245 (2013).

[4] Y. Yuan, G. Giri, A. L. Ayzner, A. P. Zoombelt, S. C. B. Mannsfeld, J. Chen, D. Nordlund, M. F. Toney, J. Huang, and Z. Bao, Nat. Commun. **5**, 3005 (2014).

[5] A. L. Briseno, S. C. B. Mannsfeld, M. M. Ling, S. Liu, R. J. Tseng, C. Reese, M. E. Roberts, Y. Yang, F. Wudl, and Z. Bao, Nature (London) **444**, 913 (2006).

[6] A. J. Gillett, A. Privitera, R. Dilmurat, A. Karki, D. Qian, A. Pershin, G. Londi, W. K. Myers, J. Lee, J. Yuan *et al.*, Nature (London) **597**, 666 (2021).

[7] M. K. Riede, R. Schueppel, K. Schulze, D. Wynands, R. Timmreck, C. Uhrich, A. Petrich, M. Pfeiffer, E. Brier, E. Reinold *et al.*, in *Photonics for Solar Energy Systems II*, edited by A. Gombert (SPIE, New York, 2008), p. 70020G.

[8] S. Xing, V. C. Nikolis, J. Kublitski, E. Guo, X. Jia, Y. Wang, D. Spoltore, K. Vandewal, H. Kleemann, J. Benduhn *et al.*, Adv. Mater. **33**, 2102967 (2021).

[9] N. Karl, in *Organic Semiconductors (Landolt-Börnstein Numerical Data and Functional Relationships in Science and Technology (New Series), Group III)*, edited by O. Madelung, M. Schulz, and H. Weiss (Springer, Berlin, 1985), Vol. 17i.

[10] N.-E. Lee, J.-J. Zhou, L. A. Agapito, and M. Bernardi, Phys. Rev. B **97**, 115203 (2018).

[11] F. Ortmann, F. Bechstedt, and K. Hannewald, New J. Phys. **12**, 023011 (2010).

[12] K. Hannewald and P. A. Bobbert, Appl. Phys. Lett. **85**, 1535 (2004).

[13] N. Karl, K.-H. Kraft, J. Marktanner, M. Münch, F. Schatz, R. Stehle, and H.-M. Uhde, J. Vac. Sci. Technol. A **17**, 2318 (1999).

[14] N. Karl, Synth. Met. **133–134**, 649 (2003).

[15] S. I. Pekar, Zh. Eksp. Teor. Fiz **16**, 335 (1946).

[16] S. I. Pekar, J. Phys. USSR **10**, 341 (1946).

[17] T. Holstein, Ann. Phys. **8**, 343 (1959).

[18] K. Hannewald and P. A. Bobbert, Phys. Rev. B **69**, 075212 (2004).

[19] K. Hannewald, V. M. Stojanović, J. M. T. Schellekens, P. A. Bobbert, G. Kresse, and J. Hafner, Phys. Rev. B **69**, 075211 (2004).

[20] F. Ortmann, F. Bechstedt, and K. Hannewald, Phys. Rev. B **79**, 235206 (2009).

[21] F. Ortmann, F. Bechstedt, and K. Hannewald, J. Phys.: Condens. Matter **22**, 465802 (2010).

[22] A. Troisi and G. Orlandi, J. Phys. Chem. A **110**, 4065 (2006).

[23] N. Vukmirović, C. Bruder, and V. M. Stojanović, Phys. Rev. Lett. **109**, 126407 (2012).

[24] S. Fratini and S. Ciuchi, Phys. Rev. Lett. **103**, 266601 (2009).

[25] S. Fratini, S. Ciuchi, D. Mayou, G. T. de Laissardière, and A. Troisi, Nat. Mater. **16**, 998 (2017).

[26] A. Troisi, Phys. Rev. B **82**, 245202 (2010).

[27] S. Fratini, D. Mayou, and S. Ciuchi, Adv. Funct. Mater. **26**, 2292 (2016).

[28] S. Hutsch, M. Panhans, and F. Ortmann, Phys. Rev. B **104**, 054306 (2021).

[29] T. Nematiaram, D. Padula, A. Landi, and A. Troisi, Adv. Funct. Mater. **30**, 2001906 (2020).

[30] J. H. Fetherolf, D. Golež, and T. C. Berkelbach, Phys. Rev. X **10**, 021062 (2020).

[31] S. Giannini, A. Carof, M. Ellis, H. Yang, O. G. Ziogos, S. Ghosh, and J. Blumberger, Nat. Commun. **10**, 3843 (2019).

[32] A. Carof, S. Giannini, and J. Blumberger, Phys. Chem. Chem. Phys. **21**, 26368 (2019).

[33] G. Czycholl, *Theoretische Festkörperphysik - Von den klassischen Modellen zu modernen Forschungsthemen* (Springer-Verlag, Berlin, 2007).

[34] R. S. Sánchez-Carrera, P. Paramonov, G. M. Day, V. Coropceanu, and J.-L. Brédas, J. Am. Chem. Soc. **132**, 14437 (2010).

[35] A. Girlando, L. Grisanti, M. Masino, I. Bilotti, A. Brillante, R. G. Della Valle, and E. Venuti, Phys. Rev. B **82**, 035208 (2010).

[36] A. Girlando, L. Grisanti, M. Masino, A. Brillante, R. G. Della Valle, and E. Venuti, J. Phys. Chem. C **135**, 084701 (2011).

[37] V. Coropceanu, R. S. Sánchez-Carrera, P. Paramonov, G. M. Day, and J.-L. Brédas, J. Phys. Chem. C **113**, 4679 (2009).

[38] Y. Yi, V. Coropceanu, and J.-L. Brédas, J. Phys. Chem. C **137**, 164303 (2012).

[39] Y. Li, Y. Yi, V. Coropceanu, and J.-L. Brédas, Phys. Rev. B **85**, 245201 (2012).

[40] Z. Tu, Y. Yi, V. Coropceanu, and J.-L. Brédas, J. Phys. Chem. C **122**, 44 (2018).

[41] T. Nematiaram, S. Ciuchi, X. Xie, S. Fratini, and A. Troisi, J. Phys. Chem. C **123**, 6989 (2019).

[42] M. Panhans, S. Hutsch, J. Benduhn, K. S. Schellhammer, V. C. Nikolis, T. Vangerven, K. Vandewal, and F. Ortmann, Nat. Commun. **11**, 1488 (2020).

[43] See Supplemental Material at http://link.aps.org/supplemental/10.1103/PhysRevB.105.165136 for details of the derivation of vibrational disorder, which includes Refs. [79–81].

[44] I. G. Lang and Y. A. Firsov, Sov. Phys. JETP **16**, 1301 (1963).

[45] F. Ortmann and S. Roche, Phys. Rev. B **84**, 180302(R) (2011).

[46] R. Kubo, M. Yokota, and S. Nakajima, J. Phys. Soc. Jpn. **12**, 1203 (1957).

[47] R. Kubo, J. Phys. Soc. Jpn. **12**, 570 (1957).

[48] M. Panhans and F. Ortmann, Phys. Rev. Lett. **127**, 016601 (2021).

[49] Z. Fan, J. H. Garcia, A. W. Cummings, J. E. Barrios-Vargas, M. Panhans, A. Harju, F. Ortmann, and S. Roche, Phys. Rep. **903**, 1 (2021).

[50] R. Haydock, V. Heine, and M. J. Kelly, J. Phys. C **8**, 2591 (1975).
[51] S. Roche and D. Mayou, Phys. Rev. Lett. **79**, 2518 (1997).
[52] A. Weiße, G. Wellein, A. Alvermann, and H. Fehske, Rev. Mod. Phys. **78**, 275 (2006).
[53] F. Ortmann and S. Roche, Phys. Rev. Lett. **110**, 086602 (2013).
[54] D. Mayou, Phys. Rev. Lett. **85**, 1290 (2000).
[55] C. R. Groom, I. J. Bruno, M. P. Lightfoot, and S. C. Ward, Acta Crystallogr. B **72**, 171 (2016).
[56] H. C. Alt and J. Kalus, Acta Crystallogr. B **38**, 2595 (1982).
[57] T. Kubar, P. B. Woiczikowski, G. Cuniberti, and M. Elstner, J. Phys. Chem. B **112**, 7937 (2008).
[58] E. F. Valeev, V. Coropceanu, D. A. da Silva Filho, S. Salman, and J.-L. Brédas, J. Am. Chem. Soc. **128**, 9882 (2006).
[59] J. Blumberger, Chem. Rev. **115**, 11191 (2015).
[60] M. J. Frisch, G. W. Trucks, H. B. Schlegel, G. E. Scuseria, M. A. Robb, J. R. Cheeseman, G. Scalmani, V. Barone, G. A. Petersson, H. Nakatsuji *et al.*, Gaussian 16 Revision C.01 (Gaussian, Inc., Wallingford CT, 2016), https://gaussian.com/citation/.
[61] R. Krishnan, M. J. Frisch, and J. A. Pople, J. Chem. Phys. **72**, 4244 (1980).
[62] C. Lee, W. Yang, and R. G. Parr, Phys. Rev. B **37**, 785 (1988).
[63] A. D. Becke, J. Chem. Phys. **98**, 5648 (1993).
[64] P. E. Blöchl, Phys. Rev. B **50**, 17953 (1994).
[65] G. Kresse and D. Joubert, Phys. Rev. B **59**, 1758 (1999).
[66] G. Kresse and J. Hafner, Phys. Rev. B **47**, 558 (1993).
[67] G. Kresse and J. Furthmüller, Comput. Mater. Sci. **6**, 15 (1996).
[68] Y. C. Cheng, R. J. Silbey, D. A. Da Silva Filho, J. P. Calbert, J. Cornil, and J. L. Brédas, J. Chem. Phys. **118**, 3764 (2003).
[69] F. Giustino, Rev. Mod. Phys. **89**, 015003 (2017).
[70] B. Aradi, B. Hourahine, and T. Frauenheim, J. Phys. Chem. A **111**, 5678 (2007).
[71] M. Elstner and G. Seifert, Philos. Trans. R. Soc. A **372**, 20120483 (2014).
[72] X. Xie, A. Santana-Bonilla, and A. Troisi, J. Chem. Theory Comput. **14**, 3752 (2018).
[73] B. Hourahine, B. Aradi, V. Blum, F. Bonafé, A. Buccheri, C. Camacho, C. Cevallos, M. Y. Deshaye, T. Dumitrică, A. Dominguez *et al.*, J. Chem. Phys. **152**, 124101 (2020).
[74] M. Gaus, A. Goez, and M. Elstner, J. Chem. Theory Comput. **9**, 338 (2013).
[75] M. Gaus, X. Lu, M. Elstner, and Q. Cui, J. Chem. Theory Comput. **10**, 1518 (2014).
[76] Y. Yang, H. Yu, D. York, Q. Cui, and M. Elstner, J. Phys. Chem. A **111**, 10861 (2007).
[77] S. Grimme, J. Antony, S. Ehrlich, and H. Krieg, J. Chem. Phys. **132**, 154104 (2010).
[78] W. Warta and N. Karl, Phys. Rev. B **32**, 1172 (1985).
[79] L. Isserlis, Biometrika **12**, 134 (1918).
[80] G. C. Wick, Phys. Rev. **80**, 268 (1950).
[81] P. Danielewicz, Ann. Phys. **152**, 239 (1984).

5 Publication: Understanding the electronic pi-system of 2D covalent organic frameworks with Wannier functions

Summary:

Covalent organic frameworks (COF) are an extremely interesting class of organic materials since they allow to combine different organic molecules into a single covalently bonded crystal structure. However, choosing high performing building blocks for a certain application requires some care. Traditionally, chemists use empirical concepts like π-conjugation to rationalize design decisions. From a theoretical standpoint these concepts are rather vague and often ambiguous [88] hampering structure-property predictions. In contrast, a detailed analysis of the electronic structure from first principles can provide more and better insights.

In the following publication [89] we perform such a detailed analysis for a family of seven hexagonal COFs which have the same symmetry but consist of different chemical elements in the linker nodes. We analyze chemical trends and correlate them with measures of aromaticity like nuclear independent chemical shifts (NICS) and the Shannon entropy of the ground state density. Furthermore, the calculation of maximally localized Wannier functions (MLWF) yields molecular orbitals which are in the shape of typical π-, σ- and lone-pair orbitals and agree with chemical intuition. Moreover, their rigorous mathematical definition enables quantitative calculations. We find that the electronic structure of the π-system completely decouples and is very similar between the investigated COFs. The shapes of the bands are determined by the symmetry of the COFs and is therefore similar for all investigated COFs. However, the bandwidths depend on the chemical specifies and the polarization of bonds. In fact, the cumulative bandwidth of all π-bands nicely correlates with other measures of aromaticity. This is, however, not always true for single bands, e.g., bands near the Fermi-level might not follow the same trends. As a consequence, aromaticity or cumulative bandwidth are not suitable predictors of effective masses and transport properties.

Using the description in term of MLWF we could also analyze the impact of doping and disorder on bandwidths and delocalization of charge carriers. Both aspects are important for applications. We found that the delocalization of charge carriers mainly depends on the energetic differences between building blocks (onsite energies) and is hardly related to the NICS-aromaticity (of the building blocks). Only for large amounts of disorder aromatic building blocks seem to be more resilient. Furthermore, we have investigated the effect of bond torsions that can break π-conjugation.

Individual contribution:

Statement from the publication: "Initial structure creation and relaxation together with the numerical calculations of NICS values, Wannier functions, electronic structures and IPR values were performed by K.M. Numerical calculations for the evaluation of bond torsion and related measures were carried out by J.G. All authors contributed to the discussion and writing of the paper. F.O. supervised the work." [89]

scientific reports

Check for updates

OPEN

Understanding the electronic pi-system of 2D covalent organic frameworks with Wannier functions

Konrad Merkel, Johannes Greiner & Frank Ortmann✉

We investigate a family of hexagonal 2D covalent organic frameworks (COFs) with phenyl and biphenyl spacer units and different chemical linker species. Chemical trends are elucidated and attributed to microscopic properties of the π-electron-system spanned by atomic p_z-orbitals. We systematically investigate the electronic structure, delocalization of electronic states, effects of disorder, bond torsion, and doping, and correlate these with variable π-conjugation and nucleus-independent chemical shift (NICS) aromaticity. Molecular orbitals are obtained from maximally localized Wannier functions that have σ- and π-character, forming distinct σ- and π-bands for all valence states. The Wannier-orbital description goes beyond simple tight-binding models and enables a detailed understanding of the electronic topology, effective electronic coupling and delocalization. It is shown that a meaningful comparison between COFs with different chemical elements can only be made by examining the entire π-electron system, while a comparison of individual bands (e.g., bands near the Fermi energy) can be a insufficient to derive general design rules for linker and spacer monomer selection. We further identify delocalized states that are spread across tens or hundreds of pores of the 2D COFs and analyze their robustness against structural and energetic disorders like out-of-plane rotations of molecular fragments, different strength of energetic disorder and energetic shifts due to chemical doping.

Layered 2D COFs[1–3] are attracting huge scientific interest because they combine different worlds, namely the construction paradigm of covalently linked molecular building blocks such as in linear polymers with the intriguing features of inorganic 2D materials such as graphene or transition-metal dichalcogenides. After pioneering synthetic works demonstrating the feasibility of 2D COFs[4] and development of advanced synthetic methodologies[5–7] for tuning crystallinity, pore size or surface area[8–10], the research directions for 2D COFs have diversified greatly[11–13], where the electronic properties are a common theme. Recent improvements in material quality[14], have triggered the quest for unveiling the intrinsic electronic properties of 2D COFs[15]. Moreover, the active control over these by synthetical strategies would be desirable. This requires a local monomer-based understanding of the emergence of these properties that includes the type of linkage between the monomers[1–3] which in itself controls the electronic coupling and macroscopic observables such as charge transport parameters. To rationalize the influence of both building blocks and their electronic coupling, one uses effective lattice models[16–19] for specific electronic bands to explain intriguing band features, which however, are not well-connected to the molecular building units used by synthetic chemists and not to the linkage chemistry.

From a chemist's perspective, these electronic properties are rooted in the π-conjugation[1,20], which is also associated with thermal and chemical stability. This concept is one of the most-frequently cited ones in 2D COF research. For semiconducting 2D COFs, π-conjugation is frequently connected with improved electronic properties, delocalization of states and good charge-carrier transport, but this connection is usually not supported or quantified and hence remains elusive. While for single molecules a number of different measures for π-conjugation or aromaticity, that quantify the entire π-electron system, have been suggested, e.g. resonance energy[21,22], aromatic stabilization energy[23–25], multicenter bond index[26,27], Bird index[28], Fluctuation index[29], Shannon aromaticity[30] or nucleus independent chemical shift (NICS)[31–34], and are routinely simulated for monomers, this has not been done for 2D COFs. Notwithstanding, it is expected that also for 2D COFs, π-conjugation is an important prerequisite for dispersive electronic bands[35], low band gaps, low effective masses[36] and that it affects optical properties or allows for high carrier mobilities[37]. In this sense, the route towards better π-conjugated systems is believed to be an important design principle[38] provoking claims of "high π-conjugation" or "full π-conjugation" in recent literature. However, only scant attention has been paid to investigate these measures for 2D COFs and assess their suitability in rationalizing the global electronic structure or to understand

TUM School of Natural Sciences, Technical University of Munich, Munich, Germany. ✉email: frank.ortmann@tum.de

delocalization of electrons in these materials, which is necessary for engineering their properties by synthetic approaches.

Here we investigate a family of prototypical hexagonal 2D COFs with aromatic and non-aromatic linker molecules in a combined ab initio and model study. The role of the π-orbitals for their electronic structure and the tendency to form delocalized π-systems, is analyzed with regard to the chemical nature of the linker unit. Toward this end, localized Wannier orbitals (WO) from first-principles DFT calculations are used to establish topological electronic lattice models. These *WO lattice models* have the advantage over mere *effective lattice models* (representing only few bands) that they are complete and contain all information about the system, including the band entanglement. They also resemble the Lewis structure closely, i.e. they are close to chemical intuition and are thus preferable and universally applicable to any 2D COF. Two manifestations of global π-conjugation are found, namely the effective coupling of π-orbitals leading to a large cumulated electronic bandwidth and the electron delocalization over linker and spacer units. Both properties are in general independent of each other and show different chemical trends. We show that whereas aromatic linkers may exhibit flat bands indicating insulating electrical characteristics, 2D COFs with non-aromatic and very polarized linkers in contrast can have a delocalized, global π-system, challenging the wisdom that formally better π-conjugation would be sufficient or necessary for better transport properties or delocalization of states.

Results and discussion

2D COF systems and NICS aromaticity. To investigate the in-plane π-conjugation, we choose seven 2D COFs in monolayer geometry with different linker molecules, which are shown in Fig. 1. All structures are fully planar and belong to the P6/mmm space group, while the sheet separation is chosen sufficiently large to avoid any interaction. For clarity, all materials are named according to their linker elements and number of phenyl rings in the spacer unit (see Fig. 1). Common aliases, if they exist, are provided in parentheses. Among the systems, COF-CC-1Ph (Fig. 1d) is included as a hydrocarbon reference system, whose phenyl linker has no polarity in its carbon-carbon bonds and potentially leads to optimized conditions for a delocalized π-system. We note that, despite obvious steric effects, also COF-CC-1Ph is studied in its planar configuration because our focus is on the comparison of the electronic properties of the seven 2D COFs in the first place, while bond torsions will be studied further below. On the other hand, COF-BO-1Ph[4] and COF-BO-2Ph[39,40] with their strongly polarized BO bonds are conventionally considered to be only weakly conjugated, if at all (*vide infra*), thus representing the opposite case in our series of test systems with variable electronic properties. The triazine linker in COF-CN-1Ph[5] and COF-CN-2Ph[41] has less strongly polarized bonds and may be considered an intermediate case. The comparision between carbon-based and boron-based linkers enables us to distinguish between aromatic and non-aromatic linker monomers (*vide infra*). BS-based linkers add another interesting variant to the family studied here. The electronic structure and wave functions of these systems are described by density functional theory (DFT)[42] for the relaxed structures (details are provided in the "Methods" section).

To characterize π-conjugation of the studied 2D COF systems, we calculate NICS, which is a well-established measure of aromaticity[31–34]. It is, in principle, applicable to macrocyclic systems and even to non-planar structures[43–45], which is a major advantage over other measures of aromaticity that are often applicable only to

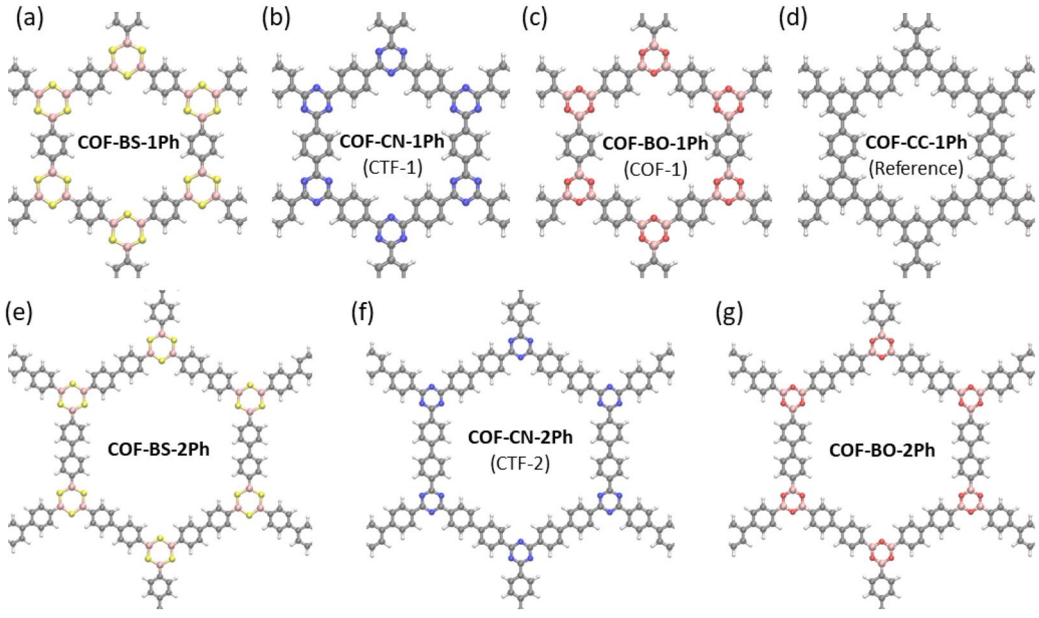

Figure 1. 2D COF structures with different linkers and phenyl (**a**–**d**) or biphenyl spacing units (**e**–**g**). Structure (**d**) serves as an idealized reference system for comparison. Chemical elements are represented with different colors: boron (pink), carbon (gray), hydrogen (white), nitrogen (blue), oxygen (red) and sulfur (yellow).

single molecules, single rings or rely on suitable non-aromatic reference systems. NICS measures the response to an external magnetic field in an NMR Gedanken experiment, where a ring current is induced in cyclically conjugated molecules, which in turn causes a magnetic field that counteracts and therefore shields the external field. The $NICS_{ZZ}$ value is defined as the negative ZZ-component of the shielding tensor (out-of-plane direction) and is usually evaluated at the center or 1 Å above the center of a cyclic molecule. A more comprehensive picture is obtained by performing NICS scans across the molecular planes[46,47].

Before we investigate NICS values for the COF pores, we start by examining the basic building blocks, i.e. the linker and phenyl rings. Figure 2 shows their $NICS_{ZZ}(1)$ values. Strongly negative values in the middle of the ring indicate aromatic molecules[33,34] as seen for phenyl- and CN-linker rings. As compared to the most aromatic monomers, both boron containing linkers show drastically reduced absolute but still non-zero $NICS_{ZZ}(1)$ values at the center. We note that they stem from sulfur or oxygen atoms and cannot be associated to aromatic ring currents. These linker units are therefore reminiscent of non-aromatic species. The NICS plots also show that the ring currents not only generate a magnetic field inside the rings, but also outside. There the direction of the magnetic field is reversed as described by Ampères law. This leads to a shielding of the external magnetic field inside the rings but amplifies the external magnetic field outside the rings in the molecular plane, as is clearly visible for all monomers. Such outfield effects are very important for a sound interpretation of NICS values of multiple ring systems such as anthracene[48,49]. In these systems, multiple ring currents around every single ring (and every combination of rings) can occur. Magnetic fields generated from one ring current also influence neighboring rings and shift the NICS value to positive values[34,46,50].

In order to address this question for 2D COFs, different contributions from all rings need to be analyzed. Our study here focuses on the induced ring current of a single 2D COF pore rather than all kinds of local ring currents, because we are interested in the characterization of global π-conjugation for 2D COFs and not local π-conjugation of single monomer units. Therefore, we need to distinguish the NICS values originating from ring currents around the COF pore (that are of interest) from all other sources of NICS originating from the peripheral building blocks. Towards this end, we split the COF pore into fragments as shown in Fig. 3a,b such that no ring current can flow analogously to an open electrical circuit. NICS values for this situation of a broken conjugation are compared to a completely closed COF pore, where ring currents are possible (Fig. 3d). The COF fragments in Fig. 3a,b are saturated with additional hydrogen atoms and the NICS maps resemble those of the monomers in Fig. 2. The NICS values of all fragments are added in Fig. 3c. Interestingly, this yields values very similar to the ones of a completely closed 2D COF pore (Fig. 3d) although the fragmented geometry prohibits

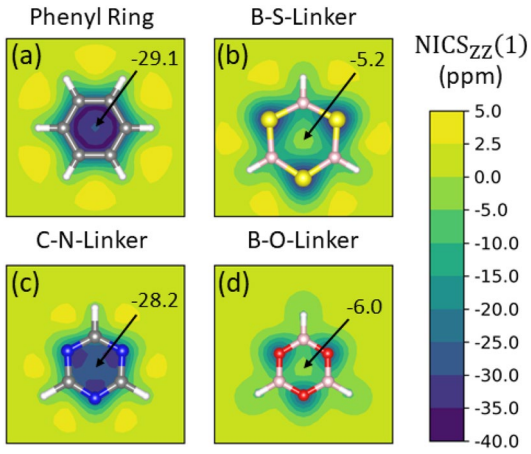

Figure 2. $NICS_{ZZ}(1)$-scan for all basic building blocks of the investigated COFs. Linker units are terminated with hydrogen.

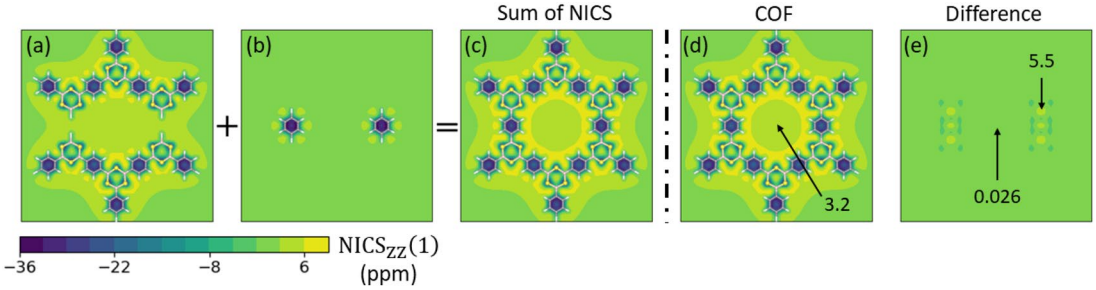

Figure 3. $NICS_{ZZ}(1)$-scans (1 Å above the molecular plane) for a single pore of COF-BS-1Ph. (**a**–**c**) The decomposition scheme that is compared with calculations of the entire pore (**d**). All other investigated COFs show similar results.

a pore ring current whereas the closed geometry might support such current. For better analysis, Fig. 3e shows the difference in the NICS values (ΔNICS) between the sum of the COF fragments and the full COF pore. This ΔNICS plot confirms that the difference vanishes. Only minor contributions that are due to the breaking of the chemical bonds at local points remain where the two phenyl rings were cut out, which is a purely local effect that is not associated to the COF pore. The same results were found for calculations of all other investigated systems. Therefore, the NICS values of the investigated COFs can be understood as the superposition of NICS values of the smaller peripheral rings surrounding the pore. Possible contributions from *pure pore-ring currents*, which would manifest in a finite ΔNICS value in Fig. 3e, are found to vanish in any of the COFs up to numerical precision of the simulations. We emphasize that several tests of more elaborate decomposition schemes for the COFs did not give measurable ΔNICS values from ring currents for any of the investigated systems (see section SI-8 in the Supporting Information).

This leads us to the conclusion that, despite clear signatures of NICS aromaticity of the different linkers, NICS calculations for an entire 2D COF are only of limited use. They cannot provide insight into the role of π-conjugation-induced formation of extended states that possibly could extend over many pores. We therefore study other measures that are more suitable here subsequently.

Orbitals and band structure. We next analyze the DFT electronic structure, which is fully described by the Bloch states $|m\boldsymbol{k}\rangle$ and the Kohn–Sham Hamiltonians $\hat{H} = \sum_{m\mathbf{k}} \epsilon_m(\mathbf{k}) \hat{a}^\dagger_{m\mathbf{k}} \hat{a}_{m\mathbf{k}}$. For a better analysis of structural and energetic disorders, which are rather intransparent in k-space, we represent the Kohn–Sham states with localized orbitals that are associated to linker or phenyl/biphenyl spacer moieties. We choose WOs in the concrete form of maximally localized Wannier functions (MLWF)[51], which are particularly well suited since they provide a natural way to obtain localized orbitals for periodic crystals (see "Methods" section for all details). It has been shown that if all occupied states (valence bands) are contained in the Wannierization procedure, MLWF reproduce typical bonding orbitals such as sp3-hybrid orbitals in Si and GaAs and σ- and π-orbitals in hydrocarbons[51,52]. They are obtained from the Bloch states by a unitary transformation according to

$$|n\boldsymbol{R}\rangle = \sum_{mk} e^{i\boldsymbol{kR}} U_{nm}(\boldsymbol{k}) |m\boldsymbol{k}\rangle, \tag{1}$$

and therefore retain all electronic information about the system. $\boldsymbol{R}$ indicates the unit cell associated to the WO and the unitary matrix $U(\boldsymbol{k})$ can be chosen such that the obtained orbitals have minimum spread[51,53]. For this reason MLWF are commonly used for band structure interpolation[54] and calculations of topological properties, e.g. Berry phases or Chern numbers[55]. The transformed Kohn–Sham–Hamiltonian in the WO basis reads

$$\hat{H} = \sum_{ij} \epsilon_{ij} \hat{a}^\dagger_i \hat{a}_j, \tag{2}$$

where $\hat{a}^{(\dagger)}_i$ (create) annihilate an electron at the i-th orbital, ϵ_{ii} are the orbital (onsite) energies and ϵ_{ij} with $i \neq j$ are transfer integrals (TI). We have checked that the transformed Hamiltonian Eq. (2) accurately reproduces the Kohn–Sham electronic structure (see Fig. SI-1 in the Supporting Information).

Figure 4 shows the resulting WOs for COF-BS-1Ph as example representing all 2D COF structures in this work. We observe that all WOs are localized within the range of $\sqrt{\langle x^2\rangle - \langle x\rangle^2} \leq 1.4$ Å which is close the C=C bond distance. They can be associated with typical bonding hybrid orbitals. As an example, Fig. 4a shows the WOs of the type X-π (X = S, N, O), which are localized at a single linker moiety (e.g. the uppermost BS linker with its WO in darker colors). It also shows the copies of the orbital at the six symmetry equivalent positions in the COF. In addition to these six X-π orbitals, Fig. 4b,c illustrates a complete set of all occurring types of WOs at linker and spacer units. Although WOs of the same type share the same shape, small deformations in the vicinity of the linker can occur and are shown in Figs. SI-2 and SI-3.

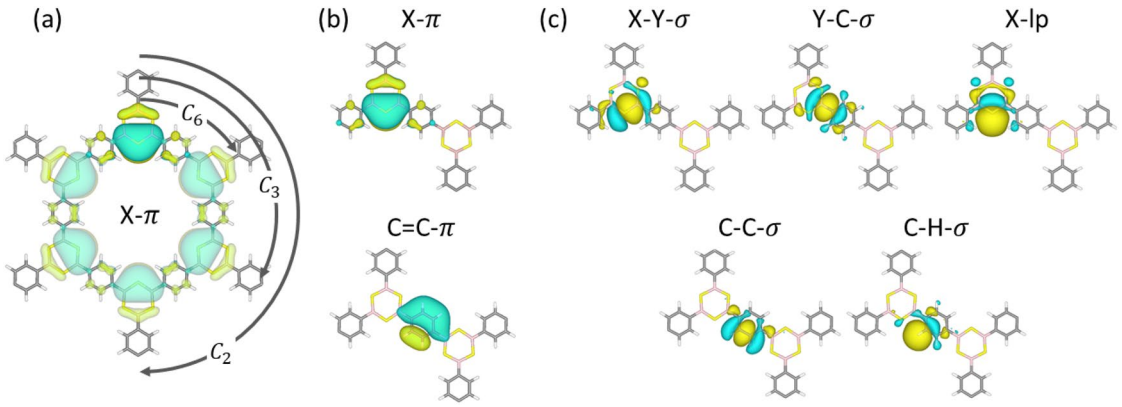

Figure 4. Illustration of Wannier orbitals obtained for all materials. (**a**) The symmetry equivalent WO of the type X-π. (**b**,**c**) All different bond-types in terms of WO at linker and phenyl rings. The notation of WO is based on the atom types (X,Y,C,H) and shapes (π, σ, lp). All studied COFs contain the same shapes of WO.

Similar to the X-π WOs at the linker, π-orbitals of type C=C-π are located at the phenyl rings (three π-orbitals per ring). The π-orbitals at linker and phenyl rings together form the π-system (Fig. 4b), which contains in total 15 π-orbitals per unit cell for COF-BS-1Ph, COF-CN-1Ph, COF-BO-1Ph and COF-CC-1Ph (Fig. 1a–d) and 24 π-orbitals per unit cell for COF-BS-2Ph, COF-CN-2Ph and COF-BO-2Ph (Fig. 1e–g). These are by symmetry the only WOs which have contributions from atomic p_z-orbitals.

Figure 4c shows all σ-orbitals (apart from symmetry equivalent copies) that represent the bonds between the chemical elements (type X-Y-σ, for which X = S, N, O, C and Y = B, C are the linker atoms). At every phenyl and linker ring there are six WOs of type C-C-σ or X-Y-σ, respectively. Together with the C=C-π and X-π orbitals we find a typical structure of alternating single and double bonds that is in agreement with the Lewis structure for all COFs. The C-C-σ orbitals at single-bond and double-bond positions have the same shape. However, they differ in other properties and, if necessary, we distinguish these two sub-types in our notation as C-C-σ_s and C-C-σ_d, respectively. In addition, lone-pair orbitals at the linker are denoted as X-lp (X = S, N, O). Note that, since COF-CC-1Ph only consists of phenyl rings as building blocks, it does not host X-π or X-lp orbitals but C=C-π and C-H-σ orbitals instead. In total one obtains 69 WOs per unit cell for COF-BS-1Ph, COF-CN-1Ph, COF-BO-1Ph and COF-CC-1Ph and 111 WOs per unit cell for COF-BS-2Ph, COF-CN-2Ph and COF-BO-2Ph.

Having established the WOs as convenient basis of our study, we turn to their electronic coupling and possible formation of globally extended states and their robustness. The distribution of such states over linker and phenyl rings, spanning over several pores or even throughout the entire 2D COF, would indicate interesting electronic and transport properties. This requires the electronic coupling between adjacent orbitals, while their energies should not differ too much.

Band structure, bandwidth, and lattice models. In order to investigate the influence of π-orbitals on the electronic structure, we analyze the π-system as a whole rather than restricting ourselves to specific bands, because a preselection of a subset of bands could be misleading. Toward this end, we determine the contribution of the π-orbitals to the Kohn–Sham-eigenstates $|n\boldsymbol{k}\rangle$ by projecting them onto all π-orbitals in a unit cell according to the weight

$$P_\pi(n,\boldsymbol{k}) := \sum_{i\in\pi\text{-WOs}} |\langle i|n\boldsymbol{k}\rangle|^2. \tag{3}$$

Figure 5a shows the electronic structure for the uppermost valence states of COF-BS-1Ph and the projection $P_\pi(n,\boldsymbol{k})$ (red color bar) together with the density of states (DOS) and the π-projected DOS (π-DOS) for COF-BS-1Ph. Band structures for all other COFs can be found in section SI-3 of the Supporting Information.

The π-orbitals only contribute to a specific subset of bands, subsequently denoted π-bands. Protected by symmetry, these π-bands are decoupled from all other bands, i.e. they do not have contributions from σ- or lone-pair-orbitals and vice versa, allowing a clear distinction of the π-system from all other bands. Although, the σ- and lone-pair-bands differ strongly between different COFs, we see that the π-system is very similar in shape and arrangement of the bands. Only 2Ph-COFs host additional π-bands, however, similarities between 1Ph and 2Ph COFs are still obvious. We can therefore conclude that the qualitative energy dispersion is mainly

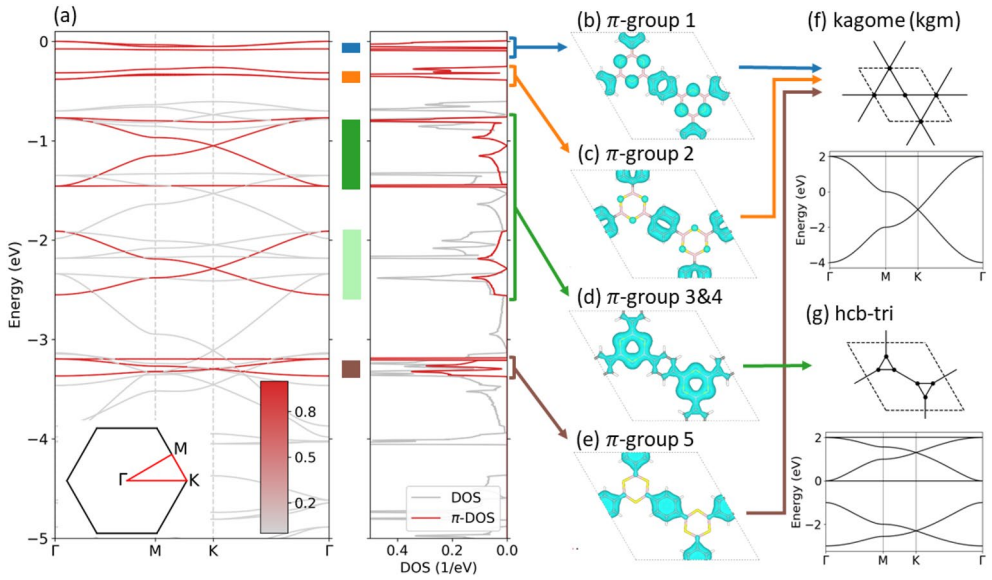

Figure 5. (**a**) Band structure of COF-BS-1Ph, projected on all π-orbitals, and density of states (DOS) for all states and π-states (π-DOS). Zero energy is put to the top of the valence bands. Colored stripes indicate the bandwidth for every group of π-bands. The Brillouin zone is shown as inset. (**b**–**e**) Partial charge densities at the Γ-point from the indicated group of π-bands, $|\sum_n \langle n\boldsymbol{k}=0|\psi\rangle|^2$ (where n is restricted to a single π-group). (**f**,**g**) Comparison to the 2D effective lattice models.

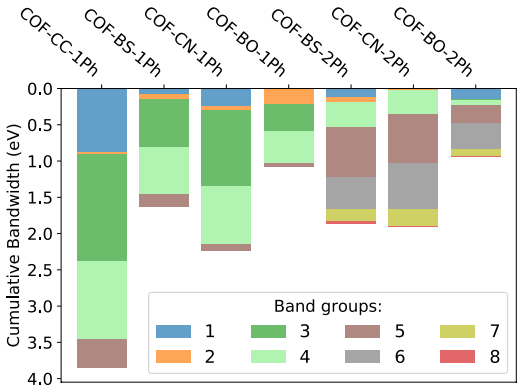

Figure 6. Electronic bandwidths for planar structures. Colors represent different groups of bands as highlighted in Fig. 5 for COF-BS-1Ph. The overall size of the bars indicate the cumulative bandwidth. Values are provided in Tables SI-1 and SI-2.

determined by the geometry and symmetry of the COF, whereas the chemical elements of the linker manifest themselves solely in the bandwidth of individual π-groups.

We briefly discuss the origin of these π-groups using COF-BS-1Ph as an example. For convenience of presentation, we indicate in Fig. 5a the different groups with colored stripes, which will be used throughout this paper. The first two π-groups (blue and orange) are distorted kagome (kgm) bands (cf. Fig. 5f for a kgm lattice and its idealized band structure)[16–18]. Their partial charge density is mainly localized at typical kgm sites as expected (cf. Fig. 5b,c). A deeper analysis of the Hamiltonian in the WO basis reveals that the distortion is not related to symmetry-breaking but originates from (small) next-nearest neighbour interactions. In agreement with previous studies[56] these distortions can be reduced by removing corresponding transfer integrals. π-group 3 and 4 (dark and light green) have the same origin and show the same partial density (cf. Fig. 5d). The corresponding real-space lattice is a honeycomb lattice in which the simple vertex is replaced by a connected trimer (cf. Fig. 5g), which we call "hcb-tri"[18,56]. The fifth group of π-bands (brown) shows a nearly ideal kgm band structure. In consistency, the corresponding partial density in Fig. 5e is located at the phenyl units, which, at first glance, seems to be a perfect manifestation of a kgm lattice that is realized by phenyl-based π-WOs (Fig. 5f). The visual identification of an effective lattice model from crystal states, however, can be tricky and caution should be exercised. For instance, in the present case, the Hamiltonian in the WO basis does not contain significant TIs between the WOs at the phenyl rings, in contradiction to the kgm lattice model. The absence of these (through space) TIs between WOs at the phenyl rings is explained by the fact that long range connections between WOs are exponentially suppressed and significant TIs only exist over short distances (few Angstroms). An overview is compiled in Figs. SI-4 and SI-5 of the Supporting Information. This case exemplifies that it is generally not permitted to infer an effective lattice model just from the band structure. The TIs that are responsible for these kgm-bands are those between WOs of the phenyl units and the BS linkers. The linkers therefore serve as bridging units that facilitate the carriers tunneling from one phenyl ring to the other through the linker (and not through space). As a consequence, the linkers, even if devoid of charge density for these bands, can have a strong impact on these bands (see "Impact of orbital energies" below). This shows that picking isolated groups of bands for an effective lattice model may not capture all its properties and can be a misleading simplification that may not correctly describe the origin and entanglement of the bands, while the formal representation in a Wannier basis is exact.

The π-system is analyzed further by quantifying its electronic bandwidth. Our focus is on the cumulated bandwidth of the entire π-system in Fig. 6, while the individual contributions are also resolved in the figure. From comparing the different COF structures, we find the cumulative bandwidths to depend sensitively on the linker type. We observe similar trends for phenyl (1Ph) and biphenyl (2Ph) cases. The reference system COF-CC-1Ph has the largest cumulative bandwidth, which confirms the conjecture of the highest degree of (global) conjugation for this material. The two boron-based COFs have much lower values. The weaker π-conjugation in presence of boron atoms leads to a reduction in the cumulated bandwidth by about a factor of two in case of BS COFs and by a factor of about three to four in case of BO COFs. This reduction is in full consistency with the combination of boron, an electron deficient atom with electron-rich oxygen or sulfur. Also, COF-BO-1Ph and COF-BO-2Ph are the COFs with the most polarized linker according to the electronegativity values of the chemical elements and Bader charges (see section SI-4 in the SI).

In contrast to the cumulated bandwidths, these chemical trends are not reflected in the top valence bands. These bands, which are responsible for (p-type) transport properties, are π-bands for almost all investigated systems except for COF-CN-1Ph, where the top valence bands originate from lone-pair orbitals. The widths of these bands do not follow the same trend as the cumulative bandwidth, which makes transport parameters like the effective mass (see Table SI-4 of the SI) uncorrelated to the overall π-conjugation, which is a rather unexpected finding. Furthermore, the top valence bands are often kgm groups which contain a flat band that yields huge effective masses (see also[56]). For transport properties it is therefore crucial if the flat band is on top or below the dispersive bands, which can even change for different COFs with the same linker, e.g. in the case of COF-BO-1Ph and COF-BO-2Ph.

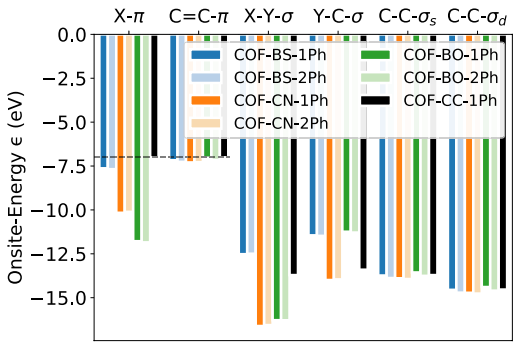

Figure 7. Orbital onsite energies for every WO and material. C-C-σ_s and C-C-σ_d denote the C-C-σ orbitals at single and double bond positions, respectively.

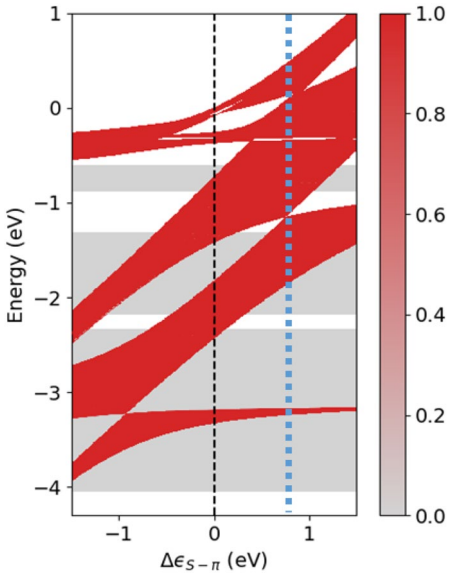

Figure 8. Impact of S-π onsite energy on the band structure of COF-BS-1Ph. Red color indicates high values of projection P_π onto π-orbitals. The black dashed line shows the original onsite energy and the blue dashed line highlights the special case where all upper π-groups touch each other. The energy scale is set to zero at the highest occupied state of the original 2D COF for better comparison.

Impact of orbital energies. Orbital energies are key electronic parameters for many applications. They determine redox potentials of the monomers, which can be used to control the COF's electronic properties. They can be further tuned by chemical doping, which is frequently performed for 2D COFs[37,57–60]. In addition, orbital energy differences have a strong impact on the band structure. For instance, they can lead to a reduction of the band width and to a gap opening in the bands. A prominent example for the latter is the difference between the atomic 2D crystals graphene vs. hexagonal BN. In 2D COFs, owing to the symmetry, WOs that belong to the same bond-type for a given COF share the same orbital energy, while differences occur for C-C-σ_s and C-C-σ_d at single and double bond positions, respectively. In contrast, the orbital energies of analogous WOs in different 2D COFs vary substantially. Figure 7 compares the WO orbital energies for all systems. Colors represent different linkers and their pale version represent the biphenyl COFs.

The C=C-π, C-C-σ_s and C-C-σ_d orbitals at the phenyl rings have, respectively, similar onsite energies for all COFs, including the reference system COF-CC-1Ph, with variations within a range of maximally 0.37 eV among each individual group, while all other orbital energies depend much more strongly on the chemical species. Indeed, the onsite energies of the linker orbitals ($\epsilon_{S\text{-}\pi}$,$\epsilon_{N\text{-}\pi}$, $\epsilon_{O\text{-}\pi}$) show big differences depending on their chemical elements and the polarization of the bond, ranging between −11.85 eV and −7.63 eV.

In order to study how the different WO energies influence the electronic structure, we focus on the X-π orbitals at the linkers, which are material dependent as discussed above and have the strongest effect on the π-system. COF-BS-1Ph is studied as a concrete representative case. It is instructive to study modifications in the WO energy by a simple model according to the replacement $\epsilon_{S\text{-}\pi} \rightarrow \epsilon_{S\text{-}\pi} + \Delta\epsilon_{S\text{-}\pi}$ while all other electronic parameters are kept fixed for the sake of transparency of the effects. Positive values for $\Delta\epsilon_{S\text{-}\pi}$ would correspond to p-type doping and could be realized by intercalation of strong electron acceptors such as F4TCNQ[59]. Figure 8 shows the changes

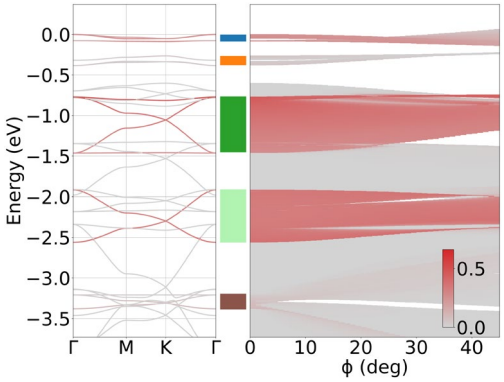

Figure 9. Band structure of COF-BS-1Ph (including projection on p_z-orbitals at linker positions) and impact of rotation of the phenyl rings on band width and projection. The energy zero is set to the valence band maximum of the planar structure.

in the band structure as a function of $\Delta\epsilon_{S\text{-}\pi}$. For clarity of presentation, the color scale in the figure indicates the maximal projection $P_\pi(E) = \max_{\boldsymbol{k}\in\Lambda}\{P_\pi(n,\boldsymbol{k}) \,|\, E_n(\boldsymbol{k}) = E\}$ (Λ is the path along Γ-M-K-Γ in the BZ) for a given energy E. This clearly distinguishes all π-bands from all other bands regardless of the values of $\Delta\epsilon_{S\text{-}\pi}$.

We observe that the shift $\Delta\epsilon_{S\text{-}\pi}$ leads to strong changes for the bands of COF-BS-1Ph for both n- and p-type doping regimes. This affects the bandwidths and energies of all π-bands, whereas all other bands remain unchanged. These changes are even qualitative since various crossovers and gap closures and openings are observed. We also find that even those π-bands, which have no charge density on the linker (S-π) are affected by the S-π onsite-energy change. For instance, the bandwidth of the fifth group of bands (at an energy below −3 eV) changes significantly with $\Delta\epsilon_{S-\pi}$, despite the fact that the charge density of this kgm-group is completely localized on the phenyl rings without any contributions from the linker (see Fig. 5e). Above, we have pointed out that there are no direct (through space) TIs between any phenyl-based WOs that lead to the kgm-bands as would be expected by a simple model. There are rather many indirect connections with TIs through the linker (see Fig. SI-4). It is these indirect connections that are influenced by the energy variation of the linker and further corroborate the above findings.

Interestingly at $\Delta\epsilon_{S\text{-}\pi} = 0.8$ eV (blue dashed line in Fig. 8), we observe that four of the five π-groups of bands join into a single one with a total band width of 2.4 eV, whereas the lowest-energy band remains separated. The upper π-groups touch each other but do not overlap. Larger shifts of $\Delta\epsilon_{S\text{-}\pi} > 0.9$ eV lead to reconstructed π-groups such that new gaps appear and flat bands change their group affiliation resulting in π-groups with different topology. More precisely, the upper two kgm-groups become a hcb-tri group and the former hcb-tri group splits into two kgm-groups, i.e. the topological groups get therefore reordered. Figure SI-10 shows three band structures for selected values of $\Delta\epsilon_{S\text{-}\pi}$ at 0.5 eV, 0.9 eV and 1.2 eV for the interested reader. These findings show that the entire π-system is important for a comprehensive understanding of the COF's electronic structure and investigations of isolated π-bands may not provide the full picture. Our results further suggest a very rich playground for manipulating band topologies with dopant-induced orbital energies. This is possible even for rather modest energy shifts, which should be accessible with conventional dopant species that have already been used for 2D COFs in the past[60–62].

Robustness and breaking of π-conjugation by bond torsion. Mechanical distortions like out-of-plane rotations of phenyl rings (around the bonds to their neighbors) may limit the delocalization of electronic Bloch states because they can modify the overlap of π-orbitals between linker and phenyl rings[63,64]. To investigate these effects on the bandwidth, we rotate all phenyl rings of the 2D COF by the same angle ϕ in a propeller like arrangement (P3 symmetry group) while keeping the linker positions fixed. Figure 9 shows the impact of such rotations on the bandwidth for COF-BS-1Ph. Complementary figures for the other structures can be found in the SI (Figs. SI-11, SI-12). For reference, the band structure for the planar geometry is reproduced (from Fig. 5) in the left panel of Fig. 9. For a better overview over different states, they are projected onto atomic p_z orbitals at the linker positions and indicated by red color (see "Methods" section for all details). Projections onto these p_z-orbitals at the linker are sufficient to characterize the global, delocalized π-system because there are no π-states that are solely localized at the linker.

Upon rotation we observe a change in the bandwidth with increasing ϕ for all highlighted π-bands and for π-band group two (orange bar), indicating that the out-of-plane-rotation reduces the effective coupling within the π-system as expected. The largest bandwidth reduction is found for the two π-groups with the largest width (dark and light green), that correspond to the hcb-tri effective model. Despite the reduction of bandwidth, the band structures of these π-groups maintain the same order for the groups for all ϕ. This is different to the onsite energy change investigated above which induced band crossovers, suggesting that structural effects have a somewhat weaker impact as compared to energetic effects. The 2D COFs with rotated groups, however, have a reduced symmetry that leads to additional band gaps in Fig. 9. These gaps exist already at small angles $\phi < 20°$ and become clearly visible for larger rotations. Despite the emergence of gaps, the band structure remains similar

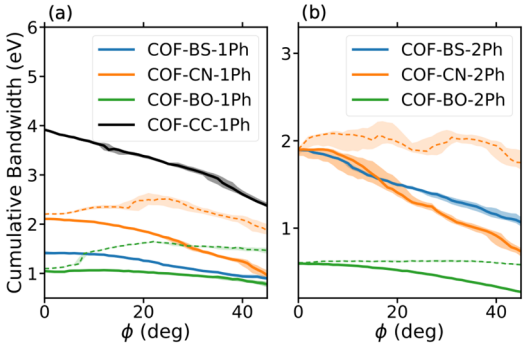

Figure 10. Cumulative bandwidth for different rotation angles ϕ for 1Ph COFs (**a**) and 2Ph COFs (**b**). Solid lines focus on the upper π-groups (near the Fermi-level) and dashed lines show the measurement for all π -groups. Colored areas indicate the numerical error of CBW due to a change of threshold parameters by 15%.

to the planar case for almost all π-groups. Only for the fifth π-group (brown) we observe fundamental changes of the band structure, where bands get mixed with energetically nearby bands resulting in a complete disappearance of this π-group. This is not surprising since the (partial) charge density of these π-group is entirely located at the rotated phenyl rings (see Fig. 5e). Interestingly, the distortion of the first (blue) and second (orange) kgm bands is reset upon rotation and eventually leads to nearly perfect kgm bands for $\phi \geq 50°$.

To quantify the visual impression in Fig. 9, we extract the (ϕ-dependent) cumulative bandwidth (see Eq. (6) for definition) in Fig. 10 for all phenyl COFs (a) and bi-phenyl COFs (b). Solid lines show the cumulative width of the π-bands that are already present in the planar systems. We see that the cumulative bandwidth (solid lines) decrease upon rotation for all phenyl COFs. Especially COF-CC-1Ph has not only the largest cumulative bandwidth but also shows the strongest decrease (linear slope). COF-BO-1Ph exhibits only small changes with increasing ϕ. In the case of 2Ph COFs (b) this trend is less pronounced.

In addition to the reducing bandwidth, in some 2D COFs additional π-bands appear that do not exist for the flat geometries ($\phi = 0$). This occurs at low energies and is accompanied by the complete change of the fifth π-group (brown). These new bands can have a large impact on the overall cumulative bandwidth which we indicate by dashed lines in Fig. 10.

We finally note that changes of the electronic structure upon rotation can also be evaluated by other quantitative measures which are compiled in the SI in section SI-7.

Density of states, disorder and delocalization. Of central importance to electronic and transport properties of 2D COFs is the delocalization of the electronic states. While the electronic coupling between π -orbitals is a central prerequisite, it may not be sufficient to delocalize electronic states beyond the size of individual pores which would be necessary for efficient charge-carrier transport[65,66].

We start by investigating the stability of the π-bands against increasing strength of energetic disorder. For this purpose we investigate large samples (supercells of $29 \times 29 \times 1$ unit cells for 1Ph COFs and $23 \times 23 \times 1$ for 2Ph COFs) that are constructed from the WO-based Hamiltonian (Eq. 2) and add electronic disorder. We use a generic uncorrelated Anderson model which shifts the onsite energy of every orbital randomly with a value $\Delta\epsilon$ from the interval $[-W/2, W/2]$, where the disorder strength W is the width of a box distribution[67]. We calculate wave functions and their energies at the center of the supercell BZ (see "Methods" section).

Figure 11 shows the DOS and the π-DOS of COF-BS-1Ph for different strengths of disorder W. π-groups are clearly distinguishable from all other valence bands and highlighted with colored stripes as before. The Dirac cones in the band structure are clearly visible in the DOS and the π-DOS with their characteristic V-shapes and are labeled by "D" at -1.1 eV and -2.3 eV. With increasing disorder, these shapes remain visible up to large disorder values ($W = 1$ eV), indicating a good robustness against disorder. Analogous behaviour of the Dirac cone states was observed for graphene, which however has much wider π-bands[68,69]. The robustness of the states for the more complex 2D COFs with rather moderate bandwidths, however, is quite surprising and suggests a similar mechanism here, which would suggest similar transport phenomena[70].

In contrast to these features, the two groups of flat π-bands (at 0 eV and -0.35 eV), which we identified as deformed kgm bands, are much more strongly affected by the disorder. These bands are broadened with increasing W and the individual DOS peaks of both bands overlap already for $W = 0.5$ eV and finally merge into a broad feature at $W = 1$ eV. The broadening is much larger than for other bands because these bands are dispersionless, which makes them more susceptible to disorder and localization as compared, for instance, to the Dirac cone states.

We next study the delocalization of the electronic states and their robustness against disorder. The question of disorder-induced localization is independent of the changes in the bandwidth (see "(Projected) inverse participation ratio" in the Methods section). Based on the clear separation of the π-system we can calculate the delocalization of the wave functions within the π-system by means of the inverse participation ratio (IPR)[71]. The IPR is a well-established measure for the spread of wave functions, which has already been used successfully for 2D-Dirac materials and topological insulators[72,73]. It is defined as

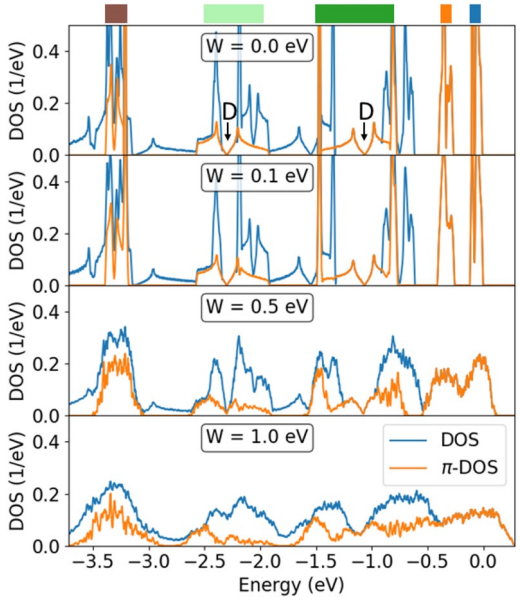

Figure 11. DOS and π-DOS for COF-BS-1Ph with different amounts of Anderson disorders W. Disorder-free case reproduced from Fig. 5a for comparison. Colored bars and energy scale are the same as in Fig. 5. Labels "D" show the Dirac points of the hcb-tri group.

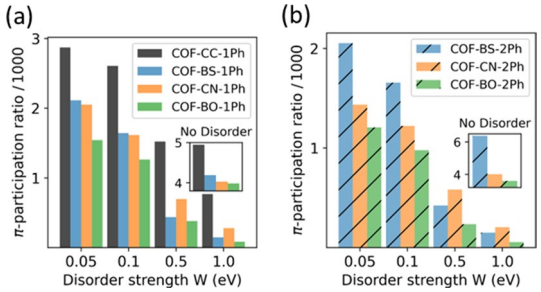

Figure 12. Participation ratio of π-states for different strength of Anderson disorders in a supercell. Calculations without disorder are shown in the inset for the same supercell.

$$\mathrm{IPR}(n) := \sum_{i=1}^{N} |\langle i \,|\, n, \boldsymbol{k} = 0 \rangle|^4, \tag{4}$$

where the sum runs over all N orbitals in a supercell. $|i\rangle$ denotes a WO and $|n, \boldsymbol{k} = 0\rangle$ is the analyzed eigen-state of the system. To focus on the π-states only, we utilize here the projected IPR (π-IPR) defined in the "Methods" section, where $|i\rangle$ is restricted to π-orbitals. Since the IPR values depend on the number of orbitals and the choice of supercell, we can only compare the phenyl COFs with each other and, separately, the biphenyl COFs with each other.

A more intuitive and closely related quantity is the participation ratio (PR), which is defined as the inverse of the IPR. It can be understood as the average number of orbitals over which a wave function is distributed. Figure 12 shows the average PR that is obtained for the entire set of π-states and compares the studied 2D COFs. In all cases one observes that the π-PR decreases with increasing disorder, which induces to a stronger localization of these states. Starting from pristine systems ($W = 0$) in which an average π-state is spread over 32% (COF-BO-1Ph) to 39% (COF-CC-1Ph) of the π-orbitals, at $W = 0.1$ eV, the average spread is reduced to 20.6% for COF-CC-1Ph and strongly suppressed to 10.0% for COF-BO-1Ph. To put this into perspective, this corresponds to an average (de-)localization over 174 and 84 pores, respectively, which are in the same order of magnitude as experimentally achieved domain sizes[14,74,75]. For the same W, electronic states of COF-BS-1Ph and COF-CN-1Ph are (de-)localized on average over 110 and 108 pores, respectively. These values are surprisingly similar and are indeed not expected given the strong differences in the NICS aromaticities of the linker monomers.

For larger strength of disorder ($W \geq 0.5$ eV) we observe a switch in the order of the PR values between COF-BS-1Ph and COF-CN-1Ph (cf. Fig. 12a) and also for the corresponding biphenyl COFs (cf. Fig. 12b), suggesting that CN-based COFs are more resilient to energetic disorder than BS-based COFs. This behavior can be correlated to the energy-resolved PR values which can vary by more than one order of magnitude for a single

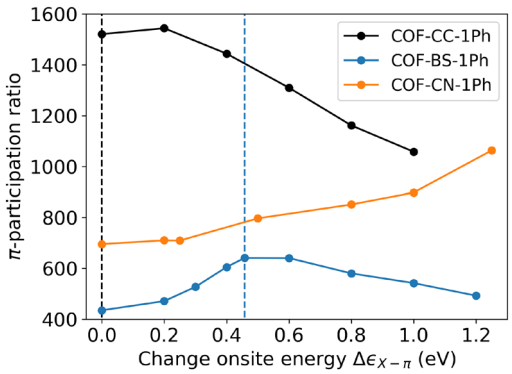

Figure 13. Changes in the delocalization of π-states (measured by the participation ratio with disorder $W = 0.5$ eV) upon shifting the linker's onsite-energy. Vertical dashed lines indicate where onsite energies for linker and phenyl rings would coincide, i.e. $|\epsilon_{\text{X-}\pi} + \Delta\epsilon_{\text{X-}\pi} - \epsilon_{\text{C=C-}\pi}| = 0$. For COF-CC-1Ph this ocurs at $\Delta\epsilon_{\text{X-}\pi} = 0$ eV, for COF-BS-1Ph at $\Delta\epsilon_{\text{X-}\pi} = 0.46$ eV and for COF-CN-1Ph at $\Delta\epsilon_{\text{X-}\pi} = 2.87$ eV).

systems (not shown as a plot). A detailed analysis of the band- and energy-resolved PR shows strong differences between band edge and band center with more delocalized states towards the middle of the bands for CN-based COFs, especially in the hcb-tri group, which increase the average PR at these energies while analogous states in the middle of the bands of BS-COFs are less delocalized. States at the band edges are much more strongly localized in both systems.

We finally study how the delocalization of electronic states can be increased upon linker-based doping for the assumed disorder regime of $W = 0.5$ eV. Figure 13 shows the changes in the π-PR for energetic shifts $\Delta\epsilon_{X-\pi}$ of up to 1.25 eV that are achievable with conventional molecular dopants even in non-porous organic systems[76]. In all cases one observes that the induced energetic differences have a strong impact on the π-PR. Vanishing energetic differences between linker and phenyl rings $|\epsilon_{\text{X-}\pi} - \epsilon_{\text{C=C-}\pi}|$ (indicated by dashed lines in Fig. 13) can be understood as resonance condition and always lead to much better delocalization. For instance the π-PR increases up to 47% for COF-BS-1Ph as compared to the undoped case. We therefore confirm that even in cases with large disorder, energetic differences of π-orbitals between linker and spacer units have a large impact. For small disorder this resonance effect is further amplified.

Conclusion

In this work, we compared a family of COFs with the same symmetry but different linker units in terms of π-conjugation, aromaticity and resulting electronic properties which are all routed in the COF's π-system. Although the electronic bands (including σ- and lone-pair-bands) of the COFs may appear quit different at first glance, we found that the π-bands are very similar in terms of band shape and arrangement. Our results show that the structure and symmetry alone determines the band dispersions qualitatively regardless of the chemistry of the linker unit. The chemical elements on the other hand control, through bond polarizations and aromaticity, the bandwidth and delocalization, quantitatively. However, the impact on single bands (e.g. bands near the Fermi level) might be very different and uncorrelated.

The understanding of electronic properties is facilitated by the transformation of the crystal Bloch states to localized Wannier orbitals with σ, π and lone-pair character. This WO representation of the electronic states resonates well with chemical intuition and is a natural basis for analyzing the π-system and allows rationalizing simpler effective topological models that are associated to certain subsets of bands. The analysis of electronic bandwidth, robustness against out-of-plane rotations, sensitivity to energetic disorder, delocalization and nuclear independent chemical shifts unveiled chemical trends that are independent of the number of phenyl rings between linkers and only depend on the chemical elements of the linker.

Our study revealed two independent effects of variable π-conjugation due to differently polarized linker bonds within the studied family. First, 2D COFs with more aromatic linker rings (as measured by NICS) show larger cumulative bandwidths and therefore larger effective TIs between the building blocks. The NICS aromaticity, however, characterizes the π-system as a whole and is not necessarily a valid descriptor for specific π-bands, such as the top valence bands. This renders the linker's aromaticity barely related to (hole) transport properties and transport parameters like effective masses of the top valence bands. A second aspect of π-conjugation is the delocalization of wave functions within the π-system. This depends mainly on energetic differences between π-orbitals at linker and spacer units and is less related to the aromaticity of the linker or cumulative bandwidth of the π-system. In fact, even non-aromatic BS linkers can lead to stronger delocalization than aromatic triazine linkers for energetic disorder that is not too strong. However, a larger coupling between building blocks (larger effective TIs) makes aromatic linkers more robust against very large disorder strengths. Other measures of aromaticity that are based on delocalization such as the Shannon aromaticity[30] (see section SI-9 in the SI) show the same trend as the π-PR, although, one should keep in mind that the Shannon aromaticity also depends on the size of the linker ring and therefore overestimates delocalization in COF-BS-1Ph and COF-BS-2Ph slightly. We note that measures of aromaticity, which are based on different physical or chemical properties, are generally not necessarily fully compatible to each other[77] which is also observed for 2D COFs.

Finally, we conclude that minimizing energetic differences between linker and spacer units, for instance by doping, increases delocalization to dozens of pores or more, depending on the disorder, which provides an intuitive and elegant way to tailor electronic properties.

Methods

Ab-initio DFT simulations and Wannier orbitals. The symmetrized structures are optimized at DFT level of theory using VASP[78,79] with PBE exchange correlation functionals and PAW pseudo potentials[80,81]. In all calculations a cutoff energy of 450 eV is used for the plane wave basis set. The relaxation was performed in two steps. First, ionic relaxation for different sizes of the unit cell are used to determine the lattice constants in a Γ-point only calculation (for Brillouin zone integration). The optimal size of the unit cell was found at the minimum of the ground state energy. This was done for every COF. In the second step a final relaxations of the optimized and symmetrized structures were performed using a $3 \times 3 \times 1$ Monkhorst-Pack $\boldsymbol{k}$-points grid. A subsequent electronic structure calculation using a Γ-centered $6 \times 6 \times 1$ Monkhorst-Pack grid is the basis for all further calculations.

We use the WANNIER90 code[82] to obtain MLWF for all valence bands. Starting projections are s-orbitals at the mid-bond positions and alternating double and single bonds are assumed according to the Lewis structure. Slightly different starting points, e.g. different orbital shapes or slightly different positions, lead to the same MLWF. Electronic properties like band structures are in perfect agreement with the DFT results. All MLWFs are real-valued within numerical precision, which shows that the optimization correctly finds a global minimum of the spread function[52]. We want to note that the non-uniqueness of the Lewis structure also reflects in a freedom of choice for MLWF, which is determined by the starting guess of the Wannierization. However, alternative configurations are equivalent and give the same results.

In situation, where π-like and σ-like orbitals are centered at the same position (double bond), the obtained MLWF from WANNIER90 are not typical π- and σ-orbitals but superpositions $|\pm\rangle = \frac{1}{\sqrt{2}}(|\pi\rangle \pm |\sigma\rangle)$. Performing the inverse transformation (i.e. symmetrization) is easily possible and yields typical π-like and σ-like molecular orbitals, where only the π-like orbitals have contributions from atomic p_z-orbitals.

Nuclear independent chemical shift (NICS). For the calculation of NICS we use the GAUSSIAN16 code[83] and the B3LYP exchange-correlation functional[84,85]. We created a structure, which contains only one pore of the COF and is saturated with hydrogen at the outermost phenyl rings. With this setting we make sure that no magnetic fields from other ring currents than the central COF-pore and their constituents disturb the result. All atoms lie in the x–y plane and NICS values are calculated 1 Å above the plane. Therefore, only the ZZ-component of the magnetic shielding tensor, which is the negative of $\mathrm{NICS}_{ZZ}(1)$, is of relevance.

Out-of-plane rotation. To measure the effect of out-of-plane rotations of the phenyl rings we perform separate band-structure calculations for all rotation angles and align them at their vacuum levels, which allows a proper comparison of band energies $E_n^{(\phi)}(\boldsymbol{k})$.

Furthermore, we define the energy dependent maximal projection as

$$P^{(\phi)}(E) = \max_{\boldsymbol{k}\in\Lambda}\{p^{(\phi)}_{z,\mathrm{linker}}(n,\boldsymbol{k}) \,|\, E_n^{(\phi)}(\boldsymbol{k}) = E\}, \tag{5}$$

where $\boldsymbol{k}$ is along the path Λ (i.e. Γ-M-K-Γ) that is representative for the Brillouin zone. Note that p_z-orbitals from the rotated phenyl rings are not included in the projection.

For quantitative results we introduce the ϕ-dependent *cumulative bandwidth* (CBW) as,

$$\mathrm{CBW}(\phi) := \int_{-\infty}^{E_F} dE\, \Theta\Big(P^{(\phi)}(E) - P_{\min}\Big), \tag{6}$$

similar to the cumulative bandwidth in the main text, where $\Theta(x)$ denotes the Heaviside-step-function and $P_{\min}$ is the minimum projection required for assigning states to a π-band. The value can easily be chosen such that individual bandwidths for $\phi = 0$ are in agreement with bandwidths in Fig. 6 (main text).

(Projected) inverse participation ratio. The inverse participation ratio (IPR)[71] is defined as the second moment of the probability density,

$$\mathrm{IPR}(n\boldsymbol{k}) := \sum_{i=1}^{N}\left(p_i^{(n\boldsymbol{k})}\right)^2, \tag{7}$$

where the sum runs over all N orbitals in a unit cell and $p_i^{(n\boldsymbol{k})}$ is the occupation probability of the orbital i for the state $|n\boldsymbol{k}\rangle$ given by

$$p_i^{(n\boldsymbol{k})} := |\langle\, i \,|\, n\boldsymbol{k}\,\rangle|^2. \tag{8}$$

Since we are first of all interested in the delocalization with respect to π-orbitals we introduce the projected IPR that measures only the delocalization within a certain subsystem $S \subseteq \mathrm{WO}$ (e.g. all π-orbitals), but is insensitive to all other contributions (e.g. from σ-orbitals). The projected S-IPR is defined in analogy to the general IPR with (renormalized) probabilities $\tilde{p}_i^{(n\boldsymbol{k})}$

$$S\text{-IPR}(n\boldsymbol{k}) = \sum_{i\in S} \left(\tilde{p}_i^{(n\boldsymbol{k})}\right)^2, \tag{9}$$

with

$$\tilde{p}_i^{(n\boldsymbol{k})} = \frac{p_i^{(n\boldsymbol{k})}}{\sum_{j\in S} p_j^{(n\boldsymbol{k})}}. \tag{10}$$

$\tilde{p}_i^{(n\boldsymbol{k})}$ is the normalized projected probability with $\sum_{i\in S} \tilde{p}_i^{(n\boldsymbol{k})} = 1$.

For the actual calculation we create a real-space $29 \times 29 \times 1$ supercell for 1Ph COFs and a $23 \times 23 \times 1$ supercell for 2Ph COFs and add Anderson onsite disorder. The disorder is generated from a uniform distribution of random numbers in the interval $[-W/2, W/2]$, where W is the strength of the disorder. A direct diagonalization using the LAPACK library[86] is performed to get eigenstates and eigen-energies at the Γ-point of the supercell. The (projected) IPR are calculated for every eigenstate and inversion provides the participation ratio for every state. The results are independent of the actual realizations of random numbers, which we tested by applying different seeds of the random number generator. Successful examples, where the IPR has been used in conjunction with Anderson disorder can be found in the literature[87].

Data availability

The data that support the findings of this study are available from the corresponding author upon reasonable request.

Received: 27 September 2022; Accepted: 16 January 2023
Published online: 30 January 2023

References

1. Feng, X., Ding, X. & Jiang, D. Covalent organic frameworks. *Chem. Soc. Rev.* **41**, 6010–6022 (2012).
2. Diercks, C. S. & Yaghi, O. M. The atom, the molecule, and the covalent organic framework. *Science* **355**, eaal1585 (2017).
3. Geng, K. *et al.* Covalent organic frameworks: Design, synthesis, and functions. *Chem. Rev.* **120**, 8814–8933. https://doi.org/10.1021/acs.chemrev.9b00550 (2020).
4. Côté, A. P. *et al.* Porous, crystalline, covalent organic frameworks. *Science* **310**, 1166–1170 (2005).
5. Kuhn, P., Antonietti, M. & Thomas, A. Porous, covalent triazine-based frameworks prepared by ionothermal synthesis. *Angew. Chem. Int. Ed.* **47**, 3450–3453. https://doi.org/10.1002/anie.200705710 (2008).
6. Spitler, E. L. & Dichtel, W. R. Lewis acid-catalysed formation of two-dimensional phthalocyanine covalent organic frameworks. *Nat. Chem.* **2**, 672–677. https://doi.org/10.1038/nchem.695 (2010).
7. Zhang, W. *et al.* Reconstructed covalent organic frameworks. *Nature* **604**, 72–79 (2022).
8. Jin, S. *et al.* Large pore donor–acceptor covalent organic frameworks. *Chem. Sci.* **4**, 4505–4511. https://doi.org/10.1039/C3SC52034J (2013).
9. Riaño, A. *et al.* An expanded 2d fused aromatic network with 90-ring hexagons. *Angew. Chem. Int. Ed.* **61**, e202113657 (2022).
10. Mu, Z. *et al.* Covalent organic frameworks with record pore apertures. *J. Am. Chem. Soc.* **144**, 5145–5154 (2022).
11. Ding, S.-Y. & Wang, W. Covalent organic frameworks (COFS): From design to applications. *Chem. Soc. Rev.* **42**, 548–568 (2013).
12. Xu, H. *et al.* Catalytic covalent organic frameworks via pore surface engineering. *Chem. Commun.* **50**, 1292–1294 (2014).
13. Yang, Y. & Börjesson, K. Electroactive covalent organic frameworks: A new choice for organic electronics. *Trends Chem.* **20**, 20 (2021).
14. Auras, F. *et al.* Synchronized offset stacking: A concept for growing large-domain and highly crystalline 2d covalent organic frameworks. *J. Am. Chem. Soc.* **138**, 16703–16710 (2016).
15. Galeotti, G. *et al.* Synthesis of mesoscale ordered two-dimensional π-conjugated polymers with semiconducting properties. *Nat. Mater.* **19**, 874–880 (2020).
16. Barreteau, C., Ducastelle, F. & Mallah, T. A bird's eye view on the flat and conic band world of the honeycomb and Kagome lattices: Towards an understanding of 2d metal-organic frameworks electronic structure. *J. Phys. Condens. Matter* **29**, 465302 (2017).
17. Springer, M. A., Liu, T.-J., Kuc, A. & Heine, T. Topological two-dimensional polymers. *Chem. Soc. Rev.* **49**, 2007–2019. https://doi.org/10.1039/C9CS00893D (2020).
18. Jiang, W., Ni, X. & Liu, F. Exotic topological bands and quantum states in metal-organic and covalent-organic frameworks. *Acc. Chem. Res.* **54**, 416–426. https://doi.org/10.1021/acs.accounts.0c00652 (2021).
19. Ni, X., Li, H., Liu, F. & Brédas, J.-L. Engineering of flat bands and dirac bands in two-dimensional covalent organic frameworks (COFS): Relationships among molecular orbital symmetry, lattice symmetry, and electronic-structure characteristics. *Mater. Horiz.* **9**, 88–98. https://doi.org/10.1039/D1MH00935D (2022).
20. Guo, J. *et al.* Conjugated organic framework with three-dimensionally ordered stable structure and delocalized π clouds. *Nat. Commun.* **4**, 2736 (2013).
21. Pauling, L. & Wheland, G. W. The nature of the chemical bond. V. The quantum-mechanical calculation of the resonance energy of benzene and naphthalene and the hydrocarbon free radicals. *J. Chem. Phys* **1**, 362–374 (1933).
22. Slayden, S. W. & Liebman, J. F. The energetics of aromatic hydrocarbons: An experimental thermochemical perspective. *Chem. Rev.* **101**, 1541–1566 (2001).
23. Dewar, M. & Schmeising, H. A re-evaluation of conjugation and hyperconjugation: The effects of changes in hybridisation on carbon bonds. *Tetrahedron* **5**, 166–178 (1959).
24. Pedley, J., Naylor, R., Kirby, S. & Francis, P. *Thermochemical Data of Organic Compounds* 2nd edn, xi+ 791 (Chapman and Hall, 1987) (**isbn 0-412-27100-1**).
25. Cyrański, M. K. Energetic aspects of cyclic pi-electron delocalization: Evaluation of the methods of estimating aromatic stabilization energies. *Chem. Rev.* **105**, 3773–3811 (2005).
26. Giambiagi, M., de Giambiagi, M. S. & Mundim, K. C. Definition of a multicenter bond index. *Struct. Chem.* **1**, 423–427 (1990).
27. Giambiagi, M., de Giambiagi, M. S., dos Santos Silva, C. D. & de Figueiredo, A. P. Multicenter bond indices as a measure of aromaticity. *Phys. Chem. Chem. Phys.* **2**, 3381–3392. https://doi.org/10.1039/B002009P (2000).
28. Bird, C. A new aromaticity index and its application to five-membered ring heterocycles. *Tetrahedron* **41**, 1409–1414 (1985).
29. Matito, E., Duran, M. & Solà, M. The aromatic fluctuation index (flu): A new aromaticity index based on electron delocalization. *J. Chem. Phys.* **122**, 014109 (2005).

30. Yu, D. *et al.* Aromaticity and antiaromaticity of substituted fulvene derivatives: Perspectives from the information-theoretic approach in density functional reactivity theory. *Phys. Chem. Chem. Phys.* **19**, 18635–18645 (2017).
31. Schleyer, P. V. R., Maerker, C., Dransfeld, A., Jiao, H. & van Eikema Hommes, N. J. Nucleus-independent chemical shifts: A simple and efficient aromaticity probe. *J. Am. Chem. Soc.* **118**, 6317–6318 (1996).
32. Chen, Z., Wannere, C. S., Corminboeuf, C., Puchta, R. & Schleyer, P. V. R. Nucleus-independent chemical shifts (NICS) as an aromaticity criterion. *Chem. Rev.* **105**, 3842–3888. https://doi.org/10.1021/cr030088+ (2005).
33. Gershoni-Poranne, R. & Stanger, A. Magnetic criteria of aromaticity. *Chem. Soc. Rev.* **44**, 6597–6615 (2015).
34. Stanger, A. Nics—past and present. *Eur. J. Org. Chem.* **2020**, 3120–3127 (2020).
35. Gutzler, R. Band-structure engineering in conjugated 2d polymers. *Phys. Chem. Chem. Phys.* **18**, 29092–29100 (2016).
36. Pham, H. Q., Le, D. Q., Pham-Tran, N.-N., Kawazoe, Y. & Nguyen-Manh, D. Electron delocalization in single-layer phthalocyanine-based covalent organic frameworks: A first principle study. *RSC Adv.* **9**, 29440–29447 (2019).
37. Mahmood, J. *et al.* Fused aromatic network with exceptionally high carrier mobility. *Adv. Mater.* **33**, 2004707 (2021).
38. Liu, J. *et al.* Solution synthesis of semiconducting two-dimensional polymer via trimerization of carbonitrile. *J. Am. Chem. Soc.* **139**, 11666–11669 (2017).
39. Evans, A. M. *et al.* Emissive single-crystalline boroxine-linked colloidal covalent organic frameworks. *J. Am. Chem. Soc.* **141**, 19728–19735. https://doi.org/10.1021/jacs.9b08815 (2019).
40. Rizzo, D. J. *et al.* Revealing the local electronic structure of a single-layer covalent organic framework through electronic decoupling. *Nano Lett.* **20**, 963–970 (2020).
41. Yu, S.-Y. *et al.* Direct conversion of aromatic amides into crystalline covalent triazine frameworks by a condensation mechanism. *Cell Rep. Phys. Sci.* **2**, 100653 (2021).
42. Martin, R. M. *Electronic Structure: Basic Theory and Practical Methods* (Cambridge University Press, 2004).
43. Peeks, M. D., Claridge, T. D. & Anderson, H. L. Aromatic and antiaromatic ring currents in a molecular nanoring. *Nature* **541**, 200–203 (2017).
44. Peeks, M. D., Jirasek, M., Claridge, T. D. W. & Anderson, H. L. Global aromaticity and antiaromaticity in porphyrin nanoring anions. *Angew. Chem. Int. Ed.* **58**, 15717–15720 (2019).
45. Rickhaus, M. *et al.* Global aromaticity at the nanoscale. *Nat. Chem.* **12**, 236–241 (2020).
46. Gershoni-Poranne, R. & Stanger, A. The NICS-XY-scan: Identification of local and global ring currents in multi-ring systems. *Eur. J. Chem.* **20**, 5673–5688 (2014).
47. Stanger, A., Monaco, G. & Zanasi, R. Nics-XY-scan predictions of local, semi-global, and global ring currents in annulated pentalene and s-indacene cores compared to first-principles current density maps. *ChemPhysChem* **21**, 65–82 (2020).
48. Fowler, P. W. & Myrvold, W. The, "anthracene problem": Closed-form conjugated-circuit models of ring currents in linear polyacenes. *J. Phys. Chem. A* **115**, 13191–13200 (2011).
49. Bultinck, P. *et al.* Electron delocalization and aromaticity in linear polyacenes: Atoms in molecules multicenter delocalization index. *J. Phys. Chem. A* **110**, 7642–7648 (2006).
50. Gershoni-Poranne, R. Piecing it together: An additivity scheme for aromaticity using Nics-XY scans. *Eur. J. Chem.* **24**, 4165–4172 (2018).
51. Marzari, N. & Vanderbilt, D. Maximally localized generalized Wannier functions for composite energy bands. *Phys. Rev. B* **56**, 12847–12865 (1997).
52. Marzari, N., Mostofi, A. A., Yates, J. R., Souza, I. & Vanderbilt, D. Maximally localized Wannier functions: Theory and applications. *Rev. Mod. Phys.* **84**, 1419–1475 (2012).
53. Souza, I., Marzari, N. & Vanderbilt, D. Maximally localized Wannier functions for entangled energy bands. *Phys. Rev. B* **65**, 035109 (2001).
54. Hamann, D. R. & Vanderbilt, D. Maximally localized Wannier functions for GW quasiparticles. *Phys. Rev. B* **79**, 045109 (2009).
55. Wang, X., Yates, J. R., Souza, I. & Vanderbilt, D. Ab initio calculation of the anomalous hall conductivity by Wannier interpolation. *Phys. Rev. B* **74**, 195118 (2006).
56. Thomas, S. *et al.* Electronic structure of two-dimensional π-conjugated covalent organic frameworks. *Chem. Mater.* **31**, 3051–3065. https://doi.org/10.1021/acs.chemmater.8b04986 (2019).
57. Meng, Z., Stolz, R. M. & Mirica, K. A. Two-dimensional chemiresistive covalent organic framework with high intrinsic conductivity. *J. Am. Chem. Soc.* **141**, 11929–11937 (2019).
58. Sahabudeen, H. *et al.* Wafer-sized multifunctional polyimine-based two-dimensional conjugated polymers with high mechanical stiffness. *Nat. Commun.* **7**, 13461. https://doi.org/10.1038/ncomms13461 (2016).
59. Rotter, J. M. *et al.* Highly conducting Wurster-type twisted covalent organic frameworks. *Chem. Sci.* **11**, 12843–12853. https://doi.org/10.1039/D0SC03909H (2020).
60. Wang, M. *et al.* High-mobility semiconducting two-dimensional conjugated covalent organic frameworks with p-type doping. *J. Am. Chem. Soc.* **142**, 21622–21627. https://doi.org/10.1021/jacs.0c10482 (2020).
61. Li, H., Li, H., Xun, S. & Brédas, J.-L. Doping modulation of the charge injection barrier between a covalent organic framework monolayer and graphene. *Chem. Mater.* **32**, 9228–9237. https://doi.org/10.1021/acs.chemmater.0c02913 (2020).
62. Ghosh, R. & Paesani, F. Unraveling the effect of defects, domain size, and chemical doping on photophysics and charge transport in covalent organic frameworks. *Chem. Sci.* **12**, 8373–8384. https://doi.org/10.1039/D1SC01262B (2021).
63. Brédas, J. L., Street, G. B., Thémans, B. & André, J. M. Organic polymers based on aromatic rings (polyparaphenylene, polypyrrole, polythiophene): Evolution of the electronic properties as a function of the torsion angle between adjacent rings. *J. Chem. Phys.* **83**, 1323–1329. https://doi.org/10.1063/1.449450 (1985).
64. Lörtscher, E. *et al.* Charge transport through molecular rods with reduced π-conjugation. *ChemPhysChem* **9**, 2252–2258. https://doi.org/10.1002/cphc.200800388 (2008).
65. Liu, C. *et al.* A unified understanding of charge transport in organic semiconductors: The importance of attenuated delocalization for the carriers. *Mater. Horiz.* **4**, 608–618. https://doi.org/10.1039/C7MH00091J (2017).
66. Merkel, K., Panhans, M., Hutsch, S. & Ortmann, F. Interplay of band occupation, localization, and polaron renormalization for electron transport in molecular crystals: Naphthalene as a case study. *Phys. Rev. B* **105**, 165136. https://doi.org/10.1103/PhysRevB.105.165136 (2022).
67. Fan, Z. *et al.* Linear scaling quantum transport methodologies. *Phys. Rep.* **903**, 1–69 (2021).
68. Amini, M., Jafari, S. A. & Shahbazi, F. Anderson transition in disordered graphene. *EPL (Europhysics Letters)* **87**, 37002. https://doi.org/10.1209/0295-5075/87/37002 (2009).
69. Xiong, S.-J. & Xiong, Y. Anderson localization of electron states in graphene in different types of disorder. *Phys. Rev. B* **76**, 214204. https://doi.org/10.1103/PhysRevB.76.214204 (2007).
70. Das Sarma, S., Adam, S., Hwang, E. H. & Rossi, E. Electronic transport in two-dimensional graphene. *Rev. Mod. Phys.* **83**, 407–470. https://doi.org/10.1103/RevModPhys.83.407 (2011).
71. Kramer, B. & MacKinnon, A. Localization: Theory and experiment. *Rep. Prog. Phys.* **56**, 1469–1564 (1993).
72. Soriano, D., Ortmann, F. & Roche, S. Three-dimensional models of topological insulators: Engineering of dirac cones and robustness of the spin texture. *Phys. Rev. Lett.* **109**, 266805. https://doi.org/10.1103/PhysRevLett.109.266805 (2012).
73. Calixto, M. & Romera, E. Inverse participation ratio and localization in topological insulator phase transitions. *J. Stat. Mech. Theory Exp.* **2015**, P06029 (2015).

74. Smith, B. J. *et al.* Colloidal covalent organic frameworks. *ACS Central Sci.* **3**, 58–65. https://doi.org/10.1021/acscentsci.6b00331 (2017).
75. Ou, Z. *et al.* Oriented growth of thin films of covalent organic frameworks with large single-crystalline domains on the water surface. *J. Am. Chem. Soc.* **144**, 3233–3241. https://doi.org/10.1021/jacs.1c13195 (2022).
76. Gaul, C. *et al.* Insight into doping efficiency of organic semiconductors from the analysis of the density of states in n-doped c60 and znpc. *Nat. Mater.* **17**, 439–444 (2018).
77. Fernandez, I. *Aromaticity: Modern Computational Methods and Applications* (Elsevier, 2021).
78. Kresse, G. & Furthmüller, J. Efficiency of ab-initio total energy calculations for metals and semiconductors using a plane-wave basis set. *Comput. Mater. Sci.* **6**, 15–50 (1996).
79. Kresse, G. & Furthmüller, J. Efficient iterative schemes for ab initio total-energy calculations using a plane-wave basis set. *Phys. Rev. B* **54**, 11169–11186 (1996).
80. Blöchl, P. Projector augmented-wave method. *Phys. Rev. B* **50**, 17953 (1994).
81. Kresse, G. & Joubert, D. From ultrasoft pseudopotentials to the projector augmented-wave method. *Phys. Rev. B* **59**, 1758 (1999).
82. Pizzi, G. *et al.* Wannier90 as a community code: New features and applications. *J. Phys. Condens. Matter* **32**, 165902 (2020).
83. Frisch, M. J. *et al. Gaussian-16 Revision C.01* (Gaussian Inc, 2016).
84. Lee, C., Yang, W. & Parr, R. G. Development of the Colle–Salvetti correlation-energy formula into a functional of the electron density. *Phys. Rev. B* **37**, 785–789 (1988).
85. Becke, A. Density-functional thermochemistry. III. The role of exact exchange (1993).
86. Anderson, E. *et al. LAPACK Users' guide* (SIAM, 1999).
87. Murphy, N. C., Wortis, R. & Atkinson, W. A. Generalized inverse participation ratio as a possible measure of localization for interacting systems. *Phys. Rev. B* **83**, 184206 (2011).

Acknowledgements

We would like to thank the Deutsche Forschungsgemeinschaft for financial support [CRC1415, projects No. OR 349/1 and No. OR 349/3 and the Cluster of Excellence e-conversion (Grant No. EXC2089)]. Grants for computer time from the Zentrum für Informationsdienste und Hochleistungsrechnen of TU Dresden and the Leibniz Supercomputing Centre in Garching are gratefully acknowledged. K.M. acknowledges M. Dorfner for fruitful discussions.

Author contributions

Initial structure creation and relaxation together with the numerical calculations of NICS values, Wannier functions, electronic structures and IPR values were performed by K.M. Numerical calculations for the evaluation of bond torsion and related measures were carried out by J.G. All authors contributed to the discussion and writing of the paper. F.O. supervised the work.

Funding

Open Access funding enabled and organized by Projekt DEAL.

Competing interests

The authors declare no competing interests.

Additional information

Supplementary Information The online version contains supplementary material available at https://doi.org/10.1038/s41598-023-28285-w.

Correspondence and requests for materials should be addressed to F.O.

Reprints and permissions information is available at www.nature.com/reprints.

Publisher's note Springer Nature remains neutral with regard to jurisdictional claims in published maps and institutional affiliations.

6 Publication: Linear Scaling Approach for Optical Excitations Using Maximally Localized Wannier Functions

Summary:

The calculation of optical properties from first principles is a very challenging task as it involves two-particle states and cannot simply be approximated at the single-particle level. Moreover, many $\boldsymbol{k}$ points are required for converged results (compared to usual calculations of the electronic structure, e.g., with DFT). This makes this type of calculation only feasible for relatively small systems. The established codes that are used for such calculations usually represent the exciton Hamiltonian in a basis of Bloch function similar to Eq. (3.58). This is beneficial since only a minimum number of basis functions is needed which results in a smaller Hamiltonian matrix with minimal rank. However, the representation is in general not sparse. The authors of BerkleyGW particularly emphasized this problem by saying: "[...] It should be pointed out that the kernel matrix is not sparse in general, so methods designed for the diagonalization of sparse matrices are not appropriate here." [65] In fact, the scaling of such an approach is $O(N^3)$ for a full diagonalization of the dense matrix or $O(N^2)$ if a Haydock-Lanczos approach is used.[63, 64, 65, 90, 91]

In the following publication [92] we propose a new method based on maximally localized Wannier functions (MLWF), which is able to evaluate optical properties in linear scaling and is therefore suitable for large systems. MLWFs represent an ideal basis set for the evaluation of excitons since they are strongly localized and at the same time require only a minimal number of basis functions to represent the electronic structure, i.e., the number of Wannier functions per unit cell is equal to the number of bands. Numerically, the Hamiltonian matrix in the basis of MLWF has therefore the same dimensions as in a basis of Bloch function. This would not be the case for other localized basis sets like a Gaussian basis set where hundreds or thousands of basis functions would be required to represent a single Bloch state and the resulting matrix would be correspondingly larger. In contrast to a Bloch basis, the resulting exciton Hamiltonian becomes sparse due to the strong localization of the MLWF and can therefore be solved very efficiently with linear scaling algorithms.

Moreover, the interaction between electrons and holes, which is included in the exciton Hamiltonian, can be efficiently evaluated using MLWF in real space. This is due to the fact that we only need to calculate the interaction between strongly localized (overlap) densities. Due to the strong localization, we can treat large electron-hole distances in a multipole expansion, which improves the computational efficiency. Furthermore, since the overlap between two MLWFs decreases exponentially, there is only a finite number of overlap densities and thus only a finite number of Coulomb integrals that need to be solved. We were able to show that the total number of Coulomb integrals which needs to be calculated in full detail saturates very quickly and becomes independent of the number of $\boldsymbol{k}$-points in the simulation (see Fig. 4 in [92]). This means that once all Coulomb integrals are evaluated, we can calculate the optical properties at any $\boldsymbol{k}$ resolution without solving additional integrals.

We demonstrate the approach for silicon, one of the most commonly used reference systems, and were able to show that the method is able to reproduce the experimental spectrum.

Individual contribution:

K.M. developed and implemented the method, which involved calculating the Coulomb integrals and numerically solving the exciton Hamiltonian in the basis of MLWF. Electronic structure calculations and cal-

culations of Wannier functions were also carried out by K.M. F.O. supervised the project. All authors contributed in writing the manuscript.

IOP Publishing J. Phys. Mater. 7 (2024) 015001 https://doi.org/10.1088/2515-7639/ad06cd

Journal of Physics: Materials

OPEN ACCESS

RECEIVED
6 June 2023

REVISED
13 September 2023

ACCEPTED FOR PUBLICATION
25 October 2023

PUBLISHED
6 November 2023

PAPER

Linear scaling approach for optical excitations using maximally localized Wannier functions

Konrad Merkel[1,2] **and Frank Ortmann**[1,2,*]

[1] TUM School of Natural Sciences, Technical University of Munich, Munich, Germany
[2] Center for Advancing Electronics Dresden, Technische Universität, Dresden, Germany
[*] Author to whom any correspondence should be addressed.

E-mail: frank.ortmann@tum.de

Keywords: absorption spectra, optical properties, semiconductor, exciton, Coulomb integrals, Wannier function, dielectric function

Abstract

We present a theoretical method for calculating optical absorption spectra based on maximally localized Wannier functions, which is suitable for large periodic systems. For this purpose, we calculate the exciton Hamiltonian, which determines the Bethe–Salpeter equation for the macroscopic polarization function and optical absorption characteristics. The Wannier functions are specific to each material and provide a minimal and therefore computationally convenient basis. Furthermore, their strong localization greatly improves the computational performance in two ways: first, the resulting Hamiltonian becomes very sparse and, second, the electron–hole interaction terms can be evaluated efficiently in real space, where large electron–hole distances are handled by a multipole expansion. For the calculation of optical spectra we employ the sparse exciton Hamiltonian in a time-domain approach, which scales linearly with system size. We demonstrate the method for bulk silicon—one of the most frequently studied benchmark systems—and envision calculating optical properties of systems with much larger and more complex unit cells, which are presently computationally prohibitive.

1. Introduction

Simulations of optical properties such as UV–vis-NIR absorption or reflection spectra are crucial for designing or improving opto-electronic devices with novel materials. In this context, accurate theoretical predictions help to find suitable materials much faster and at lower cost, thus complementing and guiding experimental efforts. However, calculating optical properties is computationally demanding, which limits calculations to small systems with only a few atoms per unit cell. The reason is that optical properties are inherently affected by many-body effects. For example, the optical response of semiconductors and insulators is determined by the Coulomb interaction between electrons and holes in a material, which leads to the formation of bound electron–hole states called excitons [1–3]. For the calculation of optical properties such as UV–vis-NIR absorption spectra it is therefore necessary to describe two-particle states of electrons and holes that are created upon optical excitation. A suitable description of such many-body effects can be derived in terms of a Bethe–Salpeter equation (BSE) [3–10] for the polarization function. For almost all real materials, however this BSE is too difficult to solve. Important simplifications can be obtained for non-spin-polarized systems, where the BSE splits into singlet and triplet parts, which can be treated independently [3]. Optical transitions, described by transition matrix elements that are diagonal in spin space, cannot induce spin-flips, and it is sufficient to calculate the singlet case only, which is already a huge simplification. Furthermore, the singlet-BSE can be rewritten into a generalized eigenvalue problem and further simplified by performing the Tamm–Dancoff approximation for electronically gapped systems [3, 11, 12]. The resulting Hamiltonian matrix is still very large and dense but can in principle be diagonalized for small system sizes using popular simulation packages [13–16]. In addition, very dense $\boldsymbol{k}$-meshes are needed

in order to obtain converged results, a problem that is known from the independent particle picture [17] and which becomes more severe for excitons. This has lead to strategies like the use of hybrid meshes [18, 19], where specific parts of the Brillouin zone are sampled with higher precision. Despite all these works on different computational aspects, it is still challenging to include exciton effects in the calculation of optical absorption spectra, in particular for systems with many atoms per unit cell.

In this paper we present an approach based on maximally localized Wannier functions (MLWF) [20, 21], which can deal with large and/or complex systems. MLWF are directly obtained from underlying quasi-particle wave functions and represent a minimal basis set that is adapted to the specific material. Moreover, they can be obtained for specific bands, e.g. near the band gap, making the calculation independent of the number of atoms in a unit cell. Furthermore, we show that the resulting representation has important computational advantages, namely that the Hamiltonian matrix becomes very sparse, and can therefore be solved very efficiently, thus enabling optical calculations of large systems. For convenience, we use the term linear scaling Wannier optics (LSWO) for the presentation of the entire approach.

2. Theory: optical properties and exciton Hamiltonian

2.1. General formalism

We start from the two-particle eigenvalue problem in Tamm–Dancoff approximation [3, 11, 12],

$$\sum_{v'c'\boldsymbol{k}'} H_{cv\boldsymbol{k},c'v'\boldsymbol{k}'} A^{\Lambda}_{c'v'\boldsymbol{k}'} = E^{\Lambda} A^{\Lambda}_{cv\boldsymbol{k}}, \tag{1}$$

where c and v label the conduction and valence bands, respectively, and A describes the exciton amplitude. The crystal momentum $\boldsymbol{k}$ is the same for electron and hole because only vertical excitations are considered in the optical limit. The hermitian singlet-exciton Hamiltonian H is given by

$$H_{cv\boldsymbol{k},c'v'\boldsymbol{k}'} = \left[E_c^{\text{cond.}}(\boldsymbol{k}) - E_v^{\text{val.}}(\boldsymbol{k})\right]\delta_{cc'}\delta_{vv'}\delta_{\boldsymbol{k}\boldsymbol{k}'} - H^{\text{SC}}_{cv\boldsymbol{k},c'v'\boldsymbol{k}'} + 2H^{\text{LFE}}_{cv\boldsymbol{k},c'v'\boldsymbol{k}'} \tag{2}$$

and consists of effective single-particle contributions from conduction and valence band structures (first term), which are diagonal with respect to $\boldsymbol{k}$, and two-particle contributions from screened electron–hole interactions H^{SC} and local field effects (LFEs) H^{LFE}, which couple different $\boldsymbol{k}$ and $\boldsymbol{k}'$ via Coulomb interaction. While the occurrence of a screened electron–hole interaction is intuitively plausible, the LFEs term seems less obvious and some comments are appropriate. LFE arise when the system is inhomogeneous on the microscopic scale, i.e. the microscopic dielectric function $\epsilon_{\boldsymbol{G}\boldsymbol{G}'}$ is not diagonal with respect to reciprocal lattice vectors $\boldsymbol{G}$ [22–24]. By including LFE in the Hamiltonian, it is ensured that one can later calculate the macroscopic rather than the microscopic dielectric tensor directly from E^{Λ} and A^{Λ}. Note that the LFE matrix elements are in the form of electron–hole pair exchange interactions [25].

H^{SC} and H^{LFE} can be obtained from single-particle Bloch functions for conduction $\phi_{c\boldsymbol{k}}(\boldsymbol{x})$ and valence states $\phi_{v\boldsymbol{k}}(\boldsymbol{x})$. A natural choice for $\phi_{c\boldsymbol{k}}(\boldsymbol{x})$ and $\phi_{v\boldsymbol{k}}(\boldsymbol{x})$ are Kohn–Sham orbitals leading to

$$H^{\text{SC}}_{cv\boldsymbol{k},c'v'\boldsymbol{k}'} = \int \mathrm{d}^3x \int \mathrm{d}^3x'\, \phi^*_{c\boldsymbol{k}}(\boldsymbol{x})\, \phi^*_{v'\boldsymbol{k}'}(\boldsymbol{x}')\, W(\boldsymbol{x}-\boldsymbol{x}')\, \phi_{v\boldsymbol{k}}(\boldsymbol{x}')\, \phi_{c'\boldsymbol{k}'}(\boldsymbol{x}), \tag{3}$$

$$H^{\text{LFE}}_{cv\boldsymbol{k},c'v'\boldsymbol{k}'} = \int \mathrm{d}^3x \int \mathrm{d}^3x'\, \phi^*_{c\boldsymbol{k}}(\boldsymbol{x})\, \phi^*_{v'\boldsymbol{k}'}(\boldsymbol{x}') \left[\frac{1}{\Omega}\sum_{\boldsymbol{G}\neq 0} \tilde{V}(|\boldsymbol{G}|)\, \mathrm{e}^{\mathrm{i}\boldsymbol{G}(\boldsymbol{x}-\boldsymbol{x}')}\right] \phi_{v\boldsymbol{k}}(\boldsymbol{x})\, \phi_{c'\boldsymbol{k}'}(\boldsymbol{x}'), \tag{4}$$

where $W(\boldsymbol{x}-\boldsymbol{x}')$ is the screened Coulomb interaction and $\tilde{V}(|\boldsymbol{q}+\boldsymbol{G}|) = \frac{4\pi e^2}{\epsilon_0}\frac{1}{|\boldsymbol{q}+\boldsymbol{G}|^2}$ is the Fourier transformed bare Coulomb potential. We emphasize that arbitrary screening functions can be used here. The possible choices include functions from many-body perturbation theory (e.g. from GW calculations), model screening functions or just a constant relative permittivity. Here, as an example, we use a model dielectric function $\epsilon^{-1}(\boldsymbol{q}) = 1 - (\eta + \alpha q^2/q_{\text{TF}}^2)^{-1}$ that has been shown to yield good results for typical semiconductors [26]. The parameter $\eta = (1-\epsilon_\infty^{-1})^{-1}$ with the electronic dielectric constant ϵ_∞ of the material, and q_{TF} is the Thomas–Fermi wave vector. The dimensionless parameter $\alpha = 1.563$ has been shown to be rather universal [26]. The screened Coulomb potential is then obtained from $W(\boldsymbol{q}) = \epsilon^{-1}(\boldsymbol{q})\tilde{V}(\boldsymbol{q})$. We assume a static screening, i.e. no time dependence, which is the most frequent approach. However, we note that current

efforts also investigate extensions to the frequency dependence of screening [27, 28]. By taking the Fourier transform we obtain the corresponding potential in real space,

$$W(\boldsymbol{x}-\boldsymbol{x}') = \frac{1}{4\pi\,\epsilon_0\epsilon_\infty|\boldsymbol{x}-\boldsymbol{x}'|} + \left(1-\epsilon_\infty^{-1}\right)\frac{\exp\left[\frac{-q_{\mathrm{TF}}|\boldsymbol{x}-\boldsymbol{x}'|}{\sqrt{\left(1-\epsilon_\infty^{-1}\right)\alpha}}\right]}{4\pi\,\epsilon_0|\boldsymbol{x}-\boldsymbol{x}'|} = V_{\mathrm{scr}}\left(|\boldsymbol{x}-\boldsymbol{x}'|\right) + \left(1-\epsilon_\infty^{-1}\right)V_{\mathrm{Yuk}}\left(|\boldsymbol{x}-\boldsymbol{x}'|\right), \tag{5}$$

which is the superposition of a screened Coulomb and a Yukawa potential. A more detailed derivation can be found in section B of the appendix.

Independently of the type of screening, the numerical evaluation of equation (1) can be quite expensive because a very fine $\boldsymbol{k}$-mesh is usually required to obtain converged results and the Hamiltonian matrix that needs to be diagonalized is very large and, in general, a dense matrix. Furthermore, the underlying Bloch functions, that are needed for the evaluation of equations (3) and (4), are delocalized which leads to additional challenges for numerical calculations. These obstacles are circumvented by transforming above equations into a localized basis of Wannier functions (WFs) which will be explained here below.

2.2. Exciton-Hamiltonian in basis of MLWF

For an efficient treatment of the exciton problem in equation (1), it is advantageous to employ a localized basis of MLWF $w_{m\boldsymbol{R}}(\boldsymbol{x})$. MLWF are routinely used to investigate single-particle observables [21, 29] and have been shown to be advantageous for many-body first-principles calculations, including electron–electron interactions and screening [30, 31], spin excitations [32] or quadratic optical response [33]. They are directly related to the underlying Bloch functions $\phi_{n\boldsymbol{k}}(\boldsymbol{x})$ by the transformation,

$$w_{m\boldsymbol{R}}\left(\boldsymbol{x}\right) := \frac{1}{\sqrt{N_\Omega}}\sum_{n\boldsymbol{k}} \mathrm{e}^{-\mathrm{i}\boldsymbol{k}\boldsymbol{R}} U_{mn}\left(\boldsymbol{k}\right)\phi_{n\boldsymbol{k}}\left(\boldsymbol{x}\right), \tag{6}$$

where $\boldsymbol{R}$ represents a unit cell vector and $U(\boldsymbol{k})$ is a unitary matrix. It can be chosen such that the obtained WFs are maximally localized, i.e. their spread $\left[\langle\boldsymbol{x}^2\rangle - \langle\boldsymbol{x}\rangle^2\right]$ is minimal. To be more precise, $U(\boldsymbol{k})$ disentangles the individual energy bands in case of band crossings or degeneracies and fixes the $\boldsymbol{k}$-dependent gauge phase $\mathrm{e}^{\mathrm{i}\theta(\boldsymbol{k})}$ that each Bloch function has. $U(\boldsymbol{k})$ can be obtained from an optimization algorithm [20, 21] for specific groups of bands, e.g. all valence bands. The obtained MLWF are orthogonal to each other and must be real valued [20]. Owing to translational symmetry, MLWF at different unit cells $\boldsymbol{R}$ have the same shape and are related to each other by $w_{m\boldsymbol{R}}(\boldsymbol{x}) = w_{m0}(\boldsymbol{x}-\boldsymbol{R})$, which is known as shift property.

For the LSWO approach it is advantageous to obtain MLWF for conduction and valence bands near the fundamental band gap separately. Therefore, the obtained MLWF keep the character of either an electron or a hole. We denote them as conduction-WF and valence-WF in the following. Even though the conduction and valence MLWF are obtained separately, they are orthogonal since valence and conduction states are non-degenerate for all $\boldsymbol{k}$-points. Hence, they represent a suitable basis for the excitonic two-particle Hilbert space.

As mentioned above, only a subspace of the two-particle Hilbert space in which electrons and holes have the same momentum is relevant for the calculation of optical properties. This means we need to transform the Bloch representation with the indexes $cv\boldsymbol{k}$ into a real-space description of MLWF with indexes $mn\boldsymbol{S}$. This mapping is achieved by a unitary transformation of the two particle basis using the matrix

$$F_{mn\boldsymbol{S},\,cv\boldsymbol{k}} = \frac{1}{\sqrt{N_\Omega}}\mathrm{e}^{\mathrm{i}\boldsymbol{k}\boldsymbol{S}} U^*_{cm}\left(\boldsymbol{k}\right)U_{nv}\left(\boldsymbol{k}\right), \tag{7}$$

where the U matrices are obtained from Wannier transformations of valence and conduction bands and the unit cell vector $\boldsymbol{S} = \boldsymbol{R} - \boldsymbol{L}$ is the distance between electron unit cell $\boldsymbol{R}$ and hole unit cell $\boldsymbol{L}$. Excitonic wave functions in the optical subspace (i.e. at vanishing photon momentum $\boldsymbol{q} \to 0$) are obtained by

$$\xi_{mn\boldsymbol{S}}\left(\boldsymbol{x},\boldsymbol{x}'\right) = \sum_{cv\boldsymbol{k}} F_{mn\boldsymbol{S},\,cv\boldsymbol{k}}\,\phi^*_{c\boldsymbol{k}}\left(\boldsymbol{x}\right)\phi_{v\boldsymbol{k}}\left(\boldsymbol{x}'\right) = \frac{1}{\sqrt{N_\Omega}}\sum_{\boldsymbol{R}} w_{m\boldsymbol{R}}\left(\boldsymbol{x}\right)w_{n,\boldsymbol{R}-\boldsymbol{S}}\left(\boldsymbol{x}'\right). \tag{8}$$

We have used that MLWF are real and therefore the excitonic wave function fulfills $\xi_{mn\boldsymbol{S}} = \xi^*_{mn\boldsymbol{S}}$. Equation (8) is a manifestation of the convolution theorem in terms of Bloch functions and corresponding MLWF. At this point we should mention that the use of the variable $\boldsymbol{R}$ (electron unit cell) as summation index by no means introduces any asymmetry in the treatment of electrons and holes. The same result can also be expressed by center of mass and relative coordinates. The center of mass motion is not relevant for optics due to translational symmetry of the crystal and only the relative distance $\boldsymbol{S}$ between electron and hole remains in $\xi_{mn\boldsymbol{S}}$.

We also use $F_{mn\boldsymbol{S},cv\boldsymbol{k}}$ to transform equation (1) into the Wannier basis,

$$\sum_{m'n'\boldsymbol{S}'} \tilde{H}_{mn\boldsymbol{S},m'n'\boldsymbol{S}'} B^{\Lambda}_{m'n'\boldsymbol{S}'} = E^{\Lambda} B^{\Lambda}_{mn\boldsymbol{S}}, \tag{9}$$

where the exciton eigenvector is obtained as

$$B^{\Lambda}_{mn\boldsymbol{S}} = \sum_{cv\boldsymbol{k}} F_{mn\boldsymbol{S},cv\boldsymbol{k}} A^{\Lambda}_{cv\boldsymbol{k}} \tag{10}$$

and the exciton Hamiltonian becomes

$$\begin{aligned} \tilde{H}_{mn\boldsymbol{S},m'n'\boldsymbol{S}'} &= \sum_{cv\boldsymbol{k}} \sum_{c'v'\boldsymbol{k}'} F_{mn\boldsymbol{S},cv\boldsymbol{k}} H_{cv\boldsymbol{k},c'v'\boldsymbol{k}'} F^*_{c'v'\boldsymbol{k}',m'n'\boldsymbol{S}'} \\ &= \tilde{H}^{\text{band}}_{mn\boldsymbol{S},m'n'\boldsymbol{S}'} - \tilde{H}^{\text{SC}}_{mn\boldsymbol{S},m'n'\boldsymbol{S}'} + 2\tilde{H}^{\text{LFE}}_{mn\boldsymbol{S},m'n'\boldsymbol{S}'}. \end{aligned} \tag{11}$$

According to equation (2) the single-particle band contributions are obtained as

$$\tilde{H}^{\text{band}}_{mn\boldsymbol{S},m'n'\boldsymbol{S}'} = H^{\text{cond.}}_{m'm}\left(\boldsymbol{S}-\boldsymbol{S}'\right)\delta_{nn'} - H^{\text{val.}}_{nn'}\left(\boldsymbol{S}-\boldsymbol{S}'\right)\delta_{mm'}, \tag{12}$$

where $H^{\text{cond.}}_{m'm}(\boldsymbol{S}-\boldsymbol{S}')$ and $H^{\text{val.}}_{nn'}(\boldsymbol{S}-\boldsymbol{S}')$ are the single-particle Wannier Hamiltonians for conduction and valence bands, respectively. They are directly accessible from the Wannier transformation of the first-principles electronic structure [20, 21].

The screened electron–hole interaction can be obtained by virtue of equation (8) and by applying the shift property of MLWF (see appendix),

$$\begin{aligned} \tilde{H}^{\text{SC}}_{mn\boldsymbol{S},m'n'\boldsymbol{S}'} &= \int \mathrm{d}^3x \int \mathrm{d}^3x'\, \xi_{mn\boldsymbol{S}}(\boldsymbol{x},\boldsymbol{x}')\, W(\boldsymbol{x}-\boldsymbol{x}')\, \xi_{m'n'\boldsymbol{S}'}(\boldsymbol{x},\boldsymbol{x}') \\ &= \sum_{\boldsymbol{A}} \tilde{W}^{mm'}_{nn'}\left(\boldsymbol{A},\boldsymbol{S},\boldsymbol{S}'\right), \end{aligned} \tag{13}$$

with the general Coulomb matrix elements

$$\begin{aligned} \tilde{W}^{mm'}_{nn'}\left(\boldsymbol{A},\boldsymbol{S},\boldsymbol{S}'\right) &= \int \mathrm{d}^3x \int \mathrm{d}^3x'\, w_{m0}(\boldsymbol{x})\, w_{m'\boldsymbol{A}}(\boldsymbol{x})\, W(\boldsymbol{x}-\boldsymbol{x}')\, w_{n',\boldsymbol{A}-\boldsymbol{S}'}(\boldsymbol{x}')\, w_{n,-\boldsymbol{S}}(\boldsymbol{x}') \\ &= \tilde{W}^{m'm}_{n'n}\left(-\boldsymbol{A},\boldsymbol{S}',\boldsymbol{S}\right), \end{aligned} \tag{14}$$

which depend on three different unit cell vectors (corresponding to three $\boldsymbol{k}$-vectors in reciprocal space). $\tilde{H}^{\text{SC}}_{mn\boldsymbol{S},m'n'\boldsymbol{S}'}$ only depends on two unit cell vectors because electrons and holes have the same momentum. For a more intuitive and physically comprehensible description, we introduce the unit cell vectors $\boldsymbol{R}_c$, $\boldsymbol{R}_v$, and $\boldsymbol{R}_D$, which correspond to the relative shifts between conduction WFs, between valence WFs, and to the electron–hole distance, respectively. We substitute $\boldsymbol{A} = \boldsymbol{R}_c$, $\boldsymbol{S} = -\boldsymbol{R}_D$ and $\boldsymbol{S}' = -\boldsymbol{R}_D + \boldsymbol{R}_c - \boldsymbol{R}_v$ in equation (14) and use the shift property of MLWF to obtain

$$\begin{aligned} &\tilde{W}^{mm'}_{nn'}\left(\boldsymbol{A}=\boldsymbol{R}_c, \boldsymbol{S}=-\boldsymbol{R}_D, \boldsymbol{S}'=-\boldsymbol{R}_D+\boldsymbol{R}_c-\boldsymbol{R}_v\right) \\ &\quad = W^{mm'}_{nn'}\left(\boldsymbol{R}_c,\boldsymbol{R}_v,\boldsymbol{R}_D\right) = \int \mathrm{d}^3x \int \mathrm{d}^3x'\, \rho_{mm'\boldsymbol{R}_c}(\boldsymbol{x})\, W(\boldsymbol{x}-\boldsymbol{x}'-\boldsymbol{R}_D)\, \rho_{nn'\boldsymbol{R}_v}(\boldsymbol{x}'), \end{aligned} \tag{15}$$

where $\rho_{mm'\boldsymbol{R}_c}(\boldsymbol{x}) = w_{m0}(\boldsymbol{x}) w_{m'\boldsymbol{R}_c}(\boldsymbol{x})$ and $\rho_{nn'\boldsymbol{R}_v}(\boldsymbol{x}) = w_{n0}(\boldsymbol{x}) w_{n'\boldsymbol{R}_v}(\boldsymbol{x})$ are (overlap) densities of two electrons and (overlap) densities of two holes, respectively.

Before we come to the integration strategy in section 3, we comment on the distance dependence of these matrix elements. Since the overlap between two different MLWF is exponentially suppressed with increasing distance, it is clear that the overlap densities vanish for large values of $\boldsymbol{R}_c$ and $\boldsymbol{R}_v$. Therefore, the corresponding Coulomb integrals equation (15) also vanish rapidly for large displacements $\boldsymbol{R}_c$ or $\boldsymbol{R}_v$. This substantially reduces the number of calculations required and constitutes a significant advantage over a plane

wave basis set. In contrast, $\boldsymbol{R}_D$ is associated with long-range Coulomb interactions, which always yields contributions that decay very slowly. Substituting back the original variables $\boldsymbol{S}$, $\boldsymbol{S}'$, and $\boldsymbol{A}$, we see that finite Coulomb integrals contribute only to matrix elements $\tilde{H}^{\mathrm{SC}}_{mn\boldsymbol{S},m'n'\boldsymbol{S}'}$ near the diagonal and $\boldsymbol{R}_D$ corresponds to the position along the diagonal. The matrix representation is therefore very sparse. This is a great advantage for numerical computations, since diagonalization or alternative treatments can be performed very efficiently and with low memory requirements. It is thus not surprising that other localized basis sets leading to sparse representations of Coulomb interactions have shown large performance advantages for GW calculations in the past [34, 35]. The diagonal elements for which $m = m'$, $n = n'$, and $\boldsymbol{R}_c = \boldsymbol{R}_v = 0$ (or alternatively $\boldsymbol{A} = 0$ and $\boldsymbol{S} = \boldsymbol{S}' = -\boldsymbol{R}_D$) are expected to yield the largest contributions to $\tilde{H}^{\mathrm{SC}}$. They represent interactions of classical charge densities with total charge of one, because MLWF are normalized. The non-diagonal elements of $\tilde{H}^{\mathrm{SC}}$ correspond to interactions where at least one density is an overlap density, i.e. $\rho_{mm'\boldsymbol{R}_c}$ or $\rho_{nn'\boldsymbol{R}_v}$ contains two different MLWF. Such overlap densities have zero total charge because MLWF are orthogonal. We therefore expect the non-diagonal elements to be significantly smaller. Finally, contributions from LFE, equation (4), are calculated in analogy to equation (13),

$$\begin{aligned}\tilde{H}^{\mathrm{LFE}}_{mn\boldsymbol{S},m'n'\boldsymbol{S}'} &= \int \mathrm{d}^3x \int \mathrm{d}^3x'\, \xi_{mn\boldsymbol{S}}(\boldsymbol{x},\boldsymbol{x})\, \bar{V}(\boldsymbol{x}-\boldsymbol{x}')\, \xi_{m'n'\boldsymbol{S}'}(\boldsymbol{x}',\boldsymbol{x}') \\ &= \int \mathrm{d}^3x \int \mathrm{d}^3x'\, w_{m0}(\boldsymbol{x})\, w_{n,-\boldsymbol{S}}(\boldsymbol{x}) \left[\sum_{\boldsymbol{G}\neq 0} \tilde{V}(|\boldsymbol{G}|)\, \mathrm{e}^{\mathrm{i}\boldsymbol{G}(\boldsymbol{x}-\boldsymbol{x}')}\right] w_{m'0}(\boldsymbol{x}')\, w_{n',-\boldsymbol{S}'}(\boldsymbol{x}')\,. \end{aligned} \tag{16}$$

This matrix is, like $\tilde{H}^{\mathrm{SC}}$, very sparse since the overlap between MLWF is exponentially suppressed with increasing distance. Consequently, only matrix elements with small values $\boldsymbol{S}$ and $\boldsymbol{S}'$, where electron and hole have closest distance, are affected by LFE. In the limiting case of strongly localized WFs only matrix elements with $\boldsymbol{S} = \boldsymbol{S}' = 0$ would contribute. We thus have a complete description of the singlet exciton Hamiltonian in the Wannier basis equation (9) that can be used to calculate optical properties.

2.3. Optical properties

The macroscopic dielectric function $\epsilon^{\mathrm{M}}(\hat{\boldsymbol{q}},\omega)$ could be calculated within the original Bloch representation directly from the solutions of equation (1) and the optical transition matrix elements $M_{cv\boldsymbol{k}}(\hat{\boldsymbol{q}})$ that can be obtained from conduction and valence Bloch functions,

$$M_{cv\boldsymbol{k}}(\hat{\boldsymbol{q}}) = \lim_{\boldsymbol{q}\to 0} \frac{e}{\sqrt{4\pi\epsilon_0}|\boldsymbol{q}|i} \int \mathrm{d}^3x \phi^*_{c\boldsymbol{k}}(\boldsymbol{x})\, \mathrm{e}^{\mathrm{i}\boldsymbol{q}\boldsymbol{x}} \phi_{v\boldsymbol{k}}(\boldsymbol{x})\,. \tag{17}$$

The macroscopic dielectric function is given as [3]

$$\epsilon^{\mathrm{M}}(\hat{\boldsymbol{q}},\omega) = 1 + \frac{4\pi}{\Omega} \sum_{\Lambda} \left| \sum_{cv\boldsymbol{k}} M^*_{cv\boldsymbol{k}}(\hat{\boldsymbol{q}})\, A^{\Lambda}_{cv\boldsymbol{k}} \right|^2 \left[\frac{1}{E^{\Lambda} - \hbar(\omega + i\eta)} + \frac{1}{E^{\Lambda} + \hbar(\omega + i\eta)} \right]. \tag{18}$$

Like in the previous section we transform these expressions into the basis of MLWF by utilizing the matrix $F_{mn\boldsymbol{S},cv\boldsymbol{k}}$ to calculate $\epsilon^{\mathrm{M}}(\hat{\boldsymbol{q}},\omega)$ directly from $B^{\Lambda}_{mn\boldsymbol{S}}$ and corresponding transition matrix elements. The transformation is applied to the scalar product in equation (18),

$$\begin{aligned}\sum_{cv\boldsymbol{k}} M^*_{cv\boldsymbol{k}}(\hat{\boldsymbol{q}})\, A^{\Lambda}_{cv\boldsymbol{k}} &= \sum_{mn\boldsymbol{S}} \sum_{c'v'\boldsymbol{k}'} M^*_{c'v'\boldsymbol{k}'}(\hat{\boldsymbol{q}})\, F^*_{c'v'\boldsymbol{k}',mn\boldsymbol{S}} \sum_{cv\boldsymbol{k}} F_{mn\boldsymbol{S},cv\boldsymbol{k}} A^{\Lambda}_{cv\boldsymbol{k}} \\ &= \sum_{mn\boldsymbol{S}} \tilde{M}^*_{mn\boldsymbol{S}}(\hat{\boldsymbol{q}})\, B^{\Lambda}_{mn\boldsymbol{S}}, \end{aligned} \tag{19}$$

where $\tilde{M}^*_{mn\boldsymbol{S}}(\hat{\boldsymbol{q}}) = \sum_{c'v'\boldsymbol{k}'} M^*_{c'v'\boldsymbol{k}'}(\hat{\boldsymbol{q}}) F^*_{c'v'\boldsymbol{k}',mn\boldsymbol{S}}$ was defined in the last step. Using equation (8) we can rewrite the transition matrix elements in terms of MLWF,

$$\tilde{M}^*_{mn\boldsymbol{S}}(\hat{\boldsymbol{q}}) = \lim_{\boldsymbol{q}\to 0} \frac{ie}{\sqrt{4\pi\epsilon_0}|\boldsymbol{q}|} \frac{1}{\sqrt{N_\Omega}} \sum_{\boldsymbol{R}} \int \mathrm{d}^3x\, w_{m0}(\boldsymbol{x})\, \mathrm{e}^{-\mathrm{i}\boldsymbol{q}(\boldsymbol{x}+\boldsymbol{R})} w_{n,-\boldsymbol{S}}(\boldsymbol{x})\,. \tag{20}$$

Taylor expanding the exponential up to linear order (higher orders are irrelevant in the optical limit $q \to 0$) [36, 37] we get

$$\tilde{M}^*_{mn\boldsymbol{S}}(\hat{\boldsymbol{q}}) = \frac{e\sqrt{N_\Omega}}{\sqrt{4\pi\epsilon_0}} \hat{\boldsymbol{q}} \int \mathrm{d}^3x\, w_{m0}(\boldsymbol{x})\, \boldsymbol{x}\, w_{n,-\boldsymbol{S}}(\boldsymbol{x})\,. \tag{21}$$

From equation (21) we can see that the transition matrix elements are proportional to transition dipole moments, i.e. dipole moments of electron–hole overlap densities, which nicely connects to expectations from finite systems. The evaluation of transition dipole moments does not cause any problems (like one would have with delocalized Bloch functions) since WFs are localized in real space. Finally, the macroscopic dielectric function becomes

$$\epsilon^{\mathrm{M}}(\hat{\boldsymbol{q}},\omega) = 1 + \frac{4\pi}{\Omega}\sum_{\Lambda}\left|\sum_{mnS}\tilde{M}^{*}_{mnS}(\hat{\boldsymbol{q}})\,B^{\Lambda}_{mnS}\right|^{2}\left[\frac{1}{E^{\Lambda}-\hbar(\omega+i\eta)}+\frac{1}{E^{\Lambda}+\hbar(\omega+i\eta)}\right]. \tag{22}$$

With equations (11), (21) and (22) the entire problem is formulated in the Wannier basis. The remaining task is to evaluate all required matrix elements for the screened Coulomb interaction and LFE in this basis, which will be discussed below.

3. Numerical evaluation of two-particle matrix elements and macroscopic dielectric function

3.1. Evaluating Coulomb matrix elements in the basis of MLWF

For the numerical evaluation of the screened Coulomb interaction we insert the model-screened potential equation (5) into equation (15) and evaluate the Coulomb and Yukawa potentials separately,

$$\begin{aligned} W^{mm'}_{nn'}(\boldsymbol{R}_c,\boldsymbol{R}_v,\boldsymbol{R}_D) = &\int \mathrm{d}^3x \int \mathrm{d}^3x'\,\rho_{mm'\boldsymbol{R}_c}(\boldsymbol{x})\,V_{\mathrm{scr}}(|\boldsymbol{x}-\boldsymbol{x}'-\boldsymbol{R}_D|)\,\rho_{nn'\boldsymbol{R}_v}(\boldsymbol{x}') \\ &+\left(1-\epsilon_{\infty}^{-1}\right)\int \mathrm{d}^3x \int \mathrm{d}^3x'\,\rho_{mm'\boldsymbol{R}_c}(\boldsymbol{x})\,V_{\mathrm{Yuk}}(|\boldsymbol{x}-\boldsymbol{x}'-\boldsymbol{R}_D|)\,\rho_{nn'\boldsymbol{R}_v}(\boldsymbol{x}'). \end{aligned} \tag{23}$$

While the integral with the Yukawa potential (second term of equation (23)) can be solved efficiently in reciprocal space, the numerical evaluation of the Coulomb integral (first term of equation (23)) is quite challenging, because the potential diverges in both real and reciprocal space for $\boldsymbol{x}\to 0$ and $\boldsymbol{q}\to 0$. However, the integral is nevertheless finite as can be shown on general grounds. The problem is still complicated by the fact that MLWF are typically obtained numerically from DFT or GW calculations and analytic forms are usually unknown. Strategies to circumvent such issues include expansions of MLWF using spherical harmonics and appropriate radial functions [38, 39], where the Coulomb integrals can be rewritten and partly solved analytically, or attempts to expand MLWF around the origin in $\boldsymbol{k}$-space by a suitable Taylor expansion. While the latter is numerically inconvenient, the expansion in spherical harmonics can provide satisfactory results for simple systems [38], especially when the WFs are expressed in a form of atomic orbitals and only a small number of expansion coefficients are needed. This, however, may not be the case, which means that in general an extreme large set of spherical harmonics becomes necessary, especially when satellite structures far away from the charge center exist. Alternatively, one might consider choosing a different system of functions where the Coulomb integrals can be solved analytically. A well-known example is Gaussian basis functions, which are routinely used in quantum chemistry codes [40]. However, an expansion of MLWF in terms of such basis functions is usually very complicated and requires sophisticated optimization and fitting algorithms. Despite some proof of principle studies [41], there are no commonly available tools to perform such an elaborated task. Here, we want to use a numerical method that yields satisfactory results for all types of MLWF and is easily applicable. This method follows the *ab-initio* philosophy in the sense that we avoid any fitting.

The numerical evaluation of the first term of equation (23) is performed in multiple steps. We start by introducing auxiliary densities $\rho^{\mathrm{aux}}_{mm'\boldsymbol{R}_c}(\boldsymbol{x})$ and $\rho^{\mathrm{aux}}_{nn'\boldsymbol{R}_v}(\boldsymbol{x})$ for each $\rho_{mm'\boldsymbol{R}_c}(\boldsymbol{x})$ and $\rho_{nn'\boldsymbol{R}_v}(\boldsymbol{x})$, respectively. These auxiliary densities are Gaussian functions with the constraint that they have the same charge as the corresponding overlap density, i.e.

$$\int \mathrm{d}^3x\,\rho^{\mathrm{aux}}_{mm'\boldsymbol{R}_c}(\boldsymbol{x}) = \int \mathrm{d}^3x\,\rho_{mm'\boldsymbol{R}_c}(\boldsymbol{x}). \tag{24}$$

The center and variance of each Gaussian function is in general not important, albeit specific choices might be numerically favorable. We continue by adding and subtracting auxiliary densities for each integral and separate four different terms,

$$\int \mathrm{d}^3x \int \mathrm{d}^3x' \left[\rho_{mm'\boldsymbol{R}_c}(\boldsymbol{x}) - \rho^{\mathrm{aux}}_{mm'\boldsymbol{R}_c}(\boldsymbol{x}) + \rho^{\mathrm{aux}}_{mm'\boldsymbol{R}_c}(\boldsymbol{x})\right] \times V_{\mathrm{scr}}(\boldsymbol{x}-\boldsymbol{x}'-\boldsymbol{R}_D)\left[\rho_{nn'\boldsymbol{R}_v}(\boldsymbol{x}') - \rho^{\mathrm{aux}}_{nn'\boldsymbol{R}_v}(\boldsymbol{x}') + \rho^{\mathrm{aux}}_{nn'\boldsymbol{R}_v}(\boldsymbol{x}')\right] = I_1 + I_2 + I_3 + I_4, \tag{25}$$

where the individual contributions are given by,

$$\begin{aligned}
I_1 &= \int \mathrm{d}^3x \int \mathrm{d}^3x' \left[\rho_{mm'\boldsymbol{R}_c}(\boldsymbol{x}) - \rho^{\mathrm{aux}}_{mm'\boldsymbol{R}_c}(\boldsymbol{x})\right] V_{\mathrm{scr}}(\boldsymbol{x}-\boldsymbol{x}'-\boldsymbol{R}_D)\left[\rho_{nn'\boldsymbol{R}_v}(\boldsymbol{x}') - \rho^{\mathrm{aux}}_{nn'\boldsymbol{R}_v}(\boldsymbol{x}')\right],\\
I_2 &= \int \mathrm{d}^3x \int \mathrm{d}^3x' \left[\rho_{mm'\boldsymbol{R}_c}(\boldsymbol{x}) - \rho^{\mathrm{aux}}_{mm'\boldsymbol{R}_c}(\boldsymbol{x})\right] V_{\mathrm{scr}}(\boldsymbol{x}-\boldsymbol{x}'-\boldsymbol{R}_D)\,\rho^{\mathrm{aux}}_{nn'\boldsymbol{R}_v}(\boldsymbol{x}'),\\
I_3 &= \int \mathrm{d}^3x \int \mathrm{d}^3x' \rho^{\mathrm{aux}}_{mm'\boldsymbol{R}_c}(\boldsymbol{x})\, V_{\mathrm{scr}}(\boldsymbol{x}-\boldsymbol{x}'-\boldsymbol{R}_D)\left[\rho_{nn'\boldsymbol{R}_v}(\boldsymbol{x}') - \rho^{\mathrm{aux}}_{nn'\boldsymbol{R}_v}(\boldsymbol{x}')\right],\\
I_4 &= \int \mathrm{d}^3x \int \mathrm{d}^3x' \rho^{\mathrm{aux}}_{mm'\boldsymbol{R}_c}(\boldsymbol{x})\, V_{\mathrm{scr}}(\boldsymbol{x}-\boldsymbol{x}'-\boldsymbol{R}_D)\,\rho^{\mathrm{aux}}_{nn'\boldsymbol{R}_v}(\boldsymbol{x}').
\end{aligned} \tag{26}$$

The last term I_4 can be evaluated analytically because only Gaussian functions are involved. For instance, choosing radial symmetrical Gaussian $\rho^{\mathrm{aux}}_{mm'\boldsymbol{R}_c}(\boldsymbol{x}) = \left(\frac{\alpha}{\pi}\right)^{3/2} \mathrm{e}^{-\alpha|\boldsymbol{x}-\boldsymbol{B}|^2}$ and $\rho^{\mathrm{aux}}_{nn'\boldsymbol{R}_v}(\boldsymbol{x}) = \left(\frac{\gamma}{\pi}\right)^{3/2} \mathrm{e}^{-\gamma|\boldsymbol{x}-\boldsymbol{C}|^2}$, one obtains [40],

$$I_4 = \frac{1}{\epsilon_0\epsilon_\infty|\boldsymbol{B}-\boldsymbol{C}-\boldsymbol{R}_D|}\,\mathrm{erf}\left[\sqrt{\frac{\alpha\gamma}{\alpha+\gamma}}|\boldsymbol{B}-\boldsymbol{C}-\boldsymbol{R}_D|\right]. \tag{27}$$

The remaining three terms I_1, I_2 and I_3 are solved in Fourier space. This is demonstrated for I_1, which, in Fourier space reads

$$I_1 = \frac{1}{(2\pi)^3}\int \mathrm{d}^3q\, \mathrm{e}^{\mathrm{i}\boldsymbol{q}\boldsymbol{R}_D} f_{mm'\boldsymbol{R}_c}(\boldsymbol{q})\,\tilde{V}_{\mathrm{scr}}(\boldsymbol{q}) f_{nn'\boldsymbol{R}_v}(-\boldsymbol{q}), \tag{28}$$

where the Fourier transformed quantities are

$$f_{mm'\boldsymbol{R}_c}(\boldsymbol{q}) = \int \mathrm{d}^3x \mathrm{e}^{-i\boldsymbol{q}\boldsymbol{x}}\left[\rho_{mm'\boldsymbol{R}_c}(\boldsymbol{x}) - \rho^{\mathrm{aux}}_{mm'\boldsymbol{R}_c}(\boldsymbol{x})\right], \tag{29}$$

$$f_{nn'\boldsymbol{R}_v}(\boldsymbol{q}) = \int \mathrm{d}^3x \mathrm{e}^{-i\boldsymbol{q}\boldsymbol{x}}\left[\rho_{nn'\boldsymbol{R}_v}(\boldsymbol{x}) - \rho^{\mathrm{aux}}_{nn'\boldsymbol{R}_v}(\boldsymbol{x})\right] \tag{30}$$

and the Fourier transformed potential $\tilde{V}_{\mathrm{scr}}(\boldsymbol{q}) \propto q^{-2}$. The divergence at $\boldsymbol{q}\to 0$ is integrable, i.e. the integral is finite for all finite regions including volumes around the origin.

Since the auxiliary densities have the same charge as the corresponding overlap densities (see equation (24)), it becomes clear that $f_{mm'\boldsymbol{R}_c}(\boldsymbol{q}=0) = f_{nn'\boldsymbol{R}_v}(\boldsymbol{q}=0) = 0$ by construction. For a discrete numerical evaluation of the integral equation (28), this means that the $\boldsymbol{q}=0$ term can be omitted, since it must be zero (finite value times zero). The only remaining task is to perform the $\boldsymbol{q}$-sum for all $\boldsymbol{q}\neq 0$, where no problems occur, and we obtain

$$I_1 \simeq \frac{\Delta V_q}{N_{\mathrm{grid}}}\sum_{\boldsymbol{q}\neq 0} \mathrm{e}^{\mathrm{i}\boldsymbol{q}\boldsymbol{R}_D} f_{mm'\boldsymbol{R}_c}(\boldsymbol{q})\,\tilde{V}_{\mathrm{scr}}(\boldsymbol{q}) f_{nn'\boldsymbol{R}_v}(-\boldsymbol{q}). \tag{31}$$

Integrals I_2 and I_3 are solved in full analogy. After summation and back substitution we obtain the desired (screened) Coulomb matrix elements equation (14).

3.2. Evaluating LFE in the basis of MLWF

The numerical calculation of LFE matrix elements in equation (16) is much easier than the screened Coulomb interaction because the used potential is not divergent ($\boldsymbol{G}=0$ is not contained). The potential in Fourier space is obtained as,

$$\tilde{\tilde{V}}(\boldsymbol{q}) = \int \mathrm{d}^3x \mathrm{e}^{-\mathrm{i}\boldsymbol{q}\boldsymbol{x}}\sum_{\boldsymbol{G}\neq 0}\tilde{V}(|\boldsymbol{G}|)\,\mathrm{e}^{\mathrm{i}\boldsymbol{G}\boldsymbol{x}} = (2\pi)^3\sum_{\boldsymbol{G}\neq 0}\tilde{V}(|\boldsymbol{G}|)\,\delta(\boldsymbol{q}-\boldsymbol{G}). \tag{32}$$

The overlap densities are now between conduction and valence WF and are known as transition densities. We denote their Fourier transform as

$$f_{mn-s}(\boldsymbol{q}) = \int \mathrm{d}^3x \mathrm{e}^{-\mathrm{i}\boldsymbol{q}\boldsymbol{x}}\rho_{mn-s}(\boldsymbol{x}). \tag{33}$$

Finally, equation (16) becomes

$$\tilde{H}^{\mathrm{LFE}}_{mn\boldsymbol{S},\,m'n'\boldsymbol{S}'} = \sum_{\boldsymbol{G}\neq 0} f_{mn-\boldsymbol{S}}\left(\boldsymbol{G}\right)\tilde{V}\left(|\boldsymbol{G}|\right) f_{m'n'-\boldsymbol{S}'}\left(-\boldsymbol{G}\right), \tag{34}$$

which can be easily evaluated numerically with a fast Fourier algorithm.

3.3. Time domain approach for calculating the macroscopic dielectric function

We have now everything at hand to construct the exciton Hamiltonian in the basis of MLWF. The remaining task would be to solve the eigenvalue equation and use equation (22) to obtain the macroscopic dielectric function ϵ^{M}. Numerically this could be done by using a sparse matrix diagonalization algorithm. However, we want to use a time-domain approach [42] which allows us to calculate ϵ^{M} without a formal high-scaling diagonalization or restrictions to a few number of eigenvalues. Therefore, we rewrite equation (22) in the time domain by taking a Fourier transform. We start with the dielectric function in the Cartesian direction $\hat{\boldsymbol{e}}_j$,

$$\epsilon^{\mathrm{M}}_{jj}\left(\omega\right) = 1 + \frac{4\pi}{\Omega}\sum_{\Lambda}\left|\sum_{mn\boldsymbol{S}}\tilde{M}^{*}_{mn\boldsymbol{S}}\left(\hat{\boldsymbol{e}}_j\right)B^{\Lambda}_{mn\boldsymbol{S}}\right|^2\left[\frac{1}{E^{\Lambda}-\hbar\left(\omega+i\eta\right)}+\frac{1}{E^{\Lambda}+\hbar\left(\omega+i\eta\right)}\right] \tag{35}$$

This is equivalent to a time-domain formulation [42],

$$\epsilon^{\mathrm{M}}_{jj}\left(\omega\right) = 1 - \frac{8\pi}{\Omega\hbar}\int_0^{\infty}\mathrm{d}t\,\mathrm{e}^{\mathrm{i}(\omega+i\eta)t}\,\mathrm{Im}\left[\sum_{mn\boldsymbol{S}}\tilde{M}^{*}_{mn\boldsymbol{S}}\left(\hat{\boldsymbol{e}}_j\right)\psi^{(j)}_{mn\boldsymbol{S}}\left(t\right)\right], \tag{36}$$

where the time-initial state is given by $\psi^{(j)}_{mn\boldsymbol{S}}(t=0) = \tilde{M}^{*}_{mn\boldsymbol{S}}(\hat{\boldsymbol{e}}_j)$ and is propagated with the exciton Hamiltonian,

$$\psi^{(j)}_{mn\boldsymbol{S}}\left(t\right) = \sum_{m'n'\boldsymbol{S}'}\left(\exp\left[\frac{-it}{\hbar}\tilde{H}\right]\right)_{mn\boldsymbol{S},\,m'n'\boldsymbol{S}'}\psi^{(j)}_{m'n'\boldsymbol{S}'}\left(t=0\right). \tag{37}$$

4. Computational details

To demonstrate our approach for the example of silicon crystals, which has been frequently studied experimentally and theoretically in the past [11, 13, 42, 43], we proceed in multiple steps. First, electronic states are obtained using density functional theory (DFT) with the PBE exchange-correlation functional and projector augmented wave (PAW) pseudo potentials [44, 45] as implemented in the VASP code [46, 47]. We use an energy cut-off of 350 eV and a $11\times11\times11$ Monkhost–Pack $\boldsymbol{k}$-points grid for converged DFT calculations. From these results, we calculate four MLWF which correspond to all valence bands and six MLWF for the lowest-energy conduction bands separately by utilizing the WANNIER90 code [48]. It was carefully checked that all obtained MLWF are real-valued and reproduce the DFT band structure very accurately. The obtained Wannier functions are very localized with maximal spreads of 2.18 Å^2 for valence WF and 5.25 Å^2 for conduction WF. Since the underlying DFTGGA calculations in generalized gradient approximation do not provide the correct band gap, we apply a scissors shift of 0.9 eV which is is similar to previously calculated quasi-particle shifts [3]. The Wannier Hamiltonians for valence and conduction bands provide all single-particle contributions of the exciton Hamiltonian equation (12). The two-particle integrals entering $\tilde{H}^{\mathrm{SC}}$ and $\tilde{H}^{\mathrm{LFE}}$ are evaluated on a regular grid in Fourier space as described in sections 3.1 and 3.2, which captures a supercell of $11\times11\times11$ primitive unit cells. The grid is determined by the Fourier space grid of the VASP calculation. (Overlap-)densities and auxiliary functions are also constructed on this real space grid and Fourier transformations (see equations (29), (30) and (33)) are performed using the FFTW library [49]. For the screening model introduced in section 2.1 we use $\epsilon_{\infty} = 11.68$ for Si. From the obtained single-particle and two-particle contributions we construct the exciton Hamiltonian equation (11) in a sparse matrix format where $\boldsymbol{S}, \boldsymbol{S}'$ are running over 61 lattice vectors in each direction for converged results. To test the capability of the LSWO approach we also performed calculations with 111 lattice vectors in each direction, which is equivalent to 1.37 million $\boldsymbol{k}$-points.

The time evolution for the calculation of ϵ^{M} (see section 3.3) is performed by a Chebyshev polynomial expansion [50, 51] of the time evolution operator, which has proven to be very accurate and efficient in the past [52–54]. We set the maximum time to 14.77 ps, use 2000 time steps and 16 polynomials. When calculating the spectrum we assumed a broadening of $\eta = 65$ meV. Figure S-2 shows the time-autocorrelation function which enters equation (36).

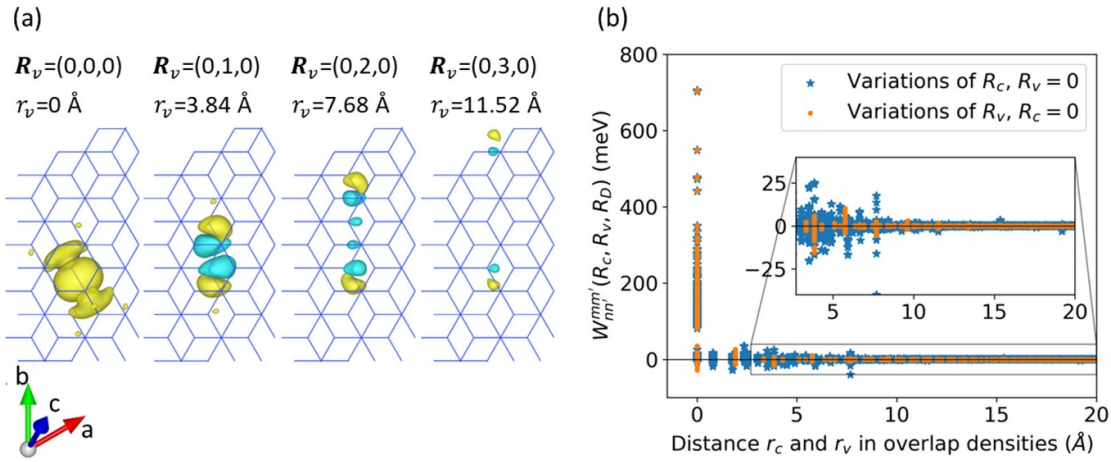

Figure 1. (a) Examples of overlap densities $\rho_{nn'\boldsymbol{R}_v}$ for valence WF with $n = n'$ and different $\boldsymbol{R}_v$. Yellow colors represent positive and blue negative values. All densities are plotted for the same iso-value magnitude of 0.001 and blue lines indicate the Si crystal. (b) Coulomb integrals for different hole–hole distances r_v and electron–electron distances r_c in the corresponding overlap densities $\rho_{nn'\boldsymbol{R}_v}$ and $\rho_{mm'\boldsymbol{R}_c}$. While $\boldsymbol{R}_v$ and $\boldsymbol{R}_c$ are only unit cell vectors, r_v and r_c also consider the position of Wannier centers within their unit cell.

We also carefully tested the implementation of the LSWO approach at multiple levels. This includes the comparison to an analytic Wannier–Mott exciton model and the reproduction of its energies. The interested reader is referred to section C.1 of the appendix for more details.

5. Results

5.1. Overlap densities and Coulomb integrals

Before discussing the optical absorption of bulk Si, we investigate more closely the distance-dependence of the two-particle contributions of the exciton Hamiltonian. We start by discussing the overlap densities $\rho_{mm'\boldsymbol{R}_c}(\boldsymbol{x})$ and $\rho_{nn'\boldsymbol{R}_v}(\boldsymbol{x})$, which contribute to the screened Coulomb interaction via equation (15). Figure 1(a) shows selected overlap densities $\rho_{nn'\boldsymbol{R}_v}$ of the valence WF (with $n = n'$ and different $\boldsymbol{R}_v$). In this case, the overlap density for $\boldsymbol{R}_v = 0$ is a classical charge density in the shape of σ-bonded combination of sp^3 hybrid orbitals. The density is positive everywhere (yellow color) with total charge of one. On the other hand, finite shifts $\boldsymbol{R}_v$ introduce negative regions (blue color) in $\rho_{nn\boldsymbol{R}_v}$ and result in a total charge of zero. It is clearly seen that large values of $\boldsymbol{R}_v$ lead to smaller overlaps as expected.

The implications of the decay of the Coulomb integrals $W^{mm'}_{nn'}(\boldsymbol{R}_c, \boldsymbol{R}_v, \boldsymbol{R}_D)$ with distance are shown in figure 1(b). Blue stars denote data with varying distance between conduction WF r_c and orange dots show data with varying distance between valence WF r_v. The distances r_c and r_v depend on the unit cell separation $\boldsymbol{R}_c$ and $\boldsymbol{R}_v$, respectively, and on the position of the Wannier centers within the unit cell. It is clearly visible that already small separations in the overlap densities of a few angstroms lead to much smaller values in the Coulomb integral. The largest Coulomb integrals are observed for $r_c = r_v = 0$, where classical charge densities (with total charge of one) interact with each other. Our above discussion has therefore been confirmed numerically. Furthermore, $W^{mm'}_{nn'}(\boldsymbol{R}_c, \boldsymbol{R}_v, \boldsymbol{R}_D)$ is more sensitive to r_v than r_c because valence WFs are more localized than conduction WFs. In both cases, the overlap densities $\rho_{mm'\boldsymbol{R}_c}$ and $\rho_{nn'\boldsymbol{R}_v}$ vanish for large separations where the Coulomb integrals become zero. As a consequence, the corresponding screened Coulomb operator $\tilde{H}^{\mathrm{SC}}$ is very sparse and the largest values contribute to the diagonal of the Hamiltonian matrix, as suggested. Similar results can be found for $\tilde{H}^{\mathrm{LFE}}$ (not shown), which leads to a very sparse total exciton Hamiltonian.

We next turn to the diagonal elements of the Hamiltonian that correspond to electron–hole interaction of classical charge densities. They are shown in figure 2 for different distances between electrons and holes, which depends on the unit cell distance $\boldsymbol{R}_D$ and the positions of the MLWF (charge centers) within a unit cell. The Coulomb integrals $W^{mm}_{nn}(0, 0, \boldsymbol{R}_D)$ become smaller with increasing distance and can be approximated for distances larger than 10 Å by the monopole–monopole interaction (gray dashed line). Notable deviations from the monopole–monopole approximation are found here only when electron and hole densities start overlapping at smaller distances. As a result of the multipole expansion, only a relatively small fraction of the Coulomb integrals need to be calculated numerically, which reduces the computational effort substantially. For example, in the present study, we only need to compute 2496 out of 5.4 million density–density Coulomb integrals in full detail (less than 0.5% for a $61 \times 61 \times 61$ supercell with four valence and six conduction WFs)

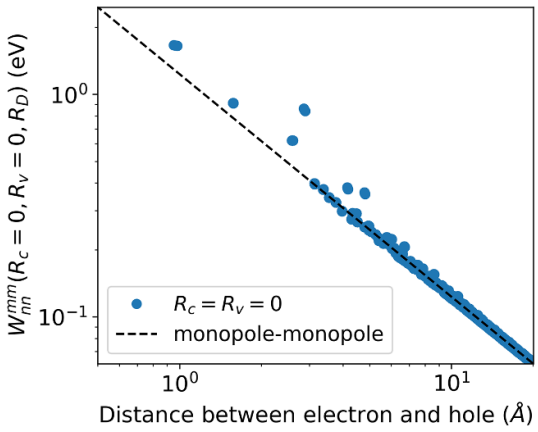

Figure 2. Screened density–density Coulomb interaction ($m = m'$, $n = n'$, $\boldsymbol{R}_c = \boldsymbol{R}_v = 0$) between conduction and valence WF. The interaction is dominated by the monopole–monopole interaction (dashed line). Only interactions between overlapping densities with small distances differ significantly.

and assume the monopole–monopole approximation for the vast majority of terms. In general, the value of 10 Å does not have to be universal and deviations from the leading monopole–monopole term could occur also at larger distances, for instance in systems with WFs that are less strongly localized. However, we are confident that systems with larger orbital spreads can also be treated very efficiently.

5.2. Optical absorption spectrum

With the obtained exciton Hamiltonian we calculate the optical absorption spectrum of Si. Figure 3(a) shows a comparison the LSWO approach (black solid line) to experimental data (orange dashed line). The spectrum contains the peaks E_1 and E_2 (naming convention from [56]), in good agreement with experiment. Most importantly, the characteristic (direct) exciton peak at $E_1 = 3.5\,\mathrm{eV}$ is a clear sign of bound exciton states that arise from electron–hole interactions. This peak is not present at GW or DFT theory level as shown by the dotted gray line. Compared to the quasiparticle spectrum, the excitonic effects result in a significantly redshifted spectrum, as generally expected which is a consequence of the electron–hole interaction. Residual deviations of the exciton spectrum to experiment might be related to the screening model (which is frequently used but still remains an approximation) or missing quasi-particle corrections in the band structure that go beyond a scissors shift. Figure 3(b) compares LSWO results to other theoretical calculations. The height of the E_1 exciton peak varies significantly among different methods, which might be related to different treatments of the screening. Our results are closely comparable to the approach by Marini [57] and performs better than others in the literature.

5.3. Scaling and performance of the LSWO approach

Finally, we discuss the performance and scaling with respect to the size of the exciton Hamiltonian, which depends on the number of valence and conduction states and the number of $\boldsymbol{k}$-points (or equivalently $\boldsymbol{S}$-points in equation (9)). The overall performance depends on two parts, i.e. firstly the calculation of all required matrix elements of the Hamiltonian and secondly the evaluation of the optical absorption spectrum using the time evolution approach. Figure 4 shows the scaling of both parts for various numbers of $\boldsymbol{k}$-points. All computations are performed on a single CPU core and normalized to a reference computation. Note that in the current implementation we do not exploit the symmetry of the crystal.

The most time-consuming part for the construction of the exciton Hamiltonian, which is shown in figure 4(a), is the evaluation of the Coulomb and LFE integrals that enter $\hat{H}^{\mathrm{SC}}$ and $\hat{H}^{\mathrm{LFE}}$. In contrast, the time required to generate the single-particle contributions of the Hamiltonian, i.e. valence and conduction bands, is negligible. As a result, the computing time scales with the number of two-particle integrals that need to be evaluated numerically on a real space grid. As we have shown in the previous section, the majority of such integrals either vanish if $\boldsymbol{R}_c$ or $\boldsymbol{R}_v$ deviate sufficiently from zero, or become analytical monopole–monopole interactions for larger values of $\boldsymbol{R}_D$. Consequently, only a finite number of integrals need to be evaluated, leading to a saturation of CPU time in figure 4(a). This plateau is already reached for a supercell of $7 \times 7 \times 7$ unit cells (corresponding to a $\boldsymbol{k}$-lattice of the same dimensions) which can be done with moderate effort. Once all integrals have been obtained, one can proceed to even denser $\boldsymbol{k}$-grids (corresponding to very large supercells $\boldsymbol{S}$) without additional effort for the computation of $\tilde{H}$.

The second step that is crucial to the performance of the LSWO method is the time evolution with the exciton Hamiltonian, which is shown in figure 4(b). This time propagation is performed in a step-by-step

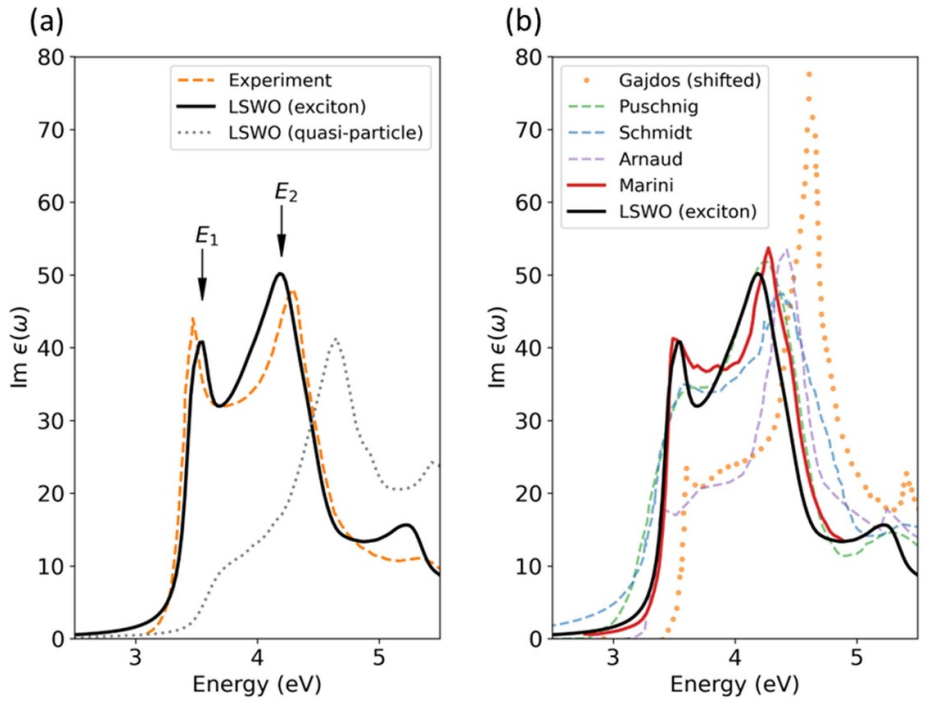

Figure 3. Absorption spectrum for silicon. (a) Comparison of the calculated MLWF-based spectrum (solid black) with calculations without electron–hole interaction (dotted gray) and experiment [55] (dashed orange). Peak labels are in agreement with previous conventions [56]. (b) Comparison with other theoretical calculations. References: Gajdos *et al* [14], Puschnig and Ambrosch-Draxl [13], Schmidt *et al* [42], Arnaud and Alouani [43], Marini [57].

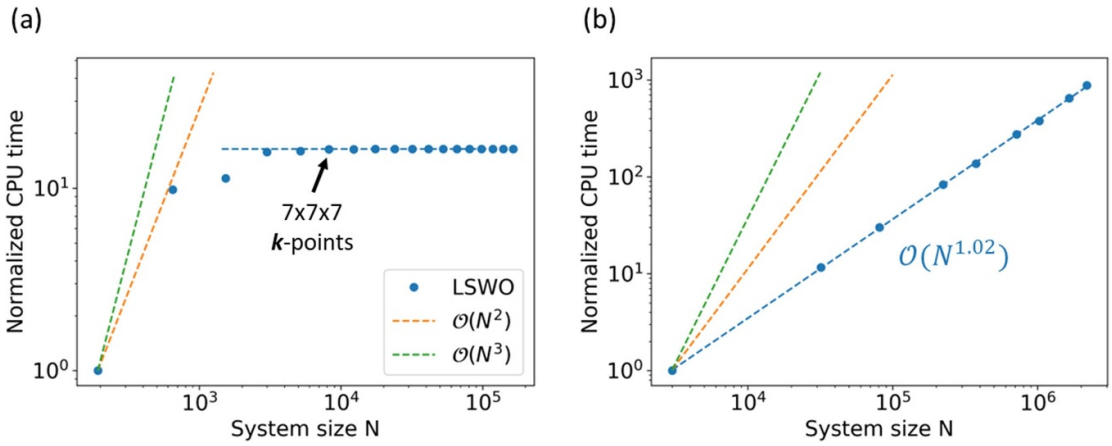

Figure 4. Scaling behavior for (a) construction of the exciton Hamiltonian and (b) calculation of the optical absorption spectrum. N is the rank of the Hamiltonian $N = N_{\mathrm{el}} \cdot N_{\mathrm{h}} \cdot N_{\boldsymbol{k}}$. For comparison, a direct diagonalization of the exciton Hamilton in the Bloch basis (dense matrix) scales with $\mathcal{O}(N^3)$. Using the time evolution approach of [42] scales with $\mathcal{O}(N^2)$. The legend is shared for both figures. Calculations are performed on a single CPU core.

fashion, where each time step has the computational complexity of a sparse matrix-vector multiplication. Such operations can be performed very efficiently in linear scaling as shown in the figure. For comparison, the time-evolution approach in a Bloch representation, where the Hamiltonian is dense, would scale with $\mathcal{O}(N^2)$ [42], which is similar to implementations that use a Lanczos–Haydock approach as implemented in the Yambo code [58]. Note that a direct diagonalization of the Hamiltonian scales with $\mathcal{O}(N^2)$ in the case of a sparse matrix or with $\mathcal{O}(N^3)$ in the case of a dense matrix.

6. Conclusion and outlook

We have presented a method for describing the exciton Hamiltonian of the BSE using MLWF, which represent a minimal, spatially localized and material-specific basis set that accurately represents the quasiparticle band structure. The electron–hole interaction, i.e. local field effects and screened Coulomb

attraction, are evaluated numerically in this basis, where the required number of two-particle matrix elements to be computed is greatly reduced due to the localized character of WFs. Moreover, Coulomb integrals where electron and hole densities have large distances can be treated very efficiently in monopole approximation. Therefore this description in real space leads to a very sparse exciton Hamiltonian that can be calculated and used with high efficiency and offers intuitive user control over the simulations. With this implementation at hand, the macroscopic dielectric function for optical properties is calculated in the time domain using a linear-scaling algorithm. We have demonstrated the approach for a Si crystal where the optical subspace was constructed with millions of simple unit cells (corresponding to millions of $\boldsymbol{k}$-points). The calculated absorption spectrum agrees well with experimental results.

In the future, we expect that the described LSWO approach will be very efficient for materials with many atoms per unit cell, which are not accessible with alternative current implementations. We hope that excitonic effects in optical spectra, which are relevant in a large number of crystalline systems, become more easily accessible.

Data availability statement

The data that support the findings of this study are available in this article, the appendix or upon reasonable request from the authors.

Acknowledgments

We would like to thank the Deutsche Forschungsgemeinschaft for financial support [CRC1415, Project Nos. OR-349/3 and OR-349/11 and the Cluster of Excellence e-conversion (Grant No. EXC2089)]. Grants for computer time from the Zentrum für Informationsdienste und Hochleistungsrechnen of TU Dresden and the Leibniz Supercomputing Centre in Garching (SuperMUC-NG) are gratefully acknowledged.

We would like to acknowledge F Bechstedt and J Furthmüller for fruitful discussions about the numerical evaluation of Coulomb integrals.

Conflict of interest

There are no competing interests to declare.

Appendix A. Step-by-step derivation for screened Coulomb interaction

We insert equation (8) into $\tilde{H}^{\mathrm{SC}}$ and using the shifting property of Wannier functions, i.e. $w_{m\boldsymbol{R}}(\boldsymbol{x}) = w_{m0}(\boldsymbol{x}-\boldsymbol{R})$, we obtain

$$
\begin{aligned}
\tilde{H}^{\mathrm{SC}}_{mn\boldsymbol{S},\,m'n'\boldsymbol{S}'} &= \int \mathrm{d}^3x \int \mathrm{d}^3x'\, \xi_{mn\boldsymbol{S}}(\boldsymbol{x},\boldsymbol{x}')\, W(\boldsymbol{x}-\boldsymbol{x}')\, \xi_{m'n'\boldsymbol{S}'}(\boldsymbol{x},\boldsymbol{x}') \\
&= \frac{1}{N_\Omega} \sum_{\boldsymbol{R}\boldsymbol{R}'} \int \mathrm{d}^3x \int \mathrm{d}^3x'\, w_{m\boldsymbol{R}}(\boldsymbol{x})\, w_{m'\boldsymbol{R}'}(\boldsymbol{x})\, W(\boldsymbol{x}-\boldsymbol{x}')\, w_{n',\boldsymbol{R}'-\boldsymbol{S}'}(\boldsymbol{x}')\, w_{n,\boldsymbol{R}-\boldsymbol{S}}(\boldsymbol{x}') \\
&= \frac{1}{N_\Omega} \int \mathrm{d}^3x \int \mathrm{d}^3x' \sum_{\boldsymbol{R}\boldsymbol{R}'} w_{m0}(\boldsymbol{x}-\boldsymbol{R})\, w_{m'\boldsymbol{R}'}(\boldsymbol{x})\, W(\boldsymbol{x}-\boldsymbol{x}')\, w_{n',\boldsymbol{R}'-\boldsymbol{S}'}(\boldsymbol{x}')\, w_{n,\boldsymbol{R}-\boldsymbol{S}}(\boldsymbol{x}') \\
&= \frac{1}{N_\Omega} \sum_{\boldsymbol{R}\boldsymbol{R}'} \int \mathrm{d}^3x \int \mathrm{d}^3x'\, w_{m0}(\boldsymbol{x})\, w_{m'\boldsymbol{R}'}(\boldsymbol{x}+\boldsymbol{R})\, W(\boldsymbol{x}+\boldsymbol{R}-\boldsymbol{x}')\, w_{n',\boldsymbol{R}'-\boldsymbol{S}'}(\boldsymbol{x}')\, w_{n,\boldsymbol{R}-\boldsymbol{S}}(\boldsymbol{x}') \\
&= \frac{1}{N_\Omega} \sum_{\boldsymbol{R}\boldsymbol{R}'} \int \mathrm{d}^3x \int \mathrm{d}^3x'\, w_{m0}(\boldsymbol{x})\, w_{m'\boldsymbol{R}'-\boldsymbol{R}}(\boldsymbol{x})\, W(\boldsymbol{x}-\boldsymbol{x}')\, w_{n',\boldsymbol{R}'-\boldsymbol{S}'}(\boldsymbol{x}'+\boldsymbol{R})\, w_{n,\boldsymbol{R}-\boldsymbol{S}}(\boldsymbol{x}'+\boldsymbol{R}) \\
&= \frac{1}{N_\Omega} \sum_{\boldsymbol{R}\boldsymbol{R}'} \int \mathrm{d}^3x \int \mathrm{d}^3x'\, w_{m0}(\boldsymbol{x})\, w_{m'\boldsymbol{R}'-\boldsymbol{R}}(\boldsymbol{x})\, W(\boldsymbol{x}-\boldsymbol{x}')\, w_{n',\boldsymbol{R}'-\boldsymbol{R}-\boldsymbol{S}'}(\boldsymbol{x}')\, w_{n,-\boldsymbol{S}}(\boldsymbol{x}') \\
&= \frac{1}{N_\Omega} \int \mathrm{d}^3x \int \mathrm{d}^3x' \sum_{\boldsymbol{A}\boldsymbol{B}} w_{m0}(\boldsymbol{x})\, w_{m'\boldsymbol{A}}(\boldsymbol{x})\, W(\boldsymbol{x}-\boldsymbol{x}')\, w_{n',\boldsymbol{A}-\boldsymbol{S}'}(\boldsymbol{x}')\, w_{n,-\boldsymbol{S}}(\boldsymbol{x}') \\
&= \sum_{\boldsymbol{A}} \int \mathrm{d}^3x \int \mathrm{d}^3x'\, w_{m0}(\boldsymbol{x})\, w_{m'\boldsymbol{A}}(\boldsymbol{x})\, W(\boldsymbol{x}-\boldsymbol{x}')\, w_{n',\boldsymbol{A}-\boldsymbol{S}'}(\boldsymbol{x}')\, w_{n,-\boldsymbol{S}}(\boldsymbol{x}')
\end{aligned}
\tag{A1}
$$

with $\boldsymbol{A} = \boldsymbol{R}' - \boldsymbol{R}$ and $\boldsymbol{B} = \boldsymbol{R}' + \boldsymbol{R}$.

An alternative form can be derived easily,

$$\begin{aligned}
\tilde{H}^{\mathrm{SC}}_{mnS,\,m'n'S'} &= \sum_{\boldsymbol{A}} \int \mathrm{d}^3x \int \mathrm{d}^3x'\, w_{m0}\left(\boldsymbol{x}\right) w_{m'\boldsymbol{A}}\left(\boldsymbol{x}\right) W\left(\boldsymbol{x}-\boldsymbol{x}'\right) w_{n',\boldsymbol{A}-S'}\left(\boldsymbol{x}'\right) w_{n,-S}\left(\boldsymbol{x}'\right) \\
&= \sum_{\boldsymbol{A}} \int \mathrm{d}^3x \int \mathrm{d}^3x'\, w_{m0}\left(\boldsymbol{x}\right) w_{m'\boldsymbol{A}}\left(\boldsymbol{x}\right) W\left(\boldsymbol{x}-\boldsymbol{x}'\right) w_{n',\boldsymbol{A}-S'}\left(\boldsymbol{x}'\right) w_{n,0}\left(\boldsymbol{x}'+\boldsymbol{S}\right) \\
&= \sum_{\boldsymbol{A}} \int \mathrm{d}^3x \int \mathrm{d}^3x'\, w_{m0}\left(\boldsymbol{x}\right) w_{m'\boldsymbol{A}}\left(\boldsymbol{x}\right) W\left(\boldsymbol{x}-\left(\boldsymbol{x}'-\boldsymbol{S}\right)\right) w_{n',\boldsymbol{A}-S'}\left(\boldsymbol{x}'-\boldsymbol{S}\right) w_{n,0}\left(\boldsymbol{x}'\right) \\
&= \sum_{\boldsymbol{A}} \int \mathrm{d}^3x \int \mathrm{d}^3x'\, w_{m0}\left(\boldsymbol{x}\right) w_{m'\boldsymbol{A}}\left(\boldsymbol{x}\right) W\left(\boldsymbol{x}-\boldsymbol{x}'+\boldsymbol{S}\right) w_{n',\boldsymbol{A}+S-S'}\left(\boldsymbol{x}'\right) w_{n,0}\left(\boldsymbol{x}'\right) \\
&= \sum_{\boldsymbol{A}} \tilde{W}^{mm'}_{nn'}\left(\boldsymbol{A},\boldsymbol{S},\boldsymbol{S}'\right).
\end{aligned} \tag{A2}$$

We finally show that the hermiticity of the Hamiltonian can be traced back to relations between single Coulomb integrals $\tilde{W}^{mm'}_{nn'}(\boldsymbol{A},\boldsymbol{S},\boldsymbol{S}')$. For this we substitute $\boldsymbol{A}\rightarrow-\boldsymbol{A}$.

$$\begin{aligned}
\tilde{W}^{mm'}_{nn'}\left(-\boldsymbol{A},\boldsymbol{S},\boldsymbol{S}'\right) &= \int \mathrm{d}^3x \int \mathrm{d}^3x'\, w_{m0}\left(\boldsymbol{x}\right) w_{m'-\boldsymbol{A}}\left(\boldsymbol{x}\right) W\left(\boldsymbol{x}-\boldsymbol{x}'+\boldsymbol{S}\right) w_{n',-\boldsymbol{A}+S-S'}\left(\boldsymbol{x}'\right) w_{n,0}\left(\boldsymbol{x}'\right) \\
&= \int \mathrm{d}^3x \int \mathrm{d}^3x'\, w_{m0}\left(\boldsymbol{x}\right) w_{m'0}\left(\boldsymbol{x}+\boldsymbol{A}\right) W\left(\boldsymbol{x}-\boldsymbol{x}'+\boldsymbol{S}\right) w_{n'0}\left(\boldsymbol{x}'+\boldsymbol{A}-\boldsymbol{S}+\boldsymbol{S}'\right) w_{n,0}\left(\boldsymbol{x}'\right) \\
&= \int \mathrm{d}^3x \int \mathrm{d}^3x'\, w_{m0}\left(\boldsymbol{x}-\boldsymbol{A}\right) w_{m'0}\left(\boldsymbol{x}\right) W\left(\boldsymbol{x}-\boldsymbol{A}-\left(\boldsymbol{x}'-\boldsymbol{A}+\boldsymbol{S}-\boldsymbol{S}'\right)+\boldsymbol{S}\right) \\
&\qquad \times w_{n'0}\left(\boldsymbol{x}'\right) w_{n,0}\left(\boldsymbol{x}'-\boldsymbol{A}+\boldsymbol{S}-\boldsymbol{S}'\right) \\
&= \int \mathrm{d}^3x \int \mathrm{d}^3x'\, w_{m\boldsymbol{A}}\left(\boldsymbol{x}\right) w_{m'0}\left(\boldsymbol{x}\right) W\left(\boldsymbol{x}-\boldsymbol{x}'+\boldsymbol{S}'\right) w_{n'0}\left(\boldsymbol{x}'\right) w_{n,\boldsymbol{A}-S+S'}\left(\boldsymbol{x}'\right) \\
&= \tilde{W}^{m'm}_{n'n}\left(\boldsymbol{A},\boldsymbol{S}',\boldsymbol{S}\right).
\end{aligned} \tag{A3}$$

Performing the sum over $\boldsymbol{A}$ on both sides, we obtain the hermiticity of the Hamiltonian.

Appendix B. Model screening potential

We start from the screened Coulomb interaction as defined in section 2.1 and define $\alpha' = \alpha/q_{\mathrm{TF}}^2$ for simplicity,

$$W(\boldsymbol{q}) = \epsilon^{-1}\left(\boldsymbol{q}\right) V(\boldsymbol{q}) = \left(1-\frac{1}{\eta+\alpha' q^2}\right)\frac{1}{\epsilon_0 q^2}. \tag{B1}$$

A simple rearrangement of the terms yield the Coulomb and Yukawa potential in reciprocal space,

$$\begin{aligned}
W(\boldsymbol{q}) &= \left(1-\frac{1}{\eta}\right)\frac{1}{\epsilon_0 q^2} + \left(\frac{1}{\eta}-\frac{1}{\eta+\alpha' q^2}\right)\frac{1}{\epsilon_0 q^2} \\
&= \frac{1}{\epsilon_\infty}\frac{1}{\epsilon_0 q^2} + \frac{\alpha' q^2}{\eta\left(\eta+\alpha' q^2\right)}\frac{1}{\epsilon_0 q^2} \\
&= \frac{1}{\epsilon_0\epsilon_\infty q^2} + \frac{1}{\eta\epsilon_0}\frac{\alpha'}{\eta+\alpha' q^2} \\
&= \underbrace{\frac{1}{\epsilon_0\epsilon_\infty q^2}}_{=\text{Coulomb}} + \left(1-\epsilon_\infty^{-1}\right)\underbrace{\frac{1}{\epsilon_0}\frac{1}{q^2+\frac{q_{\mathrm{TF}}^2}{\alpha\left(1-\epsilon_\infty^{-1}\right)}}}_{=\text{Yukawa}}.
\end{aligned} \tag{B2}$$

The Fourier transform then yields equation (5).

Appendix C. Numerical details

C.1. Implementation test

Figures S-1 and S-2 show additional numerical data regarding the Coulomb interaction and time evolution, respectively.

We have carefully and extensively tested all implementations, of which we want to discuss one particular test case that demonstrates the ability to compute excitons. For this purpose, we propose a simple test system that can be solved analytically. It consists of one orbital per unit cell in a cubic lattice of length L and nearest neighbor transfer integrals for electrons and holes. The electronic structure is given by a tight-binding model,

$$\begin{aligned} H_{\mathrm{el}} &= \sum_{<ij>} -t_{\mathrm{el}}\, a_i^\dagger a_j + E_0, \\ H_{\mathrm{h}} &= \sum_{<ij>} t_{\mathrm{h}}\, h_i^\dagger h_j, \end{aligned} \tag{C1}$$

whose band energies are

$$E_{\mathrm{el}}(\boldsymbol{k}) = -2t_{\mathrm{el}}\left(\cos(k_x L) + \cos\left(k_y L\right) + \cos\left(k_z L\right)\right) + E_0, \tag{C2}$$

$$E_{\mathrm{h}}(\boldsymbol{k}) = 2t_{\mathrm{h}}\left(\cos(k_x L) + \cos\left(k_y L\right) + \cos\left(k_z L\right)\right). \tag{C3}$$

We construct the exciton Hamiltonian and include the electron–hole interaction. For simplicity we chose a static screening with ϵ_∞ and do not include local field effects. The resulting model is given by

$$H\left(\boldsymbol{k},\boldsymbol{k}'\right) = \left[E_{\mathrm{el}}(\boldsymbol{k}) - E_{\mathrm{h}}(\boldsymbol{k})\right]\delta_{\boldsymbol{k}\boldsymbol{k}'} - \frac{1}{\epsilon_\infty}\tilde{V}\left(\boldsymbol{k}-\boldsymbol{k}'\right), \tag{C4}$$

where $\tilde{V}(\boldsymbol{k}-\boldsymbol{k}')$ is the bare Coulomb potential in $\boldsymbol{k}$-space. The model system is therefore similar to the Wannier–Mott exciton model [59]. To obtain an analytical solution of this model, we perform a Taylor expansion of the band energies around $\boldsymbol{k}=0$

$$E_{\mathrm{el}}(\boldsymbol{k}) - E_{\mathrm{h}}(\boldsymbol{k}) \approx E_0 - 2\left(t_{\mathrm{el}}+t_{\mathrm{h}}\right)\left(3 - \frac{1}{2}L^2|\boldsymbol{k}|^2 + \frac{1}{24}L^4|\boldsymbol{k}|^4 - \ldots\right). \tag{C5}$$

By expanding the exciton Hamiltonian up to second order we obtain the hydrogen-like problem,

$$H\left(\boldsymbol{k}\boldsymbol{k}'\right) = \frac{\hbar^2\boldsymbol{k}^2}{2\mu}\delta_{\boldsymbol{k}\boldsymbol{k}'} - \frac{1}{\epsilon_\infty}\tilde{V}\left(\boldsymbol{k}-\boldsymbol{k}'\right) + E_{\mathrm{g}}, \tag{C6}$$

with an effective mass $\mu = \frac{\hbar^2}{2(t_{\mathrm{el}}+t_{\mathrm{h}})L^2}$ and $E_{\mathrm{g}} = E_0 - 6(t_{\mathrm{el}}+t_{\mathrm{h}})$ the band gap without electron–hole interaction. The exciton energies follow a Rydberg series,

$$E_n = E_{\mathrm{g}} - \frac{R_{\mathrm{ex}}}{n^2\epsilon_\infty^2}m \tag{C7}$$

where the exciton Rydberg energy R_{ex} and exciton Bohr radius a_{B} are,

$$\begin{aligned} R_{\mathrm{ex}} &= \frac{e^4\mu}{2\left(4\pi\epsilon_0\right)^2\hbar^2}, \\ a_{\mathrm{B}} &= \frac{4\pi\epsilon_0\epsilon_\infty\hbar^2}{\mu e^2}. \end{aligned} \tag{C8}$$

We note that this result can be further improved by calculating the energy shifts due to the k^4 term in equation (C5), which would correspond to a relativistic correction of the hydrogen atom (fine structure without spin–orbit coupling). In complete analogy, they can be calculated using perturbation theory (more details on the derivation can be found in reference [60]),

$$\Delta E_{nl} = -\frac{1}{12}\frac{E_n^2}{\left(t_{\mathrm{el}}+t_{\mathrm{h}}\right)}\left[\frac{4n}{(l+1/2)} - 3\right]. \tag{C9}$$

The analytical model will be compared with results of our Wannier implementation. Towards this end, the exciton Hamiltonian is set up in real space using the tight-binding models for valence and conduction

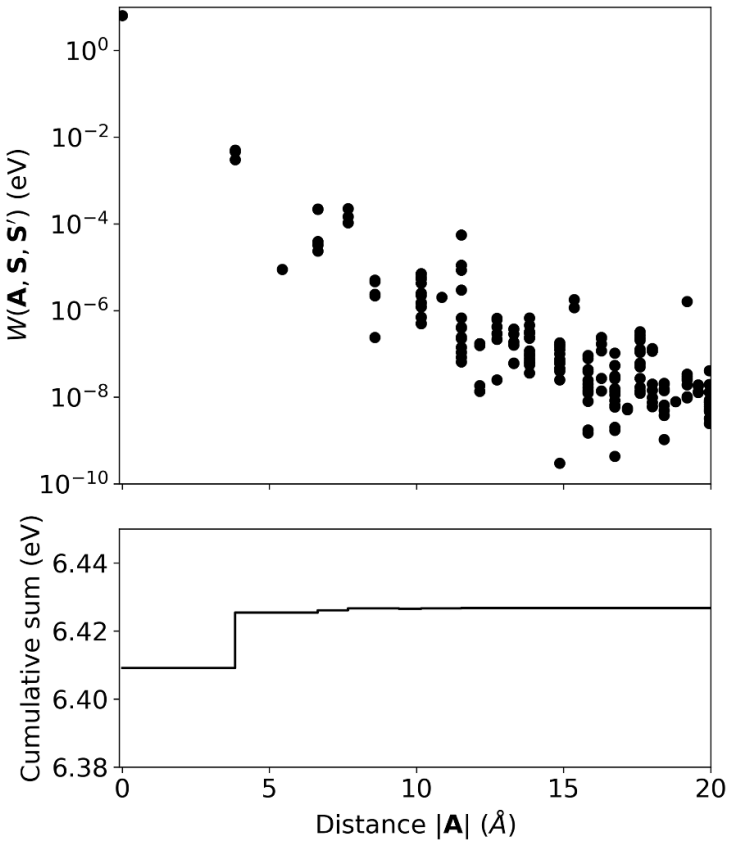

Figure S-1. Convergence of equation (13) for matrix element $S = S' = 0$, $m = m' = 1$, $n = n' = 1$.

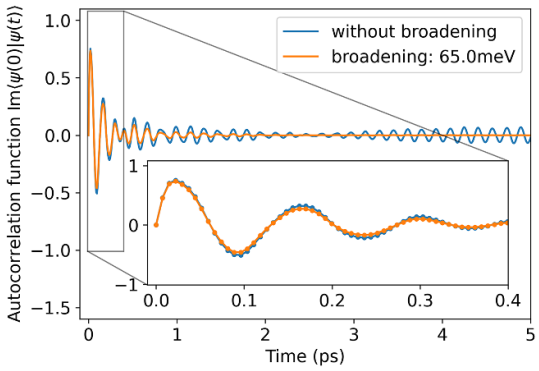

Figure S-2. Imaginary part of the autocorrelation function that enters equation (36) and is calculated using equation (37). The initial state $|\psi(t = 0)\rangle$ is normalized for convenience.

bands (see equation (C1)) and statically screened monopole–monopole interaction. The results can then compared for various model parameters (L, t_{el}, t_{h} or ϵ_{∞}). For converged numerical results, it is necessary to ensure that the size of the supercell (corresponding to the number of $\boldsymbol{k}$ points) is large enough to host the eigenfunctions (hydrogen-like wavefunctions). More specifically, it must be much larger than the exciton Bohr radius a_{B}. To avoid discretization errors, the spacing of the lattice points must be small compared to a_{B} so that the eigenfunction can be represented on a real space lattice. By varying the parameters, one can obtain converged numerical results that are arbitrary close to the analytical result. On example is shown in figure S-3, where the parameters are $L = 5$ Å, $t_{\mathrm{el}} = t_{\mathrm{h}} = 8$ eV, and $\epsilon_{\infty} = 1$. The calculations are performed in a $700 \times 700 \times 700$ supercell and we have used an efficient Lanczos algorithm to calculate the density of states. The figure shows perfect agreement between the numerical and analytical results, demonstrating the correctness of our implementation and the ability to simulate various excitons.

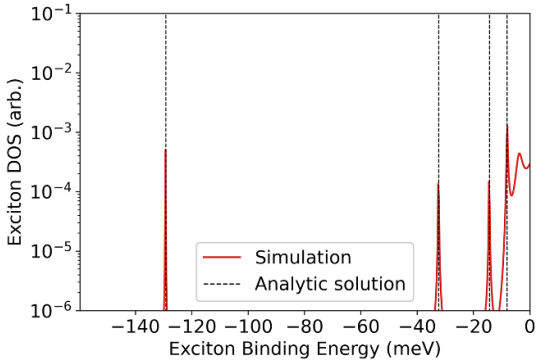

Figure S-3. Rydberg series of Wannier excitons as a test case. Analytical results are shown as vertical dashed lines.

ORCID iD

Frank Ortmann https://orcid.org/0000-0002-5884-5749

References

[1] Frenkel J 1931 On the transformation of light into heat in solids. I*Phys. Rev.* **37** 17–44
[2] Knox R S 1983 *Introduction to Exciton Physics* (Springer) pp 183–245
[3] Bechstedt F 2015 *Many-Body Approach to Electronic Excitations: Concepts and Applications / Friedhelm Bechstedt* (*Springer Series in Solid-State Sciences* vol 181) (Springer)
[4] Salpeter E E and Bethe H A 1951 A relativistic equation for bound-state problems *Phys. Rev.* **84** 1232–42
[5] Sham L J and Rice T M 1966 Many-particle derivation of the effective-mass equation for the Wannier exciton *Phys. Rev.* **144** 708–14
[6] Hanke W and Sham L J 1980 Many-particle effects in the optical spectrum of a semiconductor *Phys. Rev.* B **21** 4656–73
[7] Strinati G 1984 Effects of dynamical screening on resonances at inner-shell thresholds in semiconductors *Phys. Rev.* B **29** 5718–26
[8] Strinati G 1988 Application of the Green's functions method to the study of the optical properties of semiconductors *Riv. Nuovo Cimento (1978–1999)* **11** 1–86
[9] Onida G, Reining L and Rubio A 2002 Electronic excitations: density-functional versus many-body Green's-function approaches *Rev. Mod. Phys.* **74** 601–59
[10] Blase X, Duchemin I, Jacquemin D and Loos P-F 2020 The Bethe-Salpeter equation formalism: from physics to chemistry *J. Phys. Chem. Lett.* **11** 7371–82
[11] Benedict L X, Shirley E L and Bohn R B 1998 Theory of optical absorption in diamond, Si, Ge and GaAs *Phys. Rev.* B **57** R9385–7
[12] Rohlfing M and Louie S G 2000 Electron-hole excitations and optical spectra from first principles *Phys. Rev.* B **62** 4927–44
[13] Puschnig P and Ambrosch-Draxl C 2002 Optical absorption spectra of semiconductors and insulators including electron-hole correlations: an *ab initio* study within the lapw method *Phys. Rev.* B **66** 165105
[14] Gajdoš M, Hummer K, Kresse G, Furthmüller J and Bechstedt F 2006 Linear optical properties in the projector-augmented wave methodology *Phys. Rev.* B **73** 045112
[15] Marini A, Hogan C, Grüning M and Varsano D 2009 Yambo: an *ab initio* tool for excited state calculations *Comput. Phys. Commun.* **180** 1392–403
[16] Deslippe J, Samsonidze G, Strubbe D A, Jain M, Cohen M L and Louie S G 2012 Berkeleygw: a massively parallel computer package for the calculation of the quasiparticle and optical properties of materials and nanostructures *Comput. Phys. Commun.* **183** 1269–89
[17] Okano S *et al* 2020 Voltage-controlled dielectric function of bilayer graphene *Adv. Opt. Mater.* **8** 2000861
[18] Fuchs F, Rödl C, Schleife A and Bechstedt F 2008 Efficient $\mathcal{O}(N^2)$ approach to solve the Bethe-Salpeter equation for excitonic bound states *Phys. Rev.* B **78** 085103
[19] Schleife A, Rödl C, Fuchs F, Furthmüller J and Bechstedt F 2009 Optical and energy-loss spectra of MgO, ZnO and CdO from *ab initio* many-body calculations *Phys. Rev.* B **80** 035112
[20] Marzari N and Vanderbilt D 1997 Maximally localized generalized Wannier functions for composite energy bands *Phys. Rev.* B **56** 12847–65
[21] Marzari N, Mostofi A A, Yates J R, Souza I and Vanderbilt D 2012 Maximally localized Wannier functions: theory and applications *Rev. Mod. Phys.* **84** 1419–75
[22] Wiser N 1963 Dielectric constant with local field effects included *Phys. Rev.* **129** 62–69
[23] Hanke W and Sham L J 1975 Local-field and excitonic effects in the optical spectrum of a covalent crystal *Phys. Rev.* B **12** 4501–11
[24] Gavrilenko V I and Bechstedt F 1996 Local-field and exchange-correlation effects in optical spectra of semiconductors *Phys. Rev.* B **54** 13416–9
[25] Combescot M, Amand T and Shiau S-Y 2023 *Ab initio* quantum approach to electron-hole exchange for semiconductors hosting Wannier excitons *Phys. Rev.* B **107** 115206
[26] Cappellini G, Del Sole R, Reining L and Bechstedt F 1993 Model dielectric function for semiconductors *Phys. Rev.* B **47** 9892–5
[27] Zhang X, Leveillee J A and Schleife A 2023 Effect of dynamical screening in the Bethe-Salpeter framework: excitons in crystalline naphthalene (arXiv:2302.07948)
[28] Sangalli D, D'Alessandro M and Attaccalite C 2023 Exciton-exciton transitions involving strongly bound excitons: an *ab initio* approach *Phys. Rev.* B **107** 205203
[29] Merkel K, Greiner J and Ortmann F 2023 Understanding the electronic pi-system of 2d covalent organic frameworks with Wannier functions *Sci. Rep.* **13** 1685

[30] Koshino M *et al* 2018 Maximally localized Wannier orbitals and the extended Hubbard model for twisted bilayer graphene *Phys. Rev.* X **8** 031087
[31] Shih B-C, Zhang Y, Zhang W and Zhang P 2012 Screened Coulomb interaction of localized electrons in solids from first principles *Phys. Rev.* B **85** 045132
[32] Şaşıoğlu E, Schindlmayr A, Friedrich C, Freimuth F and Blügel S 2010 Wannier-function approach to spin excitations in solids *Phys. Rev.* B **81** 054434
[33] Garcia-Goiricelaya P, Krishna J and Ibañez Azpiroz J 2023 Including many-body effects into the Wannier-interpolated quadratic photoresponse tensor *Phys. Rev.* B **107** 205101
[34] Foerster D, Koval P and Sánchez-Portal D 2011 An O(N3) implementation of Hedin's gw approximation for molecules *J. Chem. Phys.* **135** 074105
[35] Wilhelm J, Golze D, Talirz L, Hutter J and Pignedoli C A 2018 Toward GW calculations on thousands of atoms *J. Phys. Chem. Lett.* **9** 306–12
[36] Agranovich V M and Ginzburg V 1984 *Spatial Dispersion in Crystal Optics* (Springer Berlin Heidelberg) pp 136–270
[37] Müller K *et al* 2023 Directed exciton transport highways in organic semiconductors *Nat. Commun.* **14** 5599
[38] Schnell I, Czycholl G and Albers R C 2002 Hubbard-*u* calculations for Cu from first-principle Wannier functions *Phys. Rev.* B **65** 075103
[39] Schnell I, Czycholl G and Albers R C 2003 Unscreened Hartree-Fock calculations for metallic Fe, Co, Ni and Cu from *ab initio* Hamiltonians *Phys. Rev.* B **68** 245102
[40] Gill P M 1994 *Molecular Integrals Over Gaussian Basis Functions* (*Advances in Quantum Chemistry* vol 25) (Academic) pp 141–205
[41] Bakhta A, Cancès E, Cazeaux P, Fang S and Kaxiras E 2018 Compression of Wannier functions into Gaussian-type orbitals *Comput. Phys. Commun.* **230** 27–37
[42] Schmidt W G, Glutsch S, Hahn P H and Bechstedt F 2003 Efficient $\mathcal{O}(N^2)$ method to solve the Bethe-Salpeter equation *Phys. Rev.* B **67** 085307
[43] Arnaud B and Alouani M 2001 Local-field and excitonic effects in the calculated optical properties of semiconductors from first-principles *Phys. Rev.* B **63** 085208
[44] Blöchl P 1994 Projector augmented-wave method *Phys. Rev.* B **50** 17953
[45] Kresse G and Joubert D 1999 From ultrasoft pseudopotentials to the projector augmented-wave method *Phys. Rev.* B **59** 1758
[46] Kresse G and Furthmüller J 1996 Efficiency of *ab-initio* total energy calculations for metals and semiconductors using a plane-wave basis set *Comput. Mater. Sci.* **6** 15–50
[47] Kresse G and Furthmüller J 1996 Efficient iterative schemes for *ab initio* total-energy calculations using a plane-wave basis set *Phys. Rev.* B **54** 11169–86
[48] Pizzi G *et al* 2020 Wannier90 as a community code: new features and applications *J. Phys.: Condens. Matter* **32** 165902
[49] Frigo M and Johnson S 2005 The design and implementation of FFTW3 *Proc. IEEE* **93** 216–31
[50] Weiße A, Wellein G, Alvermann A and Fehske H 2006 The kernel polynomial method *Rev. Mod. Phys.* **78** 275–306
[51] Fan Z *et al* 2021 Linear scaling quantum transport methodologies *Phys. Rep.* **903** 1–69
[52] Panhans M , Hutsch S, Benduhn J, Schellhammer K S, Nikolis V C, Vangerven T, Vandewal K and Ortmann F 2020 Molecular vibrations reduce the maximum achievable photovoltage in organic solar cells *Nat. Commun.* **11** 1488
[53] Panhans M and Ortmann F 2021 Efficient time-domain approach for linear response functions *Phys. Rev. Lett.* **127** 016601
[54] Merkel K, Panhans M, Hutsch S and Ortmann F 2022 Interplay of band occupation, localization and polaron renormalization for electron transport in molecular crystals: naphthalene as a case study *Phys. Rev.* B **105** 165136
[55] Lautenschlager P, Garriga M, Vina L and Cardona M 1987 Temperature dependence of the dielectric function and interband critical points in silicon *Phys. Rev.* B **36** 4821–30
[56] Cardona M and Peter Y Y 2005 *Fundamentals of Semiconductors* vol 619 (Springer)
[57] Marini A 2008 *Ab initio* finite-temperature excitons *Phys. Rev. Lett.* **101** 106405
[58] Alliati I M, Sangalli D and Grüning M 2022 Double k-grid method for solving the Bethe-Salpeter equation via Lanczos approaches *Front. Chem.* **9** 763946
[59] Wannier G H 1937 The structure of electronic excitation levels in insulating crystals *Phys. Rev.* **52** 191–7
[60] Griffiths D J 2012 *Quantenmechanik : Eine Einführung* (Pearson Education Deutschland GmbH)

7 Conclusion and Outlook

In this work, we have investigated the electronic and optical properties of three different classes of organic and inorganic semiconductors. We have investigated the charge transport and electron-phonon coupling in organic molecular crystals, the electronic π-system, disorder and doping in covalent organic frameworks and presented a new method for calculating optical properties that scales linearly with the system size, which is a huge advantage compared to established methods.

For all those cases we have used a real space basis of localized functions such as molecular orbitals and MLWF. They turned out to be extremely beneficial in terms of computational performance and quality of results. The reason is that only a minimal number of basis function is needed per unit cell and the resulting Hamiltonian matrix within this basis becomes very sparse. This allows the construction of large supercells consisting of millions of unit cells that can be solved very efficiently with linear scaling algorithms. In the case of transport we presented a method that is able to consider electron-phonon coupling to the entire spectrum, where low-frequency modes are treated as vibrational disorder and high-frequency modes are included using polaron-renormalization. In the case of optical calculations it was shown that the electron-hole interaction can be evaluated very efficiently in a basis of MLWF. Since the Wannier functions are directly obtained from the underlying Bloch functions (Kohn-Sham wave functions) without any approximation, they contain all information about the electronic structure and can also be used to analyze the electronic structure, delocalization and π-conjugation in detail.

For the future, we can imagine that the methods presented will be further refined and become standard computational tools. Furthermore, it is possible that the different aspects could be combined. For example, it would in principle be possible to calculate optical properties in the presence of disorder, doping or electron-phonon coupling. Similarly, the results could be used to study exciton transport and exciton diffusion.

A Appendix

Copyright Agreement

1. Reprinted from Physical Review B, 105(16), 165136 (2022) with permission from the American Physical Society.
2. Reprinted from Scientific Reports, 13(1), 1685 (2023) which is licensed under the terms of the Creative Commons Attribution 4.0 license.
3. Reprinted from Journal of Physics: Materials 7, 015001 (2023) which is licensed under the terms of the Creative Commons Attribution 4.0 license.

Supporting Information for

Interplay of band occupation, localization, and polaron renormalization for electron transport in molecular crystals: naphthalene as a case study

Konrad Merkel*, Michel Panhans*, Sebastian Hutsch*, Frank Ortmann*

* Department of Chemistry, Technische Universität München, 85748 Garching b. München, Germany

Vibrational disorder from spectral moments of the one-electron spectrum of the Holstein-Peierls Hamiltonian

We derive an approximation for the Holstein-Peierls Hamiltonian H in which the electron-phonon coupling (EPC) results in a purely electronic vibrational disorder potential defined in Eq. (13) of the main text. The derivation is based on the equivalence of the spectral moments of the DOS of the Holstein-Peierls Hamiltonian and the DOS of an electronic system with specifically tailored electronic disorder that is obtained within the static approximation of the electron-phonon coupling. In this section, we demonstrate this equivalence based on the Holstein-Peierls Hamiltonian for purely symmetric coupling including all modes with intramolecular and intermolecular symmetric coupling.

We first introduce the vibrational disorder as an ansatz in site representation as follows:

$$V^{\mathrm{S}}(T) = \sum_{\lambda ij} \sigma_{ij}^{\mathrm{S}\lambda}(T) \frac{\left(\phi_i^\lambda + \phi_j^\lambda\right)}{2} a_i^\dagger a_j, \tag{S1}$$

with standard deviation of $\sigma_{ij}^{\mathrm{S}\lambda}(T) = g_{ij}^{\mathrm{S}\lambda} \hbar\omega_\lambda \sqrt{(1 + 2\langle n_\lambda \rangle_T)}$ and a normalized Gaussian random variable ϕ_i^λ generating Gaussian random numbers for each molecular site and each vibrational mode. We calculate the DOS of this model

$$D(E) = -\frac{1}{\pi} \Im \left(\int_{-\infty}^{\infty} dt\, \Theta(t) e^{\frac{itE}{\hbar}} G(t) \right), \tag{S2}$$

using the definition of the momentum-averaged Green's function

$$G(t) = -\frac{i}{\hbar} \frac{\mathrm{Tr}_{\mathrm{el}}\left(e^{-\frac{it(H_{\mathrm{el}} + V^{\mathrm{S}}(T))}{\hbar}} \right)}{\mathrm{Tr}_{\mathrm{el}}(\mathbb{1}_{\mathrm{el}})}. \tag{S3}$$

The moments of the averaged Green's function are defined from the series expansion

$$G(t) = \left(-\frac{i}{\hbar}\right) \sum_{k=0}^{\infty} \frac{1}{k!} \left(\frac{it}{\hbar}\right)^k M^{(k)}, \tag{S4}$$

which are equivalent to the spectral moments $M^{(k)}$ of the DOS

$$M^{(k)} = \int_{-\infty}^{\infty} dE\, E^k D(E). \tag{S5}$$

In this derivation, we focus on the calculation of the spectral moments for $H_{\mathrm{el}} = 0$,

$$M^{(k)} = \frac{\mathrm{Tr}_{\mathrm{el}}\left(V^{\mathrm{s}}(T)^k\right)}{\mathrm{Tr}_{\mathrm{el}}(\mathbb{1}_{\mathrm{el}})}. \tag{S6}$$

One can show by applying Isserlis' or Wick's probability theorem [1] [2] for Gaussian random numbers that the spectral moments $M^{(k)}$ can be expressed as

$$M^{(2k)} = (2k-1)!!\ \frac{\mathrm{Tr}_{\mathrm{el}}\left(\left(\sigma^2\right)^k\right)}{\mathrm{Tr}_{\mathrm{el}}(\mathbb{1}_{\mathrm{el}})}, \tag{S7}$$

$$M^{(2k+1)} = 0, \tag{S8}$$

with an operator-valued variance σ^2. The expectation value $\mathrm{Tr}_{\mathrm{el}}\left(\sigma^{2k}\right)$ can explicitly be evaluated in the electronic momentum space:

$$\mathrm{Tr}_{\mathrm{el}}\left(\sigma^{2l}\right) = \sum_{\mathbf{k}}\left(\sigma^2_{\mathbf{kk}}\right)^l, \tag{S9}$$

with

$$\sigma^2_{\mathbf{kk}} = \sum_\lambda \frac{\hbar\omega_\lambda\sqrt{(1+2\langle n_\lambda\rangle_T)}}{4}\left(\sum_m g^{\mathrm{s}\lambda}_{0m}\, g^{\mathrm{s}\lambda}_{m0} + 2\sum_m g^{\mathrm{s}\lambda}_{00}\, g^{\mathrm{s}\lambda}_{m0} e^{i\mathbf{k}\cdot\mathbf{R}_{0m}} + \sum_{mn} g^{\mathrm{s}\lambda}_{0m} g^{\mathrm{s}\lambda}_{mn}\, e^{i\mathbf{k}\cdot\mathbf{R}_{0n}}\right). \tag{S10}$$

Here, we have used the translational invariance of the coupling constants, i.e. $g^{\mathrm{s}\lambda}_{ij} = g^{\mathrm{s}\lambda}_{0j-i} = g^{\mathrm{s}\lambda}_{0m}$. In Eq. (S9) the sum over m runs over all nearest-neighbor molecules and the sum over n runs over all nearest-neighbor molecules of m. The vectors $\mathbf{R}_{0m} = \mathbf{R}_j - \mathbf{R}_i$ correspond to the lattice vectors and are also translation invariant. We compare this result to the case of purely local coupling, which is obtained by setting $g^{\mathrm{s}\lambda}_{ij} = g^{\mathrm{s}\lambda}_{ii}\delta_{ij}$, and see that Eq. (S10) reduces to $\sigma^2_{\mathbf{kk}} = \sum_\lambda\left(\sigma^{\mathrm{s}\lambda}_{00}\right)^2$, which is the standard deviation that results from intramolecular coupling. The vibrational disorder derived from purely local coupling has been applied in previous studies [3] [4].

We now show that the same result for the spectral moments $M^{(k)}$ is obtained within the static approximation of the EPC in the Holstein-Peierls Hamiltonian. For this purpose, we consider the averaged Green's function for a single particle in the form

$$G(t) = -\frac{i}{\hbar}\frac{\mathrm{Tr}\left(e^{-\beta H_{\mathrm{ph}}} e^{\frac{itH_{\mathrm{ph}}}{\hbar}} e^{-\frac{itH}{\hbar}}\right)}{\mathrm{Tr}\left(e^{-\beta H_{\mathrm{ph}}}\right)}, \tag{S11}$$

where the trace is taken over all one-electron multiple-phonon states in this case.

We now use the Baker-Campbell-Hausdorff formula to define an approximate Green's function,

$$G_{\mathrm{stat}}(t) = -\frac{i}{\hbar}\frac{\mathrm{Tr}\left(e^{-\beta H_{\mathrm{ph}}} e^{\frac{it\left(H_{\mathrm{el}}+H_{\mathrm{el-ph}}\right)}{\hbar}}\right)}{\mathrm{Tr}\left(e^{-\beta H_{\mathrm{ph}}}\right)}, \tag{S12}$$

in which all nested commutators involving H_{ph} are neglected in the time-dependent exponent. This limit corresponds to the static treatment of the EPC, in which we assume that the mode amplitudes in $H_{\mathrm{el-ph}}$ become static.

The above expression for the averaged Green's function can be evaluated analytically in the special case where $H_{\mathrm{el}} = 0$, using Wick's theorem for independent bosons [5],

$$G_{\mathrm{stat}}(t) = \frac{\mathrm{Tr}_{\mathrm{el}}\left(e^{-\frac{t^2\sigma^2}{2\hbar^2}}\right)}{\mathrm{Tr}_{\mathrm{el}}(\mathbb{1}_{\mathrm{el}})}, \tag{S13}$$

with the operator-valued variance σ^2 that reads in the site basis,

$$\sigma^2 = \sum_\lambda \frac{1}{4}(\hbar\omega_\lambda)^2(1 + 2\langle n_\lambda\rangle_T)\{\left[\sum_{ij} g_{ij}^{s\lambda}\left(g_{ii}^{s\lambda} + g_{jj}^{s\lambda}\right) + \sum_{il} g_{il}^{s\lambda}\, g_{li}^{s\lambda} + \sum_{ijl} g_{il}^{s\lambda} g_{lj}^{s\lambda}\right] a_i^\dagger a_j - 2\sum_{ilj} g_{il}^{s\lambda} g_{lj}^{s\lambda} a_i^\dagger a_l^\dagger a_l a_j \}. \tag{S14}$$

The two-particle term in Eq. (S13) can be neglected since only one-particle averages are considered. This assumption corresponds to the limit of low charge-carrier densities [6].

Taking into account the translational symmetry of the coupling constants, we find

$$\sigma^2 = \sum_{\mathbf{k}} \sigma_{\mathbf{kk}}^2 a_{\mathbf{k}}^\dagger a_{\mathbf{k}}, \tag{S15}$$

with the same matrix elements as given in Eq. (S10). The spectral moments $M_{\mathrm{stat}}^{(k)}$ are obtained from Eq. (S13) by evaluating the power-series expansion of $G_{\mathrm{stat}}(t)$ around $t = 0$,

$$M_{\mathrm{stat}}^{(2k)} = (2k-1)!!\ \frac{\mathrm{Tr}_{\mathrm{el}}\left((\sigma^2)^k\right)}{\mathrm{Tr}_{\mathrm{el}}(\mathbb{1}_{\mathrm{el}})}, \tag{S16}$$

$$M_{\mathrm{stat}}^{(2k+1)} = 0. \tag{S17}$$

Consequently, we find that all moments of the one-electron DOS are equal, i.e.,

$$M^{(k)} = M_{\mathrm{stat}}^{(k)}, \tag{S18}$$

and thus obtain the equivalence of the introduced vibrational disorder with the static treatment of the EPC in the Holstein-Peierls Hamiltonian.

In conclusion, the approximation made in Eq. (S12) leads to an effective description of the EPC using a vibrational disorder potential, which only depends on the electronic degrees of freedom. We note that the present derivation is provided for symmetric EPC only but remains valid also in the presence of antisymmetric EPC.

In addition, it is straightforward to prove the equivalence of the spectral moments in Eq. (S18) for purely intramolecular coupling since then the operator σ^2 becomes trivial, namely

$$\sigma^2 = \sum_\lambda \left(\sigma_{ii}^{s\lambda}\right)^2 a_i^\dagger a_i, \tag{S19}$$

whose spectral moments can directly be compared with those calculated from a purely intramolecular disorder potential

$$V_{\mathrm{intra}}(T) = \sum_{i\lambda} \sigma_{ii}^{s\lambda} \phi_i^{\lambda} a_i^{\dagger} a_i \, . \tag{S20}$$

We thus introduce the substitution rule for the phonon amplitudes as

$$b_{i\lambda}^{\dagger} + b_{i\lambda} \rightarrow \phi_i^{\lambda}, \tag{S21}$$

which automatically generates the vibrational disorder potential in correspondence with the static treatment of the EPC.

References

[1] L. Isserlis, Biometrika **12**, 134 (1918).

[2] G. C. Wick, Phys. Rev. **80**, 268 (1950).

[3] S. Hutsch, M. Panhans, and F. Ortmann, Phys. Rev. B **104**, 54306 (2021).

[4] M. Panhans, S. Hutsch, J. Benduhn, K. S. Schellhammer, V. C. Nikolis, T. Vangerven, K. Vandewal, and F. Ortmann, Nat. Commun. **11**, 1488 (2020).

[5] P. Danielewicz, Ann. Phys. **152**, 239 (1984).

[6] F. Ortmann, F. Bechstedt, and K. Hannewald, Phys. Rev. B **79**, 235206 (2009).

– Supporting Information – Understanding the electronic pi-system of 2D covalent organic frameworks with Wannier functions

Konrad Merkel, Johannes Greiner and Frank Ortmann*
TUM School of Natural Sciences, Technical University of Munich

September 27, 2022

SI-1 Quality of Wannierization

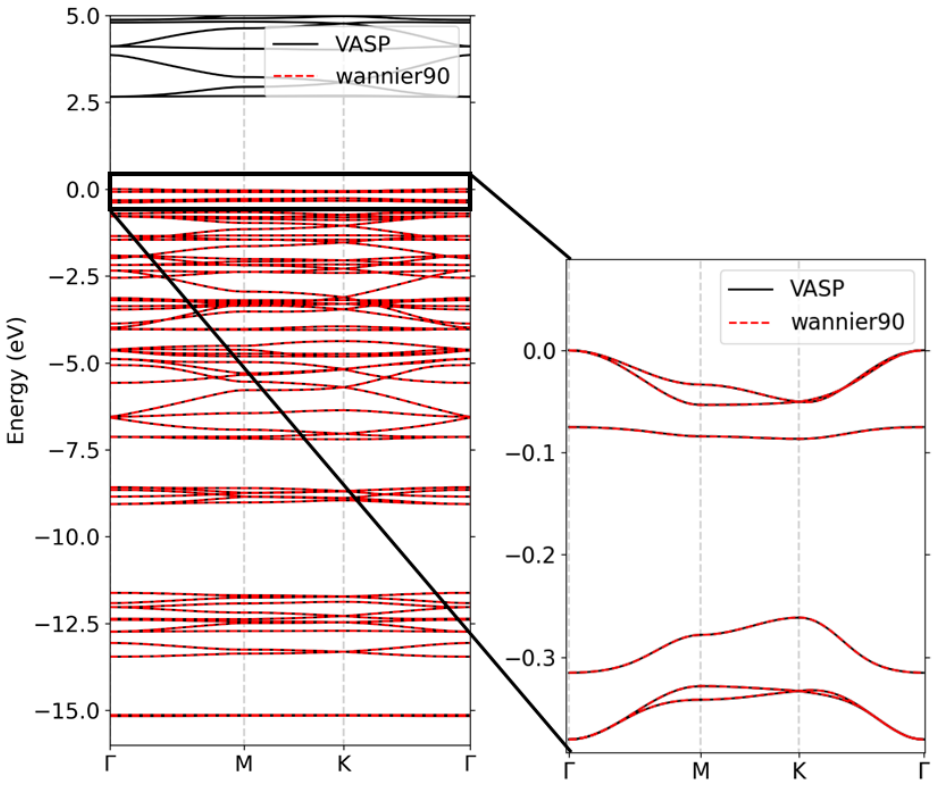

Figure SI-1: Comparison between band structure before the wannierization (VASP) and after wannierization (wannier90).

SI-2 Orbitals and Transfer Integrals

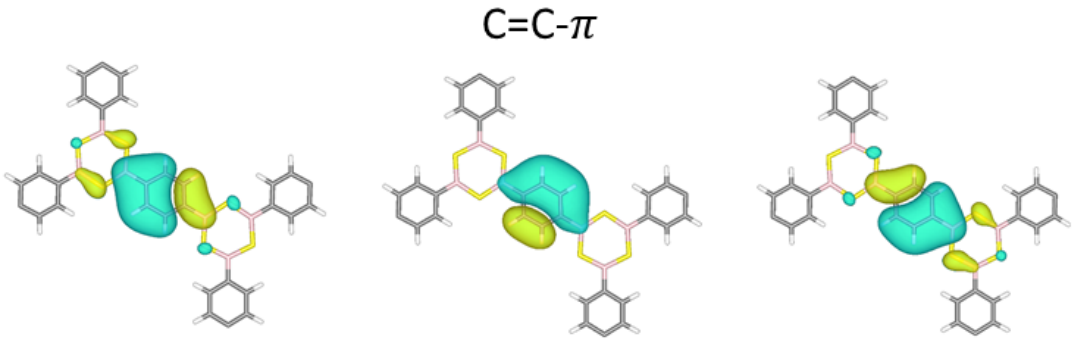

Figure SI-2: All C=C-π orbitals of a single phenyl ring. Shapes are similar but small deformations occur in the vicinity of the linker.

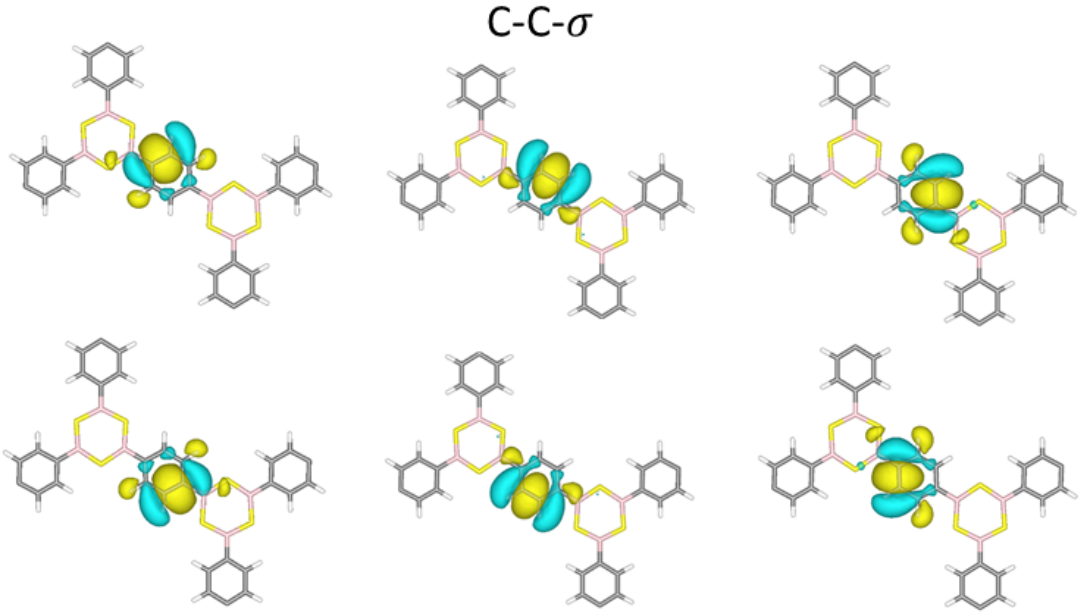

Figure SI-3: All C-C-σ orbitals of a single phenyl ring. Shapes are similar but small deformations occur in the vicinity of the linker. C-C-σ orbitals at single and double bond positions (C-C-σ_s, C-C-σ_d) have the same shape.

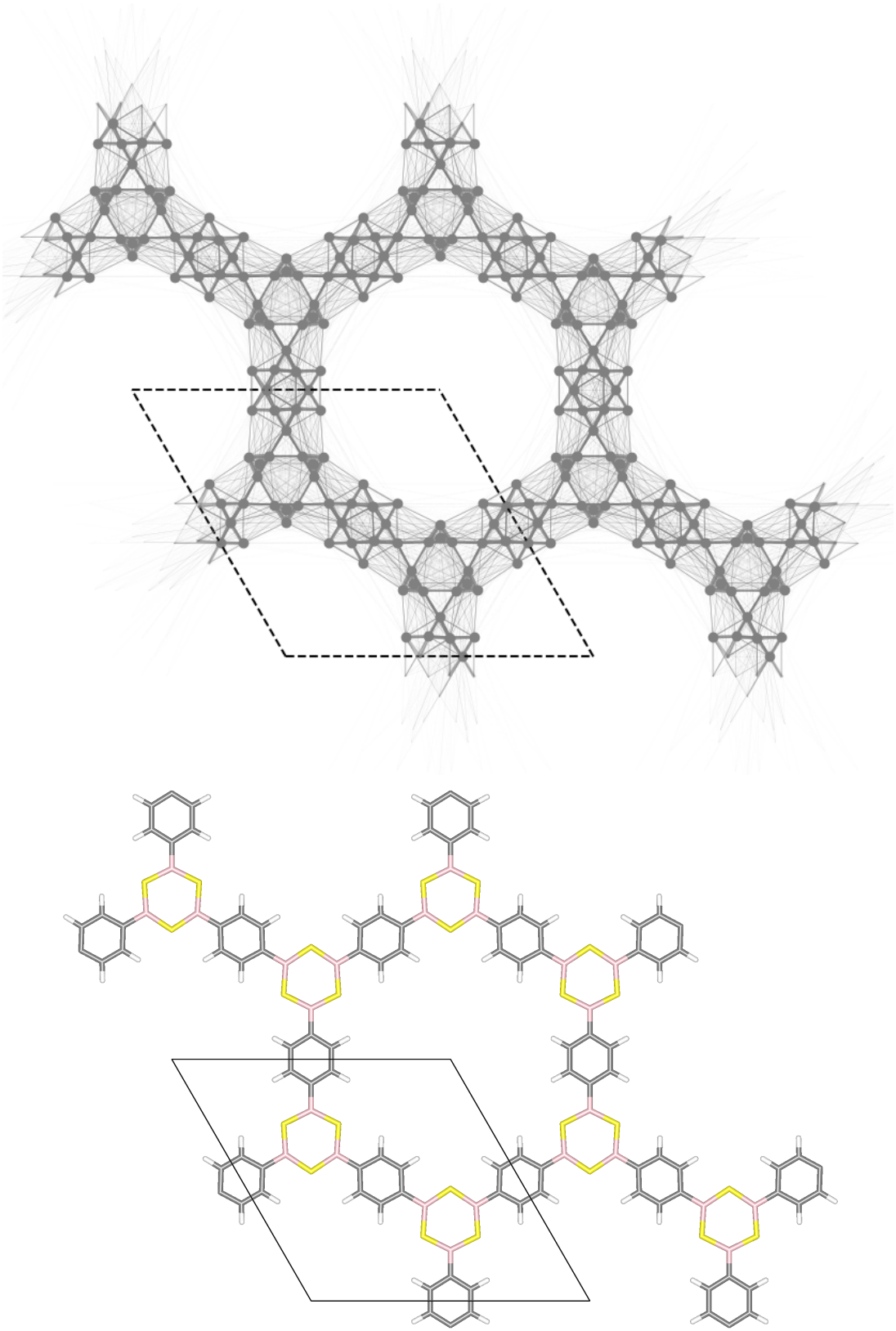

Figure SI-4: Map of transfer integrals (TI) larger than 1 meV for COF-BS-1Ph. Dots represent the center of every Wannier orbital, straight lines show the corresponding TI between orbitals, where the line width characterizes the value of the TI. The unit cell is highlighted with dashed lines. The lower panel shows the corresponding COF-pore.

(a) COF-BO-1Ph

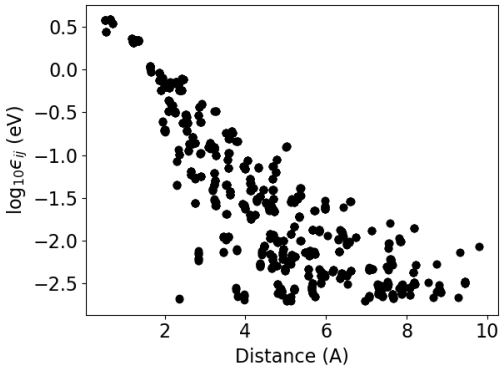

(b) COF-BO-2Ph

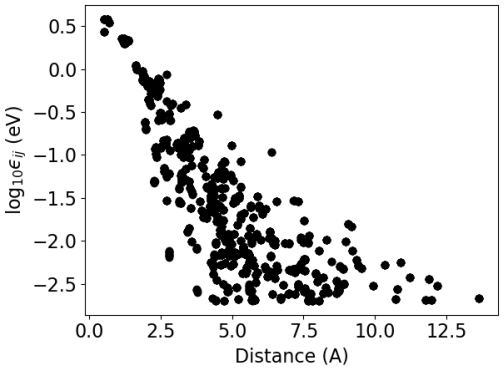

(c) COF-BS-1Ph

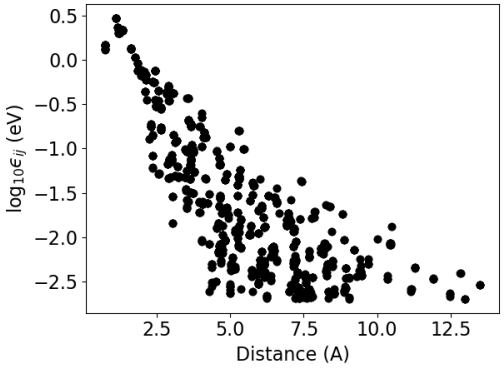

(d) COF-BS-2Ph

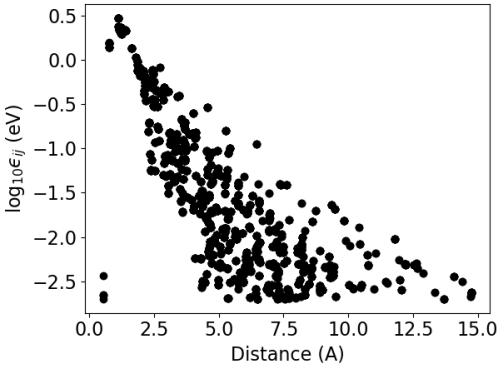

(e) COF-CN-1Ph

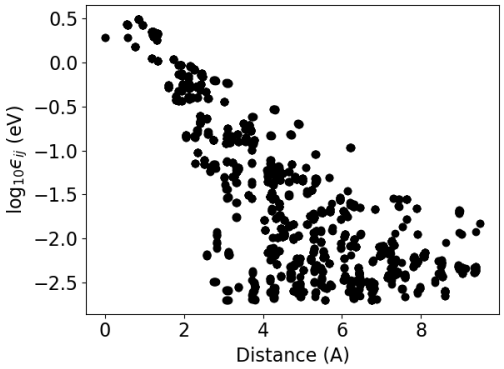

(f) COF-CN-2Ph

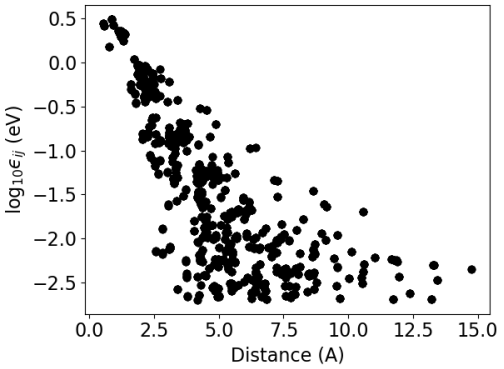

(g) COF-CC-1Ph

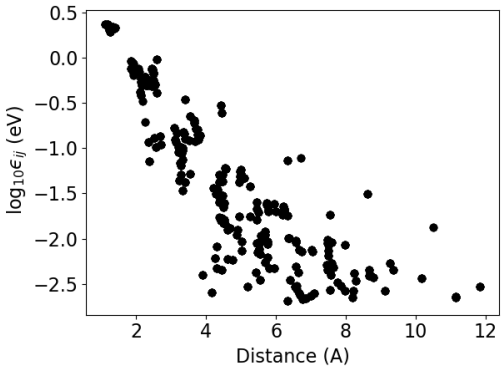

Figure SI-5: Values of Transfer integrals (log) and their distance. All figures show that TI become exponentially suppressed for large distances.

SI-3 Band Structure

The subsequent figures show the valence band structures and their projection onto the π-system for the investigated COFs. Systematic investigations of the band gap for COF-BO-1Ph, COF-BO-2Ph, COF-CN-1Ph and COF-CN-2Ph can be found in Ref.[1].

(a) COF-BO-1Ph

(b) COF-BO-2Ph

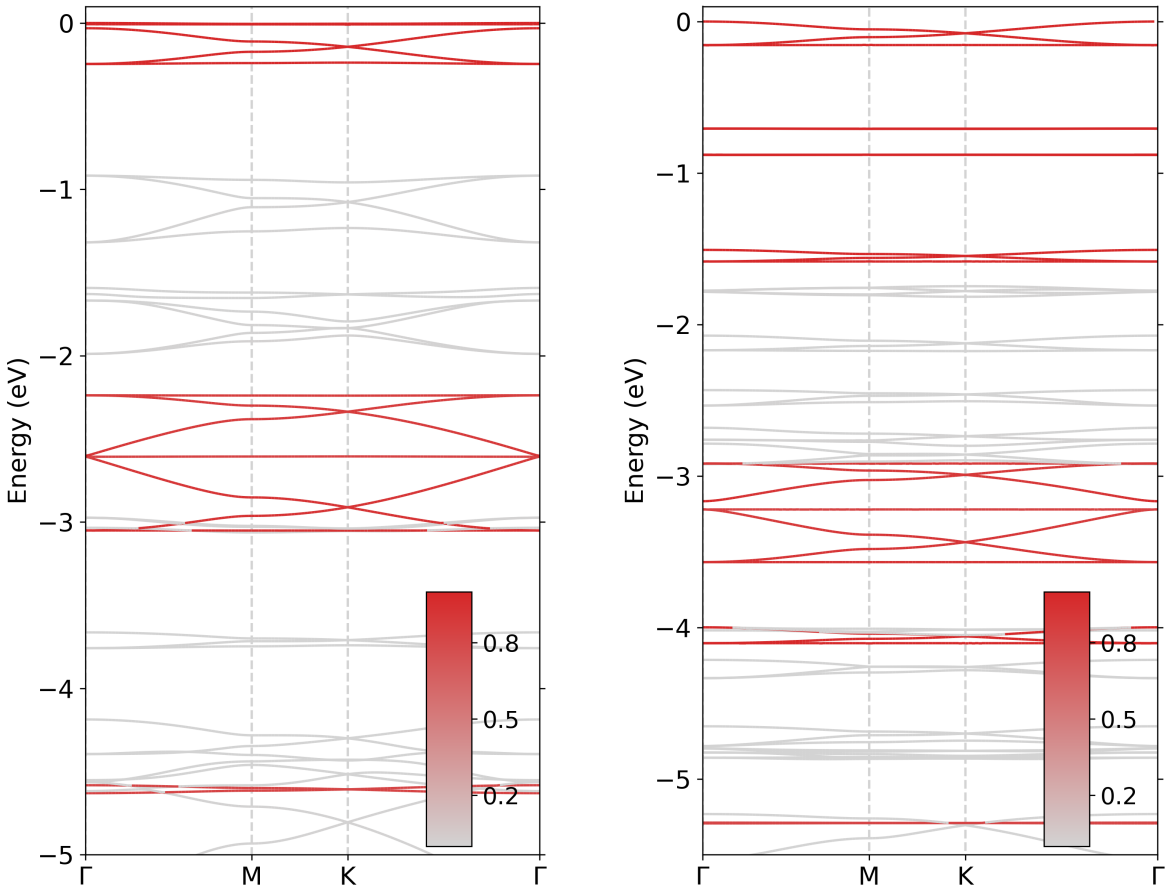

Figure SI-6: Band structures for BO-COFs

(a) COF-BS-1Ph

(b) COF-BS-2Ph

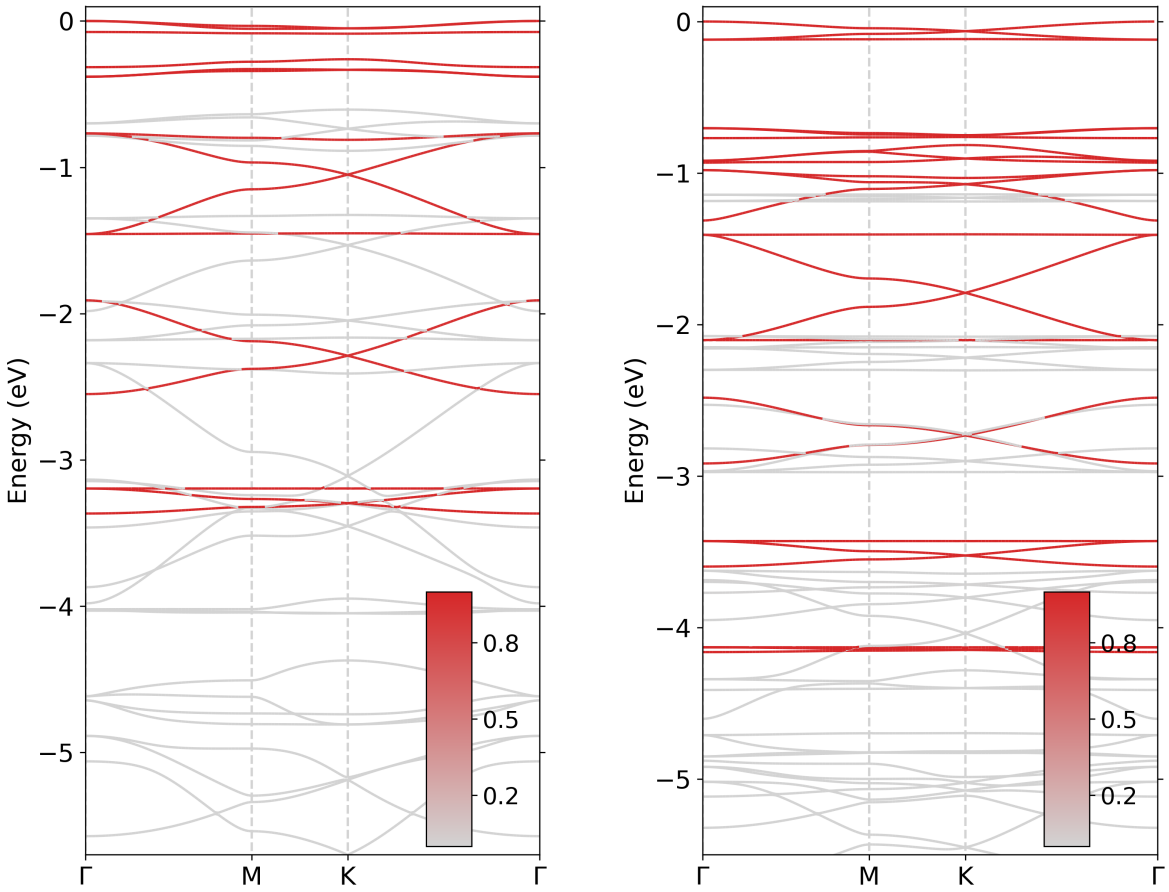

Figure SI-7: Band structures for BS-COFs

(a) COF-CN-1Ph

(b) COF-CN-2Ph

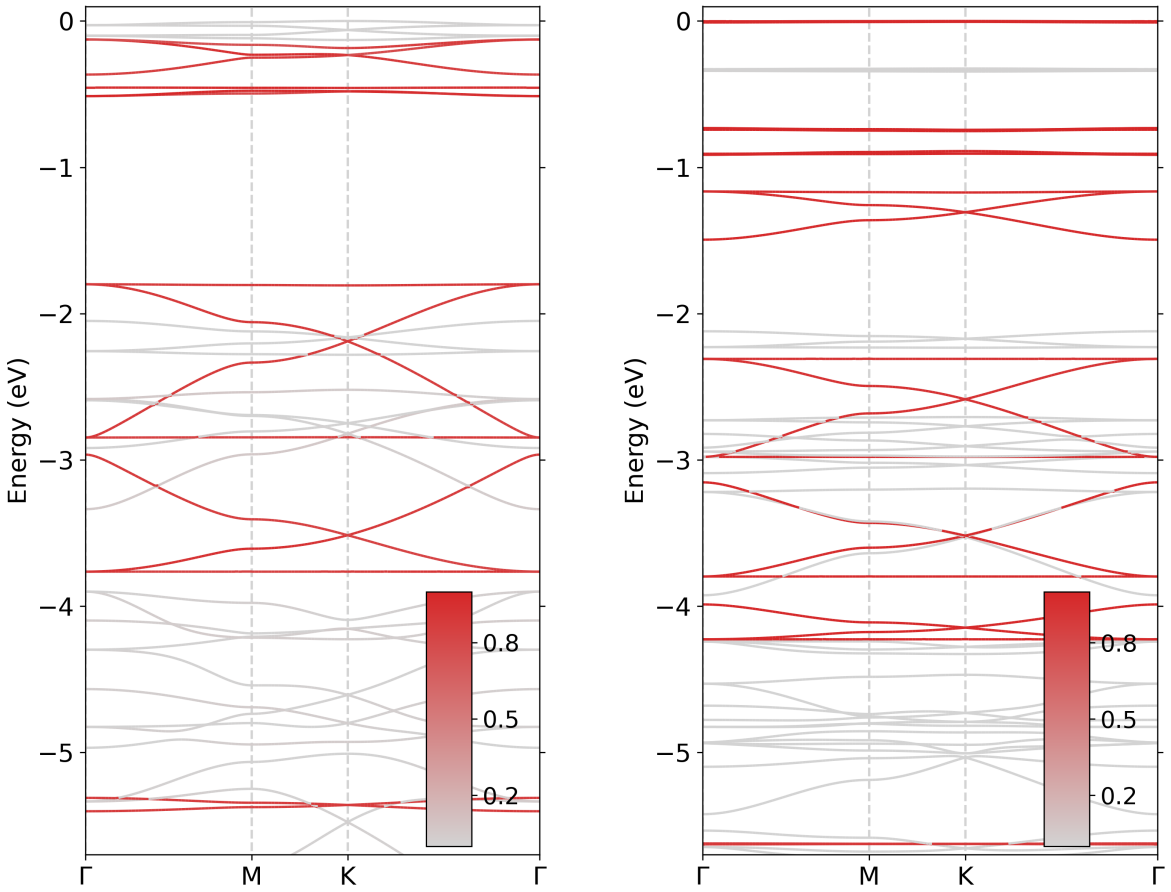

Figure SI-8: Band structures for CN-COFs

(a) COF-CC-1Ph

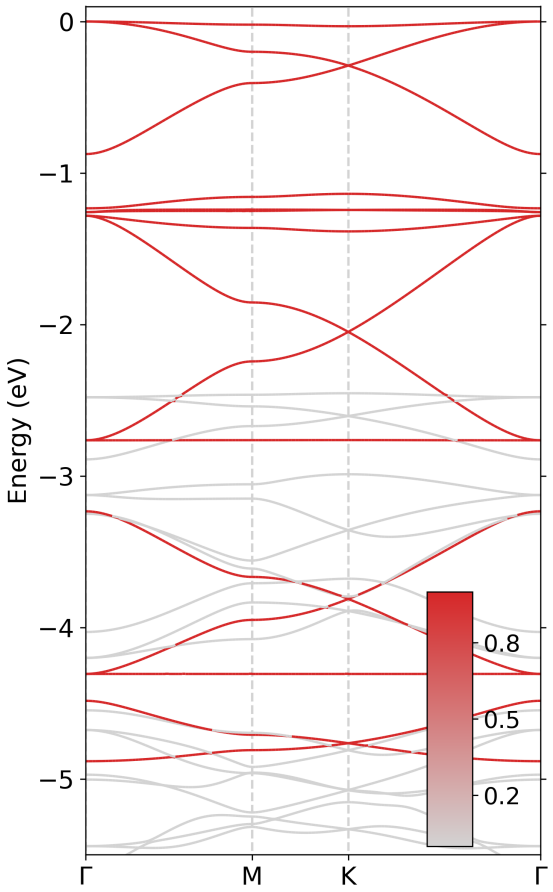

Figure SI-9: Band structure for reference COF

Table SI-1: Bandwidth of 1Ph COFs in eV

Band group	COF-CC-1Ph	COF-BS-1Ph	COF-CN-1Ph	COF-BO-1Ph
1	0.875	0.075	0.24	0.008
2	0.026	0.065	0.058	0.215
3	1.483	0.675	1.048	0.363
4	1.074	0.641	0.800	0.443
5	0.399	0.171	0.091	0.048

Table SI-2: Bandwidth of 2Ph COFs in eV

Band group	COF-BS-2Ph	COF-CN-2Ph	COF-BO-2Ph
1	0.12	0.008	0.156
2	0.066	0.011	0.0003
3	0.013	0.007	0.001
4	0.333	0.33	0.077
5	0.695	0.669	0.249
6	0.434	0.644	0.348
7	0.168	0.238	0.105
8	0.032	0.006	0.005

SI-4 Bader Charge

Bader charges[2,3] are calculated for the ground state using the bader charge analysis code[4,5]. DFT calculations are described in the methods section of the main text. Results are shown in Tab. SI-3.

Table SI-3: Bader charge of linker species for all COFs.

COF	Linker Atom 1 (X=C,B) [C]	Linker Atom 2 (Y=S,N,O,C) [C]
COF-CC-1Ph	4.1	3.9
COF-BS-1Ph	1.3	7.1
COF-BS-2Ph	1.3	7.1
COF-CN-1Ph	3.0	6.1
COF-CN-2Ph	2.9	6.2
COF-BO-1Ph	0.8	7.5
COF-BO-2Ph	0.8	7.5

SI-5 Effective Mass

Effective masses are obtained in the real space basis of MLWF as described in Ref.[6]. $\boldsymbol{k}$-derivatives of the Fourier series (c.f. Eq. (1) in the main text) can be performed analytically, where the only difficulty is the calculation of $\nabla_{\boldsymbol{k}} U_{nm}(\boldsymbol{k})$, which can be obtained by $\boldsymbol{k}\cdot\boldsymbol{p}$ perturbation theory[6,7]. The obtained effective masses in Tab. SI-4 show better or equally good agreement than direct fits of the band structure, which are always dependent on finite $\boldsymbol{k}$-differences. Degenerate bands are denoted with * or †. Components of m^* are given with respect to reciprocal lattice vectors. The eigenvalues of m^* are given in the last two columns. In general the effective mass tensors for different bands do not share the same eigensystem.

Bands near the Fermi level are very flat for all COFs except for COF-CC-1Ph ($\Delta E = 0.88\,\mathrm{eV}$). The resulting effective masses are therefore very high. Flat bands (from kgm bands) only have finite effective masses due to distortions.

The highest occupied bands are π-bands, except for COF-CN-1Ph, where the highest occupied bands originate from lone-pair (lp) orbitals at the linker and are very flat.

Table SI-4: Effective mass tensor m^* at Γ-point expressed in reciprocal basis for uppermost group of bands in units of electron rest mass m_e. Degeneracies at Γ-point among a group are marked with * or †. The underlying orbitals that correspond to the a band are given in brackets (π or lp). The effective mass tensor is symmetric $m^*_{12} = m^*_{21}$. Last two columns contain the eigenvalues of the effective mass tensor.

Material	Band	m^*_{11} (m_e)	m^*_{22} (m_e)	m^*_{12} (m_e)	Eig.val. 1 (m_e)	Eig.val. 2 (m_e)
COF-CC-1Ph	HOMO* (π)	-37.9	-42.6	35.7	-4.4	-76.1
COF-CC-1Ph	HOMO-1* (π)	-21.7	-17.1	-5.9	-25.7	-13.0
COF-CC-1Ph	HOMO-2 (π)	1.5	1.5	-0.8	2.3	0.8
COF-BS-1Ph	HOMO* (π)	-27.8	-28.1	16.2	-11.7	-44.2
COF-BS-1Ph	HOMO-1* (π)	-25.1	-24.8	10.3	-35.2	-14.7
COF-BS-1Ph	HOMO-2 (π)	-257.9	-257.7	135.1	-392.9	-122.7
COF-CN-1Ph	HOMO* (lp)	11.4	-322.3	79.7	29.4	-340.4
COF-CN-1Ph	HOMO-1* (lp)	-291.8	15.2	68.0	-306.2	29.6
COF-CN-1Ph	HOMO-2† (lp)	160.1	131.9	-166.9	313.4	-21.5
COF-CN-1Ph	HOMO-3† (lp)	8.1	33.8	83.8	-63.9	105.7
COF-CN-1Ph	HOMO-4* (π)	-26.1	-19.9	7.7	-31.3	-14.6
COF-CN-1Ph	HOMO-5* (π)	-24.9	-30.9	17.7	-9.9	-45.9
COF-CN-1Ph	HOMO-6 (π)	16.8	16.8	-8.4	8.4	25.2
COF-BO-1Ph	HOMO* (π)	-237.5	-193.3	103.9	-321.6	-109.1
COF-BO-1Ph	HOMO-1* (π)	-194.6	-239.2	112.2	-102.5	-331.3
COF-BO-1Ph	HOMO-2 (π)	-8406.2	4061.0	-13477.5	-17021.9	12676.7
COF-BS-2Ph	HOMO (π)	-33.8	-33.7	16.8	-50.6	-16.9
COF-BS-2Ph	HOMO-1* (π)	209.5	87.9	64.1	237.0	60.3
COF-BS-2Ph	HOMO-2* (π)	269.8	388.3	-301.2	22.1	636.0
COF-CN-2Ph	HOMO* (π)	7205.5	1747.0	2510.9	8184.8	767.7
COF-CN-2Ph	HOMO-1* (π)	-7256.0	-11618.3	9476.5	287.0	-19161.4
COF-CN-2Ph	HOMO-2 (π)	292.8	304.6	-159.3	139.3	458.1
COF-BO-2Ph	HOMO-0 (π)	-29.7	-29.8	14.9	-14.9	-44.6
COF-BO-2Ph	HOMO-1* (π)	1005.1	1724.6	1271.7	43.3	2686.4
COF-BO-2Ph	HOMO-2* (π)	3611.2	3015.1	-3285.0	6611.6	14.7

Similar states also exist in COF-CN-2Ph but with lower energy, which makes them unimportant for transport. For COF-CN-1Ph we have given the top nine bands to also provide information about the top bands of the π-system.

SI-6 Onsite energy

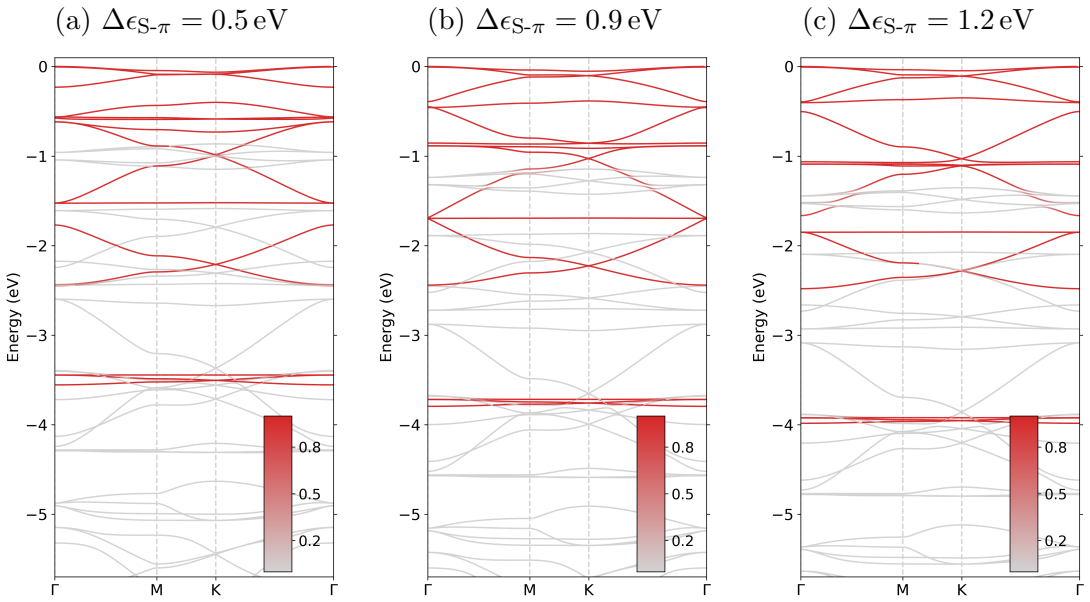

Figure SI-10: Band structure of COF-BS-1Ph for different changes of S-π onsite energy. Fermi energy is chosen individually to be the valence band maximum in each plot.

SI-7 Robustness and Breaking of π-Conjugation by Bond Torsion

(a) COF-BS-1Ph

(b) COF-CN-1Ph

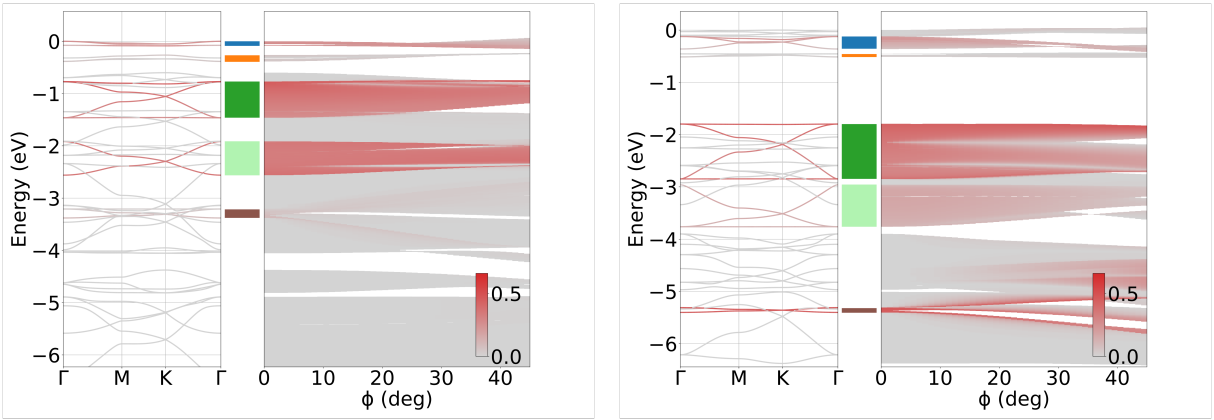

(c) COF-BO-1Ph

(d) COF-CC-1Ph

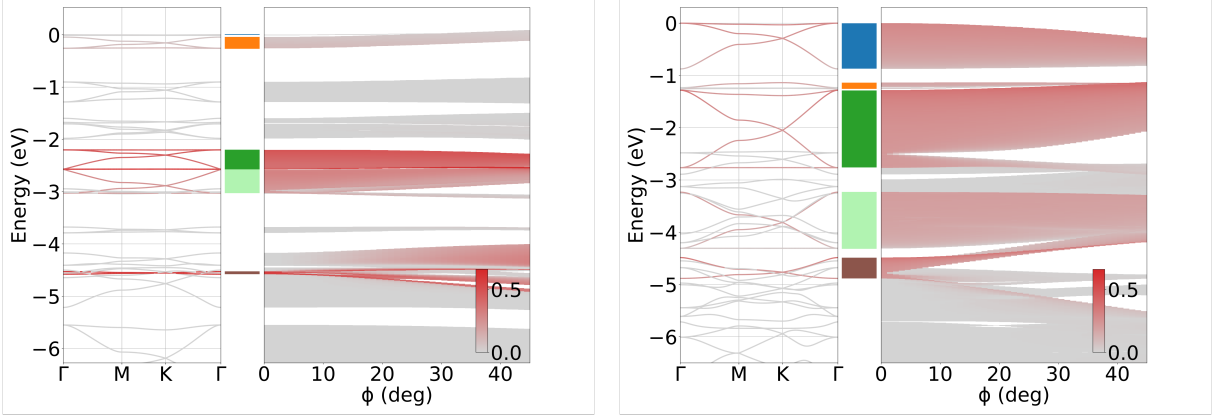

Figure SI-11: Band structure for one phenyl systems (including projection on p_z-orbitals at linker positions) and impact of rotation of the phenyl rings on band width and projection. The energy zero is set to the valence band maximum of the planar structure.

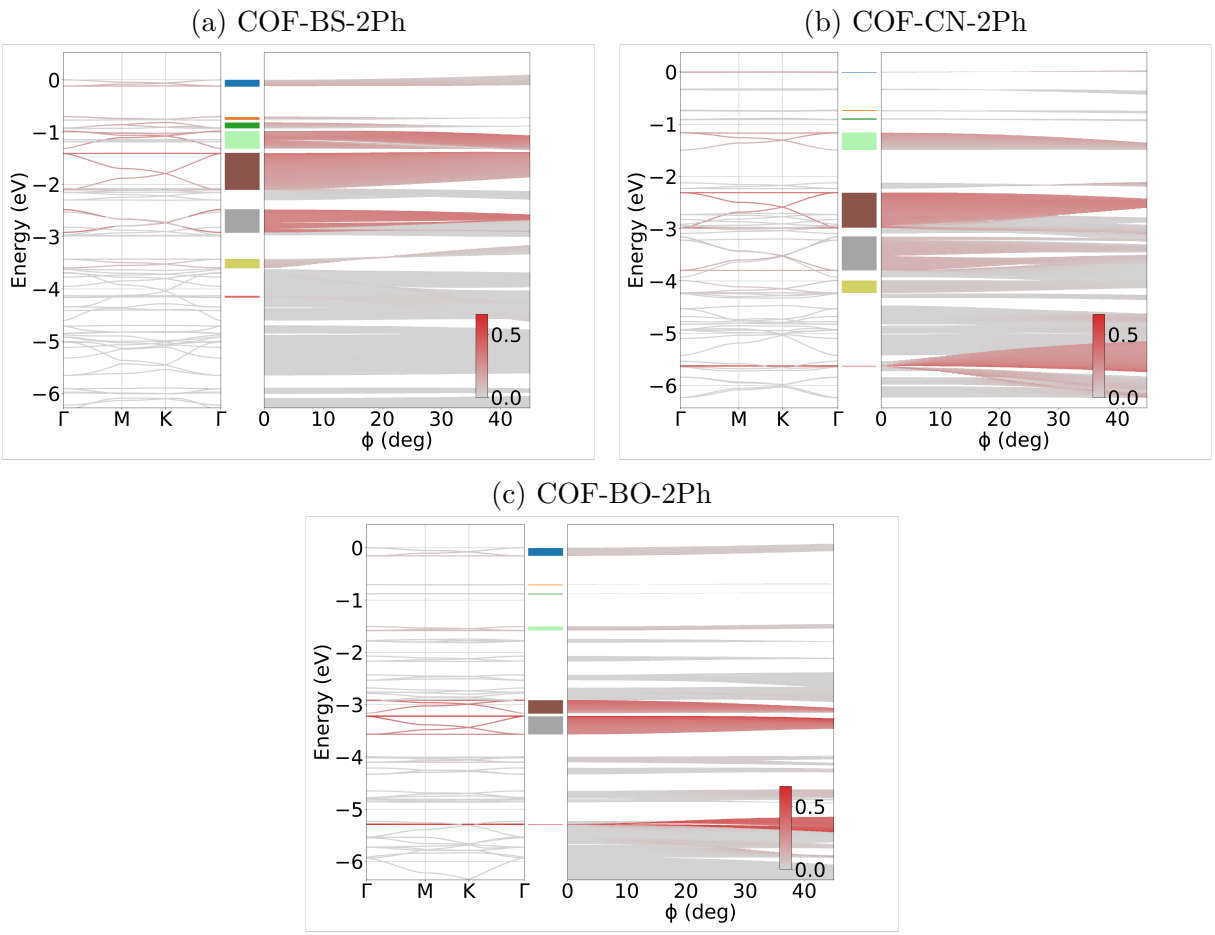

Figure SI-12: Band structure for two phenyl systems (including projection on p_z-orbitals at linker positions) and impact of rotation of the phenyl rings on band width and projection. The energy zero is set to the valence band maximum of the planar structure.

To elaborate the changes of the electronic structure we extend our analysis by comparing our results with the *projected norm* (PN) of $P^{(\phi)}(E)$, which is defined as,

$$PN(\phi) := \int_{-\infty}^{E_F} dE \ \left|P^{(\phi)}(E)\right|^2 . \tag{SI-1}$$

In contrast to CBW (see main text for definition) PN does not depend on any adjustable threshold parameter and is therefore more sensitive to small changes in $P^{(\phi)}(E)$. Including the actual values of $P^{(\phi)}(E)$ makes $PN(\phi)$ also sensitive to possible redistribution of charge density and localization like we have observed for the top kgm-bands near the Fermi-level, which relocate their charge density at the linker completely into p_x and p_y-like orbitals for large ϕ. It is therefore not surprising that $PN(\phi)$ highlights the decline of global π-conjugation even more than $CBW(\phi)$, as can be seen in Fig. SI-13(e)-(f).

In particular, $PN(\phi)$ of COF-CN-1Ph decreases faster than $PN(\phi)$ of COF-CC-1Ph, whereas for CBW it is vise versa. This effect is caused not only by the decrease in projection, but also by gaps in the third π-band (dark green), which are caused by symmetry breaking. COF-CN-1Ph and COF-CN-2Ph show the largest decline. They are therefore more sensitive to rotation as COF-BS-1Ph and COF-BS-2Ph as well as COF-CC-1Ph.

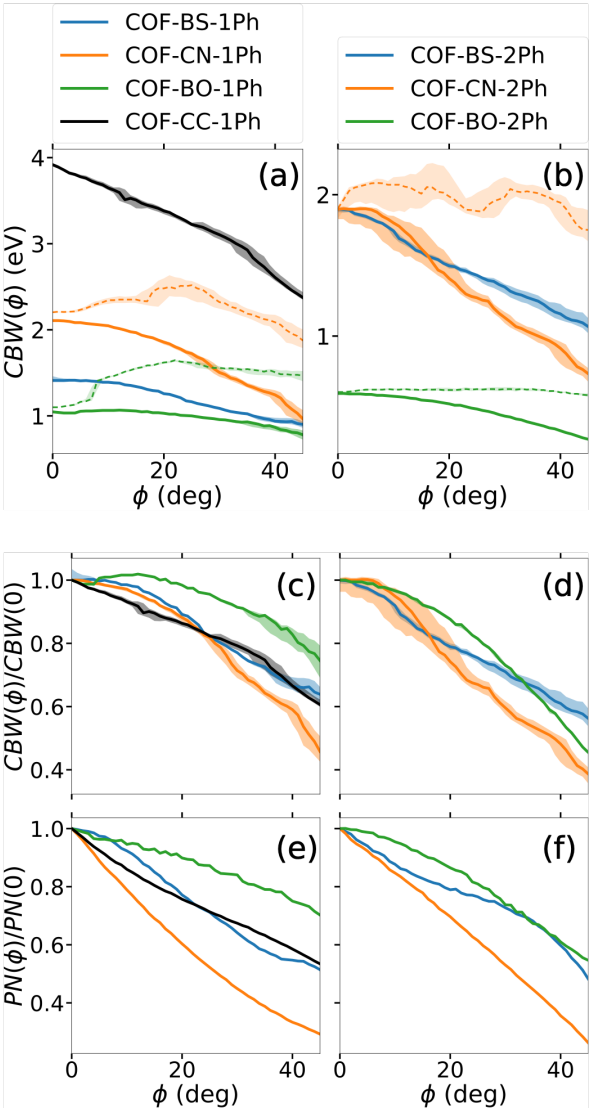

Figure SI-13: Quantitative measures that characterize the influence of rotations. (a)-(b) Cumulative bandwidth $CBW(\phi)$. (c)-(d) Normed cumulative bandwidth $CBW(\phi)/CBW(0)$. (e)-(f) Normed potential norm $PN(\phi)/PN(0)$. All solid lines focus on the upper *pi*-groups (near the Fermi-level); the dashed lines in (a)-(b) show the measurement for all π-groups. The colored areas indicate the deviations at a 15% change of P_{min}.

An initial increase in $PN(\phi)$ is observed for COF-BO-1Ph. This is also caused by a gap in a π-band due to symmetry breaking.

For all other COFs $PN(\phi)$ behaves very similarly to $CBW(\phi)$, which shows that the linker projection only changes merely upon rotation and further justifies our choice of P_{min} for $CBW(\phi)$.

SI-8 NICS

Table SI-5: Upper bounds of NICS values that originate from ring currents. All values are smaller than numerical precision of the calculation independent of the partition scheme.

COF	NICS (ppm)	Percentage of entire NICS value from COF-pore
COF-CC-1Ph	-0.13	-3.7%
COF-BS-1Ph	0.026	0.8%
COF-CN-1Ph	0.006	0.1%
COF-BO-1Ph	0.024	0.7%

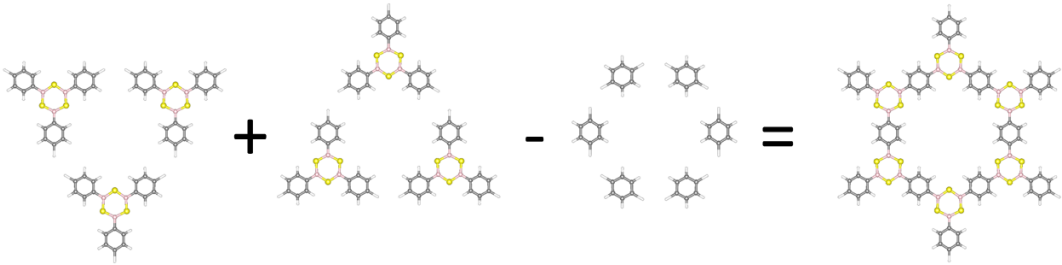

Figure SI-14: Alternative partition scheme for calculating the ring current contribution to NICS. Ring current contribution of NICS was found to be smaller than 0.03ppm, which is smaller than numerical precision for every COF.

SI-9 Shannon Aromaticity

The Shannon aromaticity[8] is defined as

$$S = -\int dr\, \rho(\boldsymbol{r}) \ln \rho(\boldsymbol{r}), \tag{SI-2}$$

which is the Shannon entropy[9] of the ground state charge density $\rho(\boldsymbol{r})$. Values for all COFs are shown in Fig. SI-15. Please note that 1Ph COFs and 2Ph COFs cannot be compared directly due to their different sizes of the unit cell.

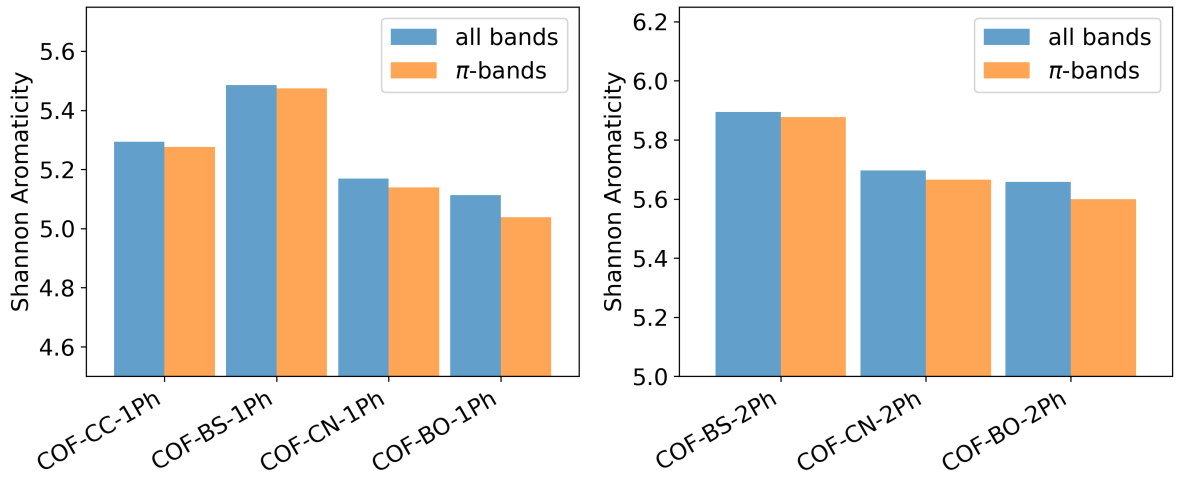

Figure SI-15: Shannon aromaticity

References

[1] Zhu, P. & Meunier, V. Electronic properties of two-dimensional covalent organic frameworks. *J. Chem. Phys.* **137**, 244703 (2012).

[2] Bader, R. F. W. A quantum theory of molecular structure and its applications. *Chem. Rev.* **91**, 893–928 (1991). URL `https://doi.org/10.1021/cr00005a013`. `https://doi.org/10.1021/cr00005a013`.

[3] Bader, R. F. W. The quantum mechanical basis of conceptual chemistry. *Monatsh. Chem.* **136**, 819–854 (2005). URL `https://doi.org/10.1007/s00706-005-0307-x`.

[4] Henkelman, G., Arnaldsson, A. & Jónsson, H. A fast and robust algorithm for bader decomposition of charge density. *Comput. Mater. Sci.* **36**, 354–360 (2006). URL `https://www.sciencedirect.com/science/article/pii/S0927025605001849`.

[5] Yu, M. & Trinkle, D. R. Accurate and efficient algorithm for bader charge integration. *J. Chem. Phys.* **134**, 064111 (2011). URL `https://doi.org/10.1063/1.3553716`. `https://doi.org/10.1063/1.3553716`.

[6] Yates, J. R., Wang, X., Vanderbilt, D. & Souza, I. Spectral and fermi surface properties from wannier interpolation. *Phys. Rev. B* **75**, 195121 (2007).

[7] Wang, X., Yates, J. R., Souza, I. & Vanderbilt, D. Ab initio calculation of the anomalous hall conductivity by wannier interpolation. *Phys. Rev. B* **74**, 195118 (2006).

[8] Yu, D. *et al.* Aromaticity and antiaromaticity of substituted fulvene derivatives: perspectives from the information-theoretic approach in density functional reactivity theory. *Phys. Chem. Chem. Phys.* **19**, 18635–18645 (2017).

[9] Shannon, C. E. A mathematical theory of communication. *Bell Syst. Tech. J.* **27**, 379–423 (1948).

Bibliography

[1] Frenkel, J. On the transformation of light into heat in solids. I. *Physical Review* **37**, 17–44 (1931).

[2] Knox, R. S. *Introduction to Exciton Physics*, 183–245 (Springer US, Boston, MA, 1983).

[3] Bechstedt, F. *Many-body approach to electronic excitations: Concepts and applications*, vol. 181 of *Springer series in solid-state sciences* (Springer, Heidelberg and New York, 2015).

[4] Gershenson, M. E., Podzorov, V. & Morpurgo, A. F. Colloquium: Electronic transport in single-crystal organic transistors. *Reviews of Modern Physics* **78**, 973–989 (2006).

[5] Ostroverkhova, O. Organic optoelectronic materials: Mechanisms and applications. *Chemical Reviews* **116**, 13279–13412 (2016).

[6] Yuan, Y. *et al.* Ultra-high mobility transparent organic thin film transistors grown by an off-centre spin-coating method. *Nature Communications* **5**, 3005 (2014).

[7] Briseno, A. L. *et al.* Patterning organic single-crystal transistor arrays. *Nature* **444**, 913–917 (2006).

[8] Reineke, S., Thomschke, M., Lüssem, B. & Leo, K. White organic light-emitting diodes: Status and perspective. *Reviews of Modern Physics* **85**, 1245–1293 (2013).

[9] Gillett, A. J. *et al.* The role of charge recombination to triplet excitons in organic solar cells. *Nature* **597**, 666–671 (2021).

[10] Riede, M. K. *et al.* Recent progress in organic solar cells based on small molecules. *Photonics for Solar Energy Systems II* **7002**, 94–101 (2008).

[11] Xing, S. *et al.* Miniaturized VIS-NIR spectrometers based on narrowband and tunable transmission cavity organic photodetectors with ultrahigh specific detectivity above 10^{14} Jones. *Advanced Materials* **33**, 2102967 (2021).

[12] Feng, X., Ding, X. & Jiang, D. Covalent organic frameworks. *Chemical Society Reviews* **41**, 6010–6022 (2012).

[13] Diercks, C. S. & Yaghi, O. M. The atom, the molecule, and the covalent organic framework. *Science* **355**, eaal1585 (2017).

[14] Geng, K. *et al.* Covalent organic frameworks: Design, synthesis, and functions. *Chemical Reviews* **120**, 8814–8933 (2020).

[15] Yang, Y. & Börjesson, K. Electroactive covalent organic frameworks: a new choice for organic electronics. *Trends in Chemistry* **4**, 60–75 (2022).

[16] Ding, S.-Y. & Wang, W. Covalent organic frameworks (COFs): from design to applications. *Chemical Society Reviews* **42**, 548–568 (2013).

[17] Xiao, L., Wang, Z. & Guan, J. Optimization strategies of covalent organic frameworks and their derivatives for electrocatalytic applications. *Advanced Functional Materials* 2310195 (2023).

[18] Auras, F. *et al.* Synchronized offset stacking: A concept for growing large-domain and highly crystalline 2D covalent organic frameworks. *Journal of the American Chemical Society* **138**, 16703–16710 (2016).

[19] Kubo, R. Statistical-mechanical theory of irreversible processes. I. general theory and simple applications to magnetic and conduction problems. *Journal of the Physical Society of Japan* **12**, 570–586 (1957).

[20] Kubo, R., Toda, M. & Hashitsume, N. *Statistical physics 2 Nonequilibrium statistical mechanics* (Springer, Berlin, 1998), 2. edn.

[21] Czycholl, G. *Theoretische Festkörperphysik - Von den klassischen Modellen zu modernen Forschungsthemen* (Springer-Verlag, Berlin Heidelberg New York, 2007), 3. edn.

[22] Nolting, W. *Grundkurs Theoretische Physik 7 Viel-Teilchen-Theorie* (Springer Spektrum, Berlin, 2015), 8. edn.

[23] Martin, R. M., Reining, L. & Ceperley, D. M. *Interacting electrons* (Cambridge University Press, 2016).

[24] Mukamel, S. *Principles of Nonlinear Optical Spectroscopy*. Oxford series in optical and imaging sciences (Oxford University Press, 1995).

[25] Mahan, G. D. *Many-particle physics* (Kluwer Academic/Plenum Publishers, New York, 2000), 3. edn.

[26] Paleari, F. *First-principles approaches to the description of indirect absorption and luminescence spectroscopy: exciton-phonon coupling in hexagonal boron nitride*. dissertation, Universite du Luxembourg (2019).

[27] Hohenberg, P. & Kohn, W. Inhomogeneous electron gas. *Physical Review* **136**, B864–B871 (1964).

[28] Kohn, W. Nobel lecture: Electronic structure of matter—wave functions and density functionals. *Reviews of Modern Physics* **71**, 1253–1266 (1999).

[29] Kohn, W. & Sham, L. J. Self-consistent equations including exchange and correlation effects. *Physical Review* **140**, A1133–A1138 (1965).

[30] Kurth, S., Perdew, J. P. & Blaha, P. Molecular and solid-state tests of density functional approximations: LSD, GGAs, and meta-GGAs. *International Journal of Quantum Chemistry* **75**, 889–909 (1999).

[31] Sousa, S. F., Fernandes, P. A. & Ramos, M. J. General performance of density functionals. *The Journal of Physical Chemistry A* **111**, 10439–10452 (2007).

[32] Mardirossian, N. & Head-Gordon, M. Thirty years of density functional theory in computational chemistry: an overview and extensive assessment of 200 density functionals. *Molecular Physics* **115**, 2315–2372 (2017).

[33] Perdew, J. P., Burke, K. & Ernzerhof, M. Generalized gradient approximation made simple. *Physical Review Letters* **77**, 3865–3868 (1996).

[34] Lee, I.-H. & Martin, R. M. Applications of the generalized-gradient approximation to atoms, clusters, and solids. *Physical Review B* **56**, 7197–7205 (1997).

[35] Sun, G. *et al.* Performance of the Vienna ab initio simulation package (VASP) in chemical applications. *Journal of Molecular Structure: THEOCHEM* **624**, 37–45 (2003).

[36] De La Pierre, M. *et al.* Performance of six functionals (LDA, PBE, PBESOL, B3LYP, PBE0, and WC1LYP) in the simulation of vibrational and dielectric properties of crystalline compounds. the case of forsterite Mg2SiO4. *Journal of Computational Chemistry* **32**, 1775–1784 (2011).

[37] Hybertsen, M. S. & Louie, S. G. First-principles theory of quasiparticles: Calculation of band gaps in semiconductors and insulators. *Physical Review Letters* **55**, 1418–1421 (1985).

[38] Onida, G., Reining, L. & Rubio, A. Electronic excitations: density-functional versus many-body Green's-function approaches. *Reviews of Modern Physics* **74**, 601–659 (2002).

[39] Hybertsen, M. S. & Louie, S. G. Electron correlation in semiconductors and insulators: Band gaps and quasiparticle energies. *Physical Review B* **34**, 5390–5413 (1986).

[40] Godby, R. W., Schlüter, M. & Sham, L. J. Trends in self-energy operators and their corresponding exchange-correlation potentials. *Physical Review B* **36**, 6497–6500 (1987).

[41] Godby, R. W., Schlüter, M. & Sham, L. J. Self-energy operators and exchange-correlation potentials in semiconductors. *Physical Review B* **37**, 10159–10175 (1988).

[42] Aryasetiawan, F. & Gunnarsson, O. The GW method. *Reports on Progress in Physics* **61**, 237 (1998).

[43] Shishkin, M. & Kresse, G. Self-consistent GW calculations for semiconductors and insulators. *Physical Review B* **75** (2007).

[44] Golze, D., Dvorak, M. & Rinke, P. The GW compendium: A practical guide to theoretical photoemission spectroscopy. *Frontiers in Chemistry* **7**, 377 (2019).

[45] Galitskii, V. M. & Migdal, A. B. Application of quantum field theory methods to the many body problem. *Soviet Physics JETP* **7**, 18 (1958).

[46] Strinati, G. Application of the Green's functions method to the study of the optical properties of semiconductors. *La Rivista del Nuovo Cimento (1978-1999)* **11**, 1–86 (1988).

[47] Hedin, L. New method for calculating the one-particle Green's function with application to the electron-gas problem. *Physical Review* **139**, A796–A823 (1965).

[48] Baym, G. & Kadanoff, L. P. Conservation laws and correlation functions. *Physical Review* **124**, 287–299 (1961).

[49] Baym, G. Self-consistent approximations in many-body systems. *Physical Review* **127**, 1391–1401 (1962).

[50] Hedin, L. & Lundqvist, S. Effects of electron-electron and electron-phonon interactions on the one-electron states of solids. In Seitz, F., Turnbull, D. & Ehrenreich, H. (eds.) *Solid State Physics*, vol. 23 of *Solid State Physics*, 1–181 (Academic Press, 1970).

[51] Salpeter, E. E. & Bethe, H. A. A relativistic equation for bound-state problems. *Physical Review* **84**, 1232–1242 (1951).

[52] Sham, L. J. & Rice, T. M. Many-particle derivation of the effective-mass equation for the Wannier exciton. *Physical Review* **144**, 708–714 (1966).

[53] Hanke, W. & Sham, L. J. Many-particle effects in the optical spectrum of a semiconductor. *Physical Review B* **21**, 4656–4673 (1980).

[54] Strinati, G. Effects of dynamical screening on resonances at inner-shell thresholds in semiconductors. *Physical Review B* **29**, 5718–5726 (1984).

[55] Blase, X., Duchemin, I., Jacquemin, D. & Loos, P.-F. The Bethe–Salpeter equation formalism: From physics to chemistry. *The Journal of Physical Chemistry Letters* **11**, 7371–7382 (2020).

[56] Pick, R. M., Cohen, M. H. & Martin, R. M. Microscopic theory of force constants in the adiabatic approximation. *Physical Review B* **1**, 910–920 (1970).

[57] Watt, S. M. Pivot-free block matrix inversion. In *2006 Eighth International Symposium on Symbolic and Numeric Algorithms for Scientific Computing*, 151–155 (2006).

[58] Mostafazadeh, A. Pseudo-Hermiticity versus PT-symmetry III: Equivalence of pseudo-Hermiticity and the presence of antilinear symmetries. *Journal of Mathematics and Physics* **43**, 3944–3951 (2002).

[59] Benedict, L. X., Shirley, E. L. & Bohn, R. B. Theory of optical absorption in diamond, Si, Ge, and GaAs. *Physical Review B* **57**, R9385–R9387 (1998).

[60] Rohlfing, M. & Louie, S. G. Electron-hole excitations and optical spectra from first principles. *Physical Review B* **62**, 4927–4944 (2000).

[61] Grüning, M., Marini, A. & Gonze, X. Exciton-plasmon states in nanoscale materials: Breakdown of the Tamm-Dancoff approximation. *Nano Letters* **9**, 2820–2824 (2009).

[62] Puschnig, P., Meisenbichler, C. & Draxl, C. Excited state properties of organic semiconductors: breakdown of the Tamm-Dancoff approximation. *arXiv preprint arXiv:1306.3790* (2013).

[63] Gajdoš, M., Hummer, K., Kresse, G., Furthmüller, J. & Bechstedt, F. Linear optical properties in the projector-augmented wave methodology. *Physical Review B* **73**, 045112 (2006).

[64] Marini, A., Hogan, C., Grüning, M. & Varsano, D. yambo: An ab initio tool for excited state calculations. *Computer Physics Communications* **180**, 1392–1403 (2009).

[65] Deslippe, J. *et al.* BerkeleyGW: A massively parallel computer package for the calculation of the quasiparticle and optical properties of materials and nanostructures. *Computer Physics Communications* **183**, 1269–1289 (2012).

[66] Kresse, G. & Hafner, J. Ab initio molecular dynamics for liquid metals. *Physical Review B* **47**, 558–561 (1993).

[67] Kresse, G. & Furthmüller, J. Efficiency of ab-initio total energy calculations for metals and semiconductors using a plane-wave basis set. *Computation Materials Science* **6**, 15–50 (1996).

[68] Kresse, G. & Furthmüller, J. Efficient iterative schemes for ab initio total-energy calculations using a plane-wave basis set. *Physical Review B* **54**, 11169–11186 (1996).

[69] Giannozzi, P. *et al.* Quantum espresso: a modular and open-source software project for quantum simulations of materials. *Journal of Physics: Condensed Matter* **21**, 395502 (2009).

[70] Wannier, G. H. The structure of electronic excitation levels in insulating crystals. *Physical Review* **52**, 191–197 (1937).

[71] Marzari, N. & Vanderbilt, D. Maximally localized generalized Wannier functions for composite energy bands. *Physical Review B* **56**, 12847–12865 (1997).

[72] Souza, I., Marzari, N. & Vanderbilt, D. Maximally localized Wannier functions for entangled energy bands. *Physical Review B* **65** (2001).

[73] Marzari, N., Mostofi, A. A., Yates, J. R., Souza, I. & Vanderbilt, D. Maximally localized Wannier functions: Theory and applications. *Reviews of Modern Physics* **84**, 1419–1475 (2012).

[74] Boys, S. F. Construction of some molecular orbitals to be approximately invariant for changes from one molecule to another. *Reviews of Modern Physics* **32**, 296–299 (1960).

[75] Foster, J. M. & Boys, S. F. Canonical configurational interaction procedure. *Reviews of Modern Physics* **32**, 300–302 (1960).

[76] Edmiston, C. & Ruedenberg, K. Localized atomic and molecular orbitals. *Reviews of Modern Physics* **35**, 457–464 (1963).

[77] Brouder, C., Panati, G., Calandra, M., Mourougane, C. & Marzari, N. Exponential localization of Wannier functions in insulators. *Physical Review Letters* **98**, 046402 (2007).

[78] Hamann, D. R. & Vanderbilt, D. Maximally localized Wannier functions for GW quasiparticles. *Physical Review B* **79** (2009).

[79] Holstein, T. Studies of polaron motion: Part I. the molecular-crystal model. *Annals of Physics* **8**, 325 – 342 (1959).

[80] Hutsch, S., Panhans, M. & Ortmann, F. Time-consistent hopping transport with vibration-mode-resolved electron-phonon couplings. *Physical Review B* **104**, 054306 (2021).

[81] Holstein, T. Studies of polaron motion: Part II. the "small" polaron. *Annals of Physics* **8**, 343 – 389 (1959).

[82] Hannewald, K. & Bobbert, P. A. Ab initio theory of charge-carrier conduction in ultrapure organic crystals. *Applied Physics Letters* **85**, 1535–1537 (2004).

[83] Hannewald, K. *et al.* Theory of polaron bandwidth narrowing in organic molecular crystals. *Physical Review B* **69**, 075211 (2004).

[84] Troisi, A. & Orlandi, G. Dynamics of the intermolecular transfer integral in crystalline organic semiconductors. *The Journal of Physical Chemistry A* **110**, 4065–4070 (2006).

[85] Troisi, A. Charge transport in high mobility molecular semiconductors: classical models and new theories. *Chemical Society Reviews* **40**, 2347–2358 (2011).

[86] Panhans, M., Hutsch, S. & Ortmann, F. Insight on charge-transfer regimes in electron-phonon coupled molecular systems via numerically exact simulations. *Communications Physics* **6**, 125 (2023).

[87] Merkel, K., Panhans, M., Hutsch, S. & Ortmann, F. Interplay of band occupation, localization, and polaron renormalization for electron transport in molecular crystals: Naphthalene as a case study. *Physical Review B* **105**, 165136 (2022).

[88] Fernandez, I. *Aromaticity: Modern Computational Methods and Applications* (Elsevier, 2021).

[89] Merkel, K., Greiner, J. & Ortmann, F. Understanding the electronic pi-system of 2D covalent organic frameworks with Wannier functions. *Scientific Reports* **13**, 1685 (2023).

[90] Ljungberg, M. P., Koval, P., Ferrari, F., Foerster, D. & Sánchez-Portal, D. Cubic-scaling iterative solution of the Bethe-Salpeter equation for finite systems. *Physical Review B* **92**, 075422 (2015).

[91] Marsili, M., Mosconi, E., De Angelis, F. & Umari, P. Large-scale GW-BSE calculations with N^3 scaling: Excitonic effects in dye-sensitized solar cells. *Physical Review B* **95**, 075415 (2017).

[92] Merkel, K. & Ortmann, F. Linear scaling approach for optical excitations using maximally localized Wannier functions. *Journal of Physics: Materials* **7**, 015001 (2023).

[93] Merkel, K., Link, V., Luoma, K. & Strunz, W. T. Phase space theory for open quantum systems with local and collective dissipative processes. *Journal of Physics A: Mathematical and Theoretical* **54**, 035303 (2020).